High-Lewis Number Premixed Flame Instabilities

A Thesis

Submitted to the Faculty

of

Drexel University

by

Yi Ma

in partial fulfillment of the

requirements for the degree

of

Doctor of Philosophy

September 2009

Acknowledgements

It has been a great blessing being a graduate student under the supervision of Dr. Howard Pearlman. My appreciation of his generosity, tolerance, support and guidance through my long journey of Ph.D. study is beyond words. He is not only a very knowledgeable scholar but also a very kind and inspiring person. What I have learned from him will benefit me for my whole life. In addition, I would like to thank my committee members, Dr. Nicholas P. Cernansky, Dr. David L. Miller, Dr. Alan Lau and Dr. Smitesh Bakrania for their time and energy to review this dissertation.

I must acknowledge a few of my colleagues in Hess Lab, Mike Foster, Rodney Johnson, Ashutosh Gupta, and Seul H. Park, among others, and my best friend Meline Zeng for their friendship and assistance for all these years. I would also like to thank two former undergraduate students, Christopher Ricciuti and Brian Fellon, for their contribution to the nano-size catalytic platinum particle project. Finally, the staff at the Machine Shop, namely Mark Shirber and Richard Miller have been very helpful modifying my experimental facility during various stages of this research.

I would like to give special thanks to my husband David B. Lenhert for his endless love, tremendous help and encouragement during my Ph.D. study. Finally, my thanks go to my parents Zhong Hejiao and Ma Qingyun for their unconditional love, care and support over the years.

This work was partially funded by NASA Office of Biological and Physical Research Grant (Grant No. NCC3-854) and NSF CBET Combustion and Plasma Systems (Grant No. 0755740). Their funding was greatly appreciated.

Table of Contents

List of Tables

List of Figures

Abstract

High-Lewis Number Premixed Flame Instabilities

Yi Ma

Howard Pearlman, Ph.D.

Lean premixtures of high-molecular weight practical fuels typically have an associated Lewis number (Le) in excess of one and are susceptible to diffusive-thermal instabilities depending on the heat loss and hydrodynamic strain. These instabilities may lead to incomplete combustion, an increase in undesirable emissions and complex pressure oscillations.

While a significant amount of work has focused on low-Lewis number cellular instabilities, the objective of this study was to explore high-Lewis number pulsating and traveling wave instabilities in burner-stabilized premixed gas flames and to improve our understanding of the role of the mixture Le, mixture composition, heat loss and ambient pressure on the onset and dynamics of the flame instabilities. To meet this objective, premixtures of n-C_4H_{10}, n-C_7H_{16} and n-C_8H_{18} mixed with O_2 diluted by N_2 or He were considered at different pressures for which high speed videos of different flame instability modes were acquired. The instability regimes included: (1) stable planar flames, (2) complex spiral or target patterns, (3) spiral waves and (4) axisymmetric target patterns, and they generally occurred in this order as the equivalence ratio was decreased for a fixed burner exit speeds. Stability diagrams were then developed as a function of equivalence ratio and burner exit flow speed for the mixtures considered. The effects of Le, heat loss and ambient pressure on the dynamics of the flame instability including the oscillation frequency in the case of target patterns and rotation rate for the rotating spiral

waves. Note that the radial propagation speed of the flamelets ranged from 2 to 5 m/s which is significantly faster than the laminar flame speed for premixed flames.

Numerical studies were also conducted using the 2-step Sal'nikov model developed by Scott-Wang-Showalter and Matkowsky with a focus on improving our understanding of the spatio-temporal structure of these unstable flames. The spatio-temporal temperature and species concentration were computed in a two-dimensional domain. The computed results were used to clarify the roles of Le and heat loss on the radial flame speed, the spacing between adjacent waves and the rotation frequency associated with the spiral waves. The numerical computations agreed favorably with the experimental observations.

1. Introduction

1.1 Overview

Self-organized target and rotating spiral waves have been observed in a wide variety of chemical and biological systems. These systems include the oxidation of malonic acid otherwise known as the Belousov-Zhabotinsky (BZ) reaction (Epstein and Pojman, 1998), the formation of spiral colonies of Dictyostelium Discoideum slime molds (Siegert and Weijer, 1989), the iodate-arsenite reaction (Ganaathisubramanian and Showalter, 1984), electrical oscillations emitted from the heart's sinoatrial node (Davidenko et al., 1992) and calcium waves in Xenopus oocytes (Lechleiter et al., 1991). While the details of the chemistry and the feedback mechanisms in these systems are clearly different, similar spatio-temporal patterns are formed over a broad range of length and time scales.

The existence of such chemical oscillators was originally discounted and believed to violate the second law of thermodynamics (Epstein and Pojman, 1998). Even Belousov's original work was rejected by the scientific community until it was later recognized that non-equilibrium thermodynamics could allow for such oscillations in reactive-diffusive systems that exist far-from-equilibrium.

In the area of combustion, similar patterns that consist of target and rotating wave instabilities were observed in the catalysis of carbon monoxide oxidation on platinum (Lauterbach et al., 1993), yet were only recently observed in gas-phase combustion. In particular, rich hydrogen-air premixtures at elevated pressure (Jomaas et al., 2007), downwardly-propagating hydrocarbon-air and hydrocarbon-oxygen premixed flames in large diameter tubes and burner-stabilized premixed flames (Pearlman and Ronney,

1994b; Pearlman and Ronney, 1994a; Pearlman, 1997) exhibit similar patterns. Like most other systems, combustion reactions are reactive-diffusive systems although thermal, in addition to mass, diffusion, can play an important role. In contrast, most other reactive-diffusive systems are nearly isothermal and species diffusion is the dominant transport process. To highlight the different modes of reaction observed in premixed gas combustion, images of target patterns (Figure 1a) and spiral waves (Figure 1b) are shown in Figure 1. For reference, these images are radial views of the flame downwardly propagating in a vertically-oriented tube opened at the top and closed at the bottom filled with a lean n-butane-oxygen mixture diluted with helium.

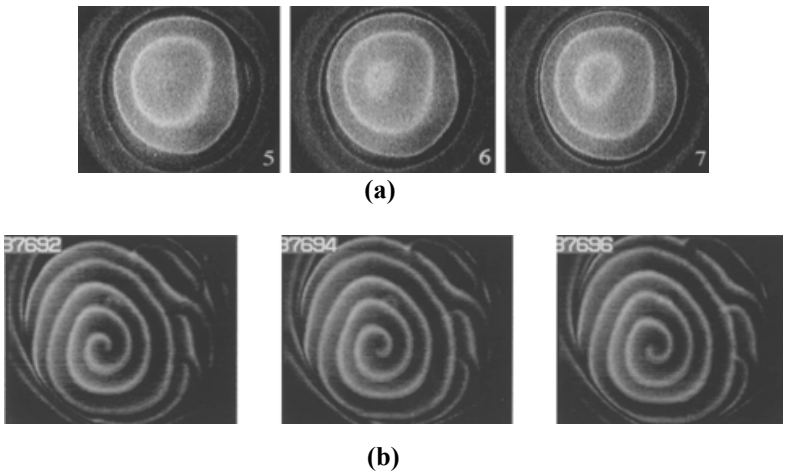

Figure 1: Time sequence of target patterns and spiral waves in propagating flame front. (a) Target pattern with successive waves emitted from pacemaker source, 1.46 % n-C_4H_{10}-21% oxygen – balance He. (b) Spiral wave rotating counter-clockwise on flame front, 0.8% n- C_8H_{18}-21% oxygen – balance He. Tube diameter is 28.5 cm i.d. and 1.5 m long. Images were taken at 1/500 sec (Pearlman and Ronney, 1994b; Pearlman and Ronney, 1994a; Pearlman, 1997).

Original observations suggest that the patterns are a manifestation of the diffusive-thermal traveling and pulsating instabilities that are predicted to occur in high-Lewis

number (Le) premixtures (Sivashinsky, 1977a; Joulin and Clavin, 1979). Subsequent experimental studies on burner-stabilized flames using lean mixtures of methane-air (Le = 0.93), rich mixtures of propane-air (Le = 1.05) and rich mixtures of butane-air (Le = 1.03) have also displayed evidence of target and spiral wave instabilities (Pearlman, 1997). The existence of these instabilities in premixtures with near unity Le's raises doubt that the high-Le diffusive-thermal instability is the driving mechanism, yet at the same time, it should be recognized that linear stability theories predict that the value of the critical Lewis number for onset of instability decreases with increasing volumetric heat loss (Joulin and Clavin, 1979).

Following these observations, efforts to predict target and spiral flames in premixed gases were undertaken by Scott and co-workers who developed a relatively simple two-dimensional, nonadiabiatic, reactive-diffusive Sal'nikov two-step skeletal model (Scott et al., 1997). That model successfully predicted the occurrence of target and spiral waves and further suggested that these modes can develop for $Le < 1$ and $Le \geq 1$ provided the system is “excitable”. Historically, excitable systems refer to such systems that have a stationary solution, yet if a sufficiently large disturbance occurs, the system becomes unstable and transitions to an "excitable state" only to return to the stationary solution later. This mechanism can be used to predict target and spiral waves in multi-dimensional systems as the solution oscillates between a stationary solution and an "excited" state. While excitable models are used to model many of the systems mentioned above, it is not clear that combustion reactions are excitable since the reactants are irreversibly converted to products and not regenerated as occurs in many of the other systems, i.e., combustion reactions are one-off reactions. Perhaps, the continuous supply

of unburned reactants in burner-stabilized flames is sufficient to maintain the oscillation, yet it is not entirely clear that they qualify as excitable systems in the conventional use of the term. More recently, Panfilov and co-workers have developed a refined model based on the same two-step Sal'nikov scheme and refute the importance of excitability in combustion systems. Instead, their model suggests that target and spiral waves can develop in premixed gases and their occurrence and spatio-temporal structure depends on several parameters that include the Le, Zel'dovich (Ze or β), heat loss and the burned to the unburned gas densities ($\sigma = \rho_b/\rho_u$) (Panfilov et al., 2003). Yuan and co-workers have also developed a fully compressible model that evaluated the coupled effects of diffusive-thermal instabilities and hydrodynamic instabilities on both laminar and turbulent flames. In particular, the roles of Le, pressure, density ratio and turbulent intensity on the onset of instability were considered. In this study, the focus was to understand the coupling of the two instability mechanisms and explore the conditions for which each of the two instability mechanisms can promote or suppress the onset of the other (Yuan et al., 2006).

The overall focus for the research conducted in this thesis was to clarify the mechanism(s) responsible for the different flame patterns and then determine their dependencies on the flow and mixture properties. Both experiments and numerical simulations were conducted. The experiments were performed on burner-stabilized premixed gas flames for pressures up to 1000 Torr with a focus on lean premixtures of high molecular weight fuels that have a Le > 1. Effects of the mixture stoichiometries, flow conditions, conduction heat loss to the burner and ambient pressure were systematically studied. Burner-stabilized flames were studied in an effort to stabilize the flame in contrast to previous studies in which the flames were moving (i.e., downwardly-

propagating flames in tubes and spherically-expanding flames), thus enabling the use of additional diagnostics without having to dynamically track the flame as it propagates in the vessel.

To compliment the experiments, numerical simulations were also conducted to analyze the role of the Le, heat loss, Ze and σ (hot gas expansion) on the flame patterns. These results were then qualitatively compared with the experimental observations. These results will be discussed in detail in Chapters 2 - 4.

1.2 Background and Literature Review

To understand and be able to predict the onset of flame instabilities, theoretical, numerical and experimental studies have focused on diffusive-thermal and hydrodynamic flame instability mechanisms. The diffusive-thermal mechanism results from an imbalance in the rate of heat and species diffusion while the hydrodynamic instability occurs as a results of the change in gas density across the flame front (Darrieus, 1938; Landau, 1944). At low-Le (Le < 1), the diffusive-thermal instability often manifests itself in the form of cellular flames as predicted from an adiabatic linear stability analysis (Sivashinsky, 1977a; Joulin and Clavin, 1979) and extensively studied by Markstein (Markstein, 1964). It has further been shown experimentally and analytically that the parameter space for the existence of cellular instabilities broadens as the volumetric heat loss increases, thus the instabilities occur more readily when the heat loss is significant as in the case of near-limit flames (Joulin and Clavin, 1979). For premixtures with sufficiently high-Le's (Le >>1), stability analyses predicted traveling, pulsating and pulsating-traveling wave instabilities, yet few experimental studies have been performed

since most premixtures have a Le near one with the exception of lean premixtures of heavy fuels that have large Le's owed to the relatively low mass diffusivity of the fuel in the mixture. Additional studies have also received recent attention in an effort to characterize the nonlinear couplings between the diffusive-thermal instability and the hydrodynamic instability (Yuan et al., 2006). In the next sections, the relevant literature on diffusive-thermal instabilities and hydrodynamic instabilities in premixed gas combustion is summarized.

1.2.1 Diffusive-Thermal Cellular Instability (Le < 1)

Cellular flame instabilities have received significant attention because it readily occurs in rich hydrocarbon-air mixtures or lean hydrogen-air mixtures (Le < 1). As early as the mid-1940s, Zel'dovich proposed a phenomenological explanation to explain the mechanism by which a perturbation may grow on an otherwise planar flame front and develops into a cellular flame or remain planar (Zeldovich, 1944). When a planar flame is spatially perturbed as shown in Figure 2 (Law, 2006), heat conduction at the crests tends to decrease the curvature of the flame by lowering the local flame temperature and thus reaction rate, thus stabilizing the flame in these regions. At the same time, heat is also focused at the concave sections, increasing the local flame temperature and resulting reaction rate and thus flame speed. Therefore, the heat diffusion has a stabilizing influence.

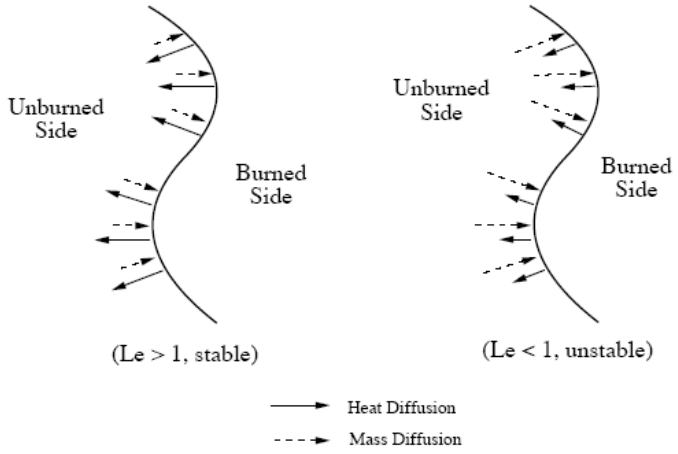

Figure 2: The mechanism of the diffusive-thermal cellular instability (Law, 2006).

In contrast, species diffusion of the rate-limiting component has the opposite effect. The regions of the flame that are convex toward the fresh mixture are locally richer relative to the plane flame configuration and the concave sections are leaner. The reaction rate and flame speed in the convex regions then increase and the front curvature increases, thus amplifying the instability. The amplification or suppression of the instability thus depends on the relative rates of heat and mass diffusion, i.e., Le, given by the ratio of the thermal diffusivity of the mixture ($\alpha_{mixture}$) to the mass diffusivity of the rate-limiting component into the mixture ($D_{\text{rate-limiting component}}$) .

For Le < 1, the diffusion of species is larger than thermal diffusion, and the convex section of the perturbed flame is amplified, while by the same argument, the concave section of the flame is suppressed. As a result, the perturbation grows. In contrast, for Le > 1, the opposite effect occurs and the flame is thermo-diffusively stable to perturbations along the flame front. However, as Le further increases, theory and experiments show that the flame eventually becomes unstable and pulsating, traveling

wave, and pulsating-traveling wave instabilities develop (Joulin and Clavin, 1979; Sivashinsky, 1983). It should also be noted that in this diffusive-thermal model, the density changes across the front are disregarded such that hydrodynamic effects cannot play a role.

1.2.1.1 Linear Stability Analyses

Barenblatt et al. performed a linear stability analysis of an adiabatic plane flame front and considered the effects of long-wave disturbances relative to the flame thermal thickness (Barenblatt et al., 1962). From this analysis, the following dispersion relation was obtained:

$$\omega = \alpha\left[\frac{1}{2}\beta(1-Le)-1\right]n^2 \qquad (1)$$

where α is the thermal diffusivity, $\beta = E_a(T_b - T_u)/RT_b^2$ is the Zel'dovich Number; $Le = \alpha / D$ is the Lewis number based on the mass diffusivity of the limiting reactant, which is assumed to be strongly deficient; ω is the growth rate-of-instability parameter; and n is the wave number. In this analysis, the temperature is also perturbed in space and time, $T \sim \exp(\omega t + \sin\cdot x)$. From this analysis, the flame is stable only if the diffusion of the rate limiting reactant is sufficiently small such that the $Le > Le_c = 1 - 2/\beta$; for typical premixed gas flames, β =15, thus $Le_c = 0.87$. For $Le < Le_c$, the flame is unstable.

Sivashinsky subsequently extended the same adiabatic stability analysis and further showed that not all perturbation wavelengths are unstable when the Le < Le_c (Sivashinsky, 1977a). In fact, short-wave disturbances were shown to lead to stable flames, while long-wave disturbances were destabilizing. In this analysis which was

found on large activation energy asymptotics and the assumption that the $Le \approx Le_c$, a modified dispersion relation was obtained with an additional stabilizing term:

$$\omega = \alpha\left[\frac{1}{2}\beta(1-Le)-1\right]k^2 - 4\alpha l_f^2 n^4 \qquad (2)$$

where l_f is the flame thickness. Thus, for $Le < Le_c$, the flame is unstable to any perturbation, yet at large wavenumbers (large n corresponds to small wavelengths, $n = 2\pi/\kappa$), $\omega < 0$ and the flames become stable.

The effects of heat loss were subsequently included in Sivashinsky's model by Joulin and Clavin (Joulin and Clavin, 1979). Their nonadiabatic analysis showed that the Le_c for onset of the low-Le cellular flame instability boundary increased with increasing heat loss and approached unity at very large values of heat loss as may exist in near-limit flames (Joulin and Clavin, 1979).

1.2.1.2 Nonlinear Stability Analyses

While linear stability analyses can predict the growth rate of infinitesimal perturbations, nonlinear analyses are required to capture the growth of instability as the perturbations are amplified. Mechanisms of nonlinear flame stabilization have been proposed by Markstein (Markstein, 1952) and Zel'dovich (Zeldovich, 1966) based on Huygens principle. Sivashinsky also derived a rigorous asymptotic relation from the constant-density flame model and pointed out that the main nonlinear effects are purely kinematic in nature, which agreed with Zel'dovich's arguments (Sivashinsky, 1977b). More recent numerical models have been developed based on the Kuramoto-Sivashinsky equation and two-dimensional analyses showed that a cellular flame can develop with an

average cell size that is larger than the critical cell size predicted by linear analyses (Michelson and Sivashinsky, 1977). Recently, the nonlinear problem was also studied by directly solving the 2D diffusive-thermal model of premixed flames (Denet and Haldenwang, 1992). In this study, it was shown that nonlinear effects play an important role in the motion of the cells, which can exhibit a chaotic self-motion similar to the Sivashinsky's model predictions (Michelson and Sivashinsky, 1977). In these linear and nonlinear models, the density was assumed to be constant, which enables the diffusive-thermal effects to be isolated yet the range of the validity of the constant density assumption is limited. The effects of thermal expansion (hydrodynamic effects) of the hot gas can be significant near Le_c and change the nature of the instability. This will be discussed below in the section on coupled effects.

1.2.1.3 Experimental Studies on Cellular Flames

Experimental studies on cellular flame instabilities have been extensively conducted since the 1960's. Perhaps, most noteworthy is Markstein's work which studied both one-dimensional experiments using a slot burner and two-dimensional experiments in freely-propagating glass tubes (Markstein, 1964). In his studies of one-dimensional cellular flames, two dynamical regimes were identified: (1) a steady regime characterized by regular cell structures along the burner length and (2) an unsteady regime in which the cells rapidly vibrated and/or translated. In his two-dimensional studies, the dynamics of the cellular flame were described to be an incessant irregular motion and too fast to be analyzed visually. Subsequent experiments have also been performed to quantify the size

of the cells as a function of the pressure, fuel type, flow rate and equivalence ratio (Mitani and Williams, 1980; Vantelon et al., 1986).

Cellular flames were also observed using high-speed schlieren photography in laminar lean propane-air flames confined in a constant-volume vessel (Groff, 1982). In this work, the transition from a smooth spherical flame front to polyhedral-cellular flames was recorded for pressures between 200-500 kPa and equivalence ratios between 0.7 to 1.0. For the lean mixture of propane-air considered, the Lewis number was estimated to be 1.8, such that these flames should not be cellularly unstable. Thus, the cellular structure observed for these conditions was caused by the hydrodynamic instability mechanism and the onset of the cellular flames corresponded to a critical flame Reynolds number (Re_{cr}) which was a function of the hot gas expansion. Cellular flames that result from hydrodynamic instabilities have been modeled theoretically by Istratov and Librovich and the predictions are in qualitative agreement with Groff's observations (Istrov and Librovich, 1966).

Using a similar setup (chamber) to that developed by Groff, Kwon and co-workers studied the effects of positive flame stretch on laminar burning velocities and conditions for transition to unstable flames based on measurements for freely propagating spherical flames in $H_2/O_2/N_2$ and $C_3H_8/O_2/N_2$ mixtures (Kwon et al., 1992). It was shown that both $H_2/O_2/N_2$ and $C_3H_8/O_2/N_2$ flames transitioned to cellular flames by hydrodynamic instability for stable diffusive-thermal conditions. Correlation of the transition for $H_2/O_2/N_2$ mixtures from stable to unstable flames was in good agreement with earlier results reported by Groff for propane-air flames.

Cellular flames were also observed in low-Le, unstable premixed flames on a flat porous-plug burner reported by Gorman and co-workers (el-Hamdi and Gorman, 1993; Gorman et al., 1994a, 1994b). Specifically, burner-stabilized flames on a water-cooled porous-plug McKenna burner were considered at low-pressure. Most of their experiments were conducted at 1/2 atm to suppress buoyancy complications. A number of different periodic states with different spatial and temporal characteristics were reported including cellular, pulsating, and chaotic dynamics (Gorman et al., 1994b). The modes observed depended on the mixture stoichiometry and burner exit flow speed. Interestingly, they observed that the dynamical modes were stable over a wider range of experimental parameters at reduced pressure than at atmospheric pressure, suggesting that buoyant convection has a destabilizing effect on the flames. While this was not discussed in their work, it is consistent with the work of Pelce and Clavin who showed buoyancy can destabilize short-wavelength disturbances in downwardly-propagating flames (Pelce and Clavin, 1982).

Recent experimental observations of cellular instabilities on spherically expanding flames of hydrogen and propane mixtures in air at elevated pressures were also reported by Law and co-workers (Law et al., 2005). The experiments were conducted in a constant pressure dual-chamber combustor with maximum pressure of 60 atm (Tse et al., 2004). Critical conditions for the onset of the cellular patterns were measured and mapped for a range of different parameters including pressure, mixture composition and equivalence ratio. For these overall lean hydrogen and propane mixtures, the fraction of oxygen consumed by the respective fuels δ was used as a mixing ratio of the fuel, where $\delta = \left(5X_{propane}\right)/\left(0.5X_{hydrogen} + 5X_{propane}\right)$. The equivalence ratio was then defined by

$\phi = \delta / \delta_{st}$ where δ_{st} is the stoichiometric value of δ. The experimental results showed that the smooth flame front became wrinkled and the critical condition of instability occurred earlier as pressure increases with fixed values of Φ and δ. This is because that the laminar flame speed ($s_{f,u}$) evaluated as dR(t)/dt decreased with the increased pressure which leads to decreasing flame thickness l_f ($l_f = (\lambda / c_P)/(\rho_u s_{f,u})$) and thus increased the trends of destabilizing. For different mixing ratios, an early onset of cellular instabilities was observed for δ = 0 (pure hydrogen) and no instability was noted for δ = 1 (pure propane) for the case of Φ = 0.8. For reference, the pure hydrogen/air mixture has Le = 0.41 and the pure propane/air mixture has a Le = 1.87. The results are consistent with the Sivashinsky's theoretical predictions (Sivashinsky, 1977a). In addition, different equivalence ratios were tested for a fixed mixing ratio δ = 0.5 where it was observed that the flame became increasingly stable as Φ increased (lean to rich) as expected.

1.2.2 Diffusive-Thermal Pulsating Target and Rotating Spiral Flame Instabilities (Le >> 1)

1.2.2.1 Theoretical and Numerical Studies

The full dispersion relation for the constant-density, adiabatic flame model reported by Sivashinsky showed that if $\frac{1}{2}\beta(Le-1) > 5$, and the real part of the instability rate ω is positive, then the flame was unstable (Sivashinsky, 1977a). This would occur for Lewis numbers that are relatively large, i.e., $Le > 10/\beta + 1$. Regions of flame stability would also occur for $-2 < I = \beta(Le-1) < 10$ (as shown in Figure 3) as determined by evaluating

solutions for which the *Re (ω) <0*. Here β is the Zel'dovich number and *Re (ω) is* the real part of the wave perturbation. Furthermore, the imaginary part of the perturbation *Im (ω)* does not vanish for cases with large Le ($Le > 10/\beta + 1$). These solutions with non-zero imaginary values of ω correspond to oscillations and travelling waves (Sivashinsky, 1983).

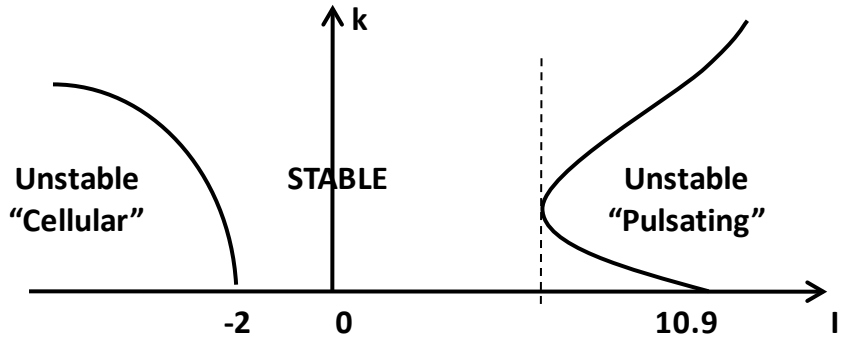

Figure 3: Predicted stability and instability regimes for premixed flames without heat loss (Sivashinsky, 1977a).

Adiabatic flames are therefore not susceptible to diffusive-thermal instabilities since Le_c for the onset of instability is generally larger than that for most premixtures. However, heat loss broadens the instability region and lowers Le_c which is destabilizing. Figure 4 shows a schematic of the stability diagram predicted by Joulin and Clavin (Joulin and Clavin, 1979). Another interesting feature of the nonadiabatic diffusive-thermal model is that it predicts two types of instabilities for high-Le cases in addition to the pulsating instability. These modes include a traveling wave instability in which a

wave travels along the reaction front and a traveling-pulsating instability that is characterized by a traveling wave that pulsates.

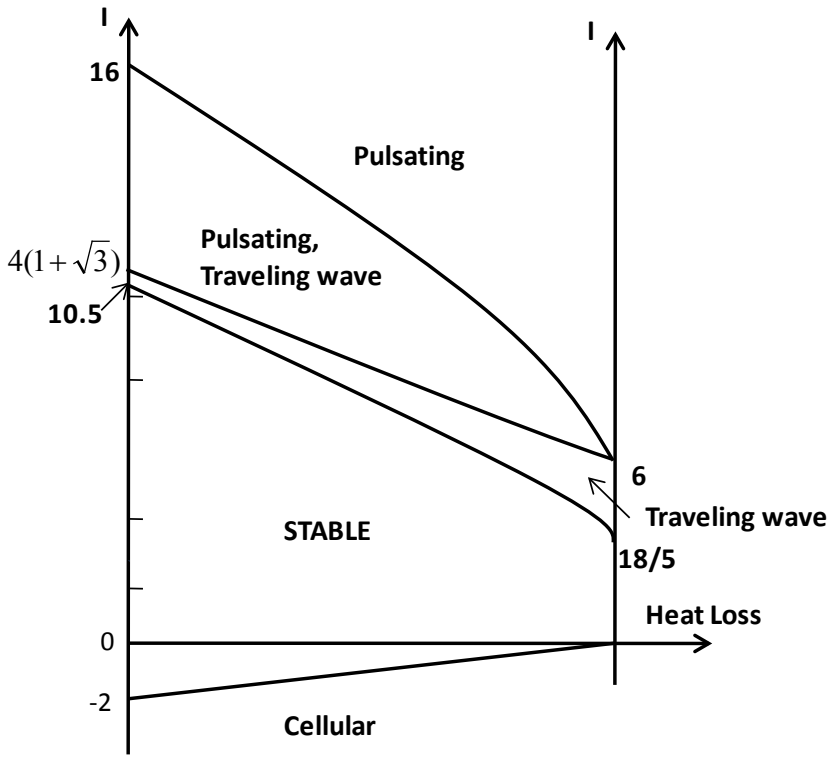

Figure 4: Instability regimes predicted by nonadiabatic stability analyses showing the effect of enhanced heat loss and its destabilizing influence on the diffusive-thermal instability (Joulin and Clavin, 1979).

A phenomenological explanation for the pulsating instability can be derived from the schematic shown in Figure 5 (Law, 2006). For flames that propagate into premixtures with Le > 1, the mass diffusion zone thickness is smaller than the thermal thickness. Axial perturbations of the flame toward the unburned reactants results in a reduction of mass diffusion thickness relative to the thermal thickness, which implies that the

concentration gradient increases more than the temperature gradient. As a result, the reaction zone is enriched and the flame front accelerates into the unburned reactants. By the same argument, a perturbation of the flame towards the products slows the reaction. Premixed flames with Le > 1 can therefore be pulsatingly unstable while flames with Le < 1 are pulsatingly stable.

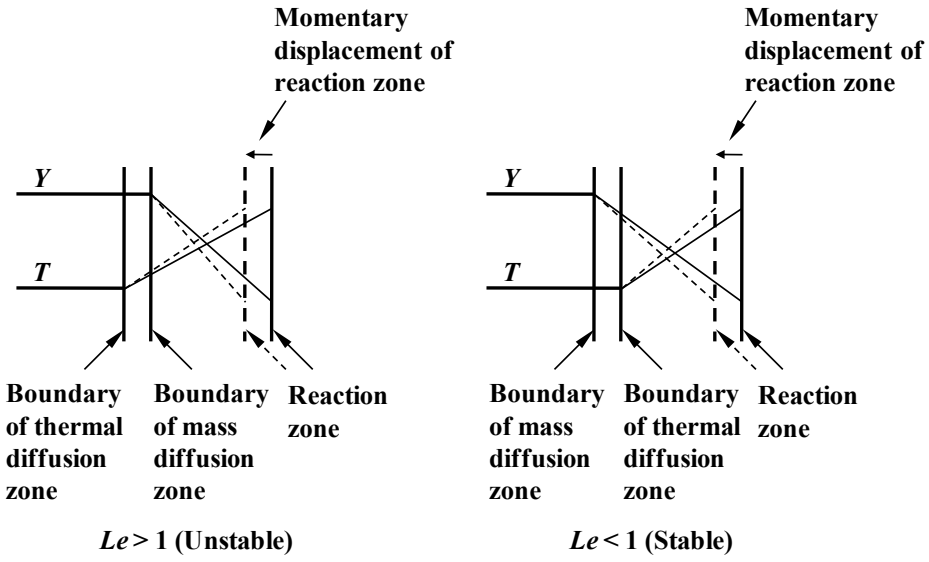

Figure 5: A phenomenological mechanism for the high-Le diffusive-thermal pulsating instability (Law, 2006).

Relatively few numerical studies have been conducted on high-Le instabilities since the Le's for onset of instability generally exceed those associated with many premixtures. Renewed interest in this area resulted from recent observations of target and spiral wave patterns in high-Le mixtures and further encouraged the development of models that

predict the onset and spatio-temporal dynamics of the instabilities are needed (Pearlman and Ronney, 1994b; Pearlman and Ronney, 1994a; Pearlman, 1997).

The first numerical two-dimensional study that addressed spiral and target patterns was reported in 1997 by Scott, Wang and Showalter who used a simple two-reaction model (the Sal'nikov model) to which they added diffusion of heat and species (Scott et al., 1997). A continuous reactant feed was assumed. The coupled species and energy equations were solved in a one-dimensional and a two-dimensional domain. The results predict target and spiral wave patterns that are qualitatively similar to the observations made in downwardly-propagating experiments for a range of Le including Le =1. However, the validity of the parameters used in the model for the overall heat loss (h) and the Zel'dovich number were later brought into question by Panfilov and co-workers (Panfilov et al., 2003).

Panfilov questioned the values of the heat loss parameter h (=3487) and Le (=1) considered by Scott, Wang and Showalter and reported that they were "not representative" of the experiments**.** Using more realistic values for Le (=4) and h ($\in [3,30]$), they then solved the same model with a different nondimensionalization in a 2D domain. Rotating spirals waves were predicted by their model as shown in Figure 6 taken from their results in order of increasing heat loss. From these images, it can be seen that as heat loss increases, the inter-wave spacing decreases and for some cases, the motion of the spiral tip is complex and simple periodic spirals may evolve into meandering spirals. In these cases, the tip of the spiral wave follows a repetitive "flower-like" trajectory. In these results, it should also be mentioned that the criteria used to

define the spiral tip was the location where intersection of the nondimensional temperature (θ) and the species concentrations (Y) were $\theta = 2.0, Y = 0.2$.

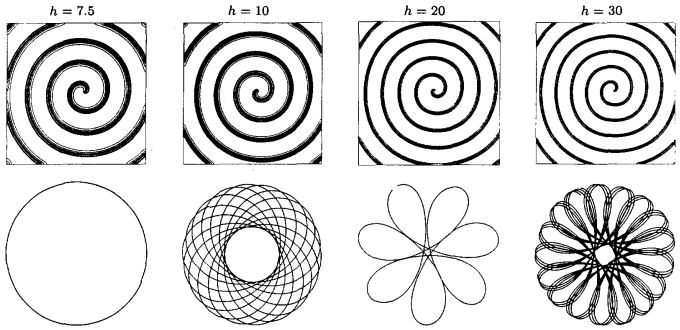

Figure 6: Temperature contours of spirals and their tip motions (Panfilov et al., 2003).

1.2.2.2 Experimental Studies on Target and Spiral Patterns

As mentioned, relatively few experiments have been conducted on target and spiral flame instabilities, yet some work in other areas may be relevant to help understand high-Le instabilities. One study reported by Gololobov on the decomposition of acetylene reposted spinning flames that were explained by high radiation thermal losses (Gololobov et al., 1981). Oscillating and spinning flames were also observed in solid phase combustion where the Le's are effectively infinite since the diffusivity of the fuel is negligibly small (Merzhanov et al., 1973). Oscillatory instability patterns were also predicted theoretically in burner-stabilized flames by Margolis (Margolis, 1980, 1981), Matkowsky and Olagunju (Matkowsky and Olagunju, 1981) and Buckmaster (Buckmaster, 1982). In these cases, high conductive heat loss to the burner was

considered and oscillatory flames were predicted even for relatively small Lewis numbers.

Well-defined exceptional observations of target and spiral waves were reported by Pearlman and Ronney in near limit, premixed flames using a mixture of heavy alkanes (n-butane, n-heptane, n-octane) diluted with 21% oxygen and a diluent (Ar, He, Ne, N_2) (Pearlman and Ronney, 1994b; Pearlman and Ronney, 1994a; Pearlman, 1997). Combinations of diluents were also considered to systematically vary the Le and thus explore the stability of the modes in premixtures with different diffusive properties. The use of different fuels also provided an opportunity to vary the chemistry and gain confidence that the instabilities were not dependent on a particular fuel chemistry. The experimental apparatus used in this study is reproduced in Figure 7. It consists of a 28.5cm i.d. diameter tube, 1.5m long, ignited at the open end (top) and closed at the bottom. The flame was imaged through a mirror mounted at a 45^o angle on the top of the tube.

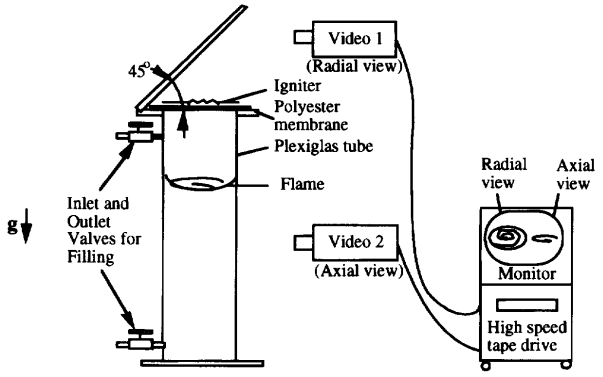

Figure 7: Experimental Apparatus (Pearlman and Ronney, 1994b; Pearlman and Ronney, 1994a; Pearlman, 1997).

In all cases, the reactants were initially well mixed and quiescent prior to ignition, yet perturbations introduced by the ignition process, buoyant flow, or otherwise were amplified and resulted in the instabilities. Two representative radial images of these downwardly-propagating flames were reproduced in Figure 1. A summary of some of the mixtures considered in prior studies is listed in Table 1.

Table 1: Summary of the premixtures studied in downwardly-propagating flames in high-Le premixtures in a vertically-oriented 28.5cm i.d. tube (Pearlman, 1997).

	Premixture	Le	λ (cm)	ω_{spiral} (Hz)	$V_{f,radial}$ (m/s)	$V_{f,axial}$ (cm/s)	Instability
1	5.8% CH_4 - 21%O_2 – balance He	1.8	-	-	-	24.5	No
2	1.46%C_4H_{10}-21%O_2-54.3% He - 23.3%Ne	3.0	-	-	-	≈ 25	No
3	0.8% n-C_8H_{18}- 21%O_2 – balance Arg	4.0	-	-	-	12.3	No
4	1.46% n-C_4H_{10}- 21%O_2 – balance He	3.3	3.6 - 4.1	111	4.2	≈ 26	Yes
5	0.8% n-C_8H_{18} - 21%O_2 – balance Ne	5.0	2.2 - 2.4	87	2.4	13	Yes
6	0.8% n-C_8H_{18}- 21%O_2 – balance He	5.4	2.4 - 2.8	143	3.8-3.9	19	Yes
7	0.92% n-C_7H_{16} - 21%O_2 – balance H	5.0	2.4 - 2.8	128	3.8	23	Yes

In mixtures 1 through 3, no evidence of instability was reported. For all others listed, target, spiral, and/or "mixed mode" instabilities (complex modes characterized by spatially distributed interacting flamelets) were observed (Pearlman, 1997). For cases that exhibited target patterns (or spiral waves), the separation distances (λ) between the concentric circular waves in the case of target patterns and adjacent windings in the case of rotating spiral waves are indicated in Table 1 and were on the order of several centimeters for the mixture considered. The peak light intensity from the video record was used to define the wave/ flame location. This spacing is expected to be governed by

the frequency associated with the chemical oscillation at the core of target pattern or spiral wave and the radial propagation speed of the outwardly expanding circular wave or normal flame propagation speed in the case of the rotating spiral wave. As expected, the axial downward flame propagation speed measured relative to the laboratory frame of reference ($V_{f,,\ axial}$) is tabulated in Table 1 and on the order of 15-25 cm/s. It was representative of lean hydrocarbon premixtures (Turns, 2000), where it is noted that the laminar burning velocity depends on the diffusive properties of the mixture and the overall reaction rate. The radial flame speeds ($V_{f,radial}$) are also tabulated along with the rotation rates (ω_{spiral}) for the cases that exhibited rotating spiral waves. Unexpectedly, the radial speeds were on the order of several meters per second. While the laminar burning velocities for Helium-diluted mixtures are higher than N_2-diluted premixtures due to the large thermal diffusivity of Helium, measured speeds were 6 - 10 times faster than the laminar burning velocity in air. These high speeds are difficult to justify since flame propagation speed scales with the square root of the thermal diffusivity of the mixture and the overall reaction rate. Thus, an increase in thermal diffusivity of the mixture by a factor of 3 can be expected to increase the flame speed 70%, significantly less than the observed radial flame speeds.

Additional tests were conducted on flat-flame, water-cooled, porous-plug burner by Pearlman (Pearlman, 1997). The burner was the same as that used by Gorman and co-workers (Gorman et al., 1994a, 1994b) and had a 60mm internal diameter sintered bronze disk, with an average pore size of 115 microns (range from 90-140 microns), surrounded by a 6.75cm wide porous bronze shroud. The porous plate and shroud were mounted in a stainless-steel housing equipped with two gas inlet ports: one for the reactant gases and

the other for the shroud gases. Four mixtures were tested at atmospheric pressure, for which target patterns and rotating spiral waves were observed, although the finite size of the burner limited the concentric circular waves and/or spiral windings observed. Table 2 summarizes the experimental parameters considered including fuel type, diluents, mixture composition and Lewis numbers for the cases considered for a given burner exit flow speed (6.4 ± 0.4 cm/s) (Pearlman, 1997). It was observed that the instabilities primarily exist in rich methane-air, lean propane-air and lean n-butane-air premixtures. Based on the scarce reactant, the computed values of the Le for each of these premixtures are 1.09, 1.85 ± 0.02, and 2.08 ± 0.04, respectively. Thus, the instabilities were mostly pronounced in mixtures with Le in excess of one.

Table 2: Range of equivalence ratios and associated Le numbers for occurrence of the high-Le number instabilities in burner-stabilized premixed gas flames at 1 atm (Pearlman, 1997).

Premixture	Range of Molar Fuel Concentration for which the High-Le Instabilities were Observed (vol. %)	Equivalence Ratio(ϕ)	Lewis Number based on Fuel over the Range of Instabilities	Lewis Number based on Oxygen over the Range of Instabilities
CH_4/Air	9.1-12.7	0.96-1.34	0.93	1.09
C_3H_8/Air	4.3-2.7	1.07-0.69	1.83-1.87	1.04-1.06
n-C_4H_{10}/Air	3.9-2.1	1.26-0.67	2.05-2.12	1.02-1.05

What is also worth noting is that target and rotating spiral wave instabilities were also observed in near stoichiometric mixtures that were slightly lean in the case of methane-air and slightly rich for propane and n-butane-air premixtures. The corresponding Le numbers for these mixtures are 0.93, 1.05 and 1.03, respectively, all of which are near

one. The experimental evidence supports Joulin and Clavin's non-adiabatic stability analysis that predicts the critical Le for the onset of instability decreases with increasing heat loss and as shown can result in the onset of instability for near unity Le. A more recent study conducted by Robbins et al using rich methane-oxygen premixtures ($1.2 < \phi < 1.4$) with Le near unity at the reduced pressure (1/2 atm) also observed a rotating spiral wave (Robbins et al., 2004).

Most recently, the experimental observation of spiral waves in expanding rich hydrogen-air flames was made by Jomass and coworkers at pressures up to 40 atm (Jomaas et al., 2007). The experiments were conducted in a dual chamber high-pressure combustor, shown in Figure 8. It consisted of two concentric aluminum cylindrical vessels. The inner vessel was initially filled with the combustible premixture and the outer chamber was initially filled with an inert gas at the same pressure. A spark igniter at the center of the vessel ignited the premixture. These spiral waves were observed using a high-speed schlieren system and were superposed on large-scale hydrodynamic cells that formed the flame surface. The length and time scales for the instabilities were sufficiently different such that the diffusive-thermal and hydrodynamic instabilities could be differentiated.

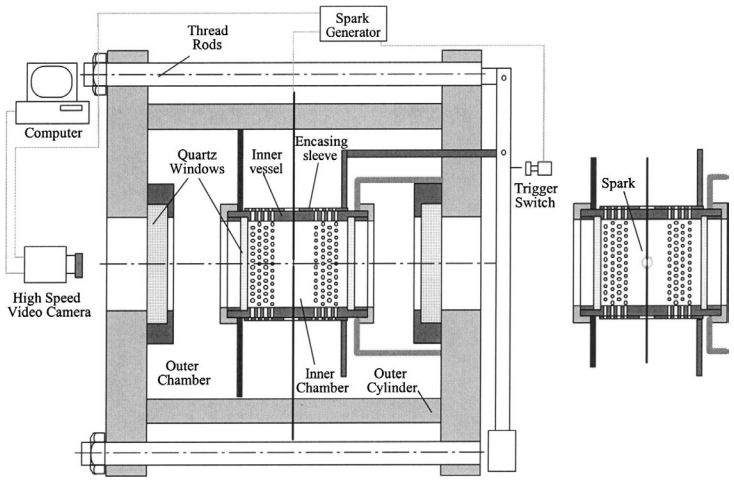

Figure 8: High pressure dual chamber combustor (Tse et al., 2004).

Figure 9 shows a representative image reported by Jomaas of a hydrogen-air spherical flame with an equivalence ratio of 4.30 at 20 atm. Combined diffusive-thermal (spiral wave) and hydrodynamic instabilities (larger cells) have been observed. Further examination shows that the spirals rotate either clockwise or counterclockwise and the spiral tip followed a meandering path on the flame surface as predicted by Panfilov and co-workers (Panfilov et al., 2003).

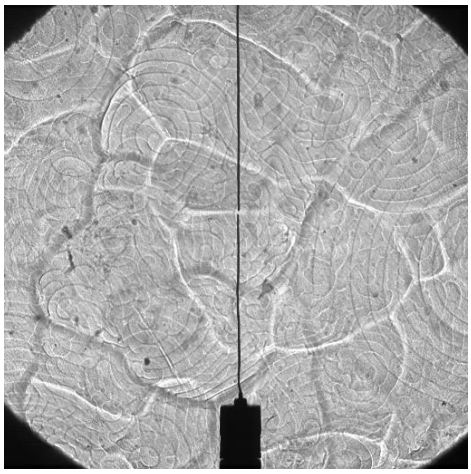

Figure 9: Spiral waves for rich hydrogen-air flame at 20 atm (Jomaas et al., 2007).

From the video record, the spiral wave velocity was determined from which it was determined that the traveling spiral wave propagated radially outwardly five times faster than the radial propagation speed of the spherically expanding flame front. Another interesting observation made by Jomass was that the spiral waves only occurred when the pressure exceeded 5 atm. Their argument was that it is due to the fact that with increasing pressure, the reaction rate of the pressure-sensitive three-body termination reaction increased relative to the two-body branching reactions, for the H-O2 branching-termination cycle, which leads to an increase in the effective activation energy of the overall reaction and thus increase in the reduced Lewis number, $\beta(Le-1)$.

1.2.3 Coupled Effects of Hydrodynamic and Diffusive-thermal Instabilities

In addition to diffusive-thermal instabilities, hot gas expansion can induce hydrodynamic instabilities as shown in the large-scale cellular structures in Figure 9. This instability was first described by Darrieus (Darrieus, 1938) and Landau (Landau, 1944) and a physical explanation for the instability is illustrated in the schematic shown in Figure 10 (Law, 2006). At the convex sections of the flame (with respect to the unburned gas), the flow streamlines diverge and at the concave sections, they converge such that the flow is deflected in the direction of the normal to the flame. Since momentum is conserved across the flame front, the flow velocity decreases in the convex sections and increases in the concave sections. This leads to further wrinkling and growth of the instability.

By treating the flame as a discontinuity in density that propagates at a constant speed in an incompressible, inviscid, nonconducting fluid, Darrieus and Landau's predictions suggested that premixed flames are unstable to disturbances of all wavelengths. However, experimental observations of smooth, steady flames stabilized in wide diameter tubes (Sivashinsky, 1983) and other configurations demonstrated that the flames were not unstable for all conditions and encouraged research into possible stabilizing mechanisms.

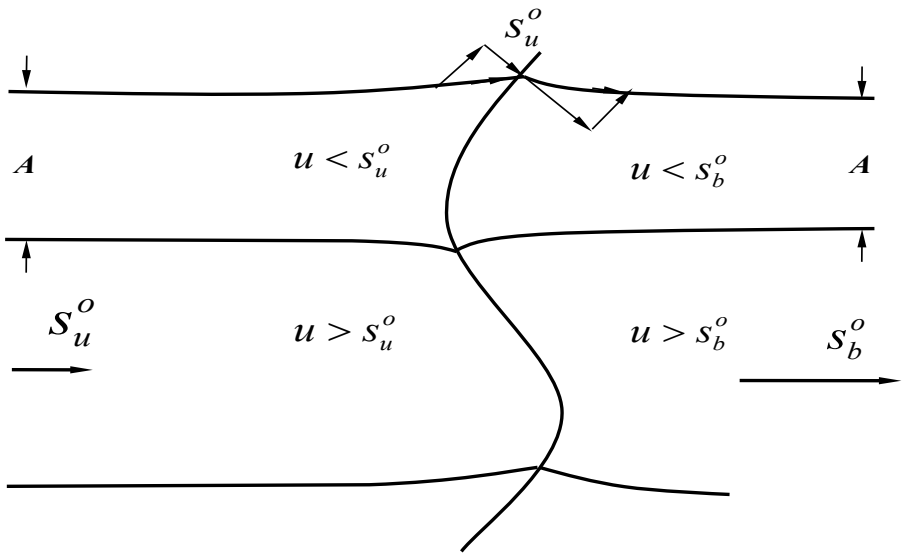

Figure 10: Hydrodynamic instability of a flame front (Law, 2006).

The effect of flame front curvature on flame stability: Markstein subsequently postulated that the local flame speed varies as a function of local flame curvature (Markstein, 1951, 1964). Specifically, he proposed that:

$$s_n = s_L\left(1 + l / R_f\right) \qquad (3)$$

Where s_n is the local flame speed normal to the flame surface, s_L the laminar planar flame propagation speed, l is a parameter called the "Markstein Length", and R_f the local radius of curvature of the flame. When l is large, the effect of curvature on burning velocity is strong and when l is small, the effect is weak. For $l > 0$, Markstein also showed that a planar flame is stable to short-wavelength disturbances, yet unstable to long-wavelength disturbances. Note that the Markstein length is not determined from

first principles such as the physical properties of the mixture, but empirically determined from data on flame speed and flame radius (Dowdy et al., 1990).

The effect of viscosity: Further mathematical studies by Frankel and Sivashinsky (Frankel and Sivashinsky, 1982) showed that viscosity can affect flame stability, albeit a secondary effect, through its temperature dependence. In addition, mass diffusion is a function of flame temperature.

The effect of buoyancy: Pelce and Clavin (Pelce and Clavin, 1982) investigated the role of buoyancy on the hydrodynamic instability of downwardly-propagating flames. They determined that buoyancy can stabilize long-wavelength disturbances. This also explains the large (~ 8 cm) smooth planar flame observed experimentally by Quinard (Quinard et al., 1984).

The effect of the flame structure on its stability: Full solutions of the Navier-Stokes equations were evaluated to study the effects of flame structure on the flame instability. Istrov and Librovich first proposed two length scales, the hydrodynamic scale and the flame thickness (Istrov and Librovich, 1966). Clavin and Williams (Clavin and Williams, 1982) and Matalon and Matkowsky (Matalon and Matkowsky, 1982) then applied a multiscale analysis and large activation energy asymptotics to derive an algebraic relation for the local flame speed as a function of Markstein length appropriate for the case of $Le \approx 1$. They also derived the expression of Markstein length in terms of fundamental physical chemical properties such as Le number and thermal expansion.

The study of finite activation energy: All of the theoretical studies mentioned so far assumed infinite activation energy. However, the activation energy, while large, is finite. To account for finite activation energy, Sharpe developed a numerical shooting method

and applied it to the problem of planar premixed flames from which a dispersion relation was derived and compared with the asymptotic result (Sharpe, 2003). This method solves the full reactive Navier-Stokes equations and was explored over a large range of the parameters including the activation energy, the Le, and the Prandtl number. Flame stability was shown to be insensitive to the activation energy for $Le \geq 1$, yet very sensitive to the activation energy for Le < 1. In contrast to diffusive-thermal models that predict that the flame stability is a function of the reduced Lewis number ℓ ($\ell = \beta(Le-1)$), which suggests that flame stability depends on the Le and the activation energy.

Fully compressible NS studies: Kadowaki investigated the combined effects of hydrodynamic and diffusive-thermal instabilities on the formation of the cellular flames for both small (Le < 1) and large Le (Le > 1) flames using the compressible NS equation (Kadowaki, 1997, 1999, 2000). For both 2D and 3D domains, all three instability mechanisms: hydrodynamic, body-force (e.g., buoyancy), and diffusive-thermal effects were considered. He found that the hydrodynamic and body-force instabilities are dominant for Le = 1 and stationary cellular flames were formed. For Le < 1, the cellular flames were obtained not only at $Le < Le_c$ but also at $Le_c < Le < 1$ which is different from the predictions from nonadiabatic stability analyses. For Le > 1 (Le = 1.0~3.0 were studied), the disturbance growth rate was found to decrease and the unstable range to narrow as the Lewis number increases. This suggests that the diffusive-thermal effect has a stabilizing influence on the formation of cellular flames.

More recent work conducted at Princeton has also considered the unsteady, two-dimensional, chemically reactive Navier-Stokes equations for compressible flows with a

single-step chemical reaction (Ju, 1995). In their study, the mass, momentum, and energy conservation equations were formulated as:

$$\frac{\partial U}{\partial t}+\frac{\partial E}{\partial x}+\frac{\partial F}{\partial y}=\frac{\partial E_v}{\partial x}+\frac{\partial F_v}{\partial y}+S \qquad (4)$$

where t, x and y are respectively the time and spatial coordinates, **U** is the vector of the conservation variables, **E** and **F** are the convective flux vectors in the x, y directions, $\mathbf{E_v}$ and $\mathbf{F_v}$ are the corresponding viscous flux vectors, and **S** is the vector of the reaction source term. The detailed forms of **U**, **E**, $\mathbf{E_v}$, **F**, $\mathbf{F_v}$ and **S** are shown below:

$$U=\begin{bmatrix}\rho_1\\ \rho_2\\ \rho u\\ \rho v\\ E\end{bmatrix}\quad E=\begin{bmatrix}\rho_1 u\\ \rho_2 u\\ \rho uu+p\\ \rho uv\\ (E+p)u\end{bmatrix}\quad E_v=\frac{1}{\mathrm{Re}}\begin{bmatrix}-\rho_1 V_{1x}\\ -\rho_2 V_{2x}\\ \tau_{xx}\\ \tau_{xy}\\ q_x\end{bmatrix}\quad F=\begin{bmatrix}\rho_1 v\\ \rho_2 v\\ \rho uv\\ \rho vv+p\\ (E+p)v\end{bmatrix}\quad F_v=\begin{bmatrix}-\rho_1 V_{1y}\\ -\rho_2 V_{2y}\\ \tau_{xy}\\ \tau_{yy}\\ q_y\end{bmatrix}\quad S=Da\begin{bmatrix}\omega_1\\ \omega_2\\ 0\\ 0\\ 0\end{bmatrix}$$

The subscripts 1 and 2 refer to the densities of the reactants and the products, respectively, ρ is the total density, u and v are the velocities in x and y directions, respectively, E is the total energy, p is the pressure, V_{ix} is the diffusion velocity in x direction and ω_i is the chemical production rate of the i^{th} species (in this case, either reactant or product), τ_{mn} is the viscous stress, q_m is the heat conduction in the m direction, Re is the Reynolds number, and Da is the Damkohler number.

The results obtained by solving these equations can be summarized as follows:

1. For Le≤1, cellular flame growth, cell splitting, cell merging, cell lateral movement and local extinction were predicted;

2. For Le < Le_c, diffusive-thermal effects enhance the hydrodynamic instability and cell splitting and merging processes are accelerated;

3. For Le_c < Le < 1, diffusive-thermal effects can stabilize the hydrodynamic instability, resulting in the steady propagation of cellular flames;

4. For Le > 1, the diffusive-thermal instability can stabilize the cellular instability growth rate which corresponds to the results of Kadowaki (Kadowaki, 1997, 1999, 2000) if linear approximations are made. On the other side, the diffusive-thermal pulsating instability can promote the hydrodynamic instability based on linear approximations, while cellular flame propagation, periodic pulsating cellular flames, and irregular pulsating cellular flames are predicted for the nonlinear case.

1.2.4 Summary of Past Work

Theoretical, numerical and experimental studies on premixed and non-premixed flame instabilities have been conducted to explore diffusive-thermal and hydrodynamic instabilities. Most attention has been focused on low-Le cellular instabilities perhaps because few experimental studies have definitively shown evidence of the high-Le instability, albeit predicted by nonadiabatic, linear stability analyses and more recent numerical simulations. Some experimental observations of high-Le instabilities were reported but without mention of the underlying mechanism. The coupling effects of the diffusive-thermal and the hydrodynamic instabilities are only now receiving attention as demonstrated in the work of the Kadowaki and Yuan (Kadowaki, 1997, 1999, 2000; Yuan, 2006; Yuan et al., 2006) who conclude that the diffusive-thermal instability can promote or suppress the hydrodynamic instability depending on the Le.

1.3 Motivation for the Present Work

Fundamental questions remain concerning the mechanisms that control the onset of flame instability and the dynamics and evolution of target and spiral wave patterns observed in high-Le premixtures. Furthermore, there is a lack of quantitative data on the effects of mixture stoichiometry, Lewis number, Zel'dovich number, ambient pressure and heat loss on the instabilities and their characteristics including their wavelength and wave speed. All of these data are needed to validate stability diagrams predicted by linear and nonlinear theories, which eventually can be used to improve the design of lean burn engines and optimized for efficiency and reduced emissions. Some of the open issues raised by prior experimental and theoretical work include:

1. The target patterns, rotating spiral waves and complex interacting flamelets observed in burner-stabilized and freely-propagating flames are thought to be a manifestation of the diffusive-thermal instability, yet it is not entirely clear how heat loss, buoyant effects, and possible hydrodynamic couplings affect the onset of instability and the patterns observed. Carefully controlled experiments and numerical simulations are therefore needed to understand the individual and coupled effects.

2. It is not clear how the details of the chemistry affect the onset and dynamics of high-Le flame instabilities. Prior flame tube studies have shown that target and spiral wave instabilities develop on downwardly-propagating flames in lean premixtures of heavy fuels (e.g, n-butane, n-heptane, n-octane diluted with oxygen and helium) that have a characteristically high-Le (Le >1) as well as burner-stabilized flames with high heat loss in near-unity Le premixtures. These preliminary results have also suggested that the wavelength of the instability decreases with higher molecular weight fuels, yet it is not

clear whether this is a diffusive effect, a chemical effect or a combined effect? From a simple scaling analysis based on diffusive properties, it can be argued that the instability wavelength may decrease with an increase in the molecular weight of the deficient component (e.g., the fuel) since diffusion times increase ($t_{diffusion} \sim V_{flame}/D$) and diffusion lengths decrease ($l_{diffusion} \sim D/V_{flame}$). Quantitative data is therefore needed to validate this assertion and analyses are needed to determine the effect of the diffusion rates on the instabilities including their effect on the separation distance between adjacent flamelets.

3. In downwardly-propagating flame tube experiments and spherically-propagating high pressure hydrogen-air flames, the propagation speed of the concentric waves that comprise the target and spiral wave patterns propagate much faster than the laminar flame propagation speed (roughly an order or magnitude faster!). Such extraordinarily high flame propagation speeds are difficult to explain based on diffusional processes and have led to the speculation that they are phase waves, where local regions of the flame react at different phases. This remains an open question.

4. The Zel'dovich number (β, a measure of the nondimensional activation energy) generally varies from a value of 6-10 for heavy alkane-air mixtures. However, sensitivity studies are needed to determine the relative importance of the Ze number noting that stability analyses suggest that the critical parameter is not simply the Le, but rather the reduced Le, which is defined as β (Le −1).

5. Experimental data that can be used to validate stability diagrams for high-Le conditions is not available with the exception of recent data reported using H_2-air mixtures at elevated pressure in a spherically-propagating flames (Jomaas et al., 2007).

This dissertation aims to clarify and help address these questions mentioned above experimentally and numerically. The overall objectives of this research are:

1. Establish a steady, burner-stabilized premixed flame from which high-speed video will be acquired in order to quantify the effects of Le, mixture composition, flow conditions, and ambient pressure on the onset and dynamics of the instabilities.

2. Quantify the critical Le and the wavelength (wavenumber) associated with the target and spiral wave patterns in high-Le premixtures to validate stability analyses, i.e., growth rate versus wavenumber for different Le's.

3. Extend current 2D models to quantify the roles of different Le, Ze and heat loss to the burner on the dynamics of target and spiral patterns.

1.4 Outline of Dissertation

This research aimed to provide an improved understanding of the roles of diffusive fluxes of heat and species, hydrodynamic effects, and heat loss on the onset and dynamics of the flame patterns. With quantitative data and a clear understanding of the mechanism and controlling parameters, one may eventually develop an active method to control such premixed flame instabilities or perhaps even exploit them for useful purposes.

In Chapter 2, the experimental apparatus and methodology are introduced. Specifically, the Variable Pressure Chamber System and the Liquid Fuel Vaporization System are described.

In Chapter 3, experimental results for lean hydrocarbon/air and lean hydrocarbon/O_2/He mixtures are summarized. The different reaction modes and flame patterns are discussed and include stable flame, spiral wave, target pattern and multi-arm

spiral waves. Stability maps are developed as functions of burner exit flow speed, heat loss, Le and equivalence ratio. In addition, qualitative comparisons between theoretical predictions and experimental observations on the heat loss and reduced Le are reported.

In Chapter 4, Sal'nikov models were developed based on prior work and adopted to explore the role of heat loss, Le and Ze on the flame patterns in two-dimensions. Multiple target patterns were simulated and compared with experimental results. Also, data on rotation rates and propagation speeds associated with spiral waves are reported and compared with the experimental observations. Temperature and species concentration profiles for the Sal'nikov model are presented and interpreted.

In Chapter 5, a summary of the high-Le flame instabilities is presented and future work is discussed.

2. Experimental Apparatus and Methodology

2.1 Overview

To study diffusive-thermal instabilities in stabilized premixed flames, a water-cooled, porous-plug McKenna burner was used (Holthuis & Associated, Sebastopol, CA). McKenna burners are widely used to produce standard flat premixed flames. The flames are assumed to be quasi-steady planar flames at least under lean and close-to-stoichiometric conditions. The burner had a 60mm internal diameter, porous sintered 316 stainless-steel disk with an average pore size of 115 microns (pore size ranges from 90-140 microns), surrounded by a 70.6 mm diameter porous bronze disk used for a shroud gas. The porous disk and shroud were mounted in a stainless-steel housing equipped with two gas inlet ports; one for the reactant gases and the other for the shroud gases. The burner was cooled with chilled water that circulated through a copper coil embedded in the 60 mm SS disk. The measurement for the complete unit of the McKenna burner was approximately 63.5 mm for the overall height and 120.6 mm for the outside diameter. A schematic graph of the McKenna burner is shown in Figure 11.

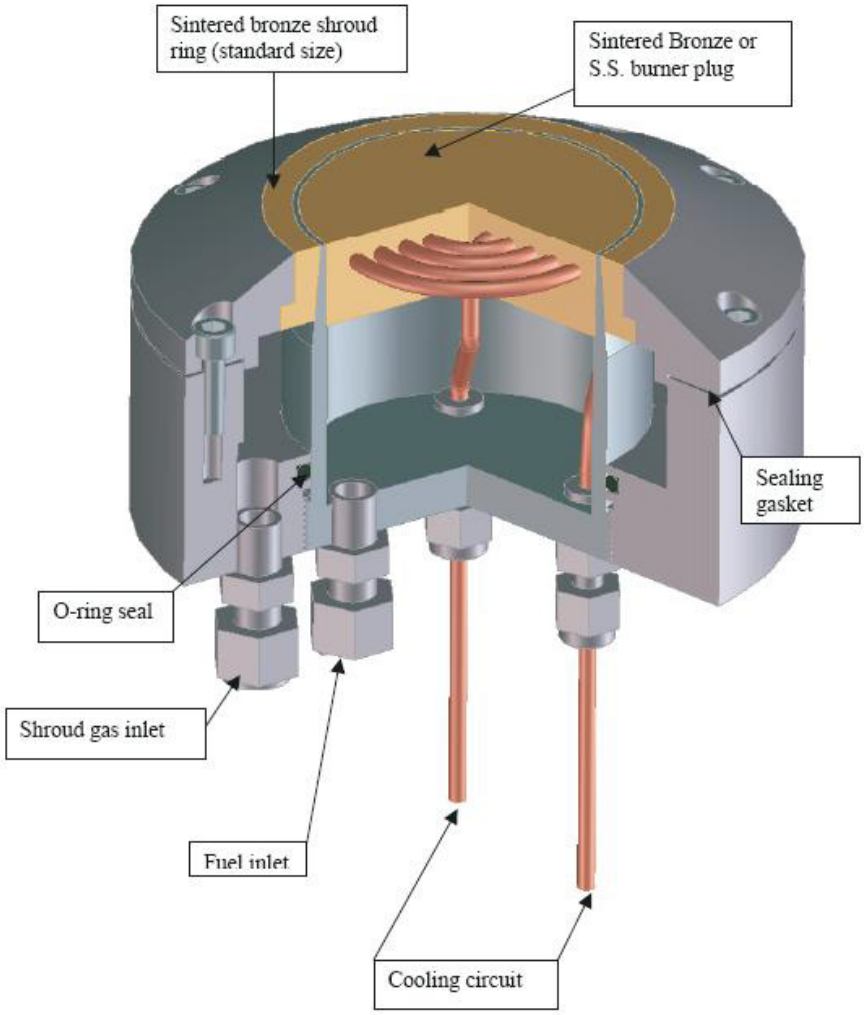

Figure 11: Schematic diagram of the McKenna porous-plug burner (Product manual from Holthuis & Associated).

The experiments were conducted at atmospheric and sub-atmospheric pressures to suppress buoyant complications. The sub-atmospheric pressure environment was maintained at constant pressure by enclosing the burner within a custom-built 26.5 liter aluminum Variable Pressure Chamber System (VPCS) equipped with optical access; details of the design are presented in Section 2.2.

Liquid and vapor fuels were investigated. Vapor fuel includes n-C_4H_{10} which was metered using an MKS^{TM} 1179A series thermal mass flow controller that had an accuracy of ±1% of the full scale (FS) of the meter (1 SLM FS). Liquid fuels included n-C_7H_{16} and n-C_8H_{18} and were initially introduced with the use of a glass bubbler through which air flowed at a prescribed mass flow rate. While bubblers are simple and easy to use, the mixture composition is not easily controlled, as it is determined by the temperature-dependent vapor pressure of the fuel. Therefore, a new spray nebulizer and vaporization chamber was developed to enable improved control of the fuel-air composition. The design was modeled after that developed at NIST (Lenhert and Manzello, 2009) and shown to be effective at vaporizing benzene and methanol.

In all cases, air or oxygen and an inert gas were metered using two MKS^{TM} 2179A which also had an accuracy of ± 1% of the full scale of the meters (10 SLM and 20 SLM). The shroud gas (e.g. Nitrogen) was metered using MKS^{TM} 1500 series thermal mass flow controller that had an accuracy of ±1% of the full scale of the meters (100 SLM).

2.2 Variable Pressure Chamber System (VPCS)

Figure 12 shows a schematic of the Variable Pressure Chamber System (VPCS) that included a McKenna burner, variable pressure chamber, pressure control system, high speed digital camera, data acquisition (DAQ) system and MKS Mass Flow Control System. Each component of the facility will be discussed in detail in the following sections.

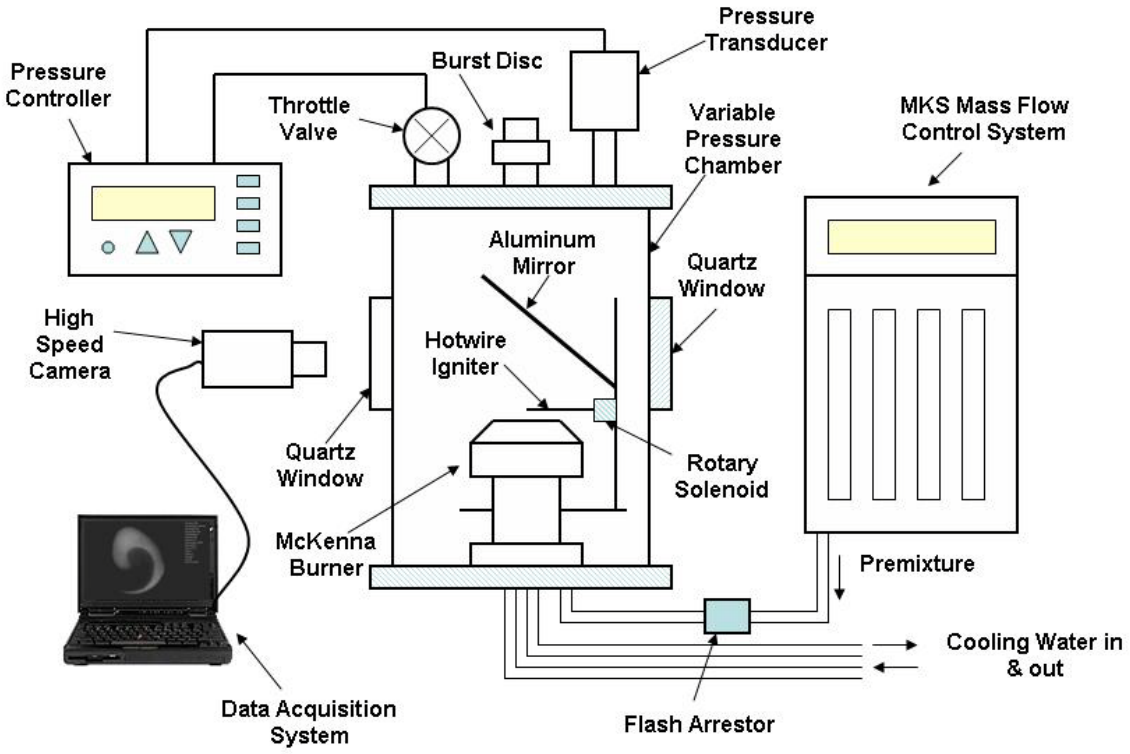

Figure 12: Schematic diagram of VPCS experimental apparatus.

2.2.1 Variable Pressure Chamber

The cylindrical pressure chamber, shown in Figure 13, was constructed from aluminum and rated for pressures up to 3 atm. The chamber was accessible through a removable top and bottom plate sealed against an upper and lower flange fitted with o-rings. V-clamps were used to compress the o-rings and thus secure the plates to the chamber. The chamber was outfitted with four windows equally spaced in the sidewall of the chamber and fitted with quartz windows or aluminum blanks depending on whether optical access was desired. A schematic of the dimensions of the pressure chamber is shown in Figure 14.

Figure 13: Image of the aluminum variable pressure chamber.

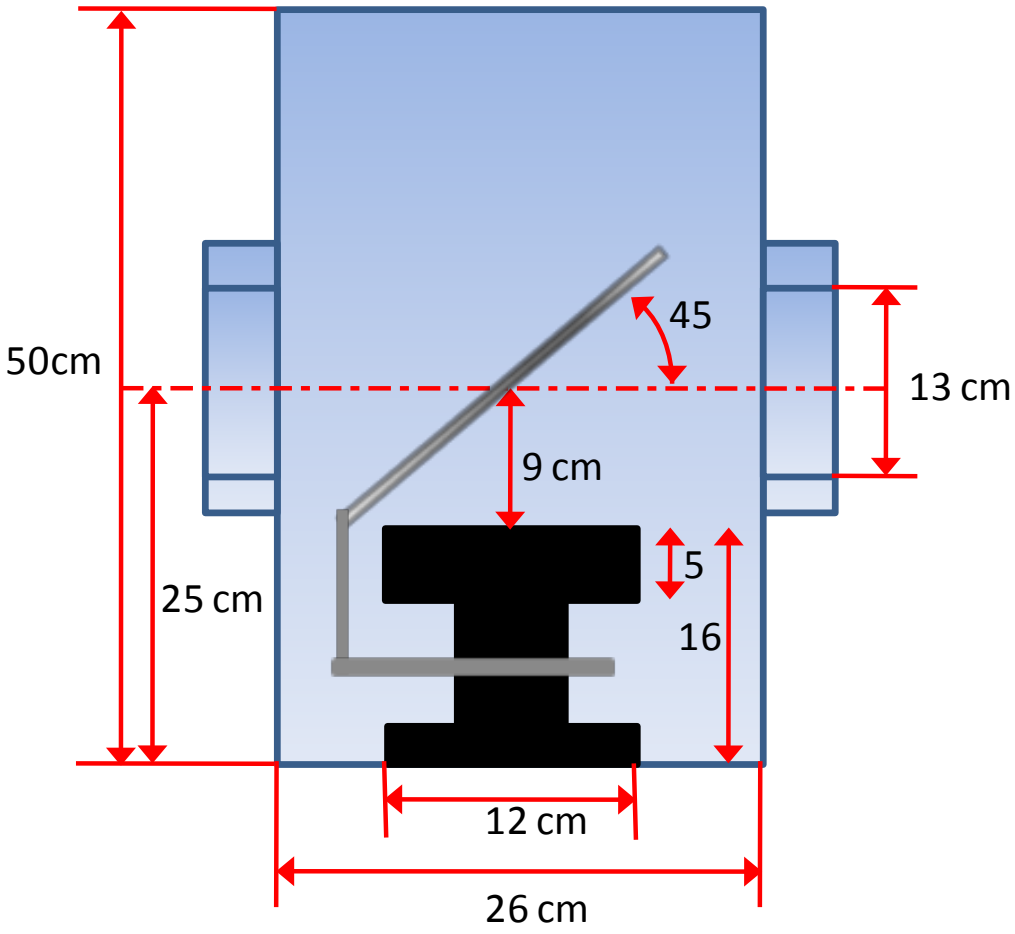

Figure 14: Schematic of dimensions of the pressure chamber and the McKenna burner (unit: cm).

To enable imaging of a complete top view of the flame through a side quartz window, an aluminized mirror was mounted above the burner surface at a 45-degree incline with a 9cm distance apart so that it won't perturb the flow of the system.

2.2.2 Pressure Control System

To maintain a constant pressure in the chamber, a pressure control system was developed. The components included: (1) a Baratron capacitance manometer to

accurately measure the pressure in a chamber; (2) an electrically adjustable butterfly throttle valve (MKS 653B) connected directly to a vacuum pump and (3) a pressure controller (MKS 651) that records and monitors the chamber pressure and relays the data to the throttle valve to appropriately adjust its position depending on the desired pressure set point.

For our application, a downstream control technique was chosen. Specifically, the Baratron capacitance manometer (Range: 1000 Torr; accuracy 0.12% of the reading) was mounted on the top plate of the pressure chamber and regulated by the pressure controller. The controller has a self-tuning algorithm that brings the system to set point faster than conventional controllers. The butterfly throttle valve was equipped with a high speed motor and gear/driver assembly to provide fast response (1.7 s from fully open to closed) to a given set point, which is controlled by the controller. The valve body was limited to a temperature of up to 150ºC which was sufficient for this application since the product of combustion were highly dilute with inert prior to passage through the valve. Figure 15 illustrates the use of the pressure controller with a throttle valve.

For safety, two high operating and vacuum (HOV) rupture discs provided by FIKE were mounted on the top plate of the chamber to relieve the pressure in the event that it exceeded 3 atm. FIKE's HOV rupture disc consisted of two parts: the seal member and a slotted top. The slotted top section controls the burst pressure of the disc. Rupture discs, also known as bursting discs, provided a leak tight seal, were rated at 3 atm in this case. One relief valve rated at 2.5 atm was mounted in the top plate of the chamber.

Figure 15: MKS Model 653B Throttle Valve and MKS Model 651 Pressure Controller (Product manual from MKS).

2.2.3 Ignition System

A hotwire igniter made of fine Kanthal wires with a resistance of 6.731 ohms/ft is used to ignite the flames in the pressure chamber. The igniter is controlled by a Ledex™ Series 195190-032 BTA rotary actuator that rotates the igniter in the plane of 4 mm above the burner surface from its initial position to the center of the burner. The electrical leads connected with the hotwire igniter and rotary actuator were connected to an electrical feedthrough mounted in the top plate of the chamber. The hotwire igniter was powered by a 12 VDC battery in series with one ohm resistor and triggered with a time delay relay for 1.3 seconds. The solenoid was powered by a 24 VDC power supply and also connected with the time delay relay. The electrical circuit for controlling the igniter system is shown in the Figure 16.

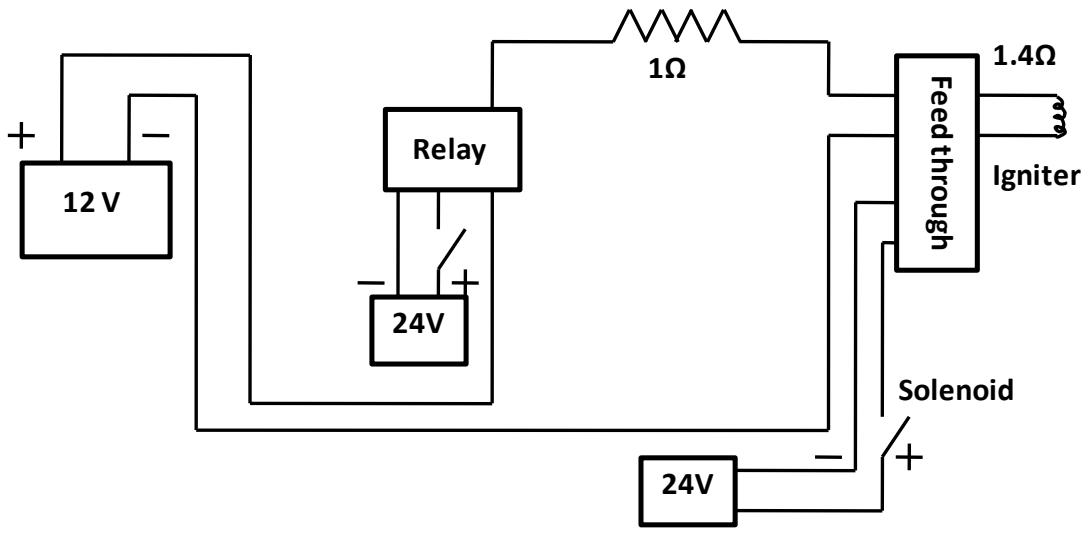

Figure 16: Electrical circuit diagram of the hot wire ignition system.

2.2.4 Mass Flow Control System (MFCS)

To control the flow of all gases including n-C_4H_{10}, O_2, N_2, He, air, and other gases, a bank of thermal mass flow controllers were used that operate by measuring the power required to maintain a pre-established temperature profile along a laminar flow sensor tube. In the flow controllers, the metered flow rate signal was continuously compared to a set point using internal PID control electronics.

Our system, shown in Figure 17, consisted of one MKS Model 1179A actuator (FS: 1000SCCM), two MKS Model 2179A actuators (FS: 10SLM, 20SLM) and one MKS Model 1559A actuator (FS: 100SLM) controlled using an MKS 647C centralized control module. All three controllers have a resolution of 0.1% of full-scale (FS) and an accuracy of ±1% of FS. Figure 18 shows the flow diagram of the mass flow control system.

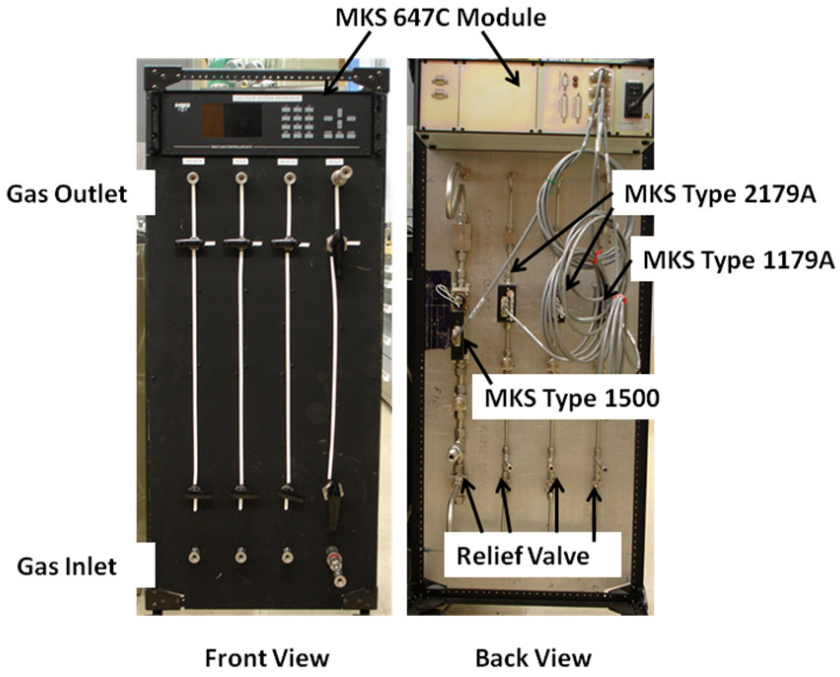

Figure 17: Front and back view of the MFCS.

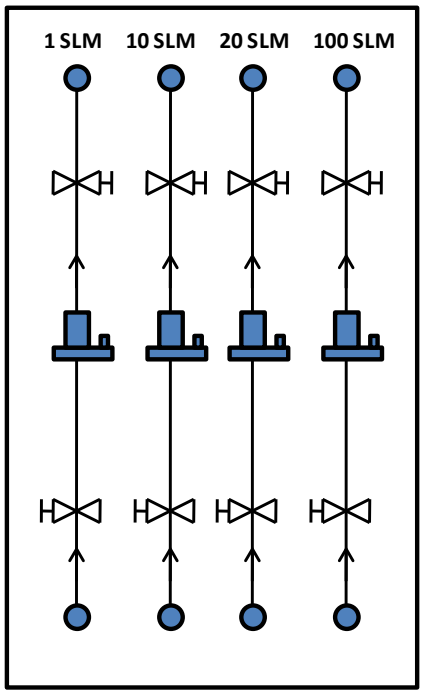

Figure 18: Schematic of flow paths for the MFCS.

2.2.5 Imaging Diagnostics and Instrumentation

To capture the spatio-temporal dynamics of the flame front, high-speed diagnostics and low-light level imaging were required. Imaging was performed using a B/W Redlake MotionXtra HG-TH mounted horizontally outside of the chamber to obtain top view images with the use of a mirror mounted above the burner surface at a 45^{o} angle.

The imaging system consisted of the camera head, control software, a camera control unit, and a display, shown in Figure 19. The camera was capable of recording up to 1,000 fps at 752 x 564 pixel resolution. The interface of the MotionCentral software is shown in Figure 20 and was used to control the camera and record the flame images.

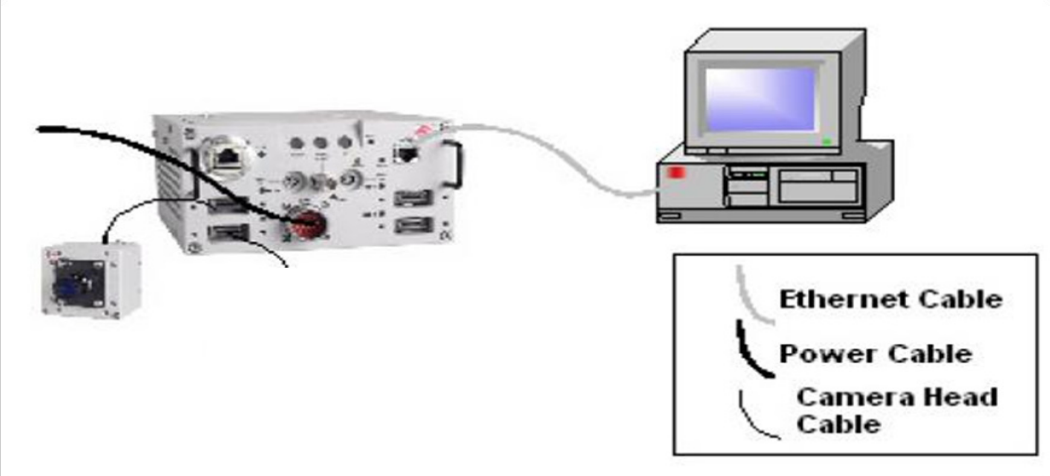

Figure 19: HG-TH controller connected with the camera head through camera head cable and computer through Ethernet cable.

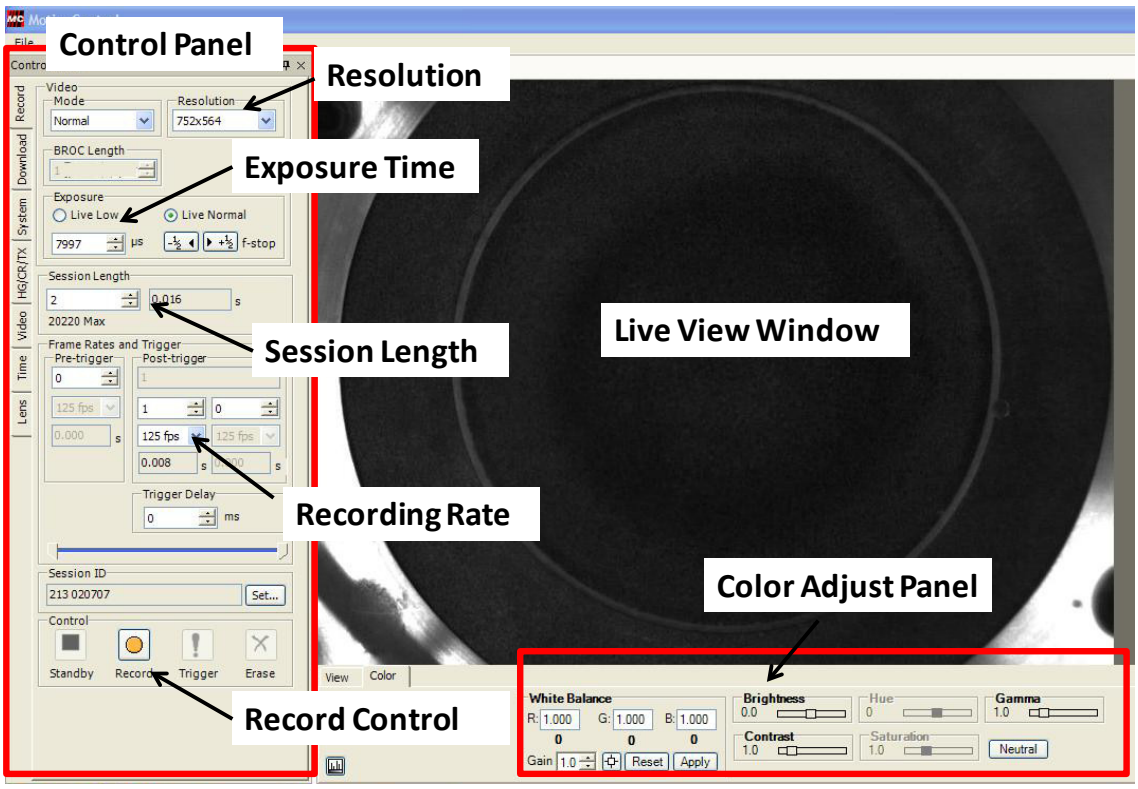

Figure 20: Main application window of MotionCentral software.

2.3 Liquid Fuel Vaporization Systems

To investigate liquid fuels, two vaporization systems were developed, a bubbler saturator system and a nebulizer & spray chamber system. First, a bubbler was used to saturate an oxygen-inert (nitrogen, helium or argon) gas mixture, prior to entry to the burner. The metered oxidizer (or portion of the oxidizer) flowed through a Pyrex bubbler, as shown in Figure 21, where it mixed with the vaporized liquid fuel and then was directed to the McKenna burner. The saturator is composed of two parts from Chemglass: CG-1858 and CG-1014.

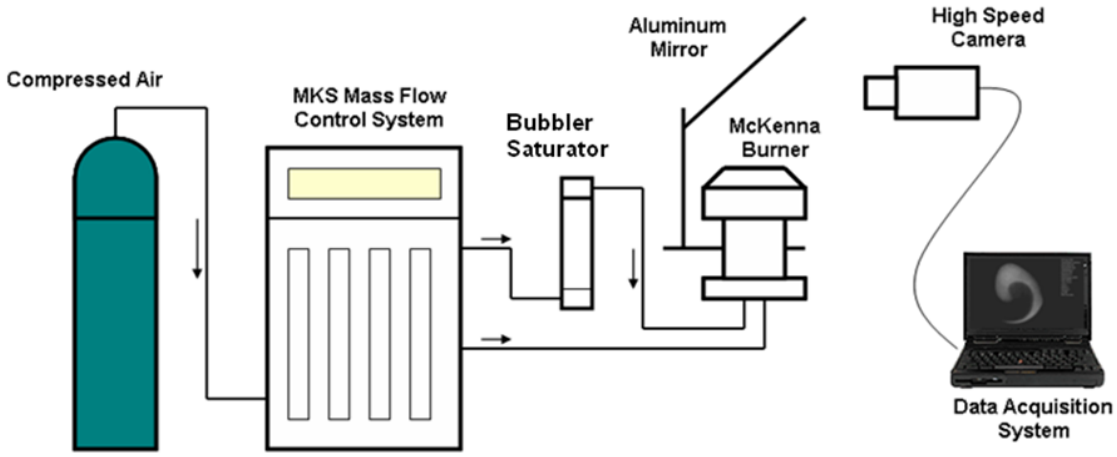

Figure 21: Schematic of experimental apparatus using liquid fuel bubbler saturator.

While the obvious advantage of this system is its simplicity and ease of use, the disadvantage is the variation in the mixture composition owed to the sensitivity of the vapor pressure of the liquid fuel at ambient temperature. For example, a 1 K change in ambient temperature (296 K vs. 297 K) results in a 5 % change in the mixture composition of a n-heptane-air premixture. For reference, the vapor pressure vs. temperature for n-heptane is shown in Figure 22.

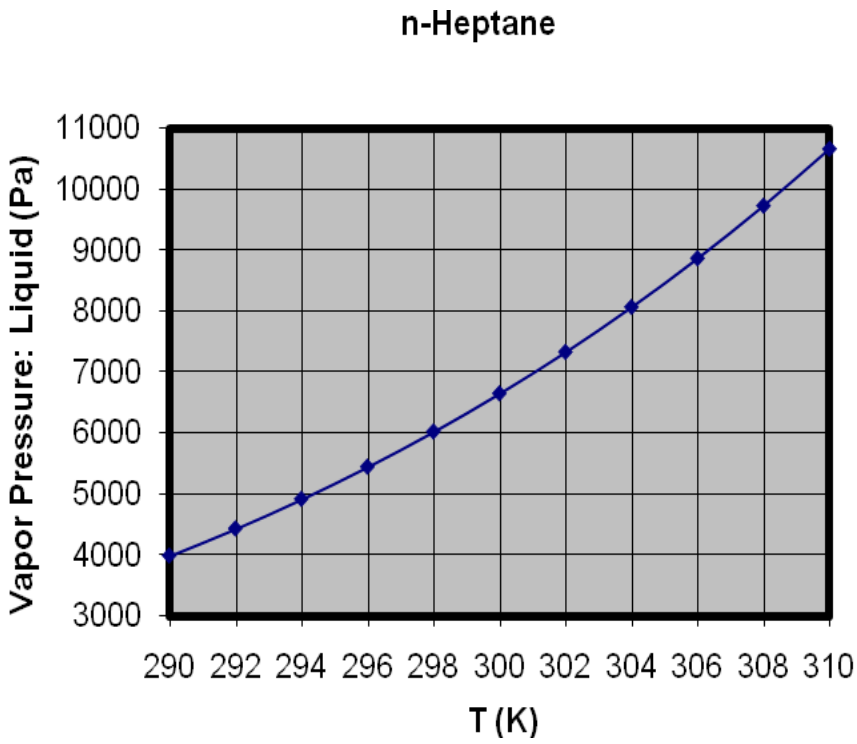

Figure 22: Liquid vapor pressure (in Pa) vs. temperature (K) for n-heptane (DIPPR Database).

To improve the accuracy of the mixture composition, a second liquid fuel delivery and vaporization system was designed, built and tested that consisted of a syringe pump, a nebulizer nozzle and a spray chamber. The system was modeled after that used by NIST (Lenhert and Manzello, 2008). A schematic of the system is shown in Figure 23.

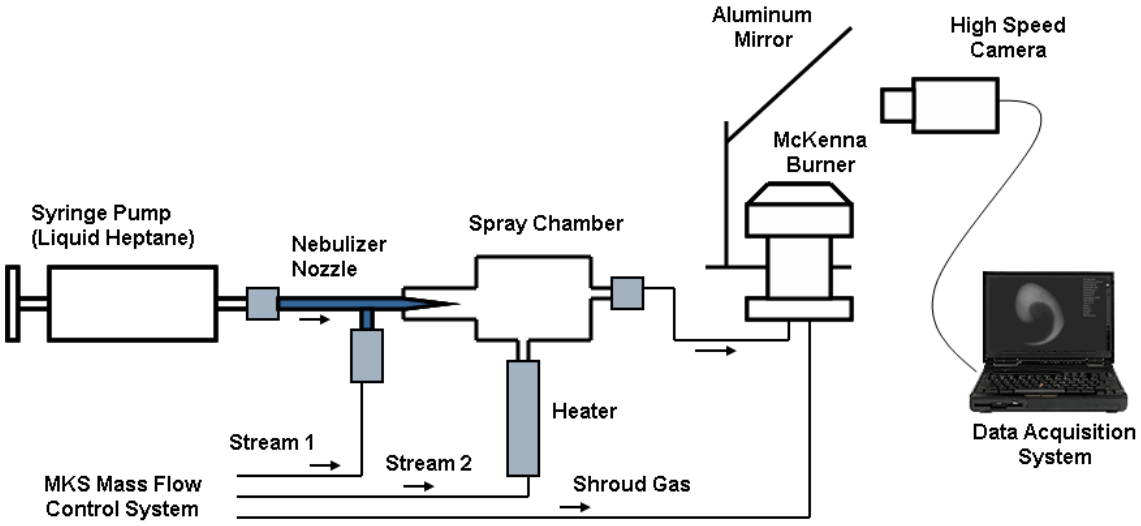

Figure 23: Schematic of experimental apparatus using spray nebulizer and vaporization system.

The Syringe Pump (Cole Parmer 74900 series) was used to meter the liquid fuel in a 60 ml, 3 cm diameter stainless-steel syringe into the nebulizer nozzle using 1/16'' tubing. The syringe and tubing were initially bled to remove any trapped air captured during the fill process. The liquid fuel flow rates ranged from 0.001µl/hr to 70.57ml/min. All control functions were performed automatically by the pump's microcontroller.

A concentric self-aspirating, glass concentric nebulizer (TA-30-A4) manufactured by Meinhard Co. was used (shown in Figure 24), that consisted of an uptake tube for liquid input, a shell with a capillary tube in the middle, a nozzle and a side arm for carrier gas input.

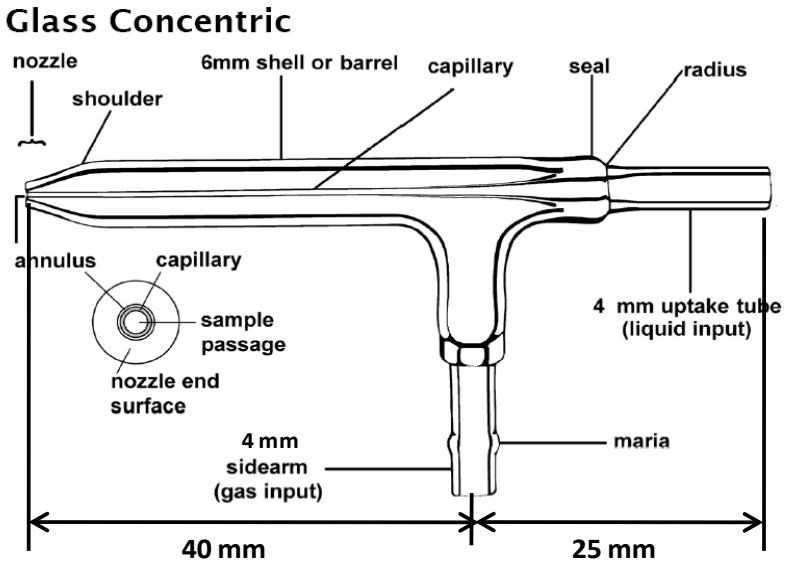

Figure 24: Schematic of the nebulizer used in the advanced vaporization system (Product manual from Meinhard).

The liquid exits the capillary tube to a low pressure region due to the rapid jet exit velocity at the capillary generated by a co-flowing gas flow (in our case the gas is air or Helium at a pressure of 1 atm at 1 L/min flow rate). The mean droplet size determined by the manufacturer of the device is given by the Nukiyama and Tanasawa equation (Nukiyama and Tanasawa, 1938-1940):

$$d_{3,2} = \frac{585}{v}\left[\frac{\gamma}{\rho}\right]^{0.5} + 597\left[\frac{\eta}{(\gamma\rho)^{0.5}}\right]^{0.45}\left[\frac{10^3 Q_l}{Q_g}\right]^{1.5} \qquad (5)$$

Here, $d_{3,2}$ is Sauter mean diameter (SMD) in μm. The SMD is defined as the diameter of a sphere that has the same volume/surface area ratio as a particle of interest. v is the velocity difference of gas-liquid in m/s. γ is the surface tension in dyn/cm. ρ is liquid density in g/cm^3. η is liquid viscosity in Poise or dyn·s/cm^2. Q_l is volume flow

rate of liquid in cm^3/s. Q_g is volume flow rate of gas in cm^3/s. Using this expression with our normal operating conditions, the mean diameter of the droplets for a representative n-heptane-air test run for a TA-30-A4 yields a mean droplet size about $15\ \mu m$.

The nebulizer was then inserted into a Pyrex vaporization chamber and sealed using two o-rings at the liquid inlet end (Figure 25). The oxidizer was then introduced from a gas inlet through an inline gas heater at 448 K for n-heptane or 463 K for n-octane. The entire spray chamber was also heated and insulated. Two temperature controllers (TC1 and TC3) were connected and TC1 controlled and displayed the temperature of the oxidizer gas as it left the heater and TC2 is a temperature display to show the temperature of the chamber surface at the entrance location. TC3 is a second temperature controller that controlled the temperature of the chamber surface to maintain the premixture's temperature.

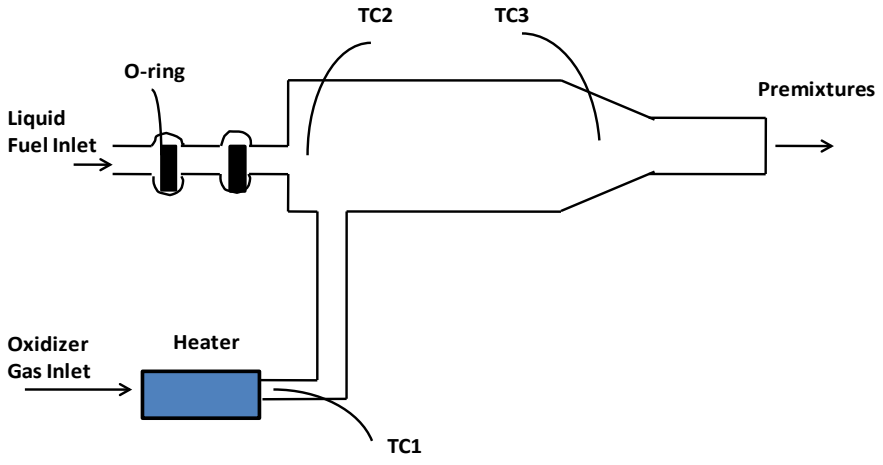

Figure 25: Vaporization chamber and temperature controllers.

To reduce the heat loss of the premixtures to the cold burner and potential condensation of the fuel, the burner "cooling" water was heated using an inline copper water heater. Four thermocouples were mounted to measure the inlet premixed gas temperature before entering the McKenna burner, the water temperature of after leaving the water heater, and temperature of "cooling" water flowing in and out of the burner, shown in Figure 26. The four thermocouples were monitored and the temperatures were displayed by NI Labview program.

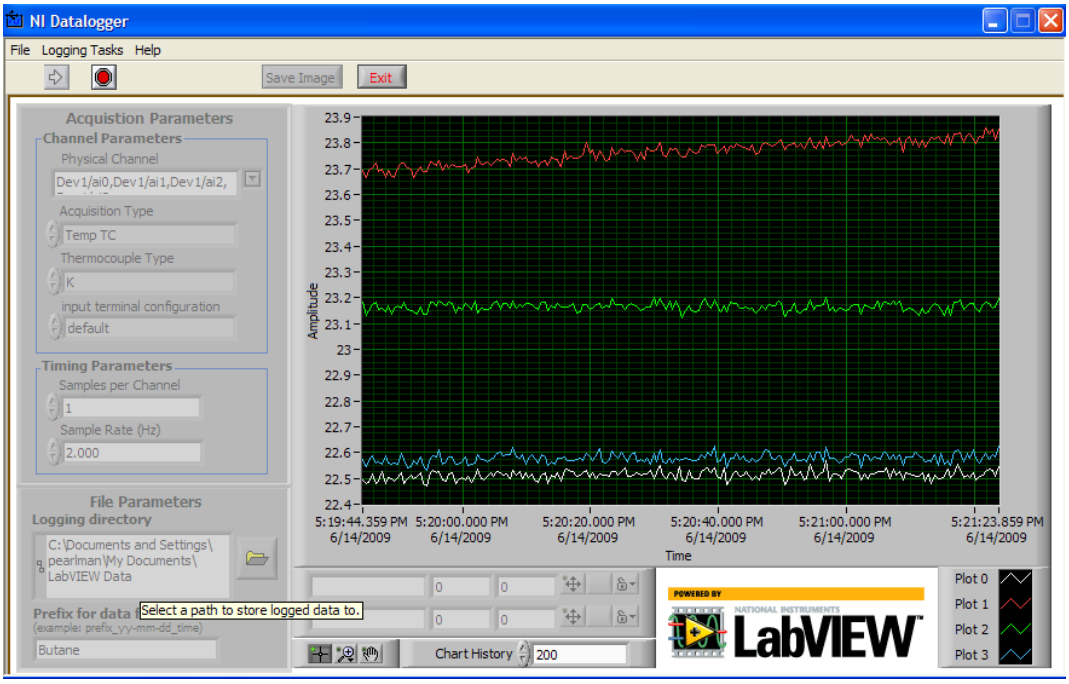

Figure 26: NI Labview display for four temperatures.

The use of a nebulizer and vaporization chamber has distinct advantages over the bubbler that include: 1) faster vaporization of the liquid fuel because of small and narrow

liquid droplet size distribution; 2) steadier liquid fuel flow rate so that the equivalence ratio of the liquid fuel mixtures are stable and controllable.

2.4 Experimental Methodology and Parameter Calculations

2.4.1 Variable Pressure Environment

During the experimental study, three different pressure ranges were examined, the atmospheric, sub-atmospheric and high pressure. Specifically, the pressure was varied from 250 Torr to 1000 Torr since the full scale for the pressure transducer was 1000 Torr.

The low pressure environment can suppress buoyancy and the dynamic patterns are expected to be more stable over a wide range of experimental parameters. For the burner-stabilized flames, both the hydrodynamic stretch induced by the nonuniformities in the flow and buoyant rise of the hot products transporting heat away from the flame can extinguish the flames at higher fuel concentrations than those required for the onset of instability. The significance of the buoyant effects on premixed flames has been evaluated by comparing the buoyant to molecular (viscous) transport. This ratio is defined as the Grashof number, $G_r = \left[\dfrac{\dfrac{\nabla\rho}{\rho} g d^3}{\nu^2} \right]$, where $\nabla\rho$ is the density difference between the hot products and cold reactants, ρ is the mean reactant density, d is the characteristic length of the process (burner diameter in our experiments) and ν is the kinematic viscosity. To reduce the effects of buoyancy is to reduce the Grashof number. Since the density of reactants is usually large relative to the density of the products

(ca. $\rho_{reac\tan ts} \approx 5\rho_{products}$), the value of $\frac{\nabla\rho}{\rho}$ is taken to be 1, and g and d are constants for our experimental conditions, so $G_r \propto \nu^{-2} \propto \frac{P^2}{T^3}$. It is seen that decreasing pressure P can decrease the Gr number so that the buoyancy effects are suppressed. Thus, sub-atmospheric pressure conditions were studied in this research.

On the other hand, at high pressure, there is a propensity of cell formation over the flame surface due to hydrodynamic and diffusive-thermal instabilities although high pressure has the stabilizing effects of positive flame stretch. For low-Le flames, the laminar flame speed ($s_{f,u}$) evaluated as dR(t)/dt decreases with increasing pressure which leads to decreasing flame thickness l_f ($l_f = (\lambda / c_P)/(\rho_u s_{f,u})$) and thus increasing the trends of destabilizing (Law et al., 2005). For high-Le flames, the overall activation energy is increased with increasing pressure so that the reduced Le number ($\ell = \beta(Le-1)$) increases and flames tend to be pulsatingly instable. The spiral waves on hydrogen-air flames were only able to be observed for pressure above 5 atm (Jomaas et al., 2007). As most of the practical combustion devices operate under high pressures for higher efficiency and work load, studies on the flame instability under high pressure are significant and necessary.

2.4.2 Calculation of Le for multi-component mixtures

For calculating the multi-component mixture's Lewis number, the thermal diffusivity of the mixture and the mass diffusivity of the deficient component of the mixture needed to be known. For the thermal diffusivity of the mixture, $\alpha = \kappa / \rho c_P$, the mixture density

ρ can be easily calculated based on the ideal gas theory for mixtures. $\rho = P \cdot MW/(R \cdot T)$, so as long as the pressure, temperature and the molecular weight of the mixture are known, we can calculate the density of the mixture. For heat capacity of the mixture $c_P = c_{P1} \cdot \chi_1 + c_{P2} \cdot \chi_2 + \cdots + c_{Pn} \cdot \chi_n$, where c_{Pn} is the heat capacity of the *n*th specie and χ_n is the species mole fraction. However, the calculation of the thermal conductivity of the mixture and mass diffusivity of the rate-limiting component to the mixture is not a simple add-on for separate species components.

To estimate the thermal conductivity of the gas mixtures, the Wassiljewa equation was used (Poling et al., 2001):

$$\lambda_m = \sum_{i=1}^{n} \frac{y_i \lambda_i}{\sum_{j=1}^{n} y_j A_{ij}} \tag{6}$$

where λ_m = thermal conductivity of the gas mixture

λ_i = thermal conductivity of pure i (data from DIPPR Database)

y_i, y_j = mole fraction of components i and j

A_{ij} = a function, defined as:

$$A_{ij} = \frac{\left(1 + \left(\frac{\lambda_{tri}}{\lambda_{trj}}\right)^{1/2} \left(\frac{M_i}{M_i}\right)^{1/4}\right)^2}{\left(8\left(1 + \frac{M_i}{M_i}\right)\right)^{1/2}} \tag{7}$$

In equation (2.2), λ_{tri} is the monatomic value of the individual translational thermal conductivity determined by:

$$\frac{\lambda_{tri}}{\lambda_{trj}} = \frac{\Gamma_j \left[\exp\left(0.0464 T_{ri}\right) - \exp\left(-0.2412 T_{ri}\right)\right]}{\Gamma_i \left[\exp\left(0.0464 T_{rj}\right) - \exp\left(-0.2412 T_{rj}\right)\right]} \qquad (8)$$

where T_{ri} is the reduced temperature of the i th component, T / T_{crit}. Γ_i is the reduced inverse thermal conductivity of species i is defined as:

$$\Gamma_i = 210 \left\{ \frac{T_{crit,i} M_i^3}{P_{crit,i}^4} \right\}^{1/6} \qquad (9)$$

here T_{crit} and P_{crit} are the vapor/liquid critical temperature (K) and pressure (bar).

$A_{ii} = 1$.

To calculate the mass diffusion coefficient of the deficient component to the mixture, the binary diffusion coefficients for the various combinations of gases need to be known. The calculation of binary diffusion coefficient was based on the Chapman-Enskog theoretical description at low to moderate pressure (Poling et al., 2001). The binary diffusion coefficient for the species pair A and B is

$$D_{AB} = \frac{0.00266 T^{3/2}}{P M W_{AB}^{1/2} \sigma_{AB}^2 \Omega_D} \qquad (10)$$

where $MW_{AB} = 2\left[\left(1/MW_A\right) + \left(1/MW_B\right)\right]^{-1}$, MW_A and MW_B are the molecular weights of species A and B, respectively; $\sigma_{AB} = \left(\sigma_A + \sigma_B\right)/2$, σ_A and σ_B are the hard-sphere collision diameters of species A and B. The collision integral, Ω_D is a dimensionless quantity defined as the following equation:

$$\Omega_D = \frac{A}{\left(T^*\right)^B} + \frac{C}{\exp\left(DT^*\right)} + \frac{E}{\exp\left(FT^*\right)} + \frac{G}{\exp\left(HT^*\right)} \qquad (11)$$

The coefficients for the collision integral are listed in the Table 3. The dimensionless temperature, T^*, is defined as $T^* = kT/(\varepsilon_A \varepsilon_B)^{1/2}$, where ε is the characteristic Lennard-Jones energy which are tabulated in the appendix B in The Properties of Gases and Liquids (Poling et al., 2001).

Table 3: Coefficients for calculation of the collision integral (Poling et al., 2001).

A	B	C	D	E	F	G	H
1.06036	0.15610	0.19300	0.47635	1.03587	1.52996	1.76474	3.89411

After the binary coefficients for the combination of all components are calculated, the effective coefficient of the deficient species into the mixture can be calculated based on the following method proposed by Wilke (Wilke, 1950):

$$D_{i,mix} = \left(\sum_{i=1, j \neq i}^{n} \frac{y_j}{D_{i,j}} \right) \tag{12}$$

Then the Le is calculated using:

$$Le = \frac{\lambda_{mix}}{\rho_{mix} c_{P\,mix} D_{i,mix}} \tag{13}$$

2.4.3 Error Analysis

There are always some errors with measuring the physical quantities. The error analysis is to estimate how much the measured value deviates from the unknown true value of the quantity. Errors can be caused by: (1) calibration of the measuring instruments; (2) incorrect measuring techniques; (3) bias of the experimenters. When we calculate a desired quantity according to some formula using some experimental measurements, the errors with the calculated value should be caused from the combination of the errors in the input quantities, which is called the propagation of the errors. The general formula to estimate the propagation of the errors is:

$$\Delta f\left(x_{1,}x_2\right)=sqrt\left(\sum\left(\frac{\partial f}{\partial x_i}\right)^2\left(\Delta x_i\right)^2\right) \qquad (14)$$

Here, Δf is the propagated uncertainty in the calculated value f. Δx_i is the absolute error for the experimental measurement quantity x_i.

In this study, an uncertainty analysis was performed to define the expanded uncertainty for the exit flow speed of the McKenna burner and equivalence ratio according to the following equations:

$$V_{exit}=Q_{total}/A=\sum Q_i/(\pi r^2) \qquad (15)$$

$$\phi=(A/F)_{stoic}/(A/F)_{actual}=(A/F)_{stoic}/(Q_{air}/Q_{fuel}) \qquad (16)$$

Here Q_{total} is the total flow rate of the sum of the flow rates of oxidizer and fuel. r is the radius of the McKenna burner, r = 3 cm. The flow rates were measured by the MKS mass flow controllers, which have the accuracy of 1% of the FS. As an example of how

to calculate the propagated errors using equation (14), the estimate of uncertainty of exit flow speed for the case # of appendix B.1 is shown here.

$$\Delta V_{exit} = sqrt\left((1/A)^2 \times (\Delta Q_{total})^2 + ((-2 \times Q_{total})/(\pi r^3))^2 \times (\Delta r)^2\right) \quad (17)$$

Here ,

$A = \pi r_2 = \pi \times (3)^2 = 28.27 cm^2$, $\Delta r = 0.1 cm$

$Q_{total} = Q_1 + Q_2 = 0.221 SLM + 7.58 SLM = 7.80 SLM = 130 cm^3/s$

$\Delta Q_{total} = \sqrt{(\Delta Q_1{}^2 + \Delta Q_2{}^2)} = \sqrt{(0.01 \times 1)^2 + (0.01 \times 10)^2} = 1.667 cm^3/s$

So we have $\Delta V_{exit} = 0.3 cm/s$.

2.5 Closure

The experimental apparatus and techniques were described in this chapter and used throughout this study to obtain the experimental results. The method to compute the Lewis number of multi-component mixtures and to analyze errors was also shown in this chapter. The experimental results will be discussed in the following chapter.

3. Experimental Studies on High-Lewis Number Premixed Gas Flame Instabilities

3.1 Introduction

Diffusive-thermal pulsating and traveling wave instabilities have been predicted by linear stability analyses for premixed gas flames that have a reduced Lewis number ($\ell = \beta(Le-1)$) sufficiently larger than one. In this formulation, β is the Zel'dovich number (non-dimensional activation energy, E/RT) and Le is the Lewis number of the premixture based on the thermal diffusivity of the mixture and the mass diffusivity of the rate-limiting component (species) into the mixture ($\alpha_{mix}/D_{rate\text{-}limit\ component}$) (Sivashinsky, 1977a; Joulin and Clavin, 1979; Sivashinsky and Matkowsky, 1981). Interestingly, the critical value for the reduced Le, i.e., $\ell_{cr} = \beta(Le-1)$ depends on the heat loss associated with the system. Specifically, Sivashinsky's adiabatic analysis has shown that $\ell_{cr} = 4(1+\sqrt{3}) \approx 10.9$ while subsequent non-adiabatic stability analyses reinforced the concept that increasing volumetric heat loss has a destabilizing effect such that ℓ_{cr} for onset of instability decreases with increasing heat loss (Joulin and Clavin, 1979).

In contrast to low-Lewis number cellularly unstable premixed flames that have been observed for more than a century (Smithells and Ingle, 1892) (Markstein, 1964), high-Lewis number instabilities eluded experimental observation for many years and in some cases were simply not recognized to be a result of the diffusive-thermal instability until recently. Some seemingly unrelated systems in which spinning flames were observed included: self-propagating high-temperature synthesis (SHS) where the reactants and products are in the solid phase (Nayagam et al., 2001), freely propagating acetylene decomposition flames (Gololobov et al., 1981) and lean propane and n-butane premixed

flames on a McKenna burner (el-Hamdi and Gorman, 1993). In all of these cases, the high-Lewis number traveling wave instability plays a key role in the spatio-temporal behavior and resulting structure of the flames. Perhaps, the limiting case is that associated with SHS in which the Le is effectively infinite because the mass diffusivity of the solid fuel is near zero. A renewed focus on the high-Lewis number diffusive thermal instability followed the observations of rotating spiral waves and target patterns on the surface of downwardly-propagating flames in vertical tubes (Pearlman and Ronney, 1994b; Pearlman and Ronney, 1994a; Pearlman, 1997). The unique spatio-temporal patterns on the flame surface were similar in appearance to those observed in excitable media, e.g., Belousov-Zhabotinskii reaction. Unlike most excitable, liquid-phase systems, however, these flames were clearly non-isothermal reactions in which thermal and chemical feedbacks were important. Perhaps, such instabilities were not observed sooner since most premixed flames have Lewis numbers near unity or below (e.g., lean methane-air: Le ~ 0.93, lean hydrogen-air: Le ~ 0.3) that required for onset of instability, $Le_c = 1+ \ell_{cr}/\beta$, where it is noted that β typically ranges from 6 to 10 and ℓ_{cr} for the adiabatic case is 10.9, such that $Le_{c,adiabatic} \sim 2.1\text{-}2.8$. It is further noted that the first definitive observations of these instabilities were made in helium-diluted premixtures at exceedingly lean conditions using heavy alkane fuels (e.g., n-butane, n-heptane, n-octane, etc). Helium was selected as a diluent since it is the largest component of the mixture and has a high thermal diffusivity that is roughly three times larger than that of nitrogen while lean, heavy fuels were selected to minimize the mass diffusivity of the rate-limiting component (fuel) into the premixture and thus maximize the Le. Typical values

considered in previous studies ranged from 2.3 to 5.4, in excess of critical Le required by non-adiabatic, linear stability analyses.

More recent experiments conducted at Princeton University aimed to understand the nonlinear couplings between the hydrodynamic and diffusive-thermal instabilities (Law et al., 2005). Much to their surprise, rotating spiral waves in addition to complex flamelet dynamics, superposed on large-scale hydrodynamic cells were observed in rich, high-pressure (> 8 atm) hydrogen-air flames using a high-speed Schlieren system. In these studies, the characteristic length and time scales associated with the hydrodynamic and diffusive-thermal instabilities were starkly different such that the manifestations of the hydrodynamic and diffusive-thermal instabilities could readily be differentiated. In their work, the authors correctly argue that the relevant parameter for the onset of the diffusive-thermal instability is the reduced Le, $\ell = \beta(\text{Le}-1)$, not simply the Le which is important to the understanding of why the diffusive-thermal instabilities occurred at elevated pressures yet were not observed at lower pressures. To explain the pressure-dependence on the onset of instability, it was argued that the reaction rate for the three-body termination reaction is pressure-sensitive and increases relative to that associated with the two-body branching reactions that are important in the H-O_2 branching-termination cycle. This results in a substantial increase in the effective activation energy of the overall reaction which increases β and thus ℓ_{cr}.

In this chapter, the parameters that determine the onset of instability, the different modes of instability, and their spatio-temporal dynamics were further explored using stationary, water-cooled porous-plug McKenna burners. In contrast to prior experiments on freely propagating or spherically expanding high-pressure premixed flames, the

motivation for these experiments is to stabilize high Le premixed flames on flat flame burners to study these instabilities in a stationary coordinate system, and thus simplify the experiment and modeling efforts required. In addition, the upstream boundary conditions would be well defined for the numerical simulations described in Chapter 4.

With respect to the organization of this chapter, a detailed presentation of new experimental results for n-butane, n-heptane, and n-octane premixed with O_2 diluted by N_2 and He is given respectively in Section 3.2, Section 3.3 and Section 3.4. Experimental results obtained at reduced and elevated ambient pressures for n-butane-O_2-He mixtures are then summarized in Section 3.5. A summary of the experimental studies is given in Section 3.6.

3.2 New Observations of High-Lewis Number Burner-Stabilized Premixed Gas Flame Instabilities in n-Butane-O_2-Inert Premixtures

To expand our understanding of the flame structure and stability of premixed flames subject to high-Lewis number instabilities, a systematic experimental study of burner-stabilized premixed flames in high-Le mixtures was performed at reduced, atmospheric and elevated pressure using three alkane fuels (n-C_4H_{10}, n-C_7H_{16}, n-C_8H_{18}) diluted with air or 21%O_2-balance He. The mixtures considered and their associated Le's are given in Table 4 (note: representative Le calculations are provided in Chapter 2.

Table 4: Computed values of the Lewis number for lean n-C_4H_{10}, n-C_7H_{16} and n-C_8H_{18} premixtures diluted with air (21% O_2-balance N_2) and 21% O_2- balance He.

Fuel	Inert	$Le_{Fuel\text{-}mixture}$
n-C_4H_{10}	air	2.28
	21%O_2-balance He	3.25
n-C_7H_{16}	air	3.45
	21%O_2-balance He	5.03
n-C_8H_{18}	air	4.02
	21%O_2-balance He	5.40

Experiments were conducted at variable pressures (P) to explore pressure effects on the flame stability. At reduced pressure, buoyant flows can be suppressed ($Ra \sim P^2$) and thus it can be shown that the observed instabilities are not buoyancy induced. Moreover, the relative importance of the different time and length scales: diffusional and chemical ($t_{diffusional}$, $t_{chemical}$) can be qualitatively studied knowing that diffusional lengths scale inversely with pressure yet the relative rates of species and thermal diffusion remain unchanged since the Le is pressure independent. It is also important to note that the only other known report of burner stabilized spiral wave instabilities was performed at sub-atmospheric pressure using rich methane-air ($1.2 < \phi < 1.4$) for which the Le was near unity (Robbins et al., 2004)

Experiments were also conducted for different burner exit flow speeds to vary the flame standoff distance and thus vary the conductive heat loss to the burner. From these results, comparisons can be obtained to support or refute non-adiabatic linear stability analysis predictions and prior results that suggest that increasing heat loss decreases the critical Le for onset of instability thereby broadening the stability envelope.

3.2.1 Flame Patterns in n-C_4H_{10}-21%O_2-balance He Premixtures on a Stainless-Steel McKenna Burner

Premixtures of n-C_4H_{10} and O_2 diluted with helium or nitrogen on a stainless-steel flat-flame, porous-plug, McKenna burner were considered. Unlike previous experiments on freely-propagating flames or spherically expanding flames, these stabilized nearly-planar flames enable the application of advanced diagnostics and simplify the means for acquiring the high-speed images. A diagram of the experimental hardware (Figure 12) and the operating procedure used to conduct all experiments were presented in chapter 2. In short, the flames were initially stabilized and the oxidizer and inert gas flow rates were then increased proportionally (thus decreasing the equivalence ratio) until the onset of instability as determined from visual observation of the flame using high speed video imaging (up to 1000 fps). The fuel flow rate was subsequently incremented and the procedure was repeated for a range of volumetric flow rates and thus different burner exit flow speeds.

Three modes of reaction were observed as a function of equivalence ratio and burner exit flow speed for lean and near-stoichiometric n-C_4H_{10}-O_2-He premixtures. They include:

(1) Stable planar flames for $0.95 < \Phi < 1.10$, 4.6 ± 0.3 cm/s $< V_{exit} < 5.6 \pm 0.4$ cm/s

(2) Irregular spatio-temporal patterns for $0.96 < \Phi < 1.12$, 3.1 ± 0.2 cm/s $< V_{exit} < 3.5 \pm 0.3$ cm/s

(3) Instability regime for $0.75 < \Phi < 0.95$, 4.2 ± 0.3 cm/s $< V_{exit} < 8.3 \pm 0.5$ cm/s

In mode (1), stable planar flames were observed and exhibited no evidence of instability. In mode (2), irregular patterns were observed characterized by flickering and pulsating motions of the flame front without any apparent regularity. In mode (3), the Instabilities Regime, four characteristic types of instability patterns were observed. They included: (1) two-arm spiral waves, (2) complex rotating spiral and target waves that were spatially distributed, yet occurred simultaneously, (3) single rotating spiral waves, and (4) target patterns. Table 5 is a summary of the range of mixture equivalence ratios and burner exit flow speeds corresponding to the different instabilities modes observed. Detailed test data has also been included in Appendix B for reference.

Table 5: Spatio-temporal patterns observed in mode (3), the instability regime, in n-C_4H_{10}-21%O_2-balance He premixtures for a range of equivalence ratios and burner exit flow speeds.

Φ	V_{exit} (cm/s)	Types of Patterns/Waves	Representative Image(s)
0.91- 0.95	4.6	Two-arm spiral waves	Figure 27
0.79-0.88	4.6-6.7	Complex spiral waves	Figure 28 & Figure 29
0.75-0.93	4.2-8.3	Spiral waves	Figure 30 & Figure 31 & Figure 33
0.75-0.84	5.5-7.1	Target patterns	Figure 32

At moderate (4.6 ± 0.3 cm/s) flow speeds, stable planar flames were observed in near stoichiometric premixtures ($0.95 \leq \Phi \leq 1.10$), while slightly leaner mixtures ($0.91 \leq \Phi \leq 0.95$) with comparable exit flow speeds exhibited multi-arm rotating spiral waves. A representative sequence of images corresponding to the two-arm spiral wave is shown in

Figure 27. In the experiment, the two spiral arms developed spontaneously as the fuel and oxidizer concentration changed. The separation distance between the spiral wave tips varied during the cycle and they periodically merged (e.g. Figure 27b) and separated (e.g. Figure 27c) during the rotation process, which may be associated with the meandering of the spiral wave tips predicted numerically by Panfilov et al. (Panfilov et al., 2003) and observed in the experiments of Robbins et al. (Robbins et al., 2004). The rotation rate was determined to be 42 Hz by post-processing the video data.

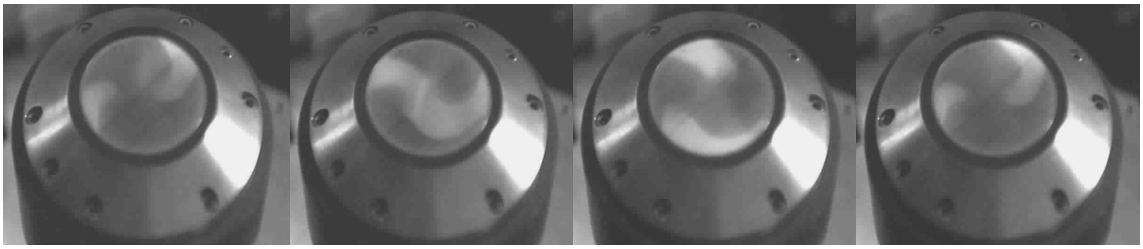

(a) **(b)** **(c)** **(d)**

Figure 27: Two co-rotating spiral waves in n-C_4H_{10}-21%O_2-balance He, $\Phi = 0.91$, $V_{exit} = 4.6 \pm 0.3$ cm/s, time between consecutive images was 1/125 sec.

At slightly leaner conditions ($0.79 \leq \Phi \leq 0.88$), complex interacting spiral waves were observed with a representative image sequence shown in Figure 28. In particular, two rotating spiral waves were observed that subsequently interacted, merged and annihilated, yet the overall spatiotemporal structure of the pattern remained irregular. The two spiral waves periodically interacted at different spatial locations, while the cores/pacemakers of the spiral waves retained their integrity. For the case shown, the frequency of rotation was 62 Hz determined from post-processing the video images and noting that one revolution required 8 frames at a framing rate of 500 fps.

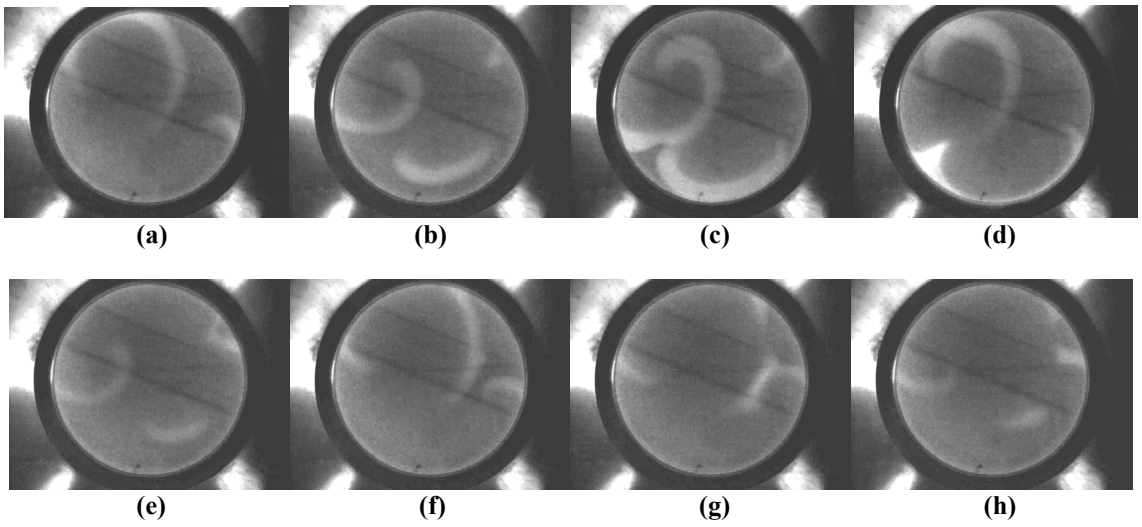

Figure 28: Interaction between multiple rotating spiral waves in n-C_4H_{10}-21%O_2-balance He, Φ = 0.88, V_{exit} = 6.1 ± 0.4 cm/s, time between consecutive images was 1/500 sec.

In addition to the interacting spiral waves on the flame surface, the interaction of a circular wave reminiscent of that formed at the core of a target pattern was also observed to coexist and interact with a rotating spiral wave as shown in Figure 29. In all cases, the waves propagate radially outwardly or rotate then annihilate each other in the region(s) where they interact, yet maintain their distinct identities. Interestingly, one wave does not dominate the long-term evolution of the instability and the site from which the circular wave originated remained spatially fixed, as did the center about which the spiral wave rotated. For this case, the revolutionary rate for one cycle of co-existing interacting patterns was 77 Hz.

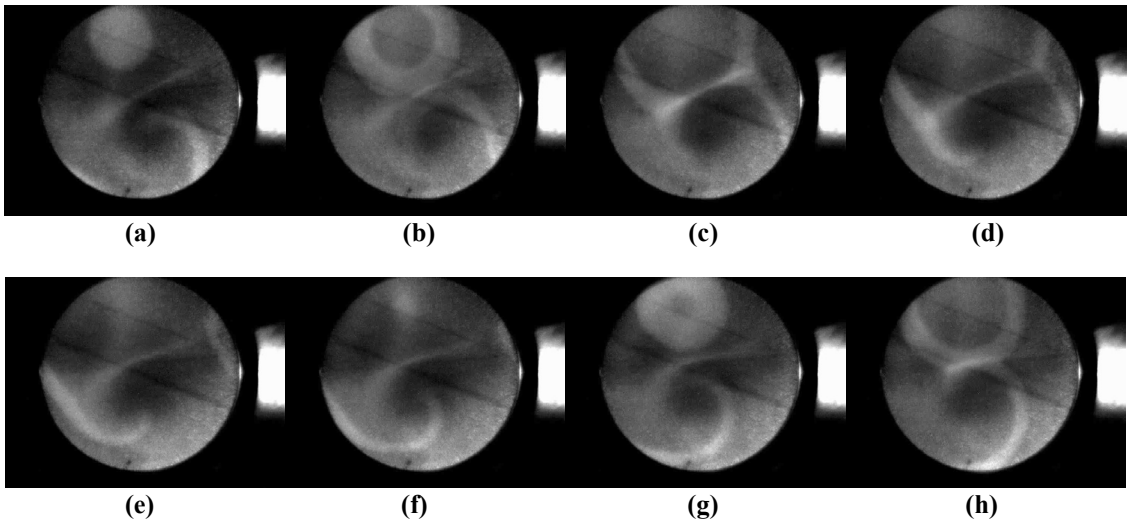

Figure 29: Interaction of spatially distributed target pattern and rotating spiral wave in n-C_4H_{10}-21%O_2-balance He, $\Phi = 0.79$, $V_{exit} = 6.7 \pm 0.4$ cm/s, time between consecutive images was 1/500 sec.

Single-arm rotating spiral waves were observed for leaner premixtures with equivalence ratios in the range of $0.75 \leq \Phi \leq 0.93$. A representative case is shown in Figure 30 for which the rotation rate ranged from 60-80 revolutions per second, on the same order yet slightly lower than those previously reported for the case of the downwardly propagating flames in tubes using the same mixture at atmospheric conditions (Pearlman and Ronney, 1994b). For the case shown, the spiral rotated steadily and the spacing between adjacent windings was 3.0 ± 0.5 cm, approximately half of the burner diameter which is comparable with prior observations in freely-propagating flames in the same premixture (Pearlman, 1997).

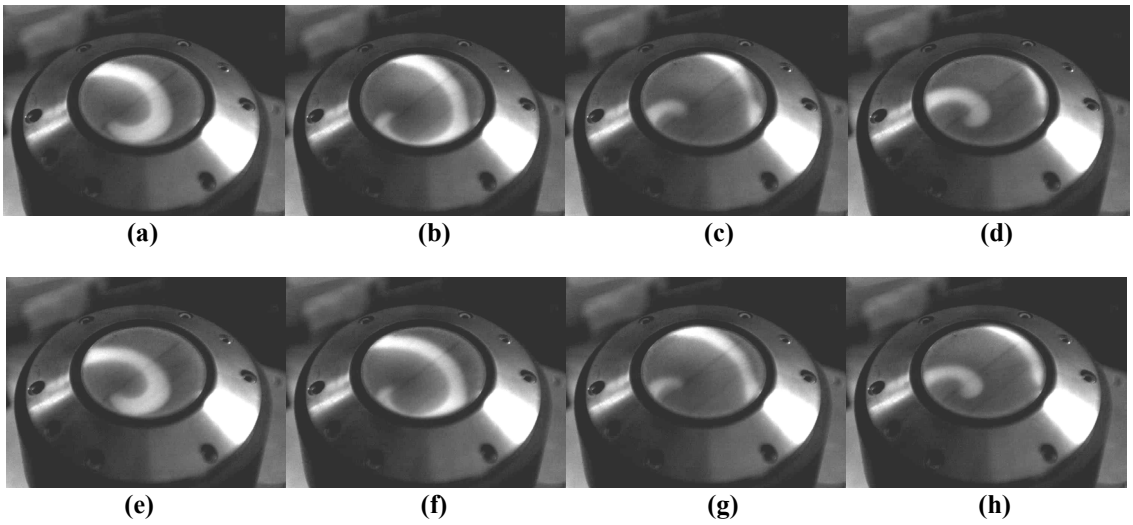

Figure 30: Single-arm rotating spiral wave in lean n-C_4H_{10}-21%O_2-balance He, Φ = 0.85, V_{exit} = 5.5 ± 0.4 cm/s, ω = 63 Hz, time between consecutive images was 1/250 sec.

For similar equivalence ratios and burner exit flow speeds as the spiral waves, target patterns were also observed and remained the dominant mode as the equivalence ratio decreased until extinction. Representative spiral waves and target patterns are shown in Figure 31 and Figure 32 for the same exit flow speed (V_{exit} = 6.2 ± 0.4 cm/s) and similar equivalence ratios, i.e., Φ = 0.82 (spiral wave) and Φ = 0.80 (target pattern). For the single rotating spiral wave in Figure 31, its rotation rate was similar to that shown in Figure 30 with a rotation rate of 71 Hz and spacing between consecutive windings was also around 3 cm. It is also interesting to note that the radially-propagating circular wave in Figure 32 that initiates slightly off-center, yet remains centered around its origin and pulsates at 50 Hz. The oscillation frequency was of the same order, yet slighter slower than the rotation rate of the rotating spiral wave observed at the similar conditions.

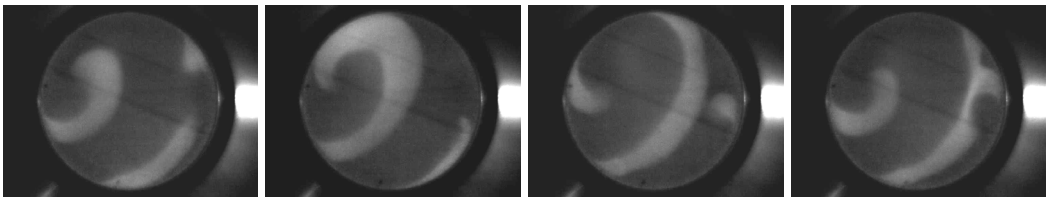

(a) (b) (c) (d)

Figure 31: Rotating spiral wave in lean n-C_4H_{10}-21%O_2-balance He, Φ = 0.82, V_{exit} = 6.2 ± 0.4 cm/s, time between consecutive images was 1/250 sec, ω = 63 rps, spacing between consecutive windings ≈ 3 cm. Note: apparent differences in the flame luminosity and thickness inferred by comparison with Figure 30 can be attributed to differences in the optics and camera settings.

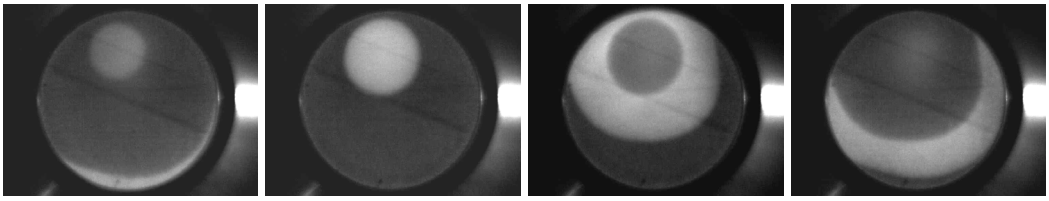

(a) (b) (c) (d)

Figure 32: Target patterns in lean n-C_4H_{10}-21%O_2-balance He, Φ = 0.80, V_{exit} = 6.2 ± 0.4 cm/s, ω = 50 Hz, time between consecutive images was 1/250 sec.

Another example of a single-arm rotating spiral wave on the burner-surface is shown in Figure 33.

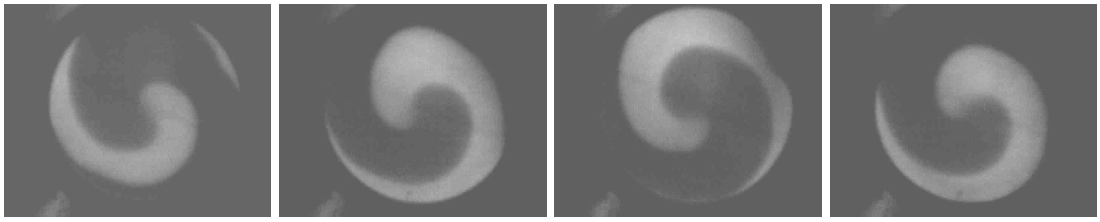

(a) (b) (c) (d)

Figure 33: Single-arm rotating spiral wave in lean n-C_4H_{10}-21%O_2-balance He premixture, Φ = 0.75, V_{exit} = 8.3 ± 0.5 cm/s, ω = 83 Hz, time between consecutive images was 1/250 sec.

3.2.2 Stability Diagram for n-C_4H_{10}-21%O_2-balance He on a Stainless-Steel McKenna Burner

A stability diagram detailing the different reaction modes as a function of the burner exit flow speed and the mixture equivalence ratio is presented in Figure 34 for the n-C_4H_{10}-21%O_2-balance He premixed flames on a stainless-steel porous-plug McKenna burner at atmospheric pressure. The modes identified include: (1) stable planar flames, (2) complex rotating spiral waves, (3) single and multi-arm rotating spiral waves, (4) circular radial waves/ target patterns, and (5) irregular patterns comprised of multiple interacting flamelets that are not clearly identifiable in modes (1) - (4). The extinction boundary is also indicated as an 'Extinction' region.

As shown, instabilities developed in these near-limit mixtures with a shift towards leaner mixtures at higher flow speeds. This trend is likely due to the increase in flame standoff distance at higher flow speeds accompanied by a decrease in conduction heat loss. With regard to the order that the instabilities occur with decreasing equivalence ratio, stable flames generally transition from complex spiral or bi-stable patterns, single rotating spiral waves to radial pulsations/ target patterns.

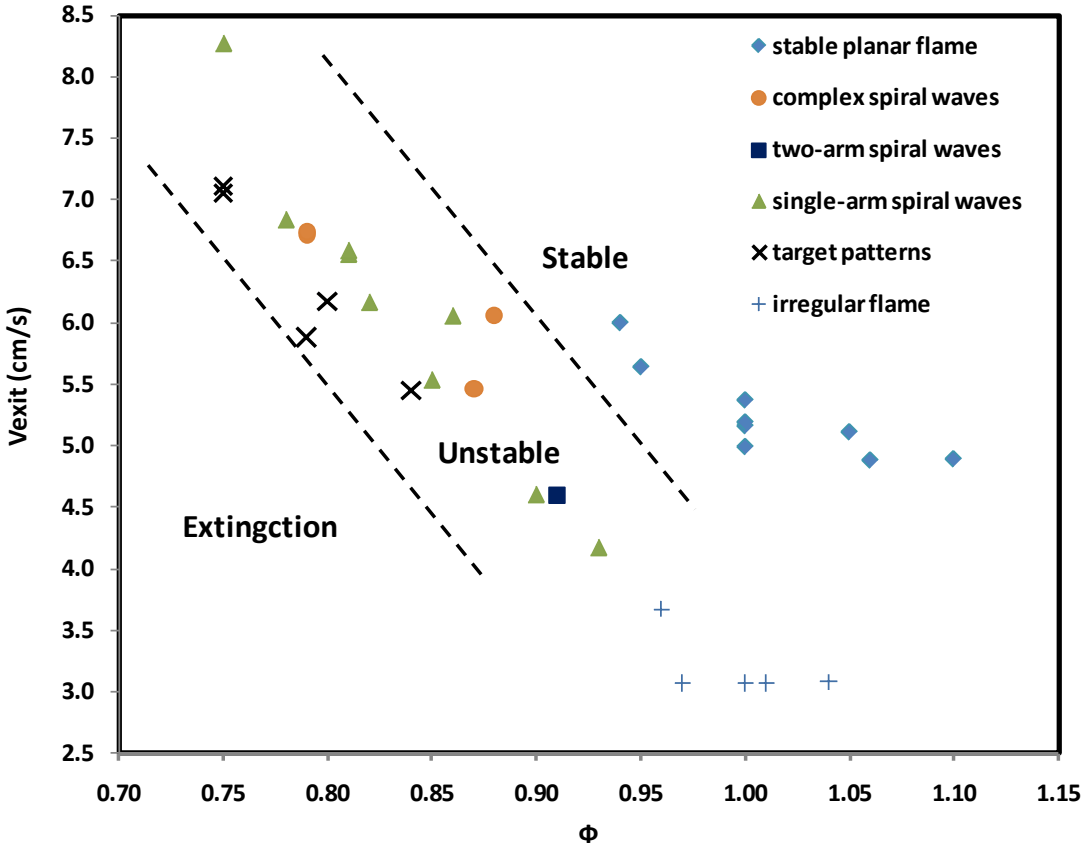

Figure 34: Stability diagram for burner stabilized premixed gas flames in an n-C_4H_{10}-21%O_2-balance He mixture at 1 atm on a stainless-steel porous-plug McKenna burner. The two dash lines are indicated to differentiate stable, unstable, and nonflammable regimes.

3.2.3 Effect of Enriched Oxygen on Burner-Stabilized, Helium Diluted Premixed Gas Flame Instabilities

Burner-stabilized premixed flames were also studied using n-C_4H_{10} diluted by 25%O_2 -balance He. Increasing O_2 mole fraction extends the lean flammability limit (due to an increase in the flame temperature) and allows exploration of the manifestation of the high-Le number flame instability for leaner conditions than can be achieved with 21% O_2 dilution. The lean extinction limits were determined to be $\Phi = 0.78$ and $\Phi = 0.73$ for

premixtures containing 21% and 25% O_2, respectively, for a burner exit flow speed of 6.0 ± 0.4 cm/s.

Similar patterns were observed for both premixtures and consisted of: complex spiral waves, single-arm rotating spiral waves and target patterns. A representative sequence of images taken of a single-arm rotating spiral wave in enriched oxygen premixture is shown in Figure 35. The shape and rotation rate were the same (83 Hz) as that observed in 21%O_2-balance He (Figure 33). The position of the spiral wave tip was manually tracked and determined to follow a complex and meandering trajectory.

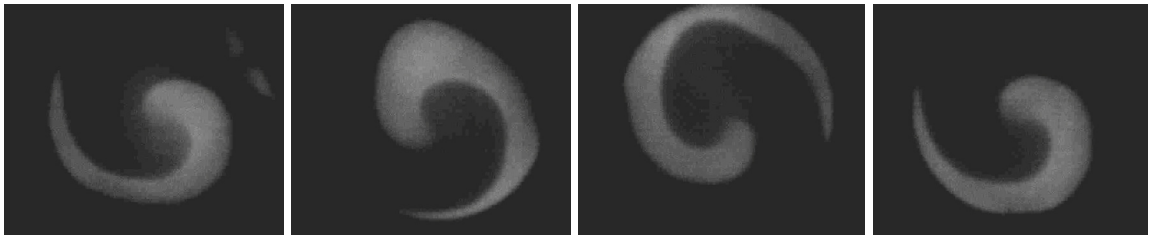

(a) **(b)** **(c)** **(d)**

Figure 35: Single-arm rotating spiral wave for lean n-C_4H_{10} diluted with 25%O_2-balance He premixture, Φ = 0.76, Vexit = 6.0 ± 0.4 cm/s, ω = 83 Hz, time between consecutive images was 1/250 sec.

Figure 36(a) displays the trajectories of the spiral tip (tracked manually using NASA's image tracking software, Spotlight version 8.0) for 100 sequential frames (0.4s) for the spiral wave shown in Figure 35. The first 7 successive revolutions taken as a subset of the data are reproduced in Figure 36(b) and numbered consecutively.

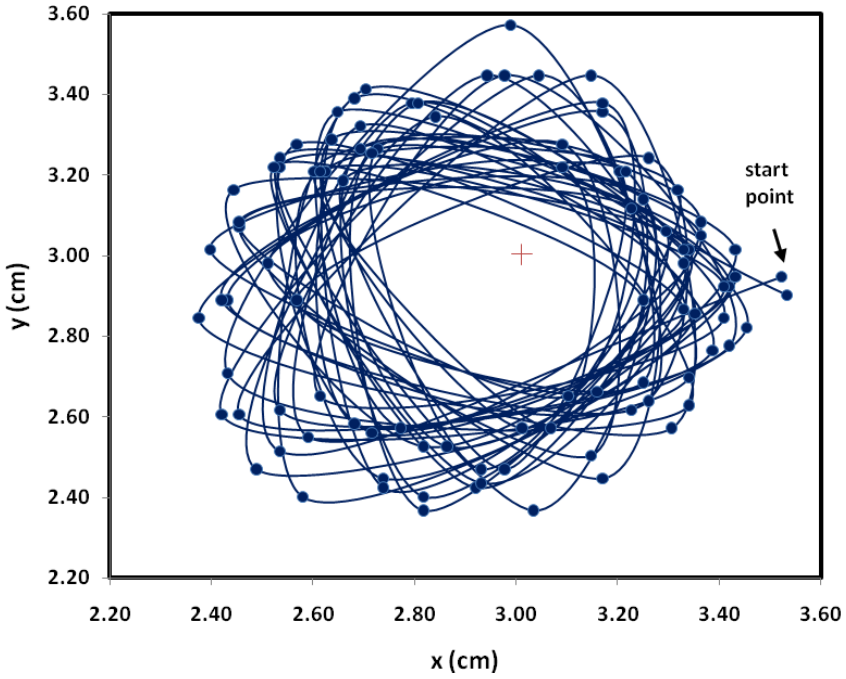

(a) Spiral wave tip trajectory

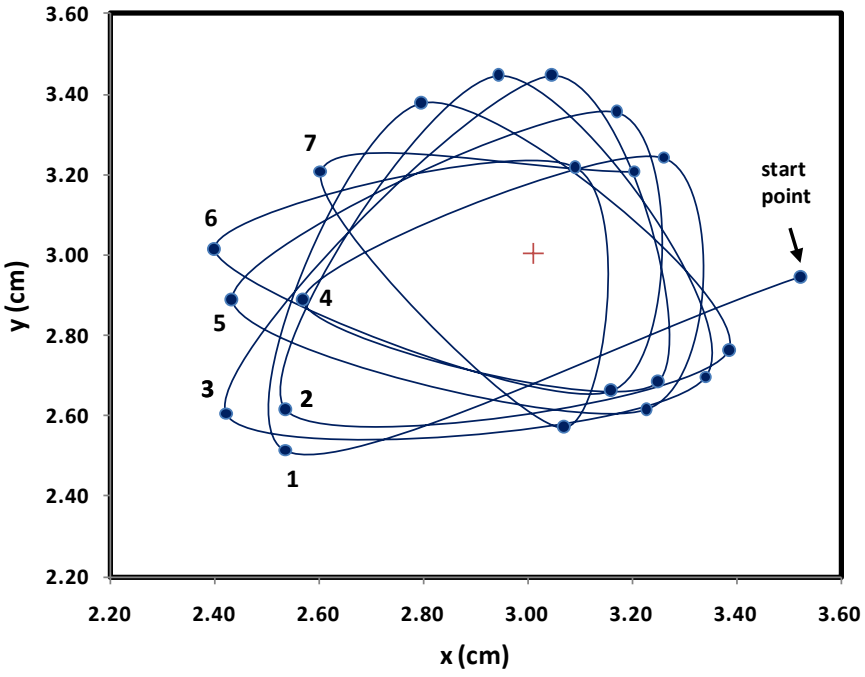

(b) 7 successive revolutions of the spiral tip trajectory

Figure 36: Meandering trajectories of the spiral wave tip associated with the spiral wave shown in Figure 35, arrow indicates the tip location for the first frame and the cross indicates the center of the burner.

As shown, the trajectory of the spiral tip follows a meandering 'petal-like' path similar to the meandering tip trajectories reported by Robbins and coworkers for a rich burner-stabilized methane-air flame at sub-atmospheric pressure (Robbins et al., 2004). Similar periodic trajectories are not uncommon in chemical systems that exhibit spiral tip motion and oftentimes meandering tip trajectories. Such "doubly" periodic dynamics and complexity have also been predicted to occur in premixed gas flames using a diffusive-thermal model based on a two-step Sal'nikov scheme, as reported by Panfilov and his coworkers (Panfilov et al., 2003) and also in this work (Chapter 4).

3.2.4 Comparison of Premixed n-C_4H_{10}-21%O_2-balance He Results Using Stainless-Steel and Bronze McKenna Burners

Additional tests were also conducted using a low-pressure bronze McKenna burner at the same conditions (i.e., mixture compositions, flow rates) where it is noted that all results reported above were obtained using a 316 stainless-steel sintered burner. Both burners had a 60.0 mm internal diameter sintered porous burner disk, while the burner disk for the bronze burner was made of bronze and jacketed by an 86.0 mm wide shroud and the burner disk for the stainless-steel burner was made of 316 stainless-steel and had a 67.5 mm shroud gas area. The size of the shroud was not expected to play a significant role, however conduction heat loss was expected to be larger for the bronze burner due to its higher thermal conductivity ($k_{bronze} = 401$ W·m^{-1}·K^{-1} vs. $k_{stainless\text{-}steel} = 16$ W·m^{-1}·K^{-1}). For these near-limit flames that are sensitive to the diffusive-thermal (and hydrodynamic) instabilities and heat loss, as predicted by nonadiabatic stability analyses, changes in stability attributed to differences in heat loss may be particularly acute.

In addition, the temperature distribution on the burner surface of the two different McKenna burners are slightly different as demonstrated experimentally in a study that measured the temperature distribution using an infrared camera following the extinction of a flat flame (initially sustained for 30 minutes to ensure steady-state prior to extinction). For the bronze burner, the temperature distribution is reproduced in Figure 37(a) and confirms uniformity in contrast to a parabolic temperature distribution measured on the stainless-steel burner for otherwise identical conditions. As shown in Figure 37(b), the maximum temperature difference between the center and the burner rim was 10K (Migliorini et al., 2008).

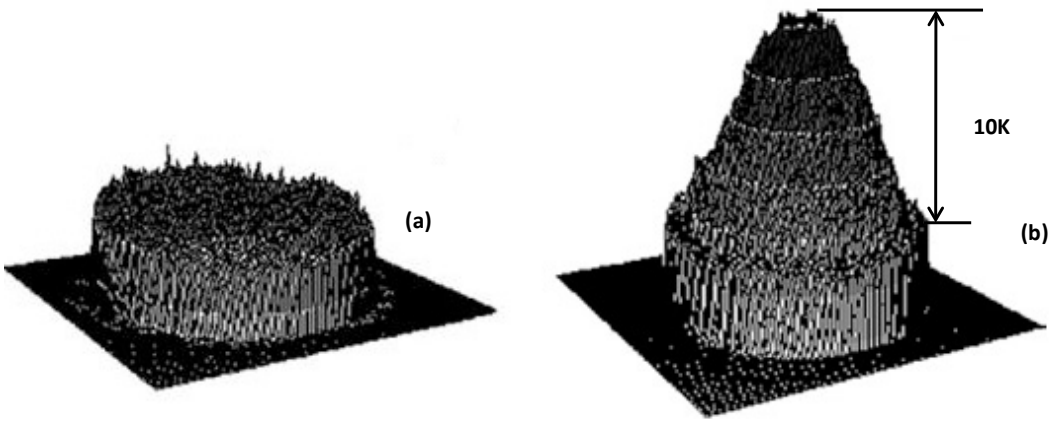

Figure 37: Temperature distribution of different burner surfaces immediately after the extinction of a flat flame for (a) bronze (b) stainless-steel porous-plug McKenna burners (Migliorini et al., 2008).

For the bronze burner, a stability map was developed and is reported in Figure 38. Similar to the results reported above, these cases were conducted by fixing the equivalence ratio at a slightly rich composition (Φ=1.1) for a given burner exit flow

speed after which the flow rates of the fuel, oxidizer, and inert gases were correspondingly decreased to maintain a given equivalence ratio. Similar to the results obtained with the stainless-steel burner, the modes observed on the bronze burner using n-C_4H_{10}-21%O_2-balance He mixture included: (1) stable planar flames, (2) complex target patterns, (3) spiral waves and (4) axisymmetric target patterns and generally occurred in that order as the equivalence ratio was decreased for a fixed burner exit velocity. The unstable regime also shifted toward leaner mixtures with increasing burner exit flow speed. This was due to an increase in the flame standoff distance and thus a decrease in conduction heat loss and broadening of the flammability limit. Differences of the stability diagram between the two burners were also observed. First, no multi-arm rotating spiral waves were observed and only a single test case that produced a rotating spiral wave. Second, the primary mode was radial pulsations/ target patterns, in contrast to the complex rotating spiral waves or bi-stable spiral and radial pulsations/ target patterns observed on the stainless-steel burner. Third, the target patterns observed using the bronze burner were axisymmetric and originated from the center of the burner, while the target patterns observed on the stainless-steel burner often originated off center. Perhaps, the nonuniformity of the burner exit temperature for the stainless-steel burner provided a sufficient perturbation that may have played an integral role in the onset of the spiral wave. Prior numerical studies (Scott et al., 1997; Panfilov et al., 2003) and those reported in Chapter 4 of this thesis suggest that rotating spiral waves are stable solutions of the governing equations and can be sustained in high-Le premixtures, while an initial temperature perturbation (an axisymmetric disturbance for the case of target patterns and a nonaxisymmetric disturbance for the case of rotating spiral waves) was also prescribed

in the numerical studies to initiate the instabilities. The diagram in Figure 38 also shows that the instability regime is dramatically narrowed while the exit flow speed exceeded 11 cm/s, which were consistent with the prior observation by Pearlman et al. (Pearlman, 1997). In their studies, there was no observation of flame instabilities for flow speeds above 11 cm/s.

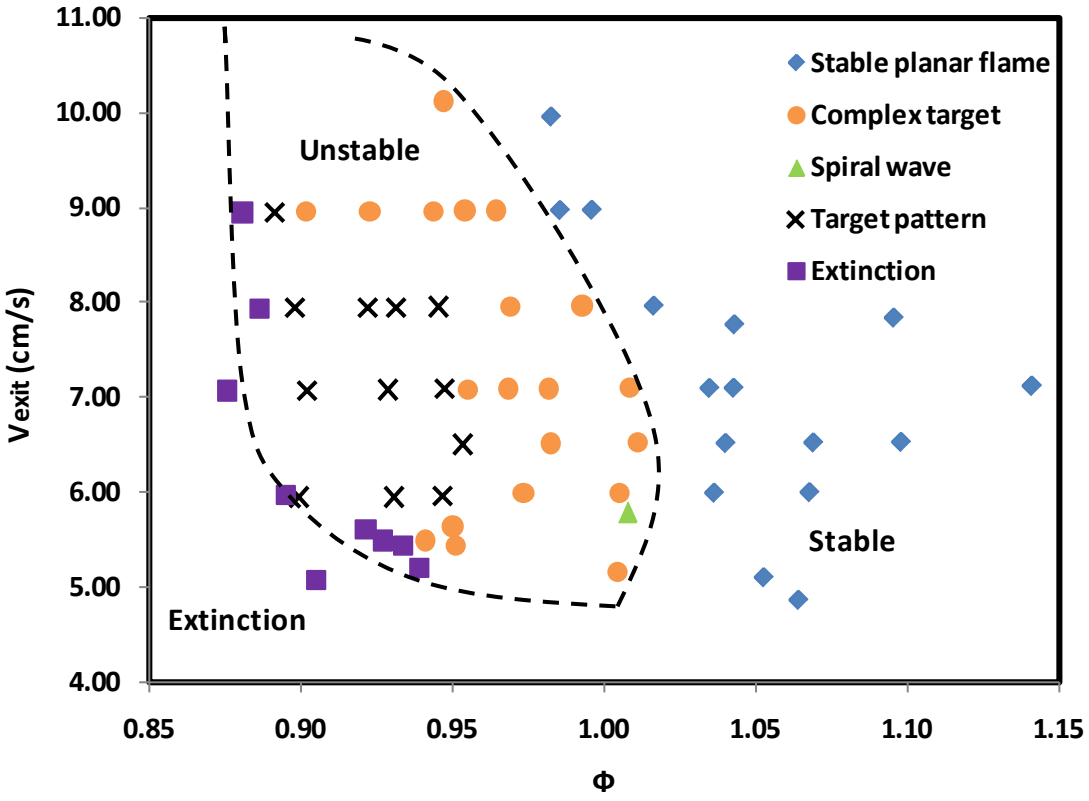

Figure 38: Stability diagram for n-C_4H_{10}-21%O_2-balance He premixtures on the bronze porous-plug burner at 1 atm.

Representative images that depict the different modes of reaction using the bronze burner are shown in Figure 39. The modes include: (a) stable planar flames, (b) complex

radially-propagating waves/ target patterns, (c) spiral waves and (d) axisymmetric circular waves/ target patterns. Each of these modes is discussed below.

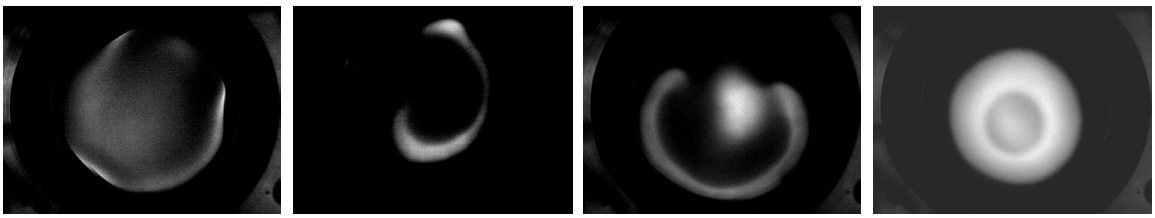

(a) **(b)** **(c)** **(d)**

Figure 39: Representative images of the unstable modes observed using n-C_4H_{10}-21%O_2-balance He premixtures on the bronze burner at 1 atm. (a) stable planar flame, (b) rotating spiral wave, (c) complex target pattern and (d) axisymmetric circular wave/ target pattern.

Case (a): Stable Planar Flames:

Stable planar, weak flames were observed for $\Phi \geq 1$ for a range of burner exit flow speeds albeit with slight fluctuations in the visible light intensity as shown in the sequence of images in Figure 40. For some cases, small azimuthal variations around the vicinity of the burner rim were observed, yet no evidence of traveling or pulsating instabilities was observed.

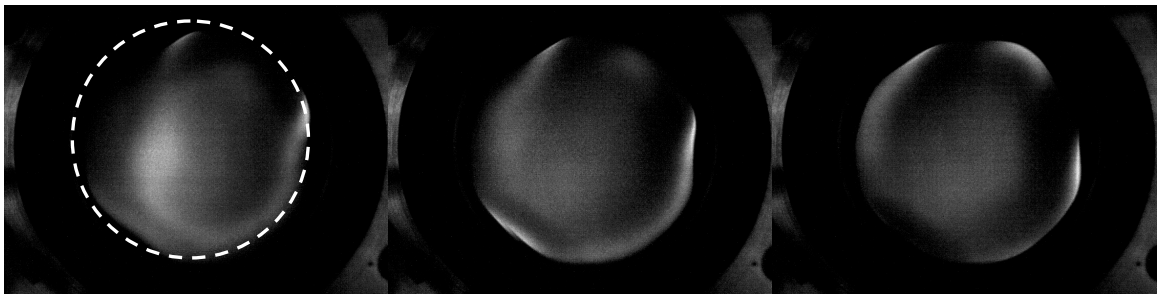

(a) (b) (c)

Figure 40: Stable planar flame in near stoichiometric n-C_4H_{10}-21%O_2–balance He premixture, Φ = 1.05, V_{exit}= 5.11 cm/s, time between consecutive images was 1/250 sec. Dashed line indicates the location of the outer rim of the burner (inner rim of the shroud gas).

Case (b): Rotating Spiral Waves:

A rotating spiral wave case qualitatively similar to that shown in Figure 30 and Figure 31 was observed for near stoichiometric flames as shown in Figure 41. The trajectory of this spiral wave tip was also manually tracked using Spotlight 8.0 and shown in Figure 42. Comparing with the spiral tip trajectory tracked before on the stainless-steel burner, it shows a different meandering path and there was an excursion between two consecutive revolutions for this case.

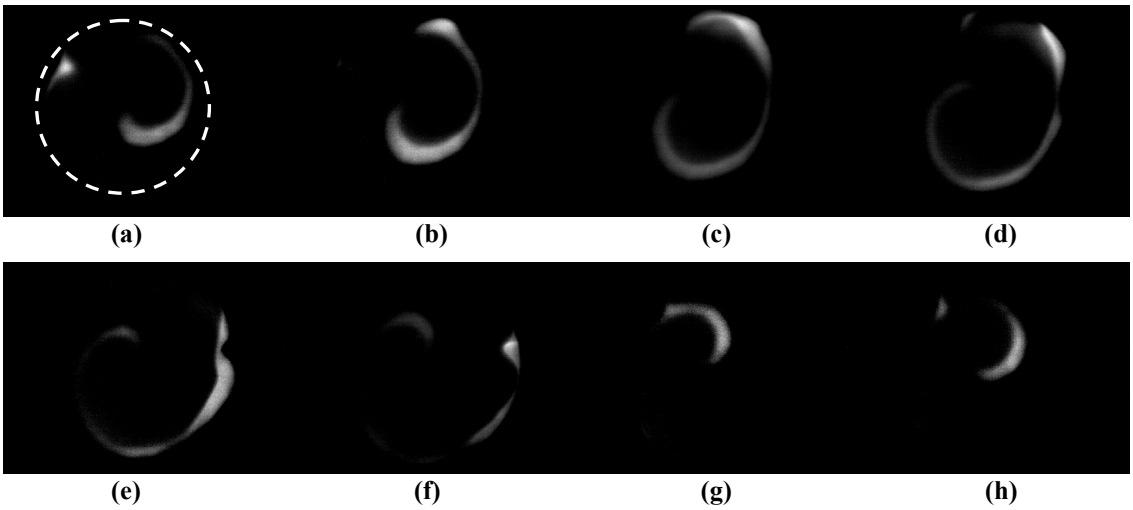

Figure 41: Rotating spiral wave in n-C_4H_{10}-21%O_2-balance He premixtures, Φ = 1.01, V_{exit} = 5.80 cm/s, time between consecutive images was 1/500 sec.

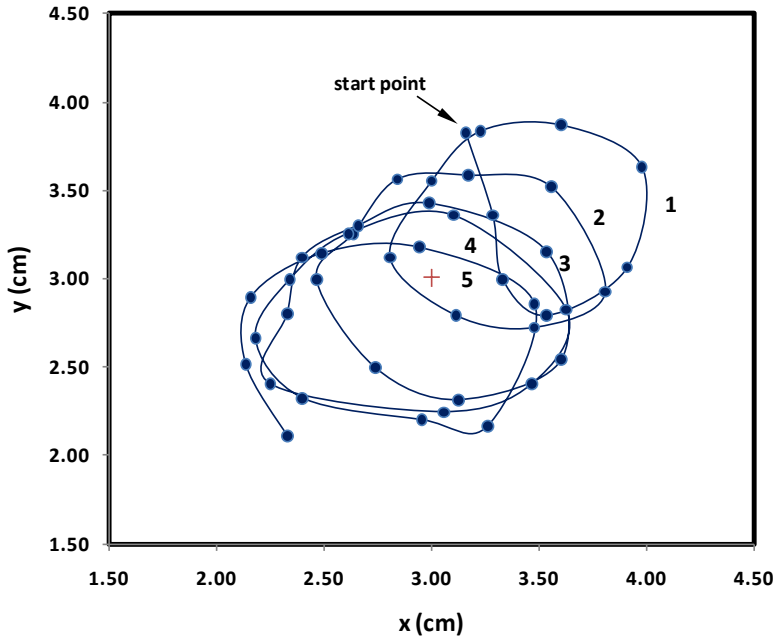

Figure 42: Five successive revolutions of the meandering spiral tip trajectory associated with the spiral wave shown in Figure 41, arrow indicates the tip location for the first frame and the cross indicates the center of the burner.

Case (c): Complex Traveling and Pulsating Target Waves:

As Φ was decreased to 0.90 ~ 1.0, complex travelling and pulsating target waves were observed. A typical complex distorted target patterns with two free ends is shown in Figure 43. As seen in Figure 43 where a radially-propagating wave evolved from a centrally-located reaction zone ('pacemaker' site) that exhibited a weak spatial nonuniformity. The wave then developed into an non-axisymmetric flame subject to an azimuthal disturbance that gave rise to two 'free ends' which subsequently propagated inwardly and interacted with the pulsating reaction zone at the center, generating a complex, distorted flame that lacked azimuthal symmetry.

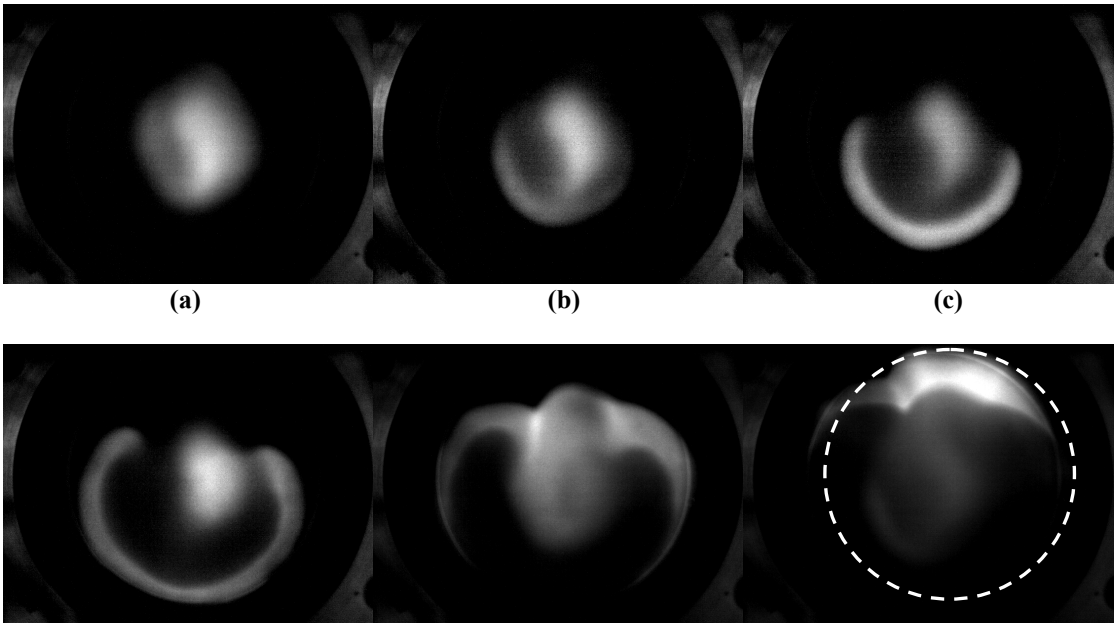

Figure 43: Complex target patterns with two free ends in n-C_4H_{10} -21%O_2–balance He premixtures, Φ = 0.95, V_{exit} = 5.64 cm/s, time between consecutive images was 1/250 sec.

Complex target patterns with multiple, spatially-distributed 'pacemaker' sites were also observed as Φ was decreased to the range of 0.9 ~ 1.0 as shown in the Figure 44. In this case, three spatially separate ignition sites occurred (Figure 44a), each propagated radially outward, interacted and merged (Figure 44b) to form a single radial propagating wave with an azimuthal perturbation that decreased with increasing radius (Figure 44c).

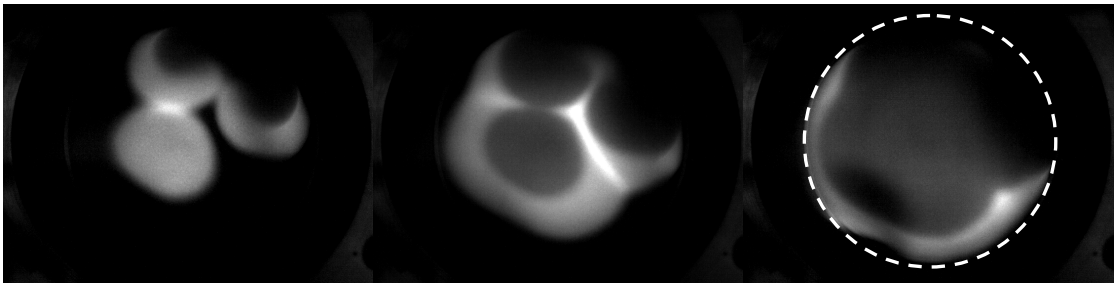

(a) **(b)** **(c)**

Figure 44: Complex radially-propagating flamelets developed from multiple 'pacemaker' sites and formed an azimuthally-distorted radially-propagating wave in n-C_4H_{10}-21%O_2–balance He premixtures, Φ = 0.94, V_{exit} = 5.60 cm/s, time between consecutive images was 1/250 sec.

Case (d): Propagating Radial Waves/ Target Patterns:

Radially propagating circular waves/ target patterns were also observed for leaner premixtures. A representative case is shown in Figure 45, where the intensity of the central region of the radial wave decreased as the peak visible light emission tracked the radius of the circular wave. As the radial extent of the flame approached the outer rim of the burner, the cycle repeated.

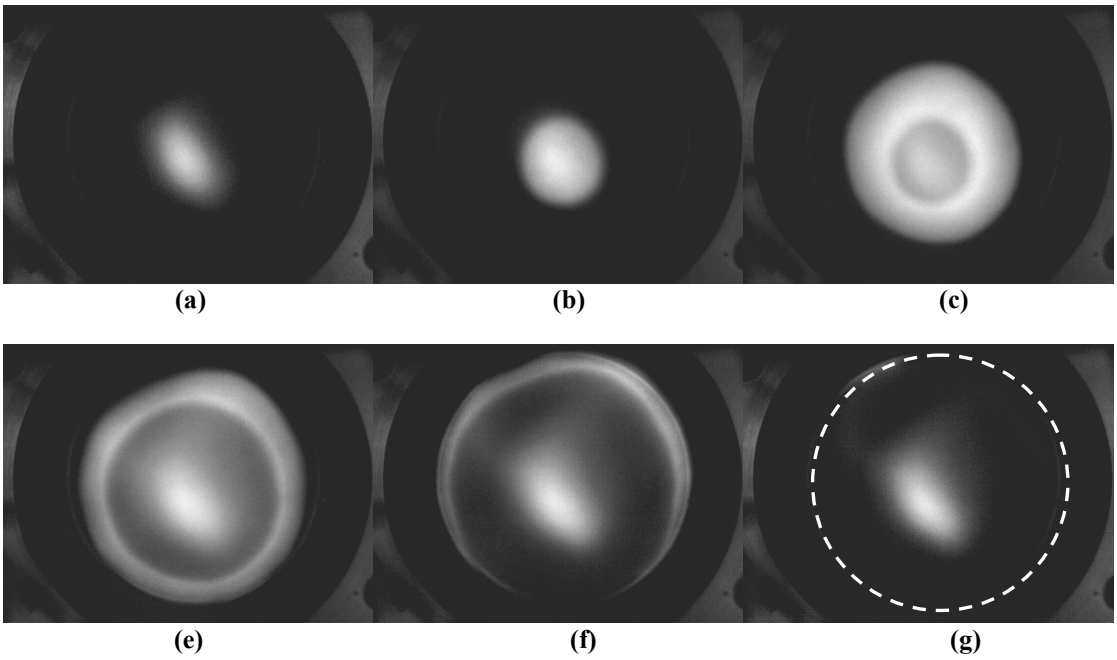

Figure 45: Target pattern with a single, centrally-located pacemaker in n-C_4H_{10} - 21%O_2 -balance He, Φ = 0.90, V_{exit} = 5.95 cm/s, ω = 50 rps, time between consecutive images was 1/250 sec.

For a representative case, the reaction modes as a function of equivalence ratio for a fixed burner exit flow speed (6.0 cm/s) are itemized in Table 6, consistent with the stability diagram in Figure 38.

Table 6: Effect of equivalence ratio on the flame dynamics in lean n-C_4H_{10}-21%O_2-balance He premixtures at V_{exit} = 6.0 ± 0.05 cm/s.

Φ	Pattern	Oscillation Frequency ω ± 5 (Hz)	Computed Radial Flame Speed V_f ± 0.05 (m/s)
1.04-1.07	Stable planar flame	N/A	N/A
0.97 - 1.00	Complex pulsations	N/A	N/A
0.90-0.95	Target patterns	50	2.45
0.89	Lean extinction limit	N/A	N/A

3.2.5 Radial Propagation Flame Speed of the Circular Waves Associated with Axisymmetric Target patterns

The radial flame propagation speed for the axisymmetric target patterns was determined from the video images. By measuring the diameter based on the peak recorded visible intensity, the flame speed was determined using the calibration of 83.5 pixels/cm. Figure 46 illustrates the methodology used to compute the radial flame propagation speed associated with cases that exhibited axisymmetric target patterns.

Specifically, the flame radius was determined using the image processing software Matrox^{TM} Inspector 3.1 where the orthogonal radii R1-R4 were measured and then averaged for each time step. The flame speed was then determined by simply differentiating sequential points knowing the time between frames, e.g., $V_f = \Delta R / \Delta t$. An average flame speed was then determined by averaging the differentiated values for the flame location. For example, the case shown in Figure 45 for n-C_4H_{10}-O_2-He for Φ = 0.90, the average radial flame speed was determined to be $V_f = 2.45 \pm 0.05$m/s, which is roughly an order of magnitude (or more) higher than the laminar flame speed for typical hydrocarbon-air flames. Such high radial propagation speeds were noted by Pearlman in freely-propagating flame studies and Jomaas in the spherically-propagation of high pressure hydrogen-air flames (Jomaas et al., 2007; Pearlman, 1997).

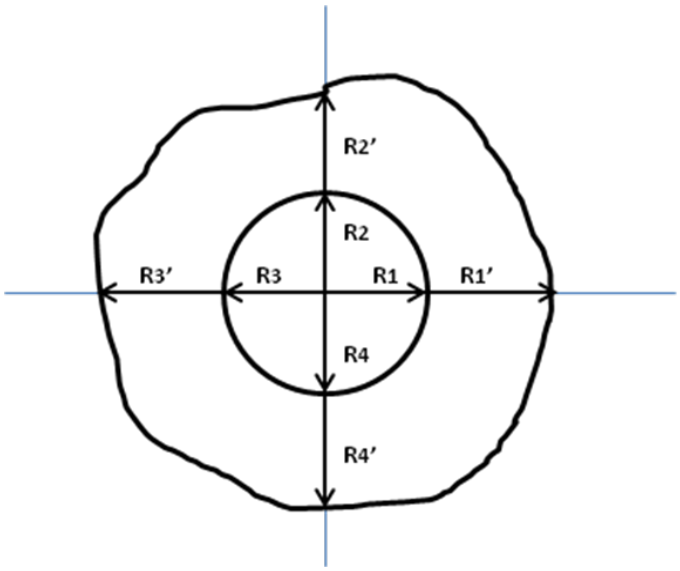

Figure 46: Computation of propagating speed of target pattern.

For a representative case at fixed equivalence ratio ($\Phi = 0.9$), the effect of burner exit flow speed ($\mathbf{V_{exit}}$) on the oscillation frequency (ω) and radial propagation speed (V_f) of the circular waves associated with cases that exhibited axisymmetric 'target' patterns is detailed in Table 7. Interestingly, the frequency and radial flame propagation speed increase with increasing burner exit flow speed, noting that the adiabatic flame temperature is unchanged at this fixed equivalence ratio.

Table 7: Effect of burner exit flow speed on the oscillation frequency and radial flame speed in lean n-C_4H_{10}-21%O_2-balance He at Φ = 0.9.

Burner exit flow speed, V_{exit} (cm/s)	Pattern	Oscillation Frequency ω ± 5 (Hz)	Computed Radial Flame Speed V_f (m/s)
5.08	Extinguish	N/A	N/A
5.95	Target	50	2.45 ± 0.05
7.08	Target	63	2.75 ± 0.1
7.94	Target	71	3.16 ± 0.2
8.95	Complex target	N/A	N/A

3.2.6 Conduction Heat Loss Calculations

To qualitatively estimate the conduction heat loss to the burner, ΔH (Watts), the temperature of the cooling water into and exiting from the burner was measured by Type K thermocouples and recorded using a National Instruments Data Acquisition System. Knowing the volumetric flow rate of the cooling water ($\dot{Q}$) by averaging the time to fill up an 80 ml beaker and fluid properties (ρ, c_p), the amount of heat transferred from the burner to the cooling water can be computed as $\Delta H = \dot{m} \cdot c_P \cdot \Delta T = \dot{Q} \cdot \rho \cdot c_P \cdot \Delta T$.

For the mixture of n-C_4H_{10} -21%O_2-balance He at an equivalence ratio of 0.95, the heat loss as a function of burner exit flow speed was evaluated (shown in Figure 47). The total conduction heat loss from the burner to the cooling water increased as the burner exit flow speed increased which was opposite to what was expected. As a consequence of maintaining the same equivalence ratio, increasing the exit flow speed also increases

the mass flux of the fuel, thus the total chemical energy to the system. Therefore, as the exit flow speed was increased, the total heat loss to the burner increased.

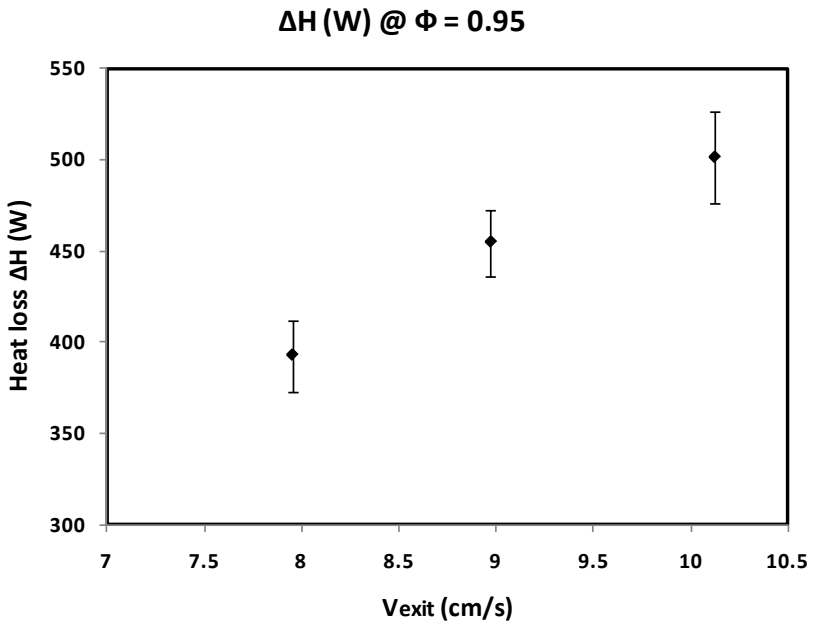

Figure 47: Total heat loss from the McKenna burner to the cooling water for different burner exit flow speeds in lean n-C_4H_{10} -21%O_2 -balance He premixtures at Φ = 0.95.

Conduction heat loss was also estimated for n-C_4H_{10} -21%O_2 -balance He premixtures as a function of equivalence ratio at two fixed burner exit flow speeds, shown in Figure 48 ((a) Vexit = 7.11cm/s; (b) Vexit = 7.95 cm/s). Within the error bars in the TC measurements, there was no significant difference among the heat loss when the equivalence ratio varied in a small range near stoichiometry.

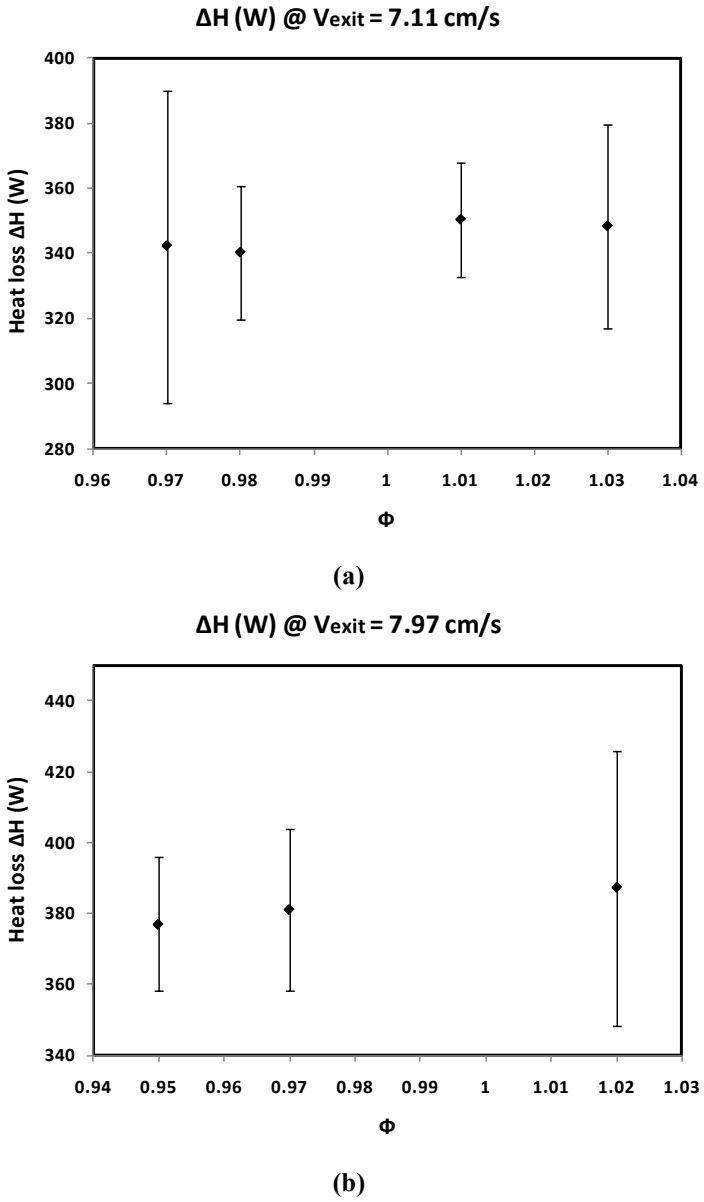

Figure 48: Heat loss from the McKenna burner to the cooling water for different Φ in n-C_4H_{10} - 21%O_2 -balance He premixtures at a fixed exit flow speed: (a) V_{exit} = 7.11 cm/s, (b) V_{exit} = 7.97 cm/s.

Table 8 shows the effects of different burner exit flow speeds on the target patterns for leaner premixtures (Φ = 0.79) when the cooling water was turned off. Without cooling water, the conduction heat loss of the flame to the burner was dramatically

reduced so that the extinction limit was extended and the flame can be stabilized in much leaner premixtures. Similar to the results in Table 7, the oscillation frequency and the radial propagation speed increased with the increasing exit flow speed.

Table 8: Effect of burner exit flow speed on flame dynamics for Φ = 0.79 with cooling water off.

Burner exit flow speed, V_{exit} (cm/s)	Pattern	Oscillation Frequency ω ± 5 (Hz)	Computed Radial Flame Speed V_f ± 0.05 (m/s)
6.76	Target	31.3	4.22
7.67	Target	41.7	4.28
8.25	Target	62.5	4.61
9.43	Complex target	71.4	4.61

3.2.7 Flame Patterns in n-C_4H_{10}-Air Premixtures

Experiments were also conducted over a broad range of mixture compositions for n-C_4H_{10}-air premixtures using a N_2 shroud. For lean premixtures (Le ≈ 2.3), no evidence of spiral waves was observed under any conditions considered. Irregular and distorted pulsating flames were however observed and a representative image sequence is shown in Figure 49 for Φ = 0.77 and V_{exit} = 3.04 cm/s case.

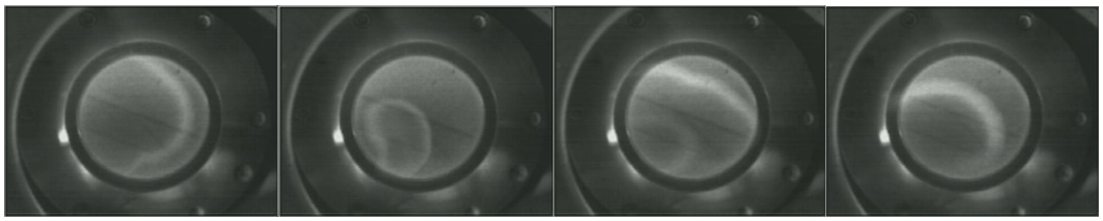

(a) (b) (c) (d)

Figure 49: Distorted pulsating flames in n-C_4H_{10}-21%O_2-balance N_2, Φ = 0.77, V_{exit} = 3.04 cm/s, time between consecutive images was 1/125 sec.

3.3 New Observations of High-Lewis Number Burner-Stabilized Premixed Gas Flame Instabilities in n-C_7H_{16}-O_2-Inert Premixtures

3.3.1 Flame Patterns in n-C_7H_{16}-O_2-Inert Premixtures using Bubbler Setup on a Stainless-Steel McKenna Burner

Experiments were also conducted using higher molecular weight fuels with the intent to increase the Le by selecting fuels with small mass diffusivities. As such, n-heptane and n-octane were considered. To vaporize, meter, and premix these fuels, the bubbler saturator apparatus (described in Chapter 2) was developed. It consisted of a glass bubbler in-line with a metered air flow. The premixture (assumed to be saturated) then flowed in parallel with a secondary air supply that was used to dilute the fuel-air stream and control the mixture composition. As with all bubblers, sensitivity of the vapor pressure of the fuel to the ambient temperature combined with the limited residence time of the air flow through the bubbler may have introduced some error in the mixture composition yet the observed reaction modes show clear evidence of the diffusive-thermal instability. Specifically, four representative cases for n-C_7H_{16}-21%O_2-balance N_2 premixtures were considered and listed in Table 9.

Table 9: Experimental results in n-C_7H_{16}-air premixtures using the bubbler setup on a stainless-steel McKenna burner; note: $P_{v,n\text{-}C7H16}$ @ 298K = 0.059 atm.

Vol. flow rate of air (SLM)	Vol. flow rate of air with n-C_7H_{16} (SLM)	Vol. flow rate of n-C_7H_{16} (SLM, assumed saturated)	Φ	Burner exit flow speed (cm/s)	Pattern
5.0	5.0	0.295	1.54	6.07	Rich planar flame
6.3	4.0	0.236	1.20	6.21	Target pattern
5.4	5.0	0.295	1.49	6.31	Target pattern
4.5	6.0	0.354	1.77	6.40	Target pattern

A representative case in which consecutive propagating wave fronts was observed (and classified in Table 9 as a 'target pattern') is shown in Figure 50. Relative to the lean n-C_4H_{10} diluted with O_2-He case, the separation distance between two consecutive waves was smaller (~ 2 cm).

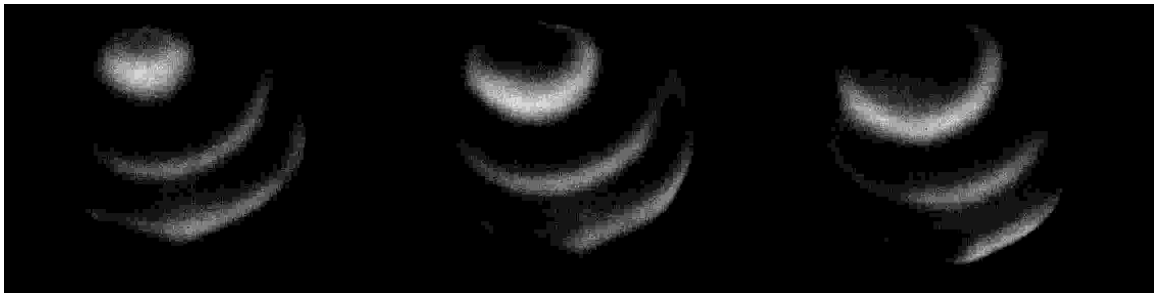

(a) (b) (c)

Figure 50: Target patterns observed in n-C_7H_{16}-air premixture using the bubbler setup on stainless-steel McKenna burner, Φ = 1.49, V_{exit} = 6.31 cm/s, time between consecutive images is 1/250 sec.

Representative experiments were also conducted using n-C_7H_{16}-21%O_2-balance He premixtures and the cases considered are listed in Table 10 along with the pattern

observed. Figure 51 also illustrates the spiral wave observed in these He-diluted n-heptane premixtures.

Table 10: Experimental results in n-Heptane-21%O_2-balance He premixtures using the bubbler setup on a stainless-steel McKenna burner; note: $P_{v,n\text{-}C7H16}$ @ 298K = 0.059 atm.

Vol. flow rate of O_2+He #1 (SLM)	Vol. flow rate of O_2+He + n-C7H16 #2 (SLM)	n-C_7H_{16} (SLM, assumed saturated)	Φ	Burner exit flow speed (cm/s)	Pattern
3.9	4.0	0.24	1.59	4.80	Spiral wave
6.3	7.0	0.42	1.65	8.09	Target pattern
7.0	8.0	0.48	1.68	9.13	Target pattern
8.7	7.5	0.45	1.45	9.82	Target pattern

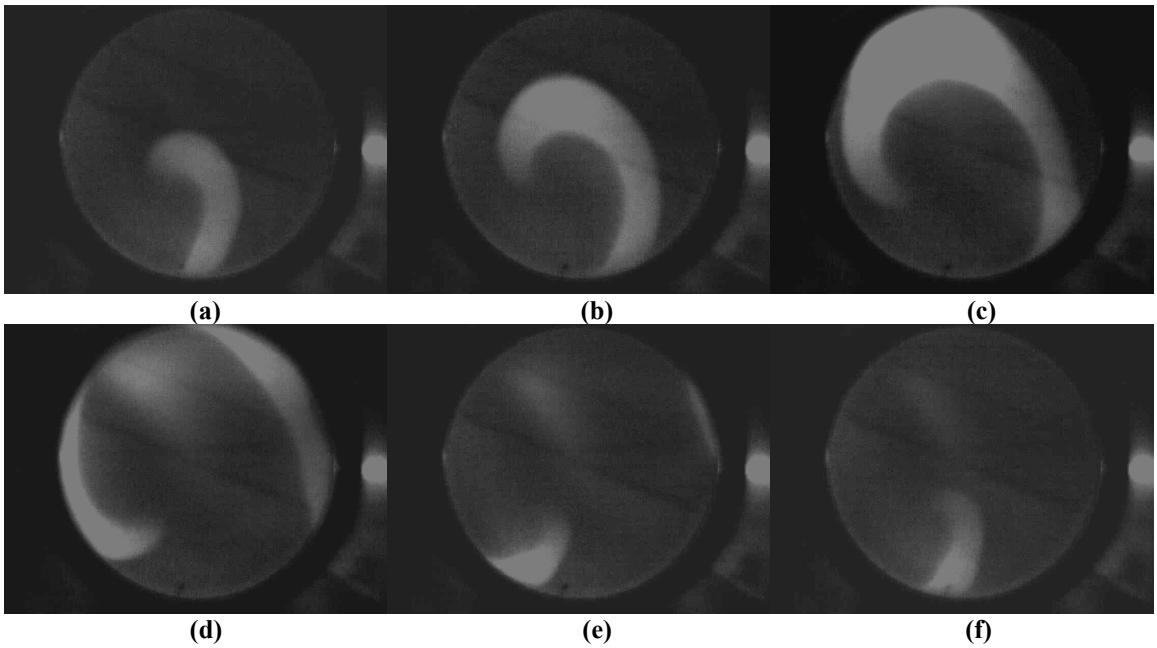

Figure 51: Spiral wave observed in n-C_7H_{16}-21%O_2-balance He premixture using the bubbler setup on stainless-steel McKenna burner, Φ = 1.59, V_{exit} = 4.80 cm/s, ω = 41 rps, time between consecutive images is 1/250 sec.

3.3.2 Flame Patterns in n-C_7H_{16}-21%O_2-balance He Premixtures using Nebulizer & Spray Chamber Setup on a Stainless-steel McKenna Burner

Because of the variable concentration of n-heptane vapor using the bubbler set-up, a new nebulizer-spray chamber experimental facility was designed and built (details were described in chapter 2). The flow rate of the liquid fuel (n-heptane or n-octane) was controlled by the Cole-Parmer syringe pump into the nebulizer through a 1/16'' tube. By adjusting the relative flow rates of the carrier gas, the nebulizer broke the liquid fuel into small droplets (diameter around 15 um in average) in the spray chamber. Please see Figure 24 for the schematic structure of the nebulizer. The stream of oxidizer was heated (175 ºC for n-C_7H_{16}, 190 ºC for n-C_8H_{18}) and injected into the spray chamber to vaporize the liquid fuel droplets instantly and the premixtures were formed and delivered into the McKenna burner. The spray chamber and the whole delivery line were heated (up to 175 ºC for n-C_7H_{16} and 190 ºC for n-C_8H_{18}) and insulated to keep the fuel vapor from condensing. The cooling water around the McKenna burner was also heated to 60 ºC to preheat the burner surface. The flow rates of the liquid fuel in vapor phase were calculated based on the densities of the liquid phases and their vapor phases at the room temperature (298K) and atmospheric pressure. The equation for calculating the flow rate of vapor phase is $Q_v = (Q_l \cdot \rho_l)/\rho_v$. Table 11 listed the densities of both n-heptane and n-octane at the temperature 298K and 1 atm (data from DIPPR database). Thus the flow rate of the fuel in vapor phase can be calculated when the flow rate of the liquid fuel controlled by the syringe pump is known.

Table 11: Densities of n-C_7H_{16} and n-C_8H_{18} in liquid and vapor phase at 298K.

@ 298K	density in liquid phase (kg/m^3)	Density in vapor phase (kg/m^3)
n- C_7H_{16}	681.7	4.09
n- C_8H_{18}	700.0	4.66

The results developed both spiral wave and target patterns in n-C_7H_{16}-21%O_2-balance He premixtures on the stainless-steel burner. Similarly, both spiral waves and target patterns were observed while using nebulizer-spray chamber set-up. The representative cases with exit flow speeds and equivalence ratios are listed in Table 12 and the preliminary stability diagram for n-C_7H_{16}-21%O_2-balance He premixtures using nebulizer-spray chamber experimental set-up on the stainless-steel porous-plug burner is shown in Figure 52.

Table 12: Experimental results in n- C_7H_{16}-21%O_2-balance He premixtures using the nebulizer & spray chamber set-up on a stainless-steel McKenna burner.

Φ	**Burner exit flow speed (cm/s)**	**Pattern**
1.00~1.05	5.11~7.05	Stable planar flame
0.96	6.00	Spiral wave
0.95	6.06	Target patter
0.94	7.24	Spiral wave
0.92	7.37	Spiral wave
0.91	6.90	Target pattern

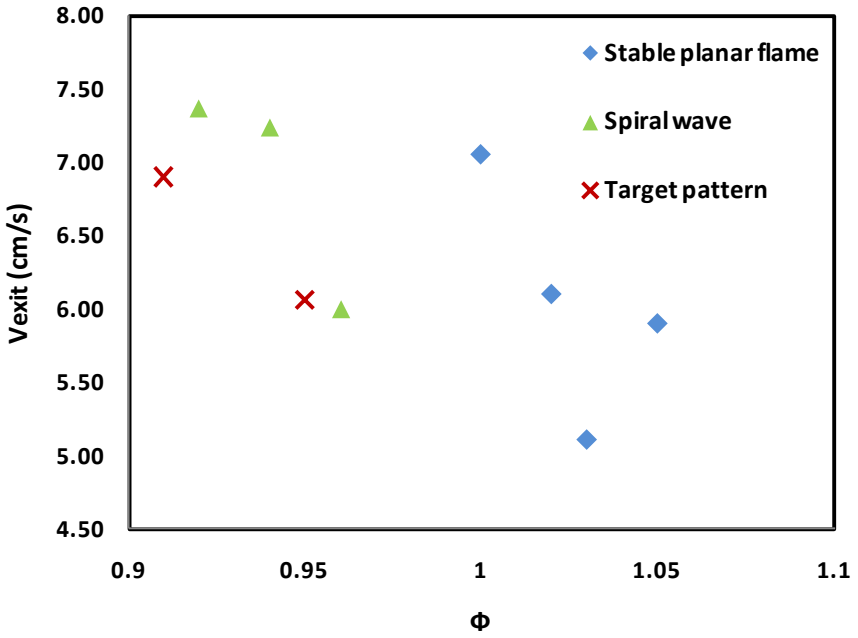

Figure 52: Stability diagram for n-C_7H_{16}-21%O_2-balance He premixtures using the nebulizer & spray chamber set-up on the stainless-steel McKenna burner.

Representative spiral waves and target patterns for n-C_7H_{16}-21%O_2-balance He premixtures are shown in Figure 53 and Figure 54 for two nearly equal burner exit flow speeds. The results were similar to the observations of n-C_4H_{10}-21%O_2-balance He premixtures, where the spiral waves were observed for slightly higher equivalence ratio and then developed into target patterns as the equivalence ratio decreased further to close to extinction limit. The spiral wave observed in Figure 53 was also reminiscent of those observed in Figure 51 except that the equivalence ratio for Figure 51 calculated based on the assumption of fully saturated of n-heptane using bubbler set-up was over 1.5.

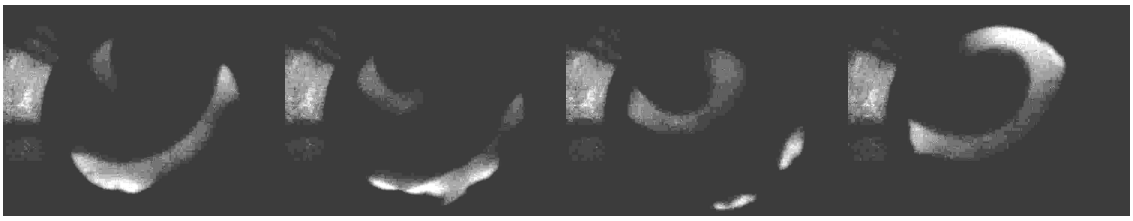

(a) (b) (c) (d)

Figure 53: Rotating spiral wave in lean n-C_7H_{16} diluted with 21%O_2-balance He, Φ = 0.96, V_{exit} = 6.0 cm/s, time between consecutive images is 1/250 sec.

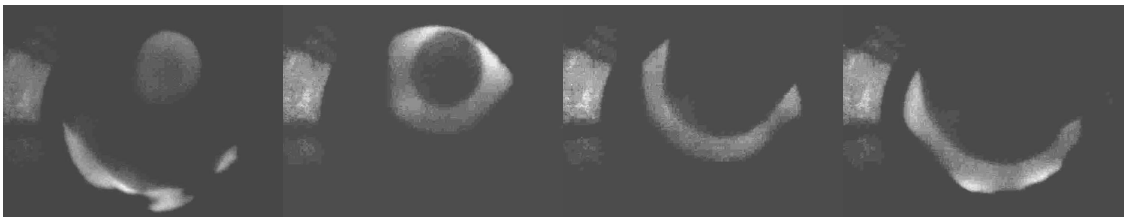

(a) (b) (c) (d)

Figure 54: Target pattern in lean n-C_7H_{16} diluted with 21%O_2-balance He, Φ = 0.91, V_{exit} = 6.9 cm/s, time between consecutive images is 1/250 sec.

3.3.3 Flame Patterns in n-C_7H_{16}-Air Premixtures using Nebulizer & Spray Chamber Setup on a Bronze McKenna Burner

Additional tests for n-C_7H_{16}-O_2-inert premixtures were conducted using the bronze McKenna burner. The results of n-C_7H_{16}-air premixtures using nebulizer & spray chamber setup on the bronze burner will be discussed in this section. To conduct the n-C_7H_{16}-air premixtures tests, the burner exit flow speed was fixed at a given value. The composition of premixtures was varying by adjusting the flow rates of both n-heptane and air from rich to lean mixtures while maintaining the fixed exit flow speed. The given exit flow speed was increased gradually to start another series of tests. Different flame

patterns were observed and recorded for different equivalence ratios at a given exit flow speed, which include:

(1) stable planar flame

(2) instabilities occur

(3) complex instability flames

(4) regular target patterns

(5) flame blow-off

All the patterns were mapped out as a function of burner exit flow speed and equivalence ratio and shown in Figure 55. The border separating stable and unstable flame pattern occurred at an equivalence ratio around 1. For the lower exit flow speed (< 6 cm/s), the critical Φ for the instability is slightly larger than 1 while for the higher exit flow speed (> 8 cm/s), the critical Φ for instabilities is slighter smaller than 1. For all exit flow speeds, after the instabilities occur at a given flow speed, the patterns evolved from complex instabilities to regular target patterns and then the flame was blown off as the equivalence ratio decreased. At the lower flow speeds, the windows for the transition from complex instabilities to regular target is narrower than that of the higher flow rate. When Φ of the premixtures was decreased further to around 0.7, the planar flames were too weak and reached the blow-off limit.

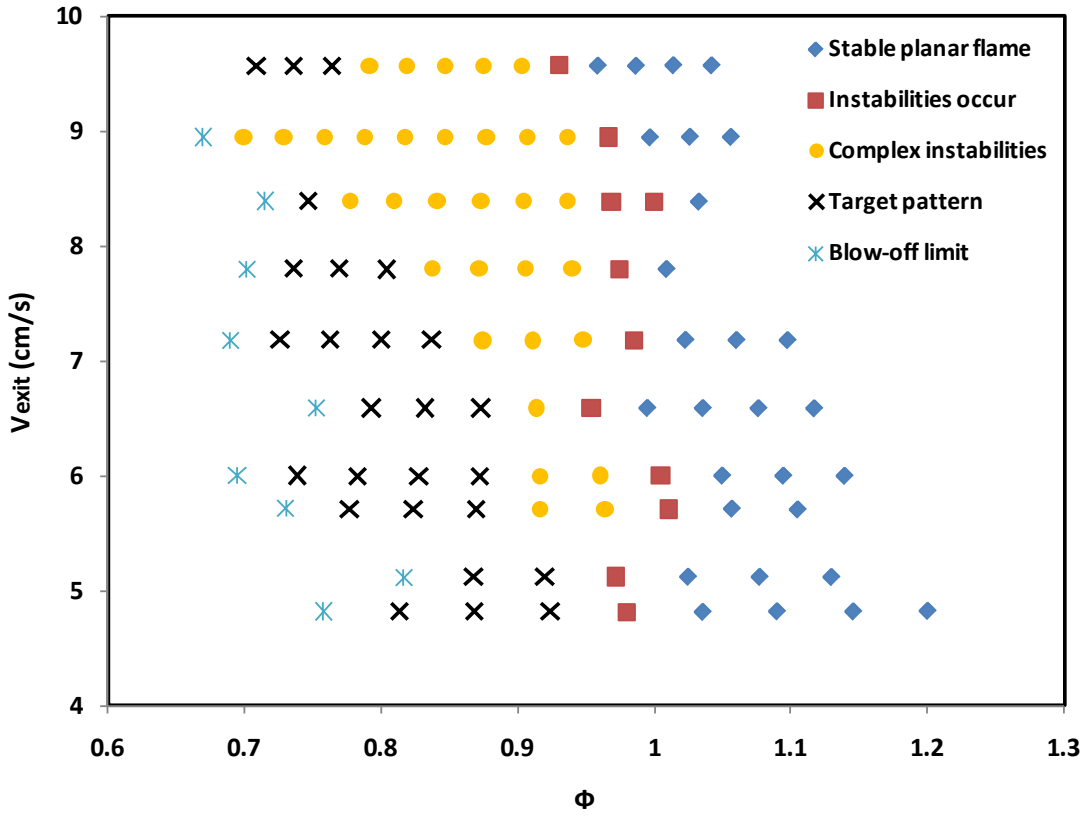

Figure 55: Stability diagram in n-C_7H_{16} - air mixtures using nebulizer & spray chamber set-up on the bronze McKenna burner.

Three representative cases are discussed below for exit flow speed of 5.71 cm/s. Figure 56 shows the stable planar flame while the premixture was rich (Φ = 1.10). The flame appeared stable and there were almost no variations for all frames. When Φ decreased to 0.96, shown in Figure 57, the flame started to show complex instabilities and pulsating flames were observed while propagating outwardly. In Figure 57, the interaction between the flame and burner rim was seen and the flame was broken into several arcs at the edge of the burner. As Φ decreased further, the flame evolved to regularly target patterns. Figure 58 shows the target pattern at Φ = 0.82. The target

patterns were similar to the previous observations of n-C_4H_{10}-O_2-He mixtures on bronze McKenna burner. The pacemaker was located nearly at the center of the burner and the target wave originated from the pacemaker and propagated outwardly until it reached the rim of the burner, while another circular target ring started from the pacemaker and repeated the revolutions.

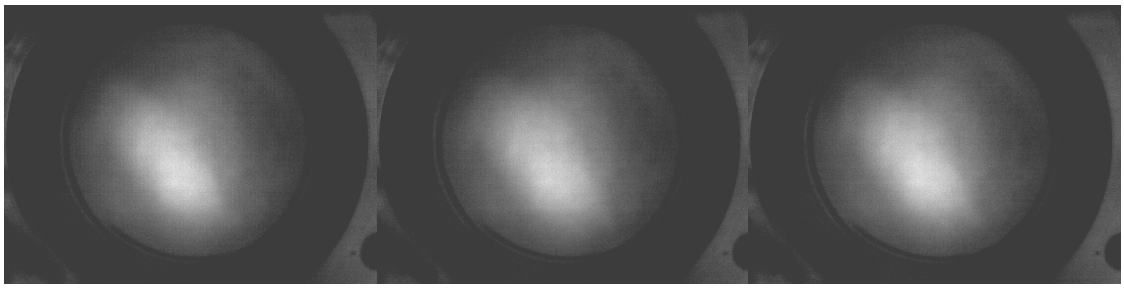

(a) **(b)** **(c)**

Figure 56: Stable planar flame in n-C_7H_{16} - air premixtures, Φ = 1.10, V_{exit} = 5.71 cm/s, time between consecutive images is 1/250 sec.

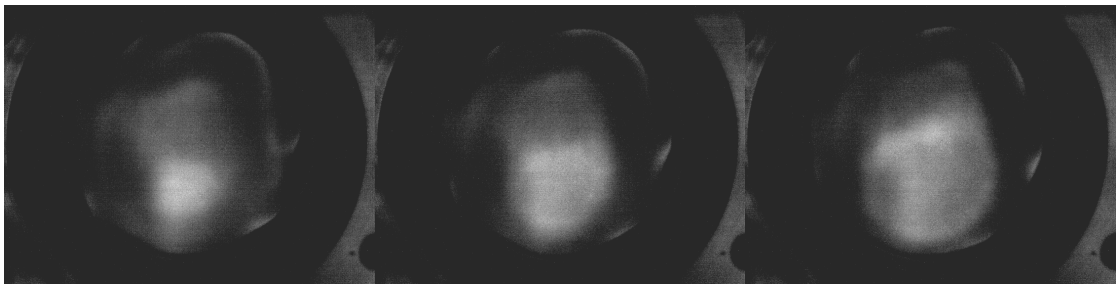

(a) **(b)** **(c)**

Figure 57: Complex instable flames in lean n-C_7H_{16} - air mixtures, Φ = 0.96, V_{exit} = 5.71 cm/s, time between consecutive images is 1/250 sec.

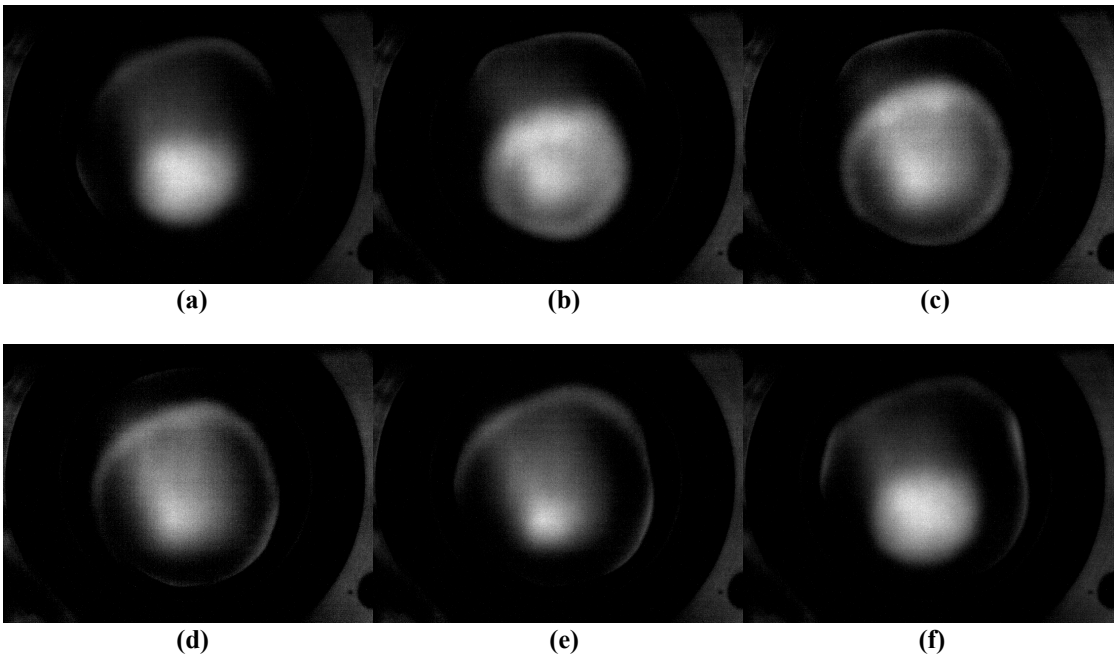

Figure 58: Target pattern in n-C_7H_{16} - air premixtures, Φ = 0.82, V_{exit} = 5.71 cm/s, time between consecutive images is 1/250 sec.

3.3.4 Flame Patterns in n-C_7H_{16}-21%O_2-balance He Premixtures using Nebulizer & Spray Chamber Setup on a Bronze McKenna Burner

Similar to the experiments of n-C_7H_{16}-air, to conduct the n-C_7H_{16}-21%O_2-balance He premixtures tests, the flow rate of liquid n-C_7H_{16} was controlled by the syringe pump. Oxygen and Helium gas flow rates were seperately controlled by the MKS mass flow controllers. Because the mass flow controller was calculated based on N_2, and the value for Helium has a 5% error based on the product manual. Thus, the flow rate for helium is ± 5% off the actual flow rate. The flow rate of liquid n-C_7H_{16} varied from 1.1 SCCM to 1.8 SCCM. For each flow rate of n-C_7H_{16}, the flow rates of oxygen and helium were controlled starting from low to high, which means the premixture composition varied from rich to lean. Figure 59 presents the stability diagram for n-C_7H_{16}-21%O_2-balance

He. When the exit flow speed was very low (< 5.0 cm/s), the premixture was hard to ignite. As the exit velocity increased ($5.5 < V_{exit} < 6.5$ cm/s), the complex target pattern was observed, but no regular and clean target patterns observed at these low flow speeds. As the burner exit flow speed increased to around 7.0 cm/s, the flame envolved from stable planar flame for equivalence ratio ≥ 1.15, then to complex instabilities over the equivalence ratio range $1.10 < \Phi < 1.15$, and finally showing clean target patterns while Φ decreased to 1.06. The flame extinguished at slightly leaner compositions. The same trend also existed for exit flow speed around 8.0 cm/s. The border to seperate stable planar flame and instabilities was around $\Phi = 1.10$ at $V_{exit} = 8.03$ cm/s. A wide range of Φ were observed for clean target patterns, from 1.09 to 0.97 for the higher flow speed because of reduced conductive heat loss to the burner. A few complicated target pattern cases were also found in the same range of Φ which means the patterns are bi-stable and can be transitioned to one another.

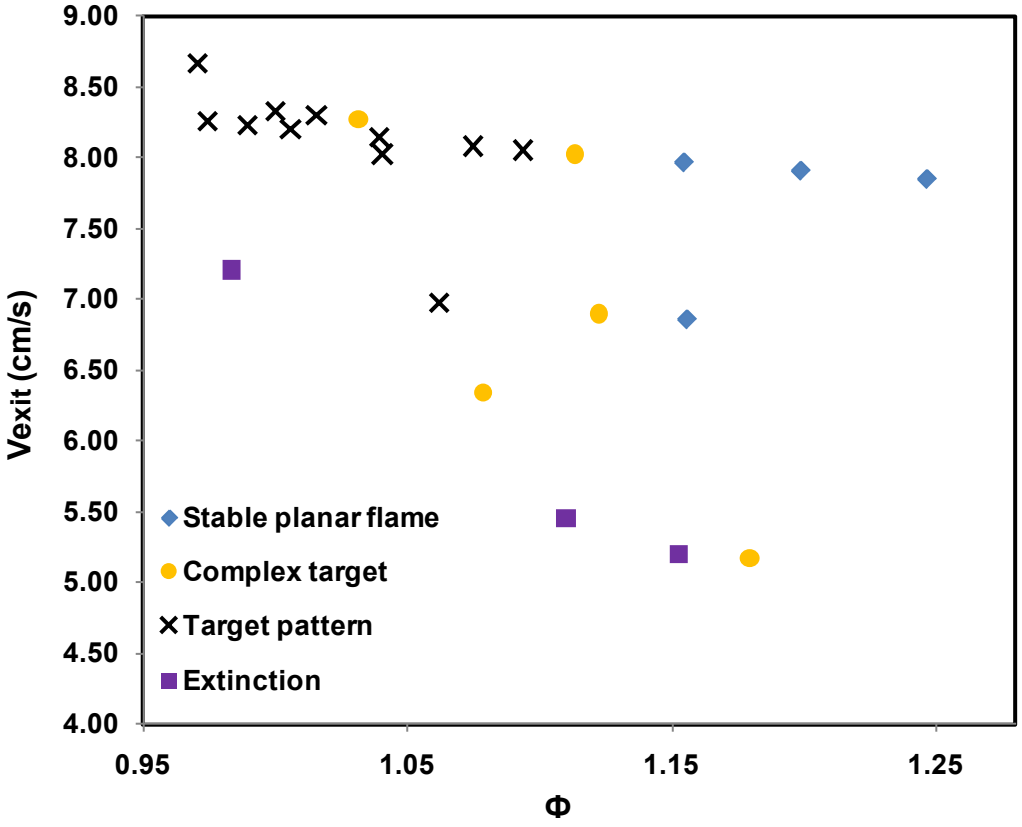

Figure 59: Stability diagram in n-C_7H_{16}–21%O_2-balance He premixtures using nebulizer & spray chamber set-up on the bronze McKenna burner.

Two representative cases of complex target patterns are shown in Figure 60 and Figure 61. In Figure 60, the incomplete circular target wave with two free ends was observed and one free end started to develop into a rotating spiral wave, but interacted with the second target wave originated from the center pacemaker. There was no complete spiral wave observed in this case.

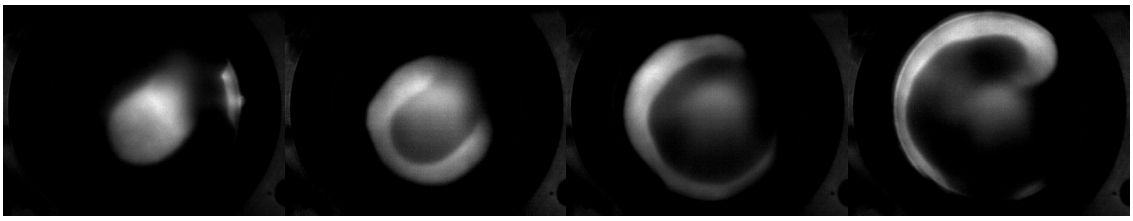

(a) (b) (c) (d)

Figure 60: Complex target pattern with free ends in n-C_7H_{16}-21%O_2-balance He premixture, Φ = 1.08, V_{exit} = 6.34 cm/s, time between frames is 1/250 sec.

In Figure 61, multiple but incomplete target rings were observed for Φ = 1.12, V_{exit} = 6.90 cm/s. The distance between the two adjacent target waves was around 2 cm.

(a) (b) (c) (d)

Figure 61: Complex target pattern with multiple rings in n-C_7H_{16}-21%O_2-balance He premixture, Φ = 1.12, V_{exit} = 6.90 cm/s, time between frames is 1/500 sec.

A typical target pattern in n-C_7H_{16}-21%O_2-balance He premixture is shown in Figure 62. The dynamics of these target patterns were almost identical to those observed in n-C_4H_{10}-21%O_2-balance He on the bronze burner. It took 7.5 frames to finish one revolution, so the frequency ω = 500/7.5 = 67 rps, which was slihgtly higher than that in n-C_4H_{10}-21%O_2-balance He premixtures (ω = 62.5 rps) for V_{exit} = 7.08 cm/s. Comparing with n-C_7H_{16}-air results shown in Figure 58, the target patterns for helium diluted mixtures were more pronounced than the patterns observed with air diluted mixtures.

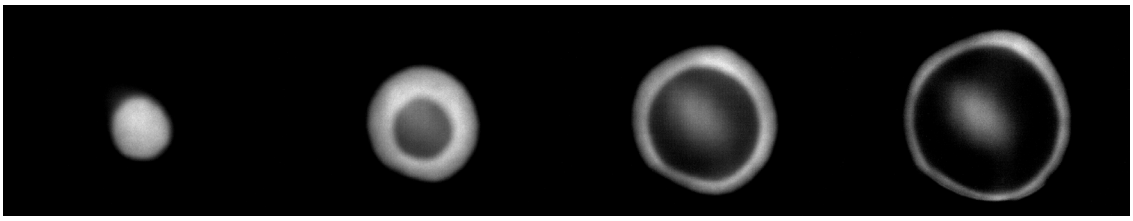

Figure 62: Target pattern in n-C_7H_{16} -21%O_2 -balance He premixture, Φ = 1.04, V_{exit} = 8.03 cm/s, time between consecutive frames is 1/500 sec.

3.4 New Observations of High-Lewis Number Burner-Stabilized Premixed Gas Flame Instabilities in n-C_8H_{18}-O_2-Inert Premixtures

3.4.1 Flame Patterns in n-C_8H_{18}-Air Premixtures using Nebulizer & Spray Chamber Setup on a Bronze McKenna Burner

Experiments with n-C_8H_{18} were conducted in the same way as the n-C_7H_{16} experiments. The total burner exit flow speed was fixed at a given value and the composition of n-C_8H_{18} and air was varying based on the fixed exit flow speed from rich to lean. There were also five flame patterns observed as a function of fuel concentration for n- C_8H_{18}-air premixtures.

1) Stable
2) Instabilities occur
3) Complex instabilities
4) Target patterns
5) Flame blow-off

The results were mapped out as a stability diagram shown in Figure 63. The border where the instabilities occurred for n-C_8H_{18}-air mixtures was approximately Φ = 1. For the lower exit velocity (V_{exit} < 7 cm/s), the equivalence ratios where the instabilities

occur were slightly higher than 1. When the exit velocity increased above 7 cm/s, the equivalence ratio to separate the stable and instable flame was slightly lower than 1. The complex instabilities were only observed over the large exit velocity range (7 cm/s < V_{exit} < 9 cm/s). Clean target patterns were observed for all the exit velocity range from 4.5 cm/s up to 9 cm/s. The blow-off limits for n-C_8H_{18}-air mixtures were also shown in the Figure 63, and it went to leaner mixture for higher exit velocity as expected.

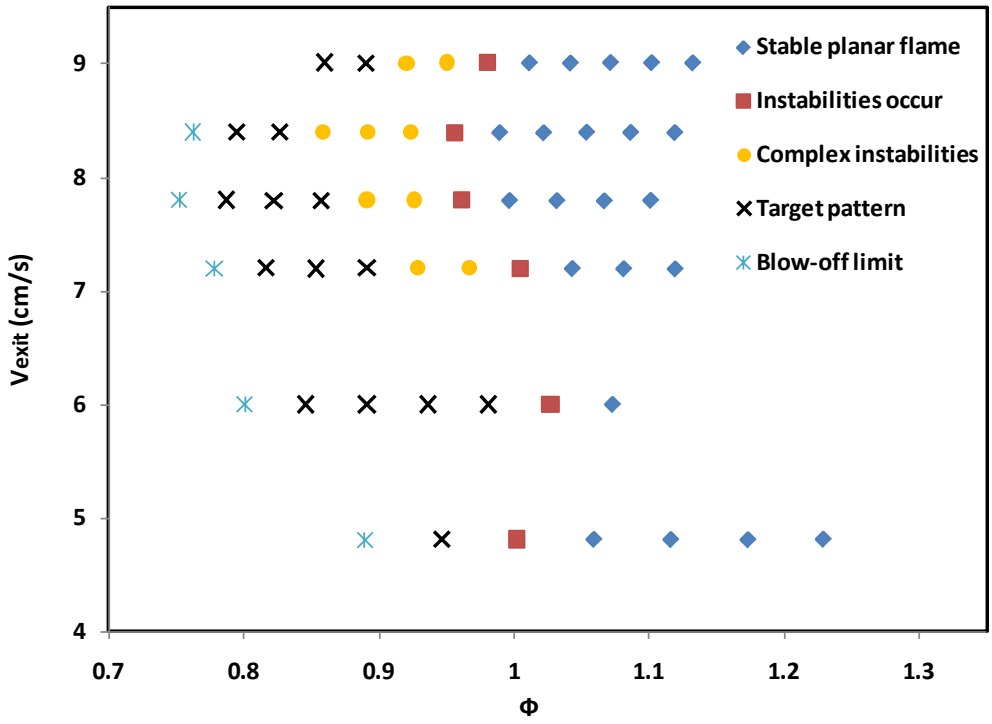

Figure 63: Stability diagram in n-C_8H_{18}-air premixtures using nebulizer & spray chamber set-up on the bronze McKenna burner.

The stable planar flame of n-C_8H_{18}-air premixtures showed almost identical dynamics as the stable flame in n-C_7H_{16}-air premixture shown in Figure 56. The complex

instability pattern when the instabilities just occurred is shown in Figure 64. Because the target patterns for n- C_8H_{18}-air premixture were similar to the target patterns observed for n-C_7H_{16}-air, they are not shown here. For both n-C_7H_{16}-air and n-C_8H_{18}-air, the pulsating target pattern did exsist but not as pronounced as helium diluted premixtures.

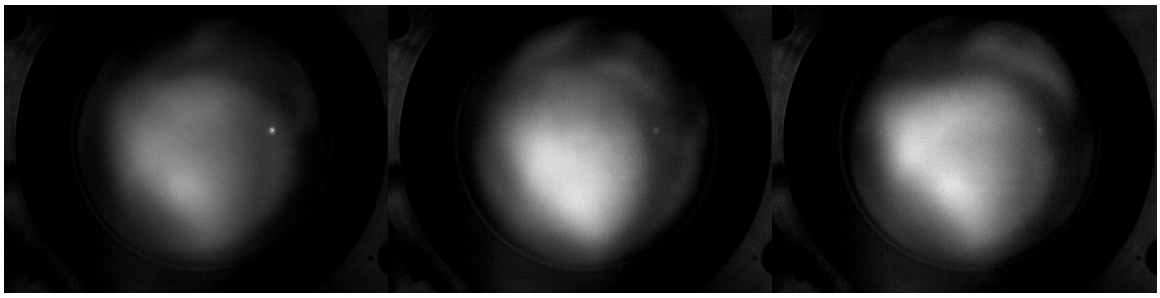

(a) **(b)** **(c)**

Figure 64: Instability occurs with complex instabilities in n-C_8H_{18}-air premixtures, $\Phi = 0.89$, V_{exit} = 9.01 cm/s, time between consecutive frames is 1/250 sec.

3.4.2 Flame Patterns in n-C_8H_{18}-21%O_2-balance He Premixtures using Nebulizer & Spray Chamber Setup on a Bronze McKenna Burner

The experiments were run for n-C_8H_{18}-21%O_2-balance He premixtures as described before. The flow rate of liquid n-C_8H_{18} varied from 1.3 SCCM to 1.8 SCCM. Four regimes were found as a function of fuel concentration for n-Octane-O_2-He premixtures for three exit flow speed windows (6.0~6.5cm/s, 7.0~7.5 cm/s, 8.0~8.5cm/s).

1) Stable
2) Bi-states of spiral wave and target pattern
3) Target pattern
4) Extinction

All results were mapped in the stability diagram shown in Figure 65. When the exit velocity was in the range of 6.0 cm/s to 6.5 cm/s, the window of the equivalence ratio for the four stability regimes was narrow, varying from 1.08 ~ 1.16. While the exit velocity was in the range of 7.0 cm/s to 7.5 cm/s, the window of the equivalence ratio for the flame transitioned from stable to extinction is 1.05 to 1.25. For the exit velocity in the range of 8.0 cm/s to 8.5 cm/s, the window of equivalence ratio for the four regimes is 1.00 to 1.24.

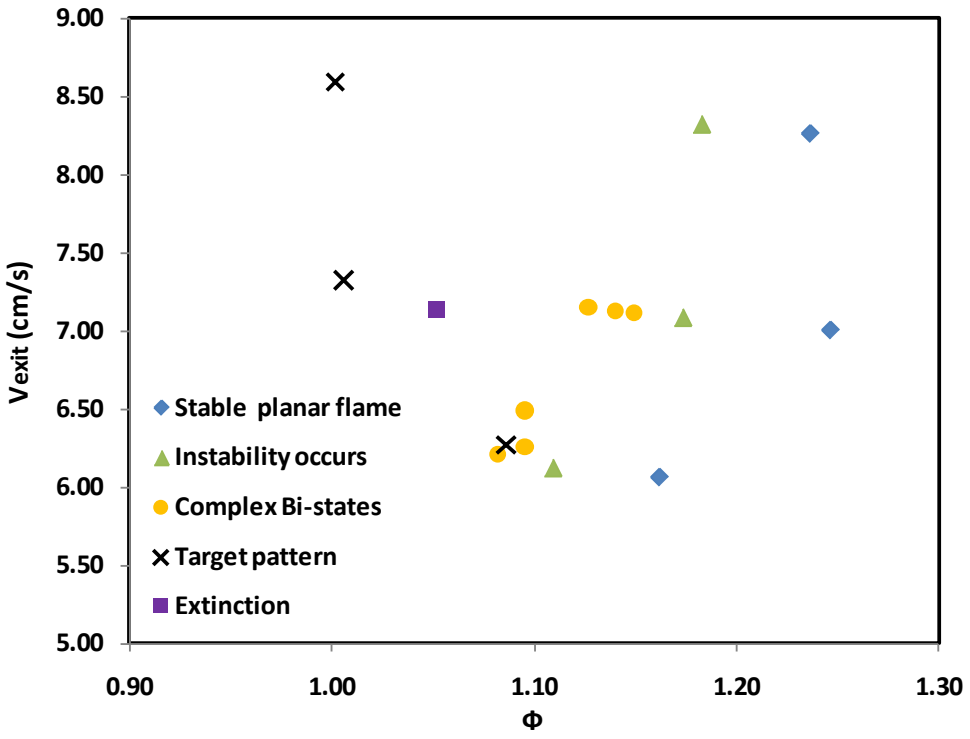

Figure 65: Stability diagram in n-C_8H_{18}-21%O_2-balance He premixtures using nebulizer & spray chamber set-up on the bronze McKenna burner.

Two representative cases are shown in Figure 66 and Figure 67. In Figure 66, complex Bi-states of the flame instabilities was recorded at 250 fps. As shown, in frame (a) two pacemakers for target patterns existed at the near center of the burner. Then two target rings were developed and interacted with each other to form one single irregular target wave with two free ends (seen in frame (c)). The two free ends of the single target wave started to evolve into a spiral wave and rotated clockwise (frame (d)~(i)). After one revolution of the spiral wave, the pacemaker of the target pattern initiated again from the center of the burner and the circular wave was propagating outwardly till it reached the rim of the burner as seen in frame (j) ~ (l).

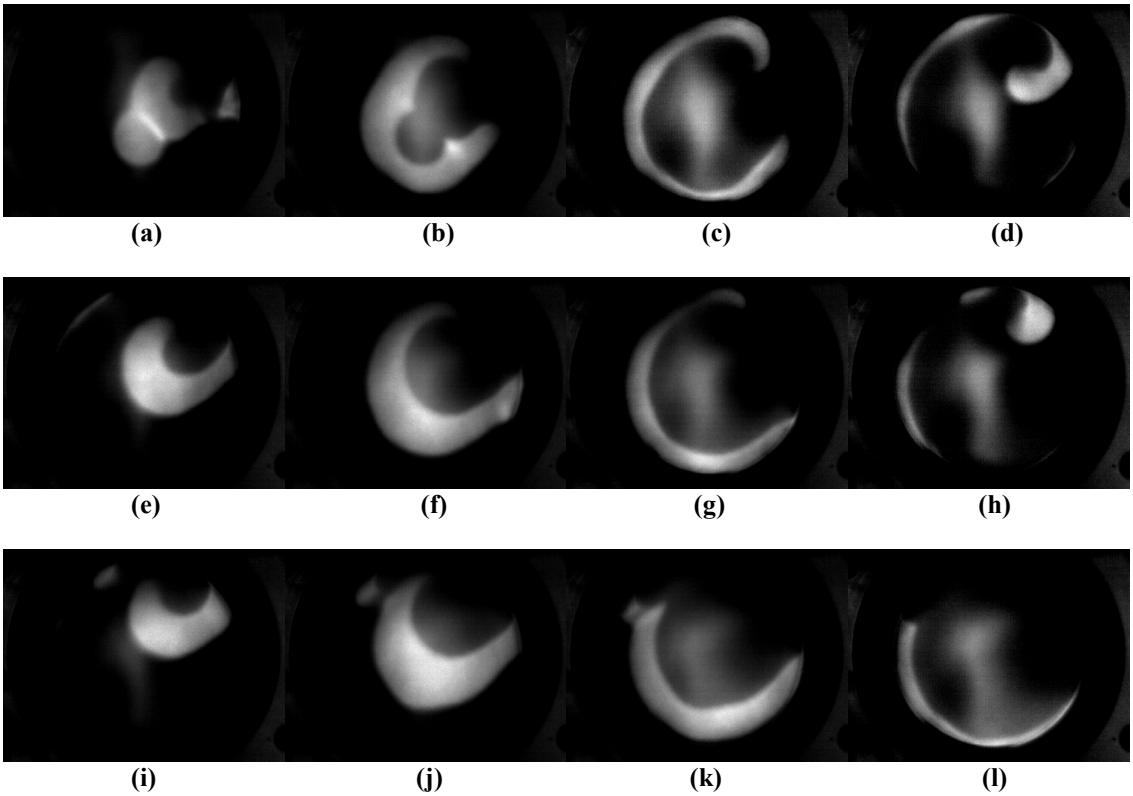

Figure 66: Complex bi-stable states of instabilities of target pattern and spiral wave for n-C_8H_{18}-O_2-He, Φ = 1.14, V_{exit} = 7.13 cm/s, time between frames is 1/250 sec.

While the exit velocity was kept in the same range as the previous case, 7.33 cm/s specifically, the equivalence ratio of the premixture for flames only ranged from 1.14 to 1.01, the clean target patterns were observed near the lean flammability limit, shown in Figure 67. The patterns showed the same dynamic characteristic as the previous target patterns observed with n-C_4H_{10}-21%O_2-balance He and n-C_7H_{16}-21%O_2-balance He premixtures. The frequency for the target patterns for n-C_8H_{18}-O_2-He is $\omega = 500/7 = 71$ Hz, which is slightly higher than n-C_4H_{10} (63Hz) and n-C_7H_{16} (67 Hz) diluted by 21%O_2 balanced with helium.

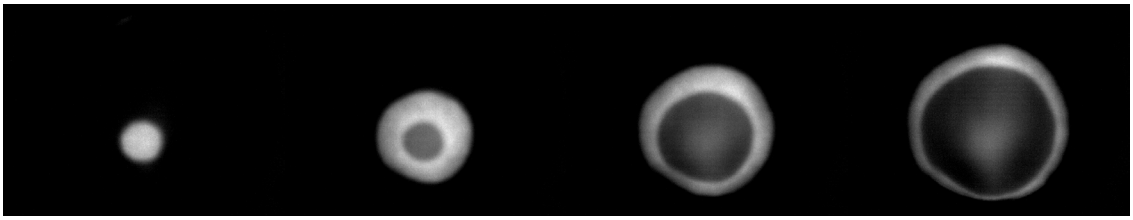

Figure 67: Target patterns in n-C_8H_{18}-O_2-He premixtures, $\Phi = 1.01$, $V_{exit} = 7.33$ cm/s, $\omega = 71$ Hz, time between consecutive frames is 1/500 sec.

So far, all three alkane fuels mixed with air and O_2 diluted by helium were tested using both stainless-steel burner and bronze burner. The comparison among the target patterns observed for these three fuels mixed with 21%O_2 diluted by helium was conducted based on the oscillation frequency and the radially propagation speed of the target pattern flames and the results were shown in Table 13. As the Lewis number increases with increasing molecular weight of different fuels, the oscillation frequency also increased and the computed radial flame propagation speed increases as well.

Table 13: Comparison of target patterns in n-C_4H_{10}, n-C_7H_{16} and n-C_8H_{18} premixed with 21%O_2 diluted by helium flames.

Premixtures	Φ	Burner exit flow speed (cm/s)	Le	Oscillation Frequency ω ± 5 (Hz)	Computed Radial Flame Speed V_f (m/s)
n-C_4H_{10}-21%O_2-balance He	0.90	7.08	**3.25**	63	2.75 ± 0.1
n-C_7H_{16}-21%O_2-balance He	1.06	6.98	**5.03**	67	2.94 ± 0.2
n-C_8H_{18}-21%O_2-balance He	1.01	7.33	**5.40**	71	3.75 ± 0.2

3.5 Effect of Pressure on the High-Lewis Number Instability Patterns in n-C_4H_{10}-21%O_2-balance He flames on a Bronze McKenna Burner

The effects of ambient pressure on the flame dynamics of the instabilities were also studied. As discussed previously in chapter 2, the low-pressure environment can suppress buoyancy so that the dynamics of the instability patterns were expected to be more regular and stable over a wider range of experimental parameters. While a change in pressure does not change the Le, it changes the thermal diffusivity of the mixture, $\alpha \propto 1/P$, which then is expected to change the characteristic length of the instability, L, since $L \propto \alpha/S_f$ (here S_f is the flame propagation speed). Therefore, at lower pressures, the flame thickness was expected to be bigger.

In 1993, Gorman and his co-workers observed different types of cellular flames with Le less than unity using a circular porous-plug flat flame burner at 0.5 atmosphere (el-Hamdi and Gorman, 1993; Gorman et al., 1994a, 1994b). They noted that the dynamic modes were stable over a wide range of experimental conditions at low pressure and the

diffusion flame was not present in the closed chamber. More recently, Gorman and his coworkers again used the circular, water-cooled, stainless-steel porous-plug burner and conducted the experiments at the chamber pressure of 250 mm Hg to study the CH_4-O_2 flames (Robbins et al., 2004). The flame exhibited several types of spiral waves which include periodic, doubly periodic, weakly chaotic and irregular rotation of a spiral front.

On the other hand, increasing pressure leads to decreasing flame thickness and thus increasing the trends of instability as discussed previously in chapter 2. The spiral waves in rich hydrogen-air flames were only able to be observed for pressure over 5 atm (Jomaas et al., 2007).

In our studies, n-C_4H_{10}-21%O_2-balance He premixture was tested at different ambient pressures in a range of 250 ~ 1000 Torr for different equivalence ratios and burner exit flow speeds. Two typical instability patterns observed at atmospheric pressure were the focus for the pressure effect studies: one is the complex rotating spiral waves shown in Figure 41, the other one is target pattern shown in Figure 68.

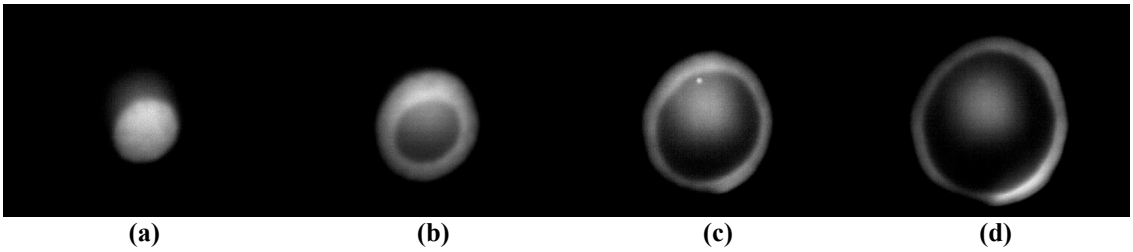

Figure 68: Target patterns with a single, centrally-located pacemaker in n-C_4H_{10} - 21%O_2 -balance He, $\Phi = 0.95$, $V_{exit} = 7.95$ cm/s, P = 760 Torr, time between consecutive images is 1/500 sec.

3.5.1 Effect of Pressure on Target Patterns

For the case that target patter was observed, shown in Figure 68, the effect of ambient pressure on the instability pattern is tabulated in Table 14.

Table 14: Effect of pressure on the dynamics of target patterns in n-C_4H_{10} -21%O_2-balance He, Φ = 0.95, V_{exit} = 7.95 cm/s.

Pressure (Torr)	Pattern	Figure
1000	Target	Figure 69
900	Target	
800	Target	
760	**Target**	**Figure 68**
600	Target	
380	Incomplete Target	Figure 70
250	Weak pulsations	Figure 71

As the pressure decreased from 760 Torr (1 atm), the flame thickness of the target pattern increased and the concentric target rings became incomplete at 380 Torr and then transitioned to pulsations without traveling wave at 250 Torr. On the contrarily, the target pattern became more pronounced as the pressuring was increased gradually from 760 Torr to 1000 Torr but the dynamics of the patterns were still the same. Figure 69 shows the target pattern observed at 1000 Torr while other experimental conditions were kept the same.

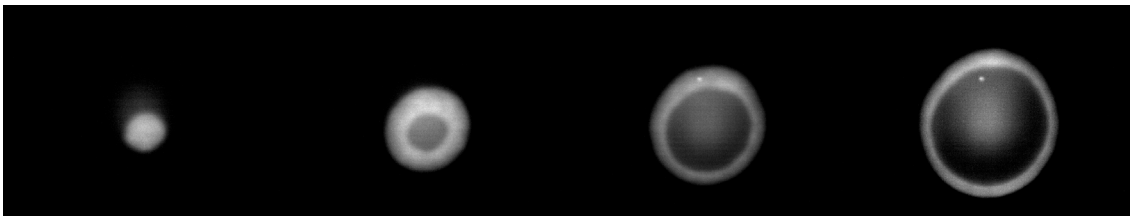

(a) (b) (c) (d)

Figure 69: Enhanced target patterns with a single, centrally-located pacemaker in n-C_4H_{10} -21%O2-balance He, Φ = 0.95, V_{exit} = 7.95 cm/s, P = 1000 Torr, time between consecutive images is 1/500 sec.

Figure 70 shows the weak incomplete target pattern with a single centrally-located pacemaker. Figure 71 shows the weak pulsations, which was almost stable planar flame at 250 Torr. These results showed that decreasing pressure sequenced the flame instabilities thus having an effect of stabilizing the premixed flames.

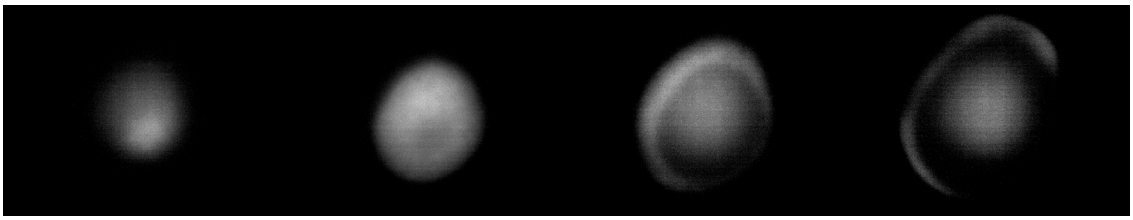

(a) (b) (c) (d)

Figure 70: Weak incomplete target patterns with a single, centrally-located pacemaker in n-C_4H_{10} -21%O2-balance He, Φ = 0.95, V_{exit} = 7.95 cm/s, P = 380 Torr, time between consecutive images is 1/500 sec.

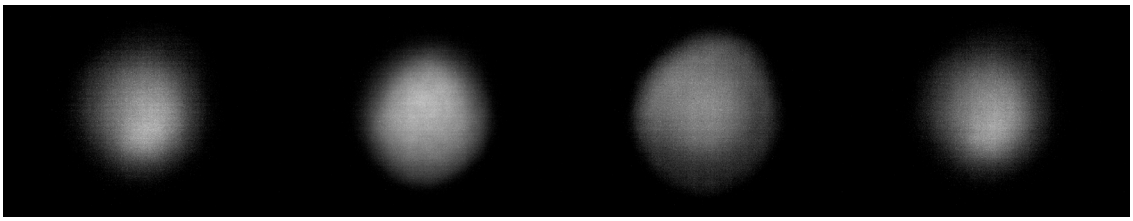

(a) (b) (c) (d)

Figure 71: Weak pulsations with a single, centrally-located pacemaker in n-C_4H_{10} - 21%O2-balance He, Φ = 0.95, V_{exit} = 7.95 cm/s, P = 250 Torr, time between consecutive images is 1/500 sec.

For studying the effects of equivalence ratio on the instability at very low pressure, the fuel and oxidizer composition was adjusted while the ambient pressure fixed at 250 Torr. The results are shown in Table 15.

Table 15: Comparison of flame patterns observed at 760 Torr (1 atm) and 250 Torr for different mixture composition, V_{exit} = 7.95 cm/s.

ϕ	P = 760 Torr	P= 250 Torr
1.06	Stable	Stable (Figure 72)
0.95	Target	Pulsation, no travelling waves (Figure 71)
0.92	Target	Pulsation, no travelling waves
0.89	**Extinction Limit**	Target
0.80	Extinction	Target
0.57	Extinction	**Extinction Limit**

At 250 Torr, the equivalence ratio was adjusted from leaner to richer starting from base case Φ = 0.95. When Φ = 1.02 and above, the pulsations disappeared and transitioned to stable planar flame. Comparing with the stable flame at one atmosphere pressure, the stable planar flame observed was more stabilized, shown in Figure 72 for Φ = 1.06.

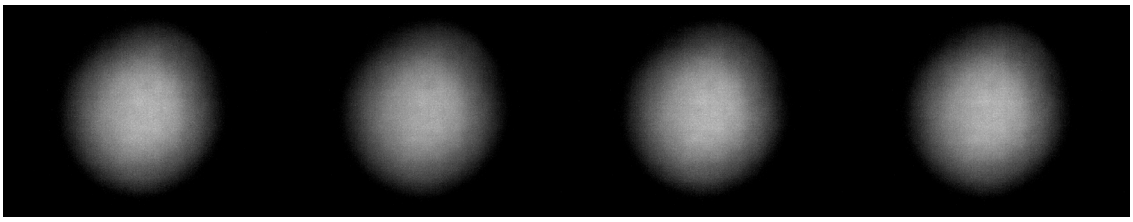

Figure 72: Stable planar flame in n-C_4H_{10}-21%O2-balance He, Φ = 1.06, V_{exit} = 7.95 cm/s, P = 250 Torr, time between consecutive images is 1/500 sec.

In Table 15, as the equivalence ratio was decreasing at 250 Torr, the flame transitioned from stable planar flame to weak pulsations and then to pronounced target patterns for Φ < 0.9 and the patterns showed similar dynamics to the target pattern observed previously. It's worth noting that the extinction limit which was Φ = 0.89 for n-C_4H_{10}-21%O_2-balance He premixture at 760 Torr (1 atm) shifted to Φ = 0.57 at 250 Torr for a fixed burner exit flow speed (specifically V_{exit} = 7.95 cm/s).

3.5.2 Effect of Pressure on Rotating Spiral Waves

Similarly, for the case that complex rotating spiral wave was observed shown in Figure 41, the effect of ambient pressure on the instability pattern is tabulated in Table 16.

Table 16: Effect of pressure on the dynamics of complex spiral wave in n-C_4H_{10} - 21%O_2 -balance He, $\Phi = 1.01$, $V_{exit} = 5.80$ cm/s.

Pressure (Torr)	Pattern	Figure
1000	Target pattern	
900	Target pattern	
800	Target pattern	
760	**Complex spiral wave**	**Figure 41**
600	Target wave followed by a weaker pulsation	Figure 73
380	Target wave followed by a weaker pulsation	
250	Pulsations	Figure 74

The patterns transitioned to pronounced target pattern as the pressure increased. Interestingly, an outwardly propagating target wave followed by a weaker pulsation was observed as the pressure decreased. Figure 73 shows the target patterns followed by the weak pulsations at 600 Torr. The flame front originated from the pacemaker in frame (g) and (h) faded away and did not propagate as a circular wave like frame (a) ~ (f). The instability patterns for pressure at 500 Torr and 380 Torr were similar to that observed at 600 Torr.

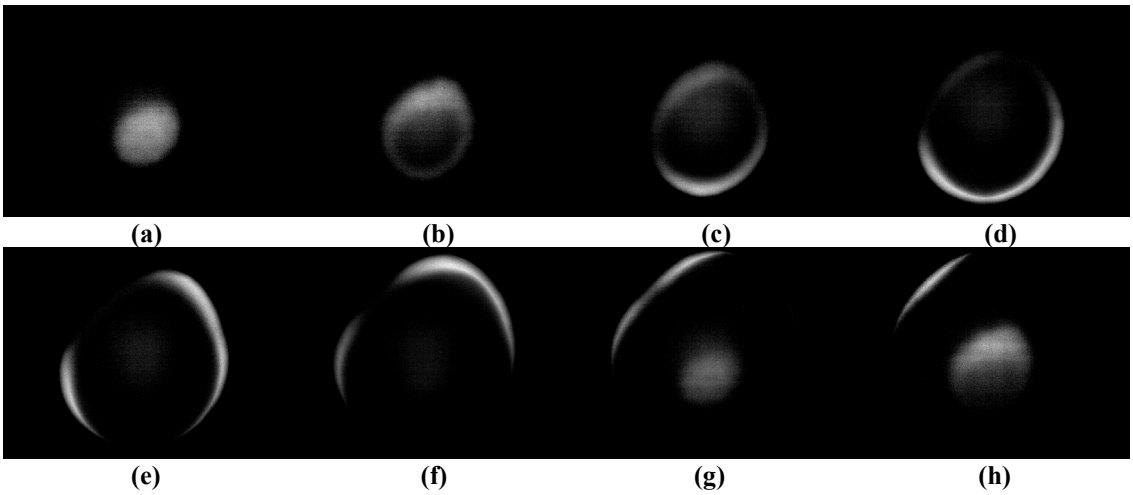

Figure 73: Target pattern with a single, centrally-located pacemaker in n-C_4H_{10} - 21%O_2 –balance He, Φ = 1.01, V_{exit} = 5.80 cm/s, P = 600 Torr, time between consecutive images is 1/500 sec.

When the pressure further decreased to 250 Torr, the target pattern disappeared and only weak pulsations were observed. Figure 74 shows the pulsations observed at 250 Torr.

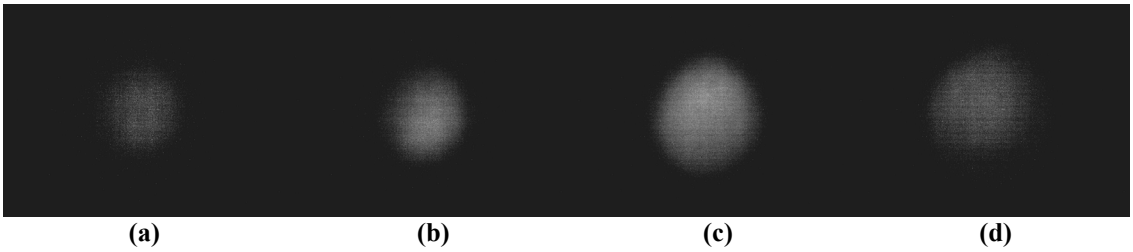

Figure 74: Weak pulsations with a single, centrally-located pacemaker in n-C_4H_{10} - 21%O_2 –balance He, Φ = 1.01, V_{exit} = 5.80 cm/s, P = 250 Torr, time between consecutive images is 1/500 sec.

The effect of mixture composition on the flame instabilities was studied at low pressure of 250 Torr. When Φ was decreasing, the patterns transitioned from weak

pulsations (Φ = 1.01 in Figure 74) to pronounced propagating target patterns followed by a weak pulsation shown in Figure 75 (Φ = 0.78). It is noted that the extinction limit which was Φ = 0.89 for n-C_4H_{10}-21%O_2-balance He premixture at atmospheric pressure when V_{exit} = 5.80 cm/s shifted to Φ = 0.77 at 250 Torr ambient pressure.

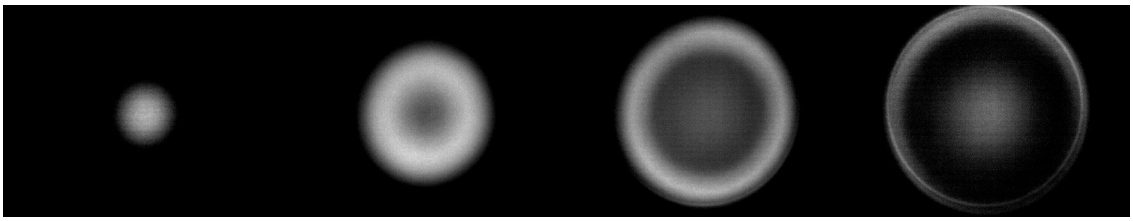

(a) (b) (c) (d)

Figure 75: Target pattern with a single, centrally-located pacemaker in n-C_4H_{10} - 21%O_2 –balance He, Φ = 0.78, V_{exit} = 5.80 cm/s, P = 250 Torr, time between consecutive images is 1/500 sec.

The effect of equivalence ratio on the flame instabilities was also studied at high pressure of 1000 Torr. Multiple target waves were observed shown in Figure 76.

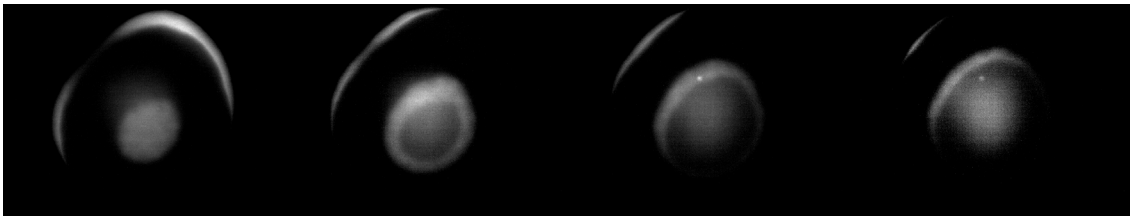

(a) (b) (c) (d)

Figure 76: Multiple target rings with a single, centrally-located pacemaker in n-C_4H_{10} - 21%O2-balance He, Φ = 0.99, V_{exit} = 7.96 cm/s, P = 1000 Torr, time between consecutive images is 1/500 sec.

As the mixture went to slightly rich side of the stoichiometry, the stable planar flame was observed for $\Phi = 1.02$, $V_{exit} = 7.96$ cm/s at 1 atm started to show the complex target patterns for the same conditions at 1000 Torr shown in Figure 77.

Figure 77: Complex target patterns in n-C_4H_{10} - 21%O2-balance He premixtures, $\Phi = 1.02$, $V_{exit} = 7.96$ cm/s, P = 1000 Torr, time between consecutive images is 1/500 sec.

As expected, decreasing pressure has a stabilizing effect on the flame instabilities. The pronounced traveling target waves transitioned to incomplete target wave then to weak pulsations as the ambient pressure decreased and the range for the flame pattern stabilized on the burner surface was widely expanded. The higher the burner exit flow speed, the leaner limit the premixtures can reach. On the contrary, increasing pressure will destabilize the flame and increase the instability extents.

3.6 Closure

A systematic study of high Le instabilities in premixed flames is performed using n-C_4H_{10}, n-C_7H_{16} and n-C_8H_{18} diluted with air or O_2-He on McKenna flat burner. Two types of McKenna burners were used: stainless-steel McKenna burner and bronze McKenna burner. Similar trends were observed for both types of burners. However,

differences were also observed for the two burners because of different heat loss. Multiple rotating spiral flames were observed for the first time and so were the coexisting rotating spiral waves and target patterns. The stability diagrams were developed for all fuel-oxidizer mixtures over a wide range of equivalence ratios and total burner exit flow speeds. Effects of ambient pressure were studied and the results were discussed in this chapter as well. It was found that decreasing the pressure will stabilize the flame.

4. Two-Dimensional Modeling Studies on Instability Pattern Formation in Premixed Gas Flames

4.1 Introduction

Complex, nonlinear physico-chemical systems can give rise to spontaneous pattern formation due to the couplings between chemical reaction and transport processes such as diffusion or convection. For a system to be self-organizing, there are two requirements: (1) the system cannot be in equilibrium and (2) there is an appropriate feedback process (Nicolis and Progogine, 1977). The feedback process is typically an autocatalytic process in which one (or more) of the intermediate chemical species produced in an elementary step is self-replicating. In premixed gas combustion, thermal feedback may also be sufficient to produce self-organizing patterns where temperature, rather than species concentration, is the autocatalyst (Scott, 1994). Most notably, the heat release from an exothermic reaction raises the bulk temperature, which, in turn, increases the reaction rate. In combustion, this feedback occurs through the Arrhenius temperature dependence of the reaction rate.

Spontaneous pattern formation has been observed in a variety of diverse fields including biology, electrochemistry, and thermochemistry (Scott, 1994). As discussed in the Introduction of this thesis, similar patterns have also been observed in the area of combustion in: freely-propagating premixed flames. burner-stabilized premixed flames and spherically expanding rich hydrogen-air flames (Jomaas et al., 2007; Ma and Pearlman, 2007; Pearlman, 1997; Pearlman and Ronney, 1994b; Pearlman and Ronney, 1994a). Rotating waves have also been observed in diffusion flames (Kim et al., 1996; Nayagam and Williams, 2000). While the kinetics in various systems are undoubtedly

different and the diffusive transport may be in the form of heat, mass, or in some cases voltage, they all display similar self-organizing, pattern formation. As discussed in Chapter 1, hydrodynamic and diffusive-thermal instabilities may render steadily propagating premixed flames unstable where the focus of this work is on the diffusive-thermal instability. This purpose of this chapter is to report the results of numerical simulations to help interpret some of the different reaction modes shown in Chapter 3 including radially pulsating waves, target patterns, rotating spiral waves and complex patterns.

It should also be mentioned that two models based on a two-step Sal'nikov scheme have been reported in the literature and have been used as the foundations for the numerical simulations reported here (Scott et al., 1997). Both models included diffusion of heat and species and were able to predict some of the patterns observed experimentally. The first model by Scott and co-workers was developed in terms of the excitability of the system for one- and two-dimensional domains (Scott et al., 1997) and was able to predict target and spiral patterns in two-dimensions (defined by the spatio-temporal temperature variation) that are qualitatively similar to those observed experimentally. Their work considered a limited range of parameter space where the characteristic time associated with heat loss was much less than that associated with chemical reaction. Interestingly, their results showed that increasing Le broadened the parameter space for instability in one-dimensional simulations while only a unity Le case was considered in two-dimensional simulations. Both target and spiral waves were predicted for Le = 1 suggesting that the diffusive-thermal instability may in fact not be the driving mechanism unless perhaps the heat loss was sufficiently large. Following

their work, Matkowsky and co-workers used the same model with parameters that were more representative of premixed gas combustion (Panfilov et al., 2003). They predicted both uniformly propagating, traveling wave and rotating spirals waves and further suggested that excitability is not a necessary condition for the existence of spiral patterns.

In this chapter, the Sal'nikov models are further developed and a detailed analysis s performed to understand the parametric dependencies on the two-dimensional patterns. The parameters include Le, Ze, heat loss and hot gas expansion. Comsol Multiphysics, a coupled PDE solver platform, was used to perform the simulations and solve the species and energy equations using a new nondimensionalization. Comparisons with previous experimental observations are discussed and good qualitative agreement is reported.

4.2 A Historical Review of Numerical Studies on Target Patterns and Spiral Waves

4.2.1 Prior Numerical Results using Scott-Wang-Showalter Model

Scott, Wang and Showalter predicted the spiral and target patterns numerically for the first time using a simple two-step Sal'nikov scheme augmented with diffusion of heat and species (Scott et al., 1997).

$$P \rightarrow A; \quad \text{rate} = k_I\, p \qquad \text{I}$$

$$A \rightarrow B + \text{heat}; \quad \text{rate} = k_{II}\,(T)a \qquad \text{II}$$

The first step of the model was assumed to be thermal neutral and the second step followed Arrhenius kinetics, i.e. $k_{II} = A\exp\left(-E_a / RT\right)$, where A is the pre-exponential factor, E_a the activation energy and R is the gas constant. A continuous reactant feed

was assumed and the model was developed in terms of the excitability of the system, rather than by assigning any special role to the Le.

The non-dimensionalized reaction-diffusion equations can be written as:

$$\frac{\partial \alpha}{\partial \tau} = \mu - \alpha f(\theta) + \nabla^2 \alpha \qquad (18a)$$

$$\frac{\partial \theta}{\partial \tau} = \frac{1}{\kappa}\left[\alpha f(\theta) - \theta\right] + (Le)\nabla^2 \theta \qquad (18b)$$

where α and θ are non-dimensionalized concentration and temperature, $\theta = {E(T - T_a)}/{RT_a^2}$, $f(\theta) = \exp\left(\frac{\theta}{1+\varepsilon\theta}\right)$ with $\varepsilon = {RT_a}/{E_a}$, $\alpha = {a}/{c_{ref}}$ with $c_{ref} = \frac{C_p}{Q}\frac{RT_a^2}{E}\frac{t_{chem}}{t_N}$, and Le is the Lewis number. Two additional nondimensional groups (κ and μ) occur with this nondimensionalization, where κ is the heat transfer time scale normalized by the chemical time $\kappa = {t_N}/{t_{chem}} << 1$ where $t_{chem} = 1/k_{II,a}$ (inverse of the reaction rate of step II evaluated at the adiabatic flame temperature). $\mu = k_I t_N \frac{Qp_0}{C_p}\frac{E_a}{RT_a^2}$ where Q is the exothermic heat release from step II, p_0 is the initial concentration of the reactants, c_p is the specific heat, ρ is the density and T_a is the ambient temperature. Note that length and time are nondimensionalized using the chemical time $t_{chem,}$ and a diffusion length $(D_A t_{chem})^{1/2}$, respectively.

The coupled species and energy equations were solved in one-dimensional and two-dimensional domains. No flux boundary conditions were applied and initial conditions were set to be $\alpha = \alpha_{ss} = \mu / f(\mu)$ and $\theta = \theta_{ss} = \mu$ everywhere in the domain. To initiate the reaction, an artificial local perturbation to the temperature was applied.

The one-dimensional results show that:

1. Wave propagation occurs for a range of μ and κ. Below a critical value of μ, no propagation occurs corresponding to lean flammability limit;
2. Wave propagation does not occur below a critical value of κ, where the heat transfer is high, or above a critical value of κ, where cooling times are on the order of the chemical reaction time and the excitability of the system is reduced or disappeared.
3. Bulk oscillations are observed for values of μ larger than 1.5. Wave propagation is also observed in some regions where the period of the bulk oscillation is longer than that required for the wave to propagate through the domain.

Two-dimensional simulations demonstrate the existence of stable, target and spiral wave patterns at unity Le for specific values of κ and μ.

1. The propagating target waves are observed when a small region of domain (in the center) is made to be oscillatory by suitably choosing μ and κ.
2. Spiral waves are also generated by allowing a single circular wave to develop and then artificially reset part of the domain to the initial conditions. This solution of the equations following the disturbance is then followed and it evolves into a steadily rotating spiral wave.

The two-dimensional patterns are qualitatively similar to the experimental observations. One concern with the model is that predicts these patterns regardless of the value of the Le and suggests that diffusive-thermal mechanism is not the dominant cause.

4.2.2 Prior Numerical Results using Matkowsky's Spiral Flame Model

Panfilov, Bayliss and Matkowsky subsequently revised the Scott-Wang-Showalter excitable model and questioned their choice of parameters, specifically the values used for the heat loss parameter h (3487), Zel'dovich number Ze (0.9) and Le (1) (Panfilov et al., 2003). With more realistic values for Le (>1), h and Ze, they resolved the same model with a different nondimensionalization in a 2D domain. The modified nondimensional equations were:

$$\theta_t = \nabla^2\theta + h\left(Y \exp\left(\frac{N(1-\sigma)(\theta-1)}{\sigma + (1-\sigma)\theta} \right) - \theta \right) \quad (19a)$$

$$Y_t = \frac{1}{Le}\nabla^2 Y - Y \exp\left(\frac{N(1-\sigma)(\theta-1)}{\sigma + (1-\sigma)\theta} \right) + 1 \quad (19b)$$

Here θ and Y are nondimensionalized temperature and concentration of intermediate species. The expressions are $\theta = (T - T_0)/(T_H - T_0)$ and $Y = \widetilde{Y} / Y_H$ where $T_H = T_0 + QM/H$ and $Y_H = M\exp(N)/k$ are homogeneous solutions of the equations. Here, T_0 is the unburned temperature, Q is the heat release, M is the continuous supply of fuel, N is the nondimensional activation energy ($N = E_a / RT_H$) and k is the preexponential factor. The nondimensionalized heat loss is $h = H\exp(N)/(k\rho c)$ where H is a heat loss coefficient, ρ is the density and c is the heat capacity. The hot gas expansion is $\sigma = T_0 / T_H$ and the $Le = \lambda / D\rho c$ where λ is the thermal conductivity. The reference time and length are $\exp(N)/k$ and $\sqrt{\kappa \exp(N)/(k\rho c)}$. In the computations, N was taken to be 4.5 and $\sigma = 0.2$ so that Ze = $N(1-\sigma)$ = 3.6. The numerical domain was fixed at 69.86 (ref. length) and the parameters Le and h were varied in the ranges of

$Le \in [1, 5.5]$ and $h \in [0.3, 30]$. This range of Le's used in the computations spanned the range of Le's tested experimentally which were in the range (Pearlman and Ronney, 1994b; Pearlman and Ronney, 1994a; Pearlman, 1997).

No-flux boundary conditions were applied on all domain boundaries and the initial conditions were defined as $\theta = Y = 1$ in the lower half domain (noting that the computational domain was divide in half horizontally) and a one-dimensional temperature disturbance was applied at $x = L/2$ in the upper half of the domain to numerically initiate the reaction.

Rotating spirals waves were predicted with nonsymmetrical numerical perturbations. Their numerical results also showed that as h increases, the spacing between adjacent spiral wave windings decreases and the corresponding number of spiral arms in a given region of space increases. For some conditions, it was also shown that the spiral tip motion can be quite complex. In some parameter space, the motion is circular and periodic and for other conditions, the spiral tip follows a meandering path as shown in Figure 6 (Chapter 1).

4.3 New Numerical Studies on the Dynamics of Target Patterns

4.3.1 Target Patterns Initiated by Single Oscillatory Region

The Scott-Wang-Showalter model was adopted for the computations reported in this section. The coupled species and energy equations were solved in a two-dimensional circular domain. For target pattern studies, it was assumed that the flames are azimuthally symmetric which would enable the problem to be reduced one-dimension. In the simulations reported here, the circular domain was simply divided into four quadrants

and the coupled equations were solved in one quadrant with no flux boundary conditions applied at the interfaces of the domains. This reduced the required computational time. The geometry used to define the computational domain is shown in Figure 78; it has 1761 elements with a maximum element size of 0.025. The domain size was R = 1 (ref. length $\sqrt{D_A t_{chem}}$).

To initiate the target pattern, a numerical perturbation was applied at the center to the temperature and intermediate species concentration (a). These initial conditions in the bulk of the domain were $T_0 = 1.4$, $a_0 = 0.2$ and the parameters used to perturb the solution and initiate the wave were $T_0 = 2.5$, $a_0 = 0.2$. The coupled partial differential equations were then integrated using a PDE solver, UMFPACK, packaged with the commercially available COMSOL Multiphysics™ software. The time step was 0.001. Both the relative and absolute tolerances on the non-dimensional temperature and species concentration were 0.001 and the maximum backwards differentiation order was five.

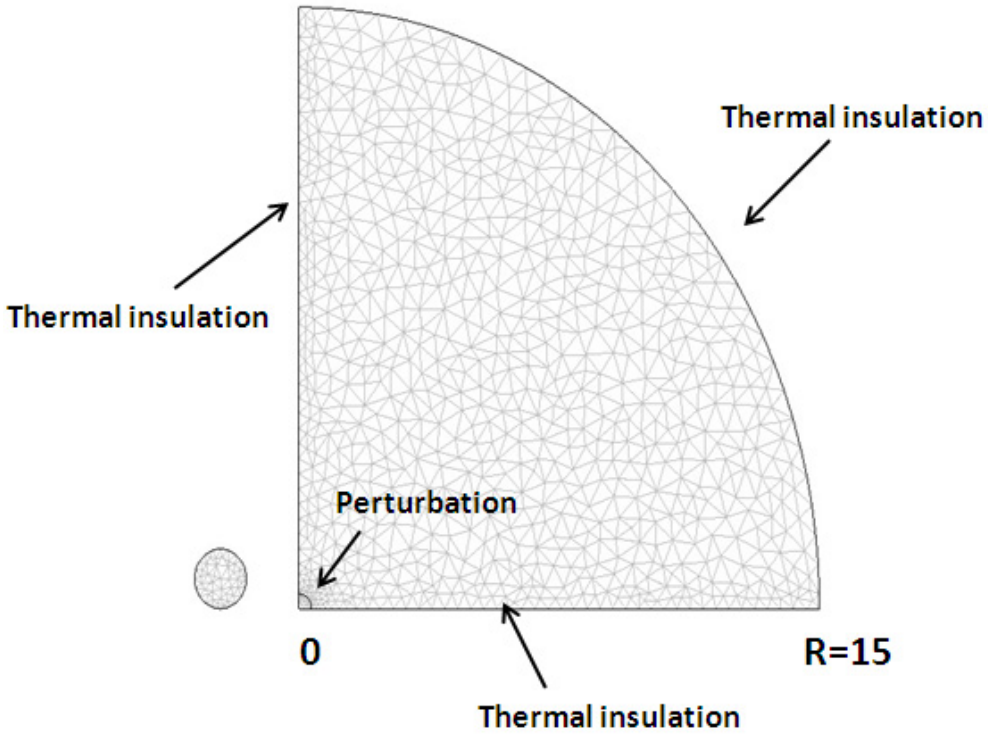

Figure 78: Quadrant domain of size R = 1 to simulate target patterns using the Scott-Wang-Showalter model, 1761 mesh elements, maximum mesh size 0.025.

For these conditions, the nondimensional temperature and species concentration profiles are shown in Figure 79 and Figure 80. As shown, a circular thermal wave originated at the center (location of the numerical perturbation) and propagated radially outward. The target wave propagated to the domain boundary followed by another circular wave emitted from the center. The radial propagating wave is reminiscent of the target pattern observed experimentally and discussed in chapter 3. The concentration field for the intermediate species is shown in Figure 80; note that peak in the intermediate species concentration proceeds the peak temperature is depleted as the thermal wave propagates radially outward. At the same time, the unburned reactants are replenished,

step 1 of the mechanism proceeds and the intermediate is generated, its concentration increases and another radial wave is generated.

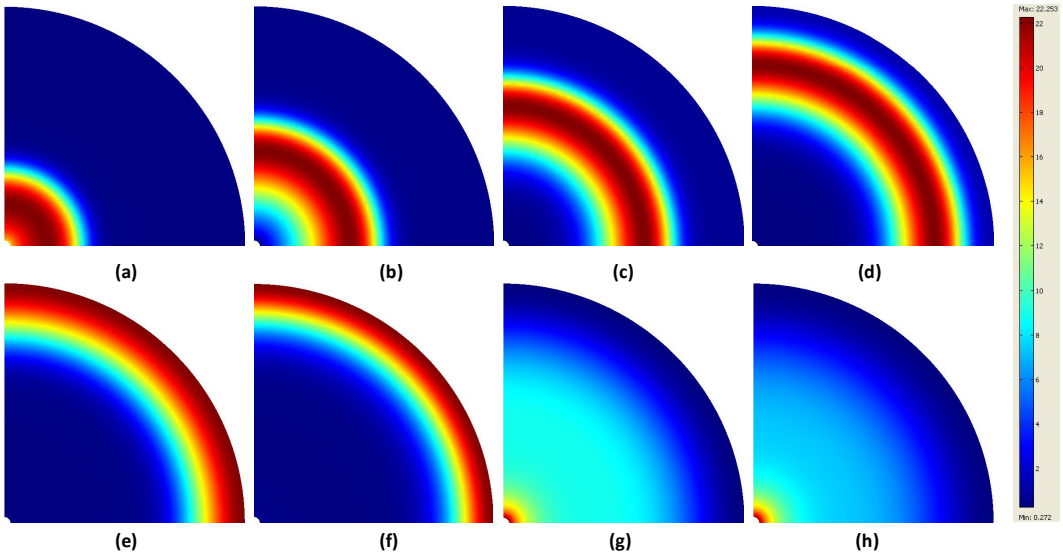

Figure 79: Temperature distribution of the circularly propagating target pattern, Le = 3, R = 1, time associated with images (a)-(h) are: 0.34, 0.345, 0.35, 0.355, 0.36, 0.365, 0.37 and 0.375 respectively.

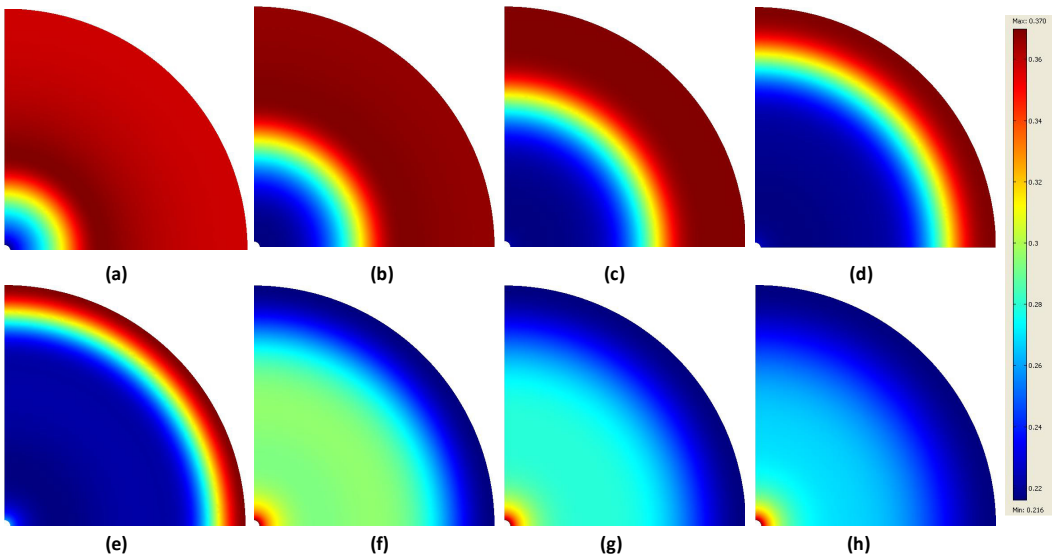

Figure 80: Concentration distribution of the circularly propagating target pattern, Le = 3, R = 1, time associated with images (a)-(h) are: 0.34, 0.345, 0.35, 0.355, 0.36, 0.365, 0.37 and 0.375 respectively.

4.3.2 Effect of Le and Heat Loss on Target Patterns

To further evaluate the effects of Le and heat loss on the target patterns, a two-dimensional square domain of nondimensional size 2 x 2 (ref length = $\sqrt{D_A t_{chem}}$) was used to develop the complete target pattern as shown in Figure 81. The domain was meshed into 7506 triangular elements with a maximum element size of 0.04. The initial conditions for the perturbation at the center of the domain (needed to initiate the reaction) was $T_0 = 2.5$ and $a_0 = 0.2$ and the outer domain was prescribed values of $T_0 = 1.4$ and $a_0 = 0.2$. The other parameters in the model were κ = 5E-4, ε = 0.18 and Le was varied between 1 and 7. Figure 81 shows a representative temperature profile associated with a circular wave initiated from the central perturbation that propagates outwardly until it interacts with the boundary of the domain. The radially expanding circular wave models those observed experimentally in n-C_4H_{10}, n-C_7H_{16} and n-C_8H_{18} in O_2-He premixtures such as those shown in Figure 45, Figure 62 and Figure 67.

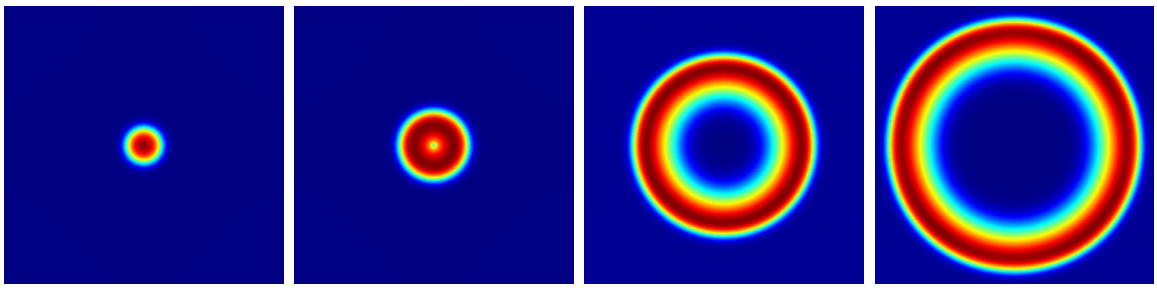

Figure 81: Temperature distribution of the radially propagating target wave in a 2x2 square domain, Le = 1, time associated with images (a)-(d) are: 0.337, 0.34, 0.35, 0.356 respectively.

To estimate the radial propagation flame speed for the case shown in Figure 81, the peak temperature was tracked using a line profile along a given radius. The temperature

profiles associated with the images in Figure 81 are shown in Figure 82. The distance that the flame propagated between each time step (Δx) was estimated at an intermediate temperature from which the flame speed was determined, $V_f = \Delta x / \Delta t$. The oscillation frequency ω was also estimated for different Le by tracking the temperature profile shown in Figure 83 and taken as the inverse of Δt is the time for one complete oscillation.

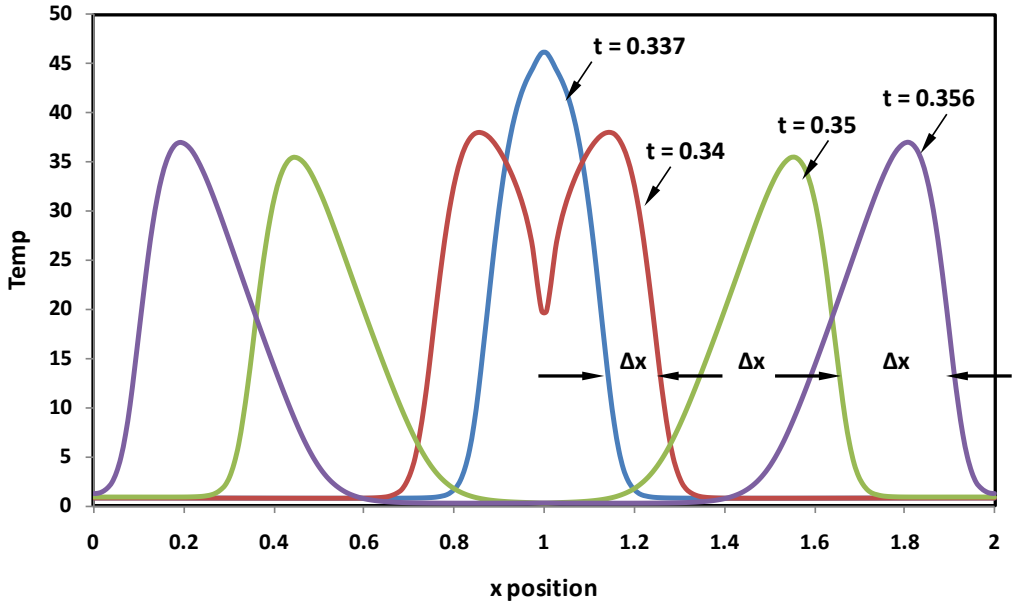

Figure 82: Radially propagating target waves at four different times for the case shown in Figure 81.

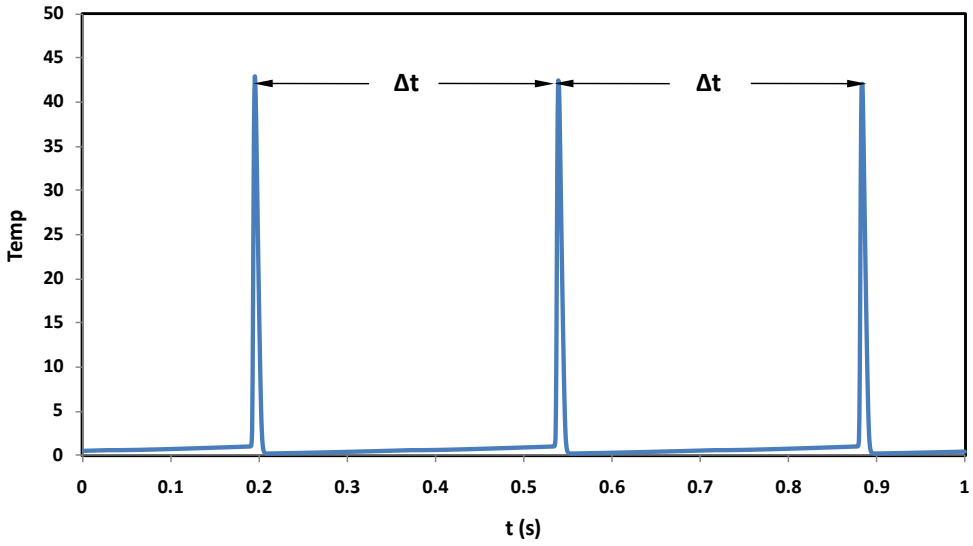

Figure 83: Temperature profile at point (0.5, 0.5) for the case shown in Figure 81.

The radial flame speeds and oscillation frequencies computed for different Le's are listed in Table 17. Clearly, the radial flame speeds and oscillation frequencies increase with increasing Le, which is consistent with the experimental observations in Table 13.

Table 17: Effect of Le on the circular waves/target patterns using Scott-Wang-Showalter model, κ = 5E-4, ε = 0.18.

Le	Nondimensional Oscillation Frequency ω	Computed Nondimensional Radial Flame Speed V_f
1	2.87	38.5
3	5.75	41.2
5	5.78	52.2
7	5.81	62.4

The effect of heat loss was also studied for a representative high Le case (Le = 3) for a range of κ ($\kappa = t_N/t_{chem}$) from 1e-6 to 5e-5. When heat loss increases, t_N decreases and temperature decreases such that the reaction rate also decreases and t_{chem} increases. As a result, increasing heat loss corresponds with decreasing κ.

Computed results of the effects of heat loss on the radial propagation of circular waves (target patterns) are listed in Table 18 where it can be seen that the radial flame speed increases with decreasing κ and the oscillation frequency also increases, albeit slightly, with decreasing κ. For smaller values of κ (1E-6) corresponding to the case of very high heat loss, radially propagating solutions were not found, which corresponds to flame quenching.

Table 18: Effect of heat loss (variable κ) on the circular waves/target patterns using Scott-Wang-Showalter model, Le = 3, ε = 0.18.

κ	Nondimensional Oscillation Frequency ω	Computed Nondimensional Radial Flame Speed V_f
5E-4	5.75	41.2
1E-4	7.14	136.0
5E-5	7.52	201.0
1E-5	7.81	502.5

4.3.3 Numerical Studies on the Interactions of Multiple Target Waves

The coupled species and energy equations were also solved in a two-dimensional square domain of size 2 x 2 (ref length $\sqrt{D_A t_{chem}}$) to explore the interaction of target wave fronts induced by multiple oscillatory regions as observed experimentally (Ma and Pearlman, 2005). The domain shown in Figure 84 was uniformly meshed with 7918 elements (the maximum element size was 0.04). No flux boundary conditions were applied to the outer boundaries. The two separate oscillatory regions were spaced a distance = 0.4 apart.

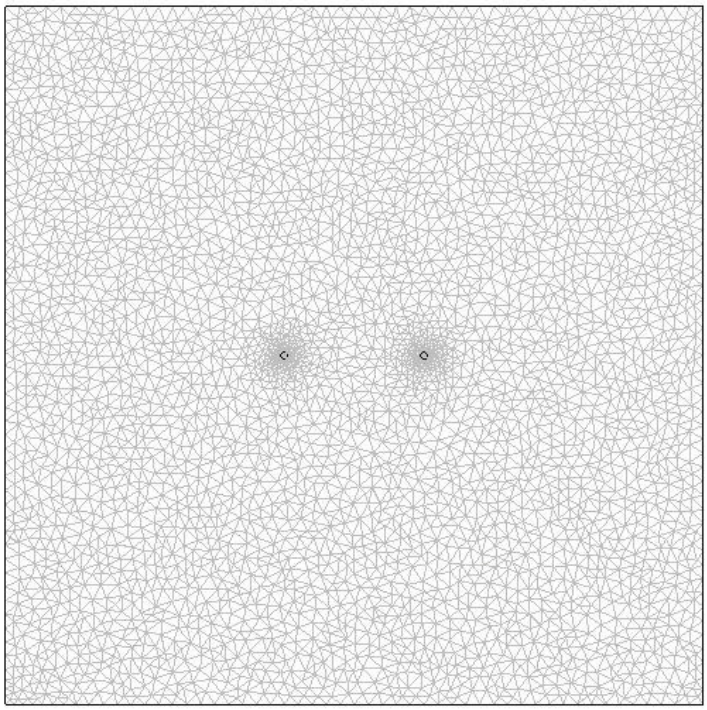

Figure 84: Meshed square domain of size 2 x 2 with 7918 mesh elements and maximum mesh size of 0.04 for 2-D Scott-Wang-Showalter multiple interacting wave front studies.

4.3.3.1 Two Identical Oscillatory Regions

The spatio-temporal evolution of the nondimensional temperature and species fields are computed solving the coupled species and energy equations (4.1) and shown in consecutive rows of Figure 85 and Figure 86. The parameters used in the bulk are: Le = 1, $\varepsilon = 0.18$, $\kappa = 5 \times 10^{-4}$, $\mu = \theta_{initial} = 1.4$ and $\alpha_{initial}$ = 0.2 and in the two oscillatory regions, $\mu = \theta_{initial} = 2.5$, $\alpha_{initial} = 0.2$.

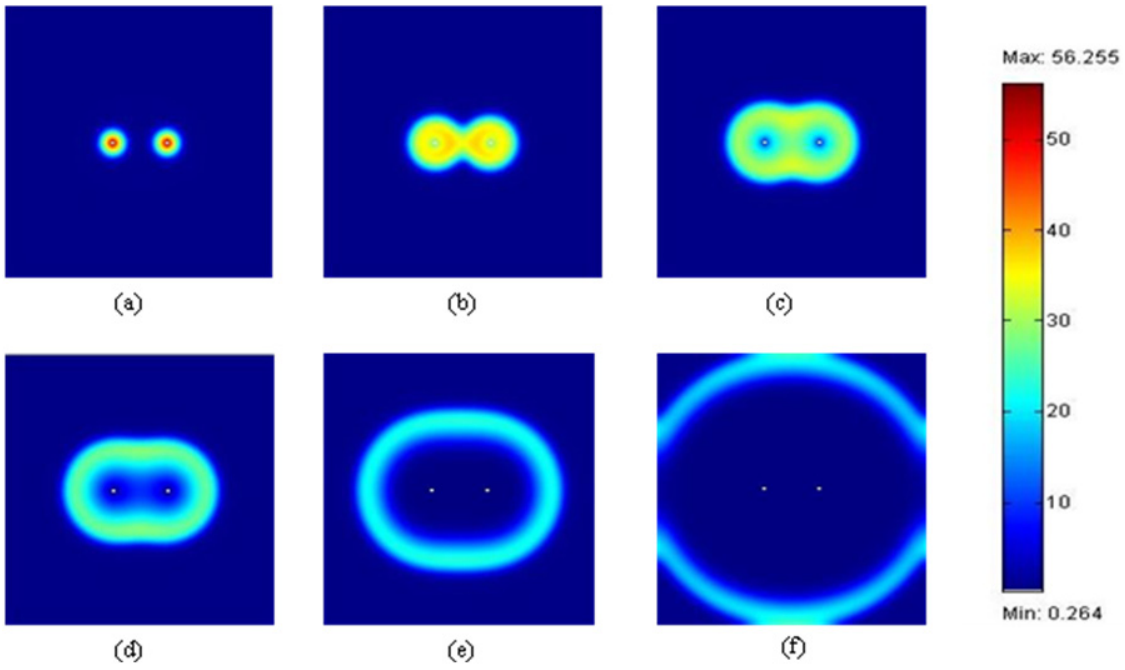

Figure 85: Temperature distribution associated with the interaction of two radial waves that develop from the same initial conditions; time associated with images (a)-(f) are: 0.163, 0.167, 0.170, 0.173, 0.179, 0.198, respectively.

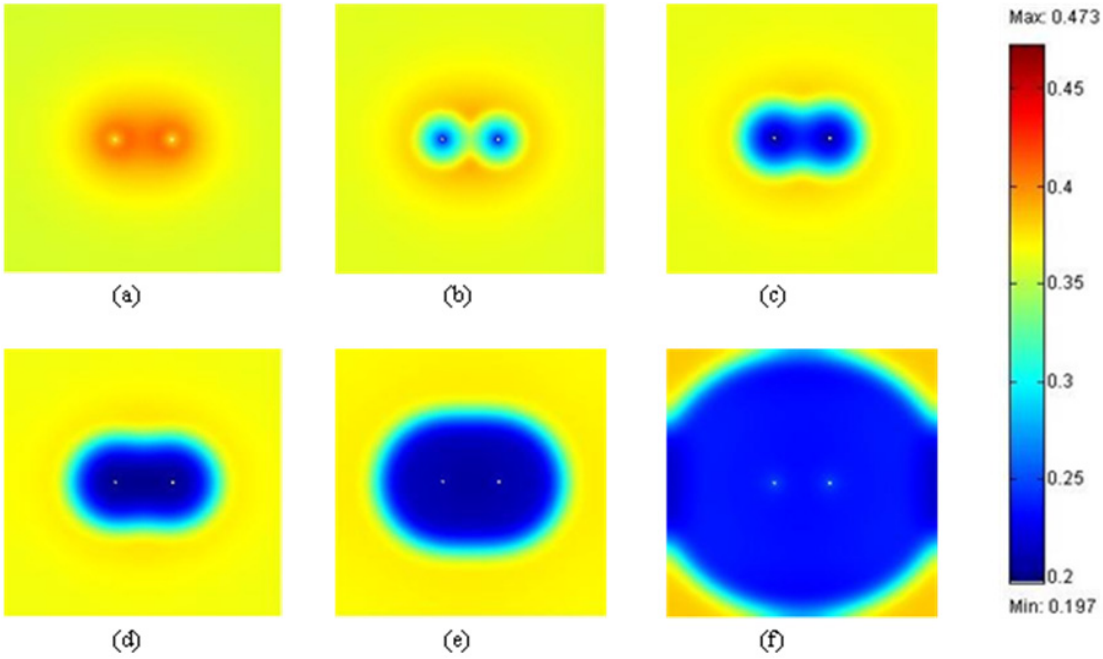

Figure 86: Concentration distribution associated with the interaction of two radial waves that develop from the same initial conditions; time associated with images (a)-(f) are: 0.163, 0.167, 0.170, 0.173, 0.179, 0.198s, respectively.

At early times, the waves emitted from each region develop independently, then interact as seen in Figure 85b where the waves reinforce one another and the highest temperature occurs in the central region on either side of the circular waves. The waves then merge and form an elliptical, radially-expanding front that propagates to the boundary. In addition, the peak values of the intermediate species occur ahead of the peak temperatures and they track closely.

4.3.3.2 Two Out-of-phase Oscillatory Regions

A representative case shows the effect of multiple sites that occurred out-of-phase due to slight variations in the concentrations at the origin of the waves. In this case, two oscillatory waves develop at different initial concentrations as shown in Figure 87. The

right oscillatory center had a slightly faster oscillation frequency and forms a radially-expanding wave followed by a wave initiated by the left oscillatory region. Both disturbances form waves that eventually interact in Figure 87(b), annihilate each other in the region of intersection due to depletion of the reactants and merge to form a distorted outwardly propagating wave front. This behavior is reminiscent of that observed experimentally in downwardly propagating flames (Pearlman and Ronney, 1994b; Pearlman and Ronney, 1994a) shown in Figure 88. .

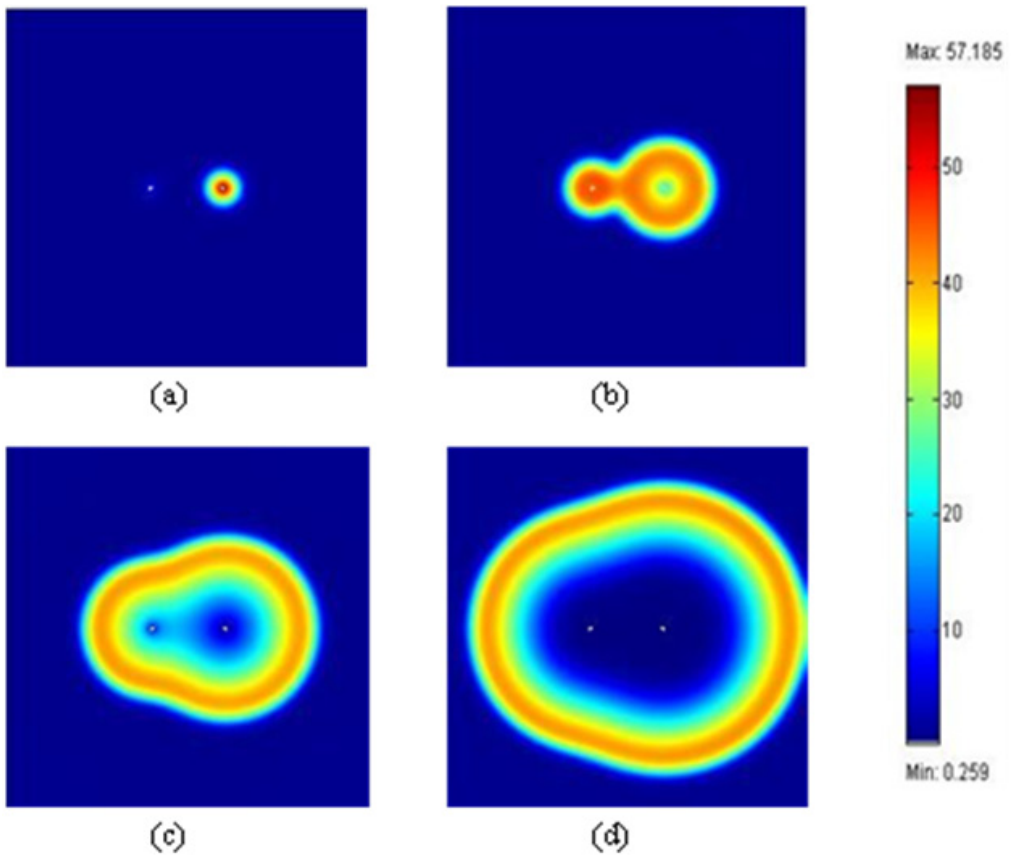

Figure 87: Temperature distribution from two spatial oscillatory centers with different initial concentrations, $\alpha_{initial,left} = 0.245$, $\alpha_{initial,right} = 0.25$, times associated with images (a)-(d) are 0.313, 0.317, 0.322 and 0.328, respectively.

Figure 88: Radial view of two "pacemaker sites" on the surface of a downwardly-propagating premixed flame in a lean mixture of 1.46%C_4H_{10}-21.0%O_2-balance He.

The effect of the different initial temperature on the development of two waves was also considered and a representative case for different initial temperatures, $\theta_{initial}$ = 2.50 and 2.45 for the left and right oscillatory regions, respectively, is shown in Figure 89. As shown, the initial temperature affects reaction rate and chemical time required for initiation of the wave. In this case, the wave starts at the left (higher temperature), followed by the wave at the right with slightly longer chemical time. They interact and merge to form a distorted outwardly expanding wave.

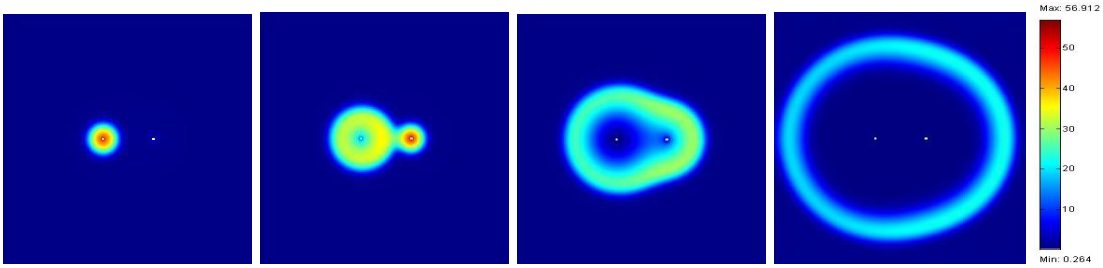

Figure 89: Temperature distribution from two spatial oscillatory centers with different initial temperatures: $\theta_{initial,left}$ = 2.5, $\theta_{initial,right}$ = 2.45, $\alpha_{initial}$ = 0.2, for both oscillatory regions, times associated with images (a)-(d) are: 0.165, 0.169, 0.175, and 0.190, respectively.

4.3.3.3 Effect of Le Number on the Multiple Target Waves

The effects of Le on the interaction between identical spatially separate perturbations are shown in Figure 90. For increasing Le (Le's = 0.5, 1, 3 and 5 were considered), the radial flame speed increased, the flames interacted at an earlier stage, and the flame thickness increased. The increase in flame speed and thickness are reasonable since the flame speed scales with $\sqrt{\alpha k(T)}$ and the thermal thickness scales with the thermal diffusivity of the mixture divided by the flame speed. Thus, one may consider that increasing Le may result from an increase in thermal diffusivity, which would increase the flame speed and the thermal thickness.

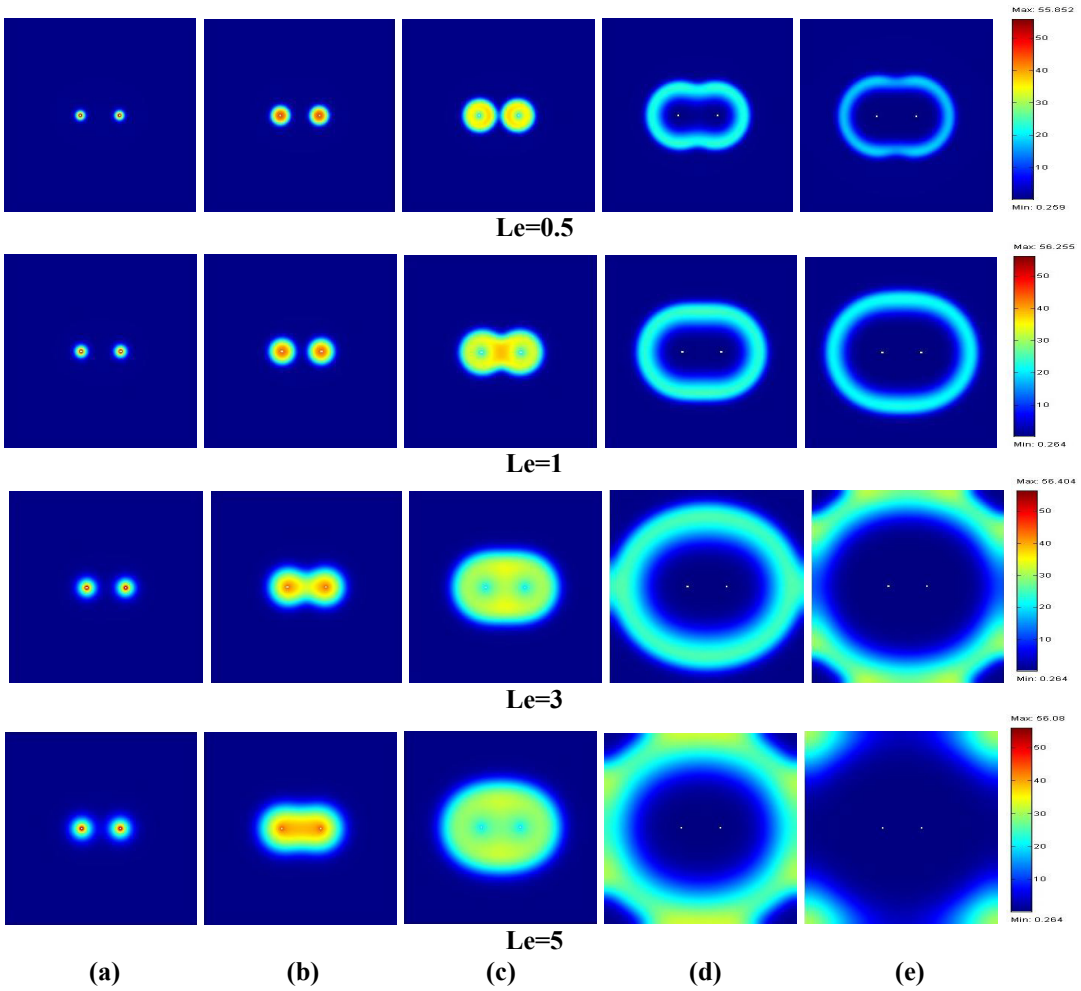

Figure 90: Comparison of non-dimensional temperature distribution for Le=0.5, 1, 3 and 5(sequential rows). In the oscillation centers, $\alpha_{initial}$ = 0.2, $\theta_{initial}$ = 2.5, times associated with images (a)-(e) are 0.163, 0.165, 0.168, 0.177, 0.182, respectively.

4.3.4 Summary of Numerical Studies on Target Patterns

The 2D Sal'nikov model was used to explore the behavior and interaction of reactive-diffusive flames initiated by single and spatially-separate oscillatory regions. The numerical results demonstrate radially propagating waves result from single perturbations and the development, interaction, and merging of multiple waves resulting from multiple

sites. Increasing Le is also predicted to result in an increase in flame speed and oscillation frequency which was also observed experimentally (Pearlman and Ronney, 1994b; Pearlman and Ronney, 1994a; Pearlman, 1997).

In accordance with the results obtained by Scott and co-workers, the model does predict target patterns for Le greater than and less than one. As discussed previously, such instabilities were observed in burner-stabilized flames using lean mixtures of methane-air (Le = 0.93), rich mixtures of propane-air (Le = 1.05) and rich mixtures of butane-air (Le = 1.03) that all have Le near one or even slightly less than one when conduction heat loss to the burner is sufficiently high (Pearlman, 1997).

4.4 New Numerical Studies on the Dynamics of Rotating Spiral Waves

4.4.1 On Rotating Spiral Arms using Scott-Wang-Showalter Model

Rotating spiral arms are also predicted using Scott-Wang-Showalter model on a 2D domain of size 4 x 4 (ref length $\sqrt{D_A t_{chem}}$). The simulations were started by first initiating a single circular wave in the upper half domain and allowing it to expand to the center of the domain. The lower half domain was then reset to the initial state. This method was also used by Scott and co-workers (Scott et al., 1997). The initial condition for the lower half domain is $\alpha_{initial} = 0.3$, $\theta_{initial} = 1.4$, $\varepsilon = 0.18$, $\kappa = 5e\text{-}4$ and Le = 1. The time step was 0.001. Both the relative and absolute tolerances on the non-dimensional temperature and species concentration were 0.001 and the maximum backwards differentiation order was five.

The circular wave started from the upper domain and quickly developed into rotating spiral arms in a counter-clockwise direction, shown in Figure 91. The rotating spiral arm

patterns was qualitatively similar to the spiral reported in Chapter 3 and those observed by Robbins and coworkers using a rich methane-oxygen mixture with Le = 1.024 (Robbins et al., 2004) shown in Figure 92.

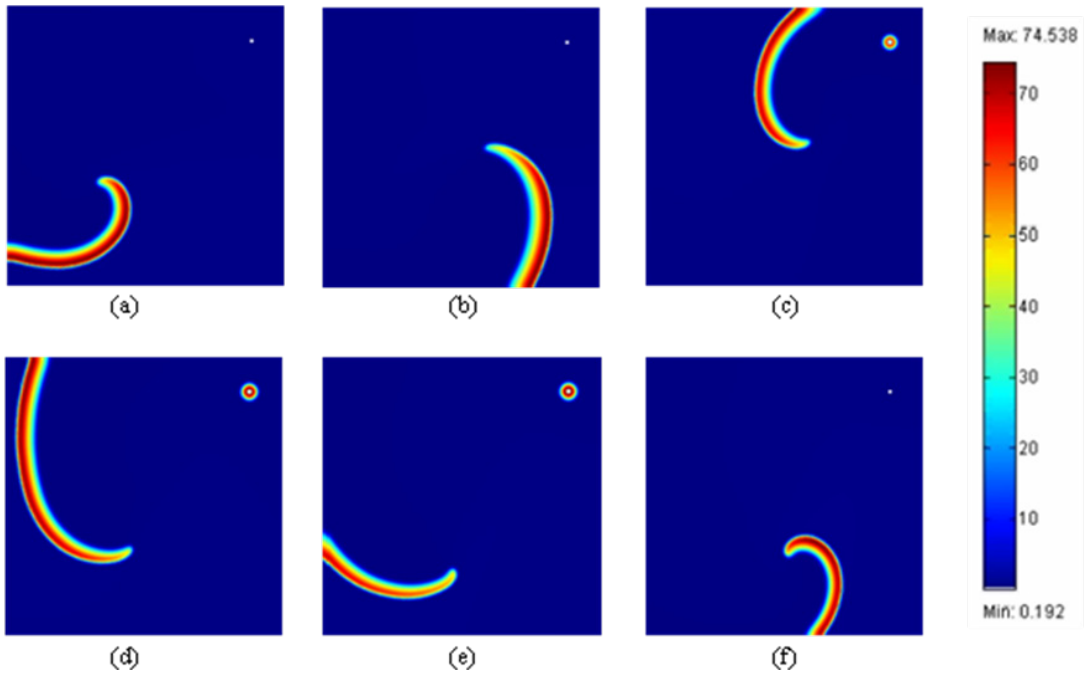

Figure 91: Temperature distribution associated with spiral arm rotating counter-clockwise. Le = 1, ε = 0.18, κ = 5x10^{-4}, time associated with images (a)-(f) are: 0.051, 0.072, 0.118, 0.140, 0.150, 0.171, respectively. The domain was uniformly meshed with 77110 elements, a maximum element size of 0.06. No flux boundary conditions were applied to the outer boundaries.

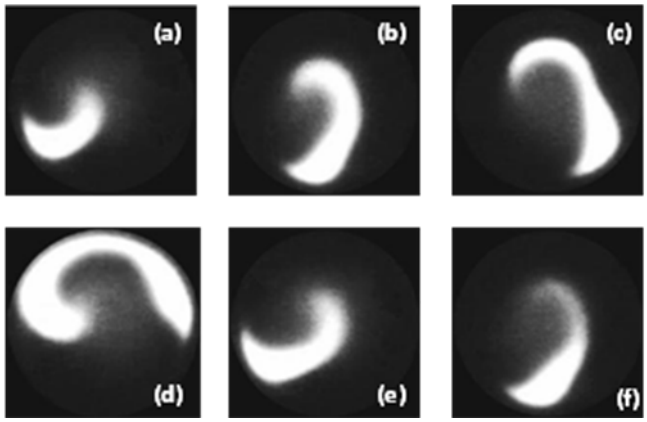

Figure 92: Typical images of spiral flames shown at 1/125sec intervals in CH_4-Oxygen mixtures, Φ = 1.41, Le = 1.024 (Robbins et al., 2004).

Using an image process software (SPOTLIGHT 8.0) developed by NASA Glenn Research Center, the trajectory of the spiral wave tip was manually tracked. For the case shown in Figure 91, an 8-petal flower shape trajectory was mapped out and is shown in Figure 93. Units for the x position and y positions are pixels based on the image's position in SPOTLIGHT (1 ref length ≈ 57 pixels). This trajectory resembles a hypocycloid motion which was observed in the form of a 6-petal flower shape trajectory observed by Robbins and coworkers shown in Figure 94 (Robbins et al., 2004).

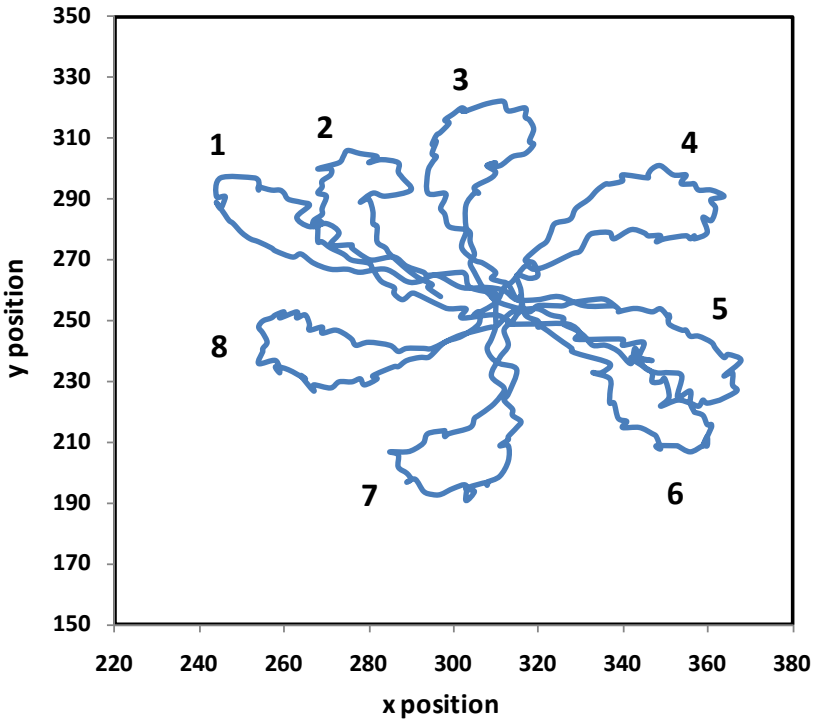

Figure 93: Meandering tip trajectory of the spiral arm predicted and shown in Figure 91.

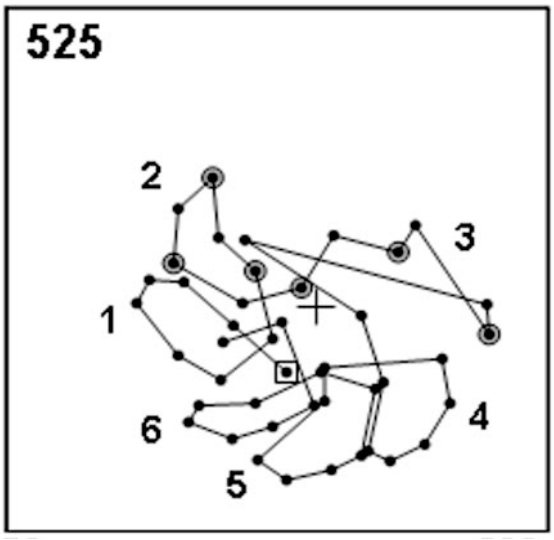

Figure 94: Experimental observations of meandering tip trajectory of spiral flames (Robbins et al., 2004).

4.4.2 On Spatio-temporal Characteristics of Rotating Spiral Waves using Matkowsky's Model

To explore the characteristics of spiral waves and the roles of different parameters such as Le, heat loss (*h*), Ze and σ, the Matkowsky's model and their parameter ranges which are more realistic of combustion conditions were adopted in this study (Panfilov et al., 2003).

A 30 x 30 numerical square domain was meshed with 22048 elements in total. The value for N and σ were fixed, e.g. N=4.5 and $\sigma = 0.2$, so that Z = N (1-σ) = 3.6. The values for Le and h varied in the range of $Le \in [1, 7]$ and $h \in [0, 20]$ because it is reported that Le was in the range of $[1, 7]$ in the experiments that showed the spiral flame patterns (Jomaas et al., 2007; Ma and Pearlman, 2007; Pearlman, 1997; Pearlman and Ronney, 1994b; Pearlman and Ronney, 1994a).

The coupled energy and species equations were solved in a 2D domain using the direct solver (UMFPACK). The relative tolerances for temperature and concentration were 0.001 and the maximum backwards differentiation order was five. The whole domain was set at initial conditions corresponding to the homogeneous solutions and then a 1D temperature pulse was introduced in the upper half domain, localized at x = L/2 from y = [L/2, L], here L is the domain length. A rotating spiral wave was developed and was the steady solution of the coupled equations. The temperature and concentration distribution are shown in Figure 95. The patterns were reminiscent to those observed in the downwardly propagating flames using lean n-C_8H_{18}-21%O_2 diluted by Helium mixtures shown in Figure 96 except the numerical predictions are propagating counter clockwise and the experimental spirals were rotating clockwise.

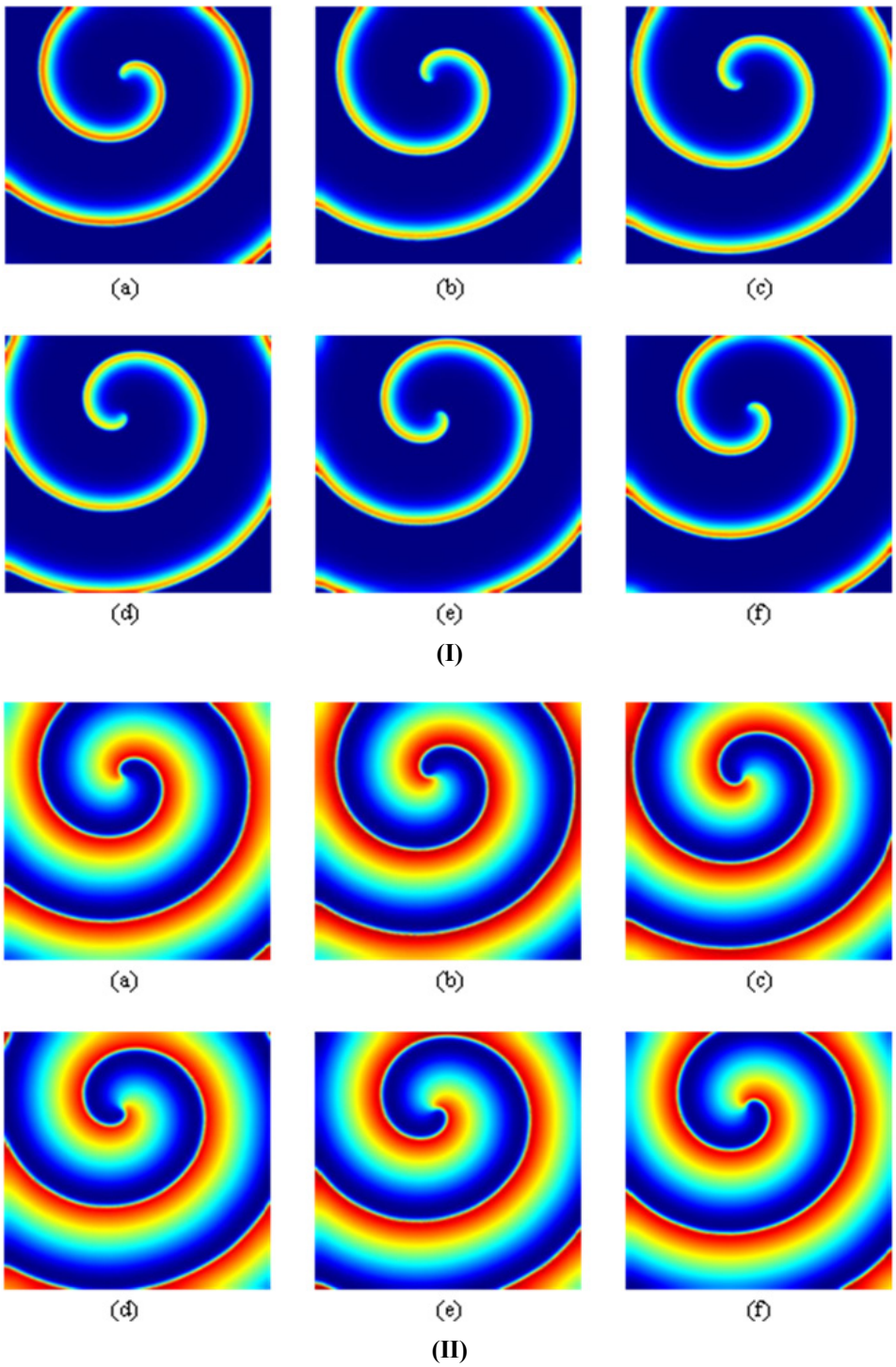

Figure 95: Rotating spiral waves with Le=3, h=12, Z=3.6, σ=0.2. (I): temperature distribution; (II): concentration distribution; time associated with images (a)-(e) are: 19.0, 19.2, 19.4, 19.6, 19.8, 20, respectively.

Figure 96: Experimental observations of spiral wave rotating counter-clockwise in flame front using 0.8%C_8H_{18}-21%O_2-He. Images taken at 1/500s of flame front propagating downward into reactant gas in a tube with i.d. = 28.5 cm.

Using Spotlight 8.0, the trajectory of the spiral tip was manually tracked for the case of Le=3, h=12, Z=3.6, σ=0.2. A clockwise periodic trajectory is obtained and shown in Figure 97.

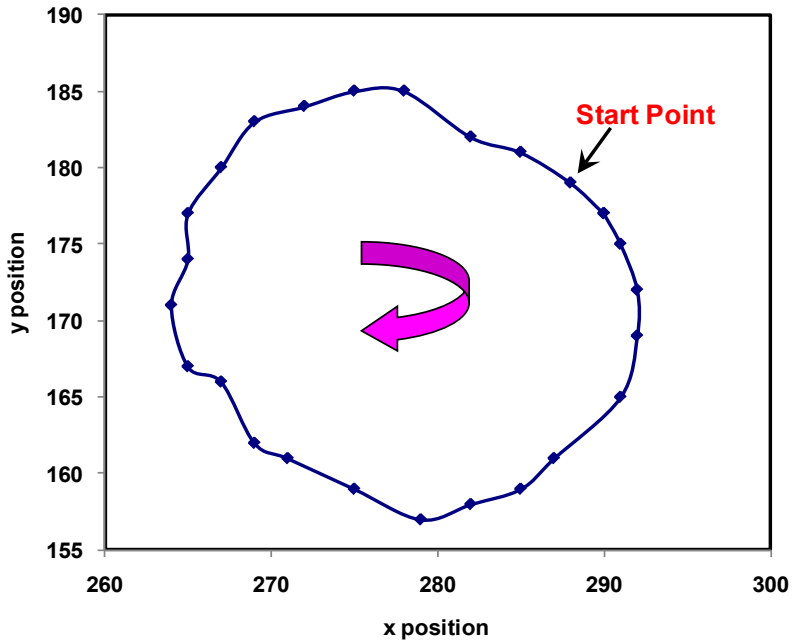

Figure 97: Periodic tip trajectory of the counterclockwise rotating spiral wave for the case shown in Figure 95 while Le=3, h=12, Z=3.6, σ=0.2.

Figure 98 shows the temperature profile at one spiral tip position varying with time from 0 to 10s. As the time between two peak temperatures is known, the approximate rotation time for one spiral wave revolution was about 1.2 ($\exp(N)/\tilde{k}$) in this case, the spiral rotation frequency can be estimated as the inverse of the time for one rotation revolution.

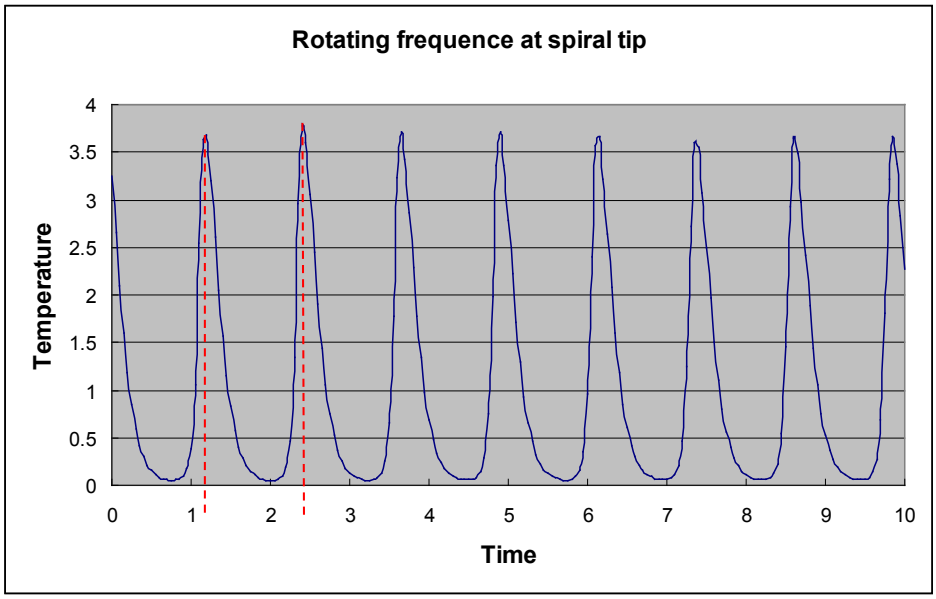

Figure 98: Rotation rate of the spiral wave for Le=3, h=12, Z=3.6, σ=0.2.

At t = 19.4s, the temperature profile was plotted at x = 13 for y from 0 to 30 to define the wave length of the spiral wave (the distance between the two adjacent spiral windings). The temperature distribution is shown in the Figure 99. As seen, the wavelength of the spiral wave was approximately about 9.7 ($\sqrt{\tilde{\kappa}\exp(N)/(\tilde{k}\tilde{\rho}\tilde{c})}$).

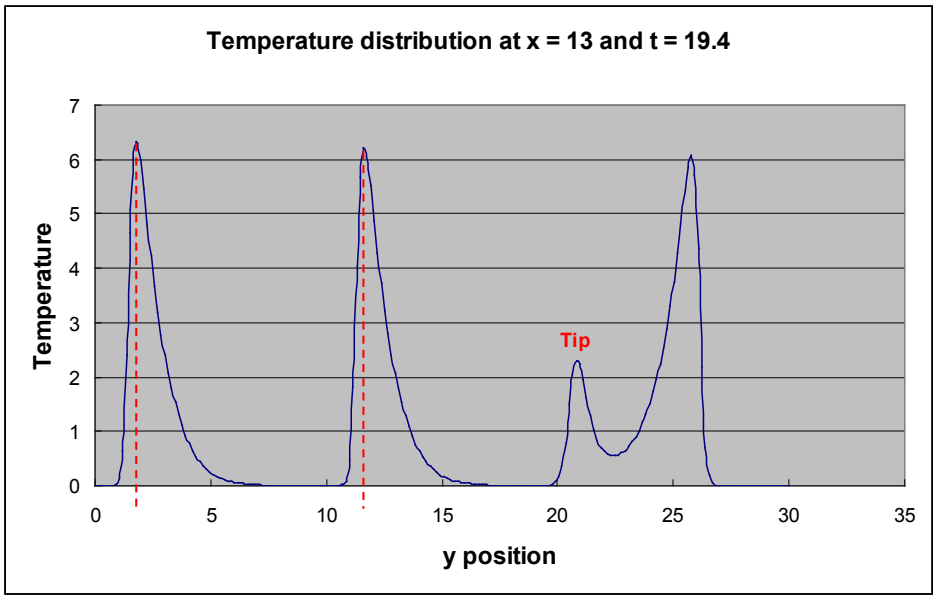

Figure 99: Separation distance between two consecutive windings of the spiral wave (wavelength λ) for Le=3, h=12, Z=3.6, σ=0.2.

4.4.3 Effect of Le and Heat Loss on Spiral Waves

The spiral waves for different Le numbers showed similar spatio-temporal patterns but different characteristic wavelength and rotation frequency. In Table 19, four typical cases are listed showing the spiral wave patterns' characteristic parameters varying with different Le number when heat loss and Zel'dovich number were kept constants. The method shown in Figure 98 and Figure 99 was used here to estimate the wavelength (separation distance between two consecutive windings) and the rotation frequency. Here the unit for wave length is the reference length $\sqrt{\tilde{\kappa}\exp(N)/(\tilde{k}\tilde{\rho}\tilde{c})}$ and the unit for rotation rate is the inverse of reference time $\exp(N)/\tilde{k}$.

Table 19: Effect of Le on the rotating spiral waves using Matkowsky's model, h = 8, Ze = 3.6, σ =0.2.

Le	Pattern	Separation distance (ref length)	Rotation rate (inverse of ref time)
1	Spiral wave	12.2	0.519
3	Spiral wave	11.2	0.625
5	Spiral wave	10.7	0.645
7	Spiral wave	10.3	0.667

As seen in Table 19, increasing Le decreases the wavelength and increases the rotation frequency of the spiral wave. When the heat loss is sufficiently large (in this case, h=8), flame will be instable and spiral waves will be formed when Le = 1.

Similarly, the role of heat loss on the spiral patterns was studied for Le was equal to 3 and the results are listed in Table 20. As seen in Table 20, increasing heat loss decreases the wavelength of the spiral and increases the rotation frequency. The tip trajectory became from simply periodic to meandering motions which means that increasing heat loss increases the complexity of the rotating spiral patterns (Panfilov et al., 2003). For Le = 3, there were no spiral patterns predicted when heat loss was smaller than 5. The results showed that heat loss has the destabilizing effects on the flame patterns.

Table 20: Effect of heat loss on the rotating spiral waves using Matkowsky's model, Le = 3, Ze = 3.6 and σ = 0.2.

h	Patterns	Separation distance (ref length)	Rotation rate (inverse of ref time)
0	No wave propagation	N/A	N/A
0.5	No wave propagation	N/A	N/A
2	Weak wave propagation followed by extinction	N/A	N/A
5	3 split spiral waves	N/A	0.447
8	Spiral wave	11.2	0.625
12	Spiral wave	9.7	0.800
15	Spiral wave	9.5	0.914
20	Spiral wave	8.8	0.952

A new spiral pattern, a 3 split rotating spiral wave, was observed for Le = 3, h = 5 and Ze = 3.6. A sequence of images of the temperature distribution for the 3 split spiral waves is shown in Figure 100. It is noted that no reminiscent experimental observations were made previously.

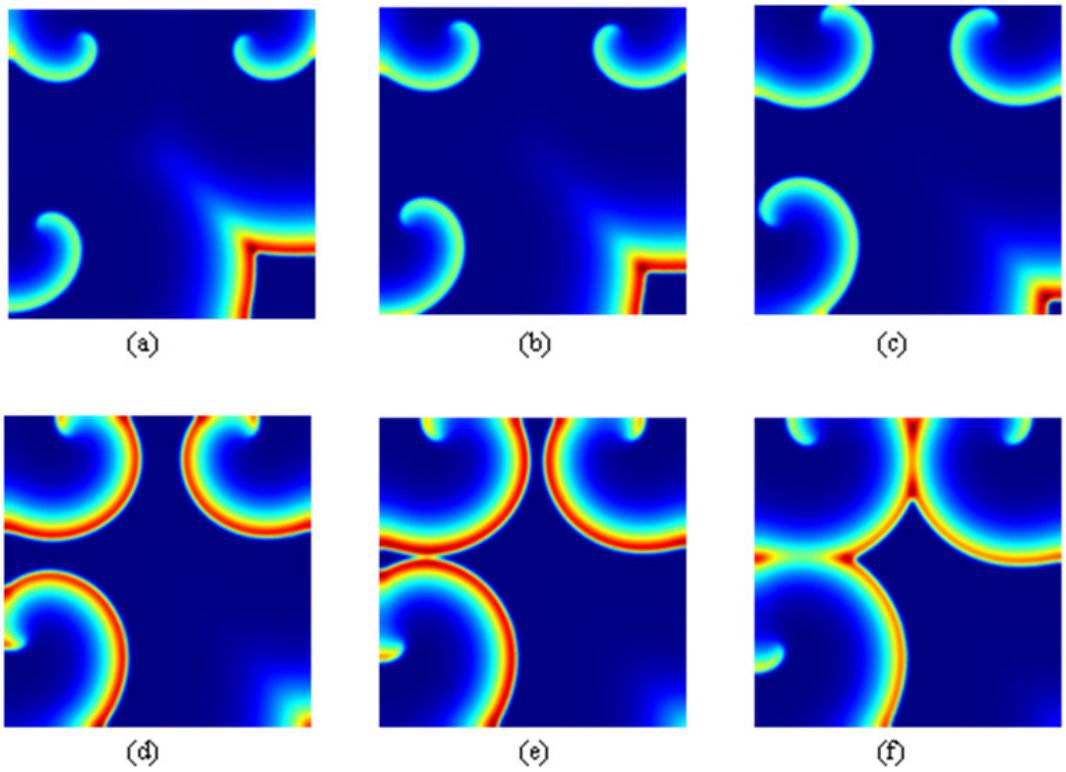

Figure 100: Temperature distribution of multiple rotating spiral waves with Le=3, h=5, Z=3.6, σ=0.2, time associated with images (a)-(e) are: 11.3, 11.5, 11.8, 12.1, 12.3, 12.5, respectively.

Qualitatively comparing the present numerical results with the previous non-adiabatic theoretical stability domains, it has found that when Le = 3, the reduced Le, $\ell = \beta$ (Le-1) = 7.6, the flame is predicted to be stable for a certain range of heat loss and become unstable as the heat loss increases. Specifically in our numerical result, the flame with Le = 3 was stable while the heat loss was smaller than 5 and then started to evolve to instable spiral waves after the value of the heat loss was around 5 (non-dimensional value). The qualitative comparison is shown in Figure 101. The position marked by the cross represents the case of Le = 3, h = 5 and Ze (or β) = 3.6.

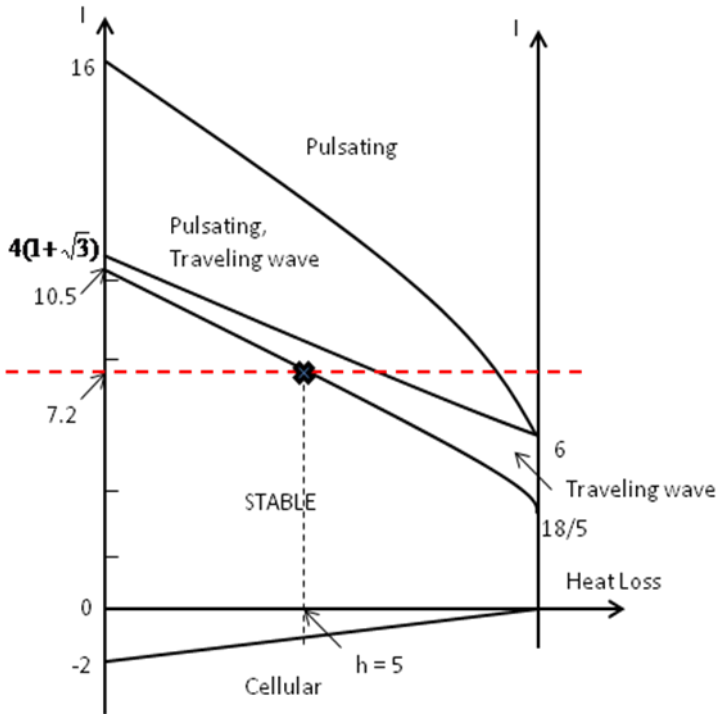

Figure 101: Qualitative comparison of numerical simulations with previous nonadiabatic theoretical predictions by Joulin and Clavin (Joulin and Clavin, 1979).

The sensitivity of spiral patterns depending on Le and heat loss is defined by how rapid the spiral wavelength (separation distance between two adjacent windings) varies with the change of Le or h and how rapid the rotation frequency changes with Le and heat loss separately. In Figure 102, the separation distance changed much faster with the heat loss than Le number because of the bigger slope of the straight line got from simulation. In Figure 103, similarly the rotation rate changes are more sensitive to the changes of heat loss than to that of Le. It is concluded that the dynamic characteristics of spiral waves are more sensitive to heat loss than to Le.

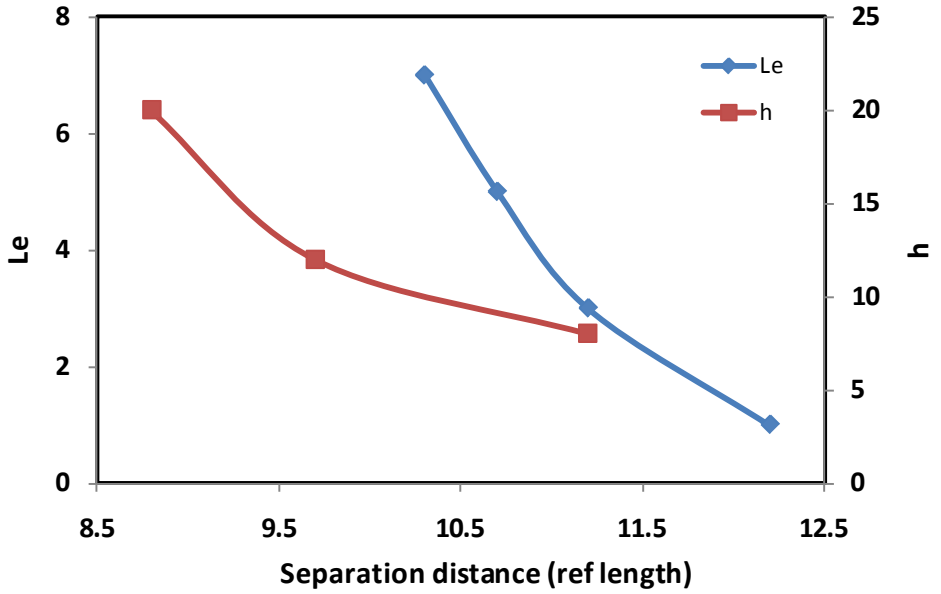

Figure 102: Sensitivity of separation distance on Le and h.

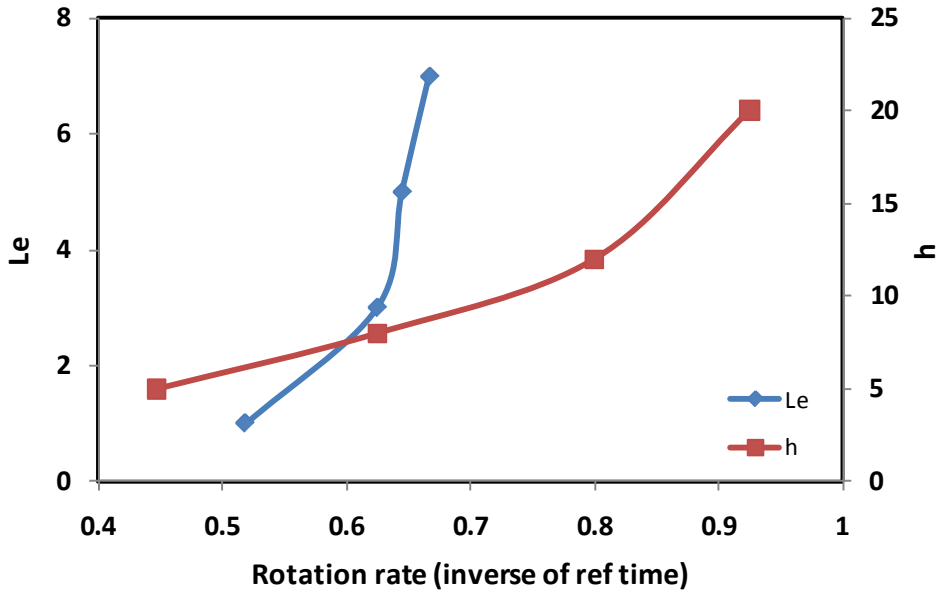

Figure 103: Sensitivity of rotation rate on Le and h.

4.5 Comparison between Numerical Predictions and Experimental Results

The 2-step Sal'nikov model successfully predicted the circularly propagating target patterns and rotating spiral waves in the premixed combustion system using two different nondimensionalizations. To compare the numerical simulations with the previous experimental observations, the effects of Le and heat loss on the target patterns and spiral waves were examined both experimentally and numerically. For target patterns, the effects of Le on the pattern dynamics from the experimental results listed in Table 13. It shows that as the Le increases, the oscillation frequency of the target pattern increases and the radial propagation flame speed increases. Numerical results about the effect of Le on the target patterns is listed in Table 17 and it also shows that as Le increases, both of the oscillation frequency and the radial flame speed increase, which shows the good consistence with the experimental observation qualitatively. The effects of the heat loss on the target patterns are explained in Table 6, Table 7 and Figure 47, as the total exit flow speed of the burner increased, the heat loss increased which led to increasing oscillation frequency and increasing radial flame speed for both cooling water on and off cases. Correspondingly, the numerical results listed in Table 18 also show that increasing heat loss increases oscillation frequency and radial flame speed, which is consistent to the trends observed experimentally as well. For quantitative comparisons, reference time scale is t_{chem} which is extremely large while the system is near the lean flame limit, about 10^{-2} s (t_{chem} is normally 10^{-4} s), and the reference length is $(D_A t_{chem})^{1/2}$ which can be estimated to be equal to $(0.1*10^{-2})^{1/2} \approx 0.032$ cm assuming $D_A = 0.1$ cm^2/s (note, $\alpha = 0.3$ cm^2/s for 21%-He at 300K). The oscillation frequency $\omega = 5.75/t_{chem} = 575$ Hz for Le = 3 which is an order faster than the experimental observations, 63Hz. The radial

propagation flame speed v_f = 41.2*0.032cm/10^{-2}s = 1.32 m/s, which is same order as the experimental results of the radial flame speed on the McKenna burner.

For spiral waves, it is known that the spacing between sequential spiral windings from above analysis is approximately 10 times the thermal reference length given by $\sqrt{\tilde{\kappa}\exp(N)/(\tilde{k}\tilde{\rho}\tilde{c})}$ and the time for one spiral wave revolution is about $1.2\exp(N)/\tilde{k}$. Here $\tilde{k}/\exp(N)$ is the reaction rate, which may be taken to be the inverse of a chemical time t_{chem}. Assuming α= 1cm^2/s (note, α = 0.3 cm^2/s for 21%-He at 300K) and $t_{chem} \sim 10^{-2}$ s, $\sqrt{\tilde{k}/\exp(N)} \sim \sqrt{1/10^{-2}s} \sim 10s^{-0.5}$, such that $10\sqrt{\tilde{\kappa}\exp(N)/(\tilde{k}\tilde{\rho}\tilde{c})} = 10\sqrt{1cm^2/s}/10s^{-0.5}$ = 1cm, which is about the same order of magnitude as the inter-wave spacing observed in our experiments (Ma and Pearlman, 2007). However the spacing observed by Jomaas and co-workers at high pressure was significantly smaller than the results reported in our experiments noting that the thermal thickness scales as 1/P (Jomaas et al., 2007). With respect to the predicted rotation rate ~ $1.2\exp(N)/\tilde{k}$ = 1.2/10^{-2}s = 120 Hz which is same order of magnitude fast as the experimental observations as well.

4.6 Closure

Numerical studies on high-Le number diffusive-thermal instabilities have been conducted based on a two-step Sal'nikov model. The spatio-temporal evolution of the target patterns emitted from one oscillatory pacemaker, two identical oscillatory pacemakers and two different oscillatory pacemakers were predicted based on the model developed by Scott, Wang and Showalter and compared with the experimental

observations. The effects of Le and heat loss on the target patterns were examined and the results showed the same qualitative trends as the experiment. Using a variant of the model developed by Matkowsky and coworkers, rotating spiral patterns were predicted for different Le and heat losses. The rotation frequency and the separation distance of the spiral waves predicted by the model were compared with the experimental observations and were in qualitative agreement.

5. Summary, Conclusions, and Recommendations

This study has succeeded in experimentally observing target patterns and spiral waves in burner-stabilized premixed flames for a variety of heavy hydrocarbon fuel mixtures with high-Le under various ambient pressures (250 ~ 1000 Torr). Several unique flame instability patterns were observed for the first time, such as multiple rotating spiral arms and co-existing bi-stable states of spiral and target waves. The pulsating instabilities are consistent with the theoretical predictions by diffusive-thermal pulsating models. Furthermore, the stability maps for heavy alkanes with air and 21%O_2-balance He premixture were obtained for the first time as a function of equivalence ratio and flow speed. Numerically a two-step Sal'nikov 2D model has been adopted and succeeded in simulating both target patterns and rotating spiral waves. It was also used to quantify the role of Le, Ze and heat loss to the burner on the observed patterns. The comparison between the experiments and numerical simulations qualitatively agree.

5.1 Summary of the Experimental Studies on High-Le Flame Instabilities

An investigation of high-Le flame instabilities in n-C_4H_{10}, n-C_7H_{16} and n-C_8H_{18} premixed with air or 21%O_2-balance He over a range of equivalence ratios, total mixture flow speeds and pressures was completed using porous-plug McKenna burners. Specifically, a standard stainless-steel McKenna burner and a low pressure bronze McKenna burner were used to investigate the effects of heat loss on high-Le instabilities.

For lean n-C_4H_{10}-air premixtures, the Le was around 2.3 so that the reduced Le (ℓ) for typical combustion ranges from 6.5 ~ 10.4 which is less than the critical value

necessary for the onset of the instabilities. Consequently, no evidence of spiral waves was observed at the equivalence ratios and burner exit flow speeds considered. Only irregular and distorted pulsations were observed because the conduction heat loss to the burner destabilized the flame. For both n-C_7H_{16}-air and n-C_8H_{18}-air premixtures, complex target patterns and regular target patterns were observed.

For lean n-C_4H_{10}-21%O_2-balance He, the Le was 3.2 so that the reduced Le (ℓ) is larger (estimated to be 11 ~ 17) than the critical value for the onset of the instabilities. Using the stainless-steel burner, five instability flame patterns were observed including: irregular pulsating flame, multiple rotating spiral arms, complex co-existing spiral-target flame, spiral flame and target patterns. The stability diagram for the stainless-steel McKenna burner was developed as a function of equivalence ratio and burner exit flow speed. In order of decreasing concentration, the flame patterns transitioned from a stable to a complex instability pattern, then to a spiral and finally to a target pattern prior to extinction at the lean flammability limit. Instabilities were observed in near-limit mixtures with a shift towards leaner mixtures at higher flow speeds.

Similarly, complex target patterns and target patterns were observed for the bronze McKenna burner. As the exit flow speed increased for fixed equivalence ratio, the instabilities transitioned from complex target patterns to target patterns and then back to complex target patterns again at relatively high exit flow speeds (~ 10 cm/s). Only one case of a rotating spiral wave was observed using the bronze McKenna burner in n-Butane-21%O_2-balance He premixtures. The stability diagram for the modes on the bronze burner was similar to that associated with the stainless-steel burner, but several key differences were observed. First, no multi-arm rotating spiral waves were observed

and only a singular test case that manifests the rotating spiral wave was observed. Second, the primary mode was radial pulsations/ target patterns, in contrast to the complex rotating spiral waves or bi-stable spiral and radial pulsations/ target patterns observed on the stainless-steel burner. Third, the target patterns observed using the bronze burner were axisymmetric and originated from the center of the burner, while the target patterns observed on the stainless-steel burner often originated off center.

The oscillation frequency for both spiral waves and target patterns for two burners range from 40 to 70 Hz. The larger the exit flow speed, the higher frequency the rotation rate and oscillation frequency is. Heat loss estimation using the measurement of the cooling water temperature in and out of the burner shows that the higher the flow speed, the more heat loss was, which means that increased heat loss has a destabilizing effect on the premixed combustion. Correspondingly, the travelling speed of the target patterns for lean n-Butane-21%O_2-balance He range from 2.45 ~ 4.61 m/s which are 10 times faster than the laminar flame speed.

For both n-C_7H_{16}-21%O_2-balance He and n-C_8H_{18}-21%O_2-balance He premixture, rotating spiral waves, complex target patterns and target patterns were observed. The oscillation frequency for a typical n-C_7H_{16}-O_2-balance He target pattern was 67 Hz and 71 Hz for a typical n-C_8H_{18}-O_2-balance He target pattern, both of which were slightly faster than that observed for a typical n-C_4H_{10}-O_2-balance He target pattern at the same exit flow speed. This result suggests that the oscillation frequency of the instability is a function of Le and increases with increasing Le. Correspondingly, the travelling speed of the target wave for n-C_7H_{16}-O_2-balance He was 2.94 m/s and 3.75 m/s for a n-C_8H_{18}-O_2-

balance He wave, which was only slightly faster than that observed for an n-C_4H_{10}-O_2-balance He target wave.

Effects of pressure were also studied on the flame instability in n-C_4H_{10}-21%O_2-balance He premixtures using the bronze McKenna burner. Decreasing pressure was observed to have a stabilizing effect on the flame. Specifically, as the pressure decreased, well-defined axisymmetric target patterns were observed to transition to complex target patterns then to radial pulsations and eventually to stable planar flames for a given equivalence ratio and exit flow speed.

5.2 Summary of the Numerical Studies on High Le Flame Instabilities

A simple two-step Sal'nikov skeletal model was used to explore the effects of Le and heat loss on the premixed flame instabilities. This diffusive-thermal model was previously developed by Scott and co-workers and also refined by Panfilov and co-workers to predict target and spiral wave patterns.

In particular, the effects of Le and heat loss on the target patterns were studied using the Scott-Wang-Showalter version of Sal'nikov model {Scott, 1997 #18} in addition to the interaction between two radially-propagating flame fronts that originated from two identical pacemaker sites. The simulations captured the development, interaction and merging of wavelets which was qualitatively consistent with the experimental observations of complex target patterns with multiple pacemakers. Nonaxisymmetric and distorted flame fronts were also numerically predicted using two slightly different pacemaker sites and showed some qualitative similarities with the experimental observations.

Rotating spiral arms were also simulated using the Scott-Wang-Showalter model on a 2D square domain initiated by a temperature perturbation in the upper half of the domain. Similar to the numerical simulations reported by Panfilov and co-workers, the spiral wave tip was tracked and observed to show an 8-petal flower shape meandering trajectory for certain cases. A similar meandering behavior was also reported by Gorman and co-workers in methane-oxygen premixed flames on a porous-plug McKenna burner.

Additional numerical simulations of rotating spiral flames were also conducted using Panfilov and Matkowsky's slightly modified form of the Sal'nikov model and adjusted parameters. The effects of Le and heat loss on the spiral patterns were then systematically investigated. The simulations showed that as the Le increases, the separation distance between two consecutive windings decreased and the rotation rate of the spiral wave increased. Furthermore, the numerical simulations showed that when the heat loss was sufficiently large, premixed flames became unstable and spiral waves developed for Le = 1. This phenomenon was experimentally verified during this study. As heat loss increases, the separation distance of the spiral wave decreased and the rotation rate increased. Interestingly, the tip trajectory transitioned from simply periodic to meandering motions, which suggests that increasing heat loss has a destabilizing effect on the flame patterns and increases the complexity of the rotating spiral waves.

5.3 Summary of the Comparison between Experimental and Numerical Results on High-Le Flame Instabilities

Both experimental observations and numerical simulations showed that as the Le and heat loss increase, the flame became increasingly unstable. In particular, the oscillation

frequency and the radial flame speed increased (target pattern cases) and the rotation rate (for spiral wave cases) increased while the distance between two adjacent spiral windings decreased. While quantitative comparison cannot be expected between the experiments and simulations due to many assumptions in the model (i.e., 2D, constant density, 2-step chemistry, etc.), the trends are consistent with those observed in the experiments.

5.4 Recommendations for Future Work

The research outlined in this dissertation will contribute to improving our understanding of high-Le flame instabilities in premixed combustion and will provide experimental data on burner-stabilized flames for more detailed model validation. In particular, the effects of Le, heat loss, mixture composition and pressure on the flame dynamics have been explored. Some recommendations for future work in the area of high-Le flame instabilities include:

1. Quantification of the temperature and species profiles associated with the flame patterns are needed. Perhaps, fine-wire thermocouples mounted in an array in a plane adjacent to the burner surface could be performed along with optical species concentration measurements for select species. Since the frequency of the instabilities is in the range of 60-100 Hz, fine-wire thermocouples (0.025 mm diameter wire or smaller) can be used as their response time should be sufficiently short to capture the high frequency fluctuations. Note that a response time of 0.05 s in still air and 0.004 s with forced flow is reported for Type-K thermocouples taken from the Omega Temperature Handbook. Care should also be taken to suppress catalytic surface reactions by coating the thermocouples, yet this may adversely affect the response times. Consideration

should also be given to prior thermocouple rake designs used in flat-flame burner studies (Cundy and Morse, 1986; Ahuja and Miller, 1993). In addition, the burner exit velocity of the reactant gas mixture above the burner surface should also be measured and quantified using a hot-wire anemometer or particle imaging velocimetry. It is important to characterize the uniformity of the flow field and quantify how the uniformity may influence the flame patterns.

2. Self-excited acoustic waves often accompanied these flame instabilities at lean conditions and are common in near-limit, lean combustion systems (Gonzalez, 1996; Peracchio and Proscia, 1999). These cannot be predicted from the constant density models considered in this work. Here it is noted that the audible frequency appeared to increase as the equivalence ratio decreased. As such, the rotating spiral waves that occurred in slightly richer premixtures were accompanied by a lower frequency than the target patterns. Acoustic effects have also been studied in other burner-stabilized premixed flames (Schreel et al., 2002) and the mechanism responsible is due to the coupling of the heat release from the flame and the pressure waves generated and reflected from the burner surface. Future studies can explore such flame-acoustic couplings to understand the mechanisms that enable the amplification of the pressure waves.

3. To reduce the conductive heat loss, a high-temperature downstream boundary condition can be established by perhaps using two counter-propagating premixed flames in a stagnation flow geometry as shown in Figure 104. In this case, the flammability limits are expected to be broadened and perhaps enable a wider range of parameters that can be accessed to study these instabilities. Alternatively, heat loss can be varied by

controlling the cooling water temperature such that the role of heat loss on the flame patterns can be quantified.

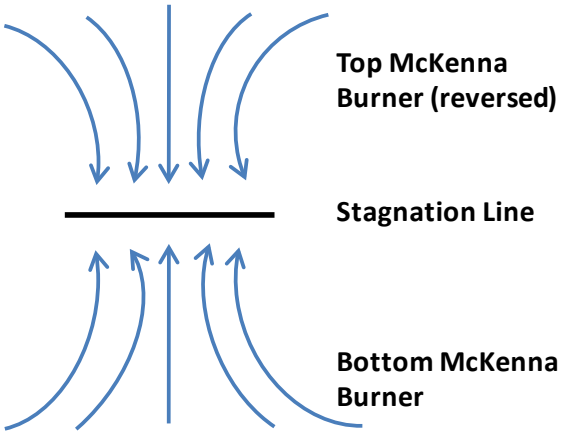

Figure 104: Stagnation flame plane created by two McKenna burners.

4. Investigate rich hydrogen-air mixtures using the McKenna burner at various pressures. As noted in the literature review, spiral waves were observed on the surface of spherically expanding hydrogen flames at elevated pressures (Jomaas et al., 2007). Although no instability was observed for pressure under 5 atm in their studies, it would be interesting to conduct the hydrogen-air mixture using the McKenna burner at variable pressure. A new variable pressure chamber will be needed to allow operation up to 5 atm. Furthermore, hydrogen flames only radiate in the ultraviolet and infrared regions so a new visualization system will be needed, such as a schlieren/shadowgraph or a narrowband high-speed camera that is sensitive in the UV and/or IR to capture OH* and/or H_2O.

5. Yuan and coworkers derived a fully compressible model to investigate the combined effects of hydrodynamic and diffusive-thermal instabilities on the formation of the cellular flames (Yuan, 2006). This model may be extended to simulate the high-Le flame instabilities reported herein.

List of References

Ahn, J., Eastwood, C., Sitzki, L., Ronney, P. D. (2005). Gas-phase and catalytic combustion in heat-recirculating burners. *Proc. Combust. Inst., 30*, 2463-2472.

Ahuja, S. and Miller, D. L. (1993). Design of a constant tension thermocouple rake suitable for flame studies. *Rev. Sci. Instrum., 64*(5), 1358-1359.

Atwood, P., McNicol, B. and Short, R. (1980). The electrocatalytic oxidation of methanol in acid electrolyte: preparation and characterization of noble metal electrocatalysts supported on pre-treated carbon-fibre papers. *J. Applied Electrochemistry, 10*, 213-222.

Barenblatt, G. I., Zeldovich, Y. B. and Istratov, A. G. (1962). On diffusional-thermal stability of a laminar flame. *Zh. Prikl. Mekh. Tekh. Fiz., 4*, 21-26.

Buckmaster, J. (1982). Instability of the porous plug burner flame. *SIAM J. Appl. Math., 43*, 1335.

Bui, P., Vlachos, D. and Westmoreland, P. (1997). Catalytic ignition of methane/oxygen mixtures over platinum surfaces: Comparison Of detailed simulations and experiments. *Surface Science, 385*, 1029-1034.

Carrette, L., Friedrich, K. and Stimming, U. (2001). Fuel cells - fundamentals and applications. *Fuel Cells, 1*(1), 5-39.

Cho, P. and Law, C. K. (1986). Catalytic Ignition of Fuel/Oxygen/Nitrogen Mixtures Over Platinum. *Combustion and Flame, 66*, 159-170.

Clavin, P. and Williams, F. A. (1982). Effects of molecular diffusion and of thermal expansion on the structure and dynamics of premixed flames in turbulent flows of large scale and low intensity. *J. Fluid Mech., 116*, 251-282.

Cortie, M. B. and Van der Lingen, E. (2002). Catalytic gold nano-particles. *Materials Forum, 26*, 1-14.

Cundy, V. A. and Morse, J. S. (1986). Constant-tension thermocouple rake suitable for use in flame mode combustion studies. *Rev. Sci. Instrum., 57*(6), 1209-1210.

Darrieus, G. (1938). Propagation d un front de flame. 6th Int. Congr. Appl. Mech. Paris, France.

Davidenko, J. M., Pertsov, A. V., Salomonsz, R., Baxter, W. and Jalife, J. (1992). Stationary and drifting spiral waves of excitation in isolated cardiac muscle. *Nature, 355*, 349-351.

Denet, B. and Haldenwang, P. (1992). Numerical study of thermal-diffusive instability of premixed flames. *Combust. Science and Technology, 86*, 199-221.

Deutschmann, O., Maier, L., Riedel, U., Stroemman, A. and Dibble, R. (2000). Hydrogen asssisted catalytic combustion of methane on platinum. *Catalysis Today, 59*, 141-150.

Dowdy, D. R., Smith, D. B. and Taylor, S. C. (1990). The use of expanding spherical flames to determine burning velocities and stretch effects in hydrogen/air mixtures. *Proc. Combust. Instit., 23*.

Egolfopoulos, F., Du, D. and Law, C. K. (1992). A comprehensive study of methanol kinetics in freely-propagating and burner-stabilized flames, flow and static reactors, and shock tubes. *Combust. Sci. and Tech., 83*(1), 33-75.

el-Hamdi, M. and Gorman, M. (1993). Deterministic chaos in laminar premixed flames: Experimental classification of chaotic dynamics. *Combust. Sci. and Tech., 94*, 87-101.

Epstein, I. R. and Pojman, J. A. (1998). *Introduction to Nonlinear Chemical Dynamics, Oscillations, Waves, Patterns and Chaos*. New York: Oxford University Press.

Frankel, M. L. and Sivashinsky, G. I. (1982). The effect of viscosity on hydrodynamic stability of a plane flame front. *Combust. Sci. and Tech., 29*, 207-224.

Ganaathisubramanian, N. and Showalter, K. (1984). Washout effects in pumped tank reactors. *J. Am. Chem. Soc., 106*, 816-817.

Gloaguen, F., Leger, J. and Lamy, C. (1997). Electrocatalytic oxidation of methanol on platinum nanoparticles electrodeposited onto porous carbon substrates. *Journal of Applied Electrochemistry, 27*, 1052 - 1060.

Gololobov, I. M., Granovskii, E. A. and Gostinstev, Y. A. (1981). Two combustion modes at the limit of luminous flame propagation. *Combustion, Explosion and Shock Waves, 17*, 22.

Gonzalez, M. (1996). Acoustic instability of a premixed flame propagating in a tube. *Combustion and Flame, 107*(3), 245-259.

Gorman, M., el-Hamdi, M. and Robbins, K. A. (1994a). Experimental observation of ordered states of cellular flames. *Combust. Sci. and Tech., 98*, 37-45.

Gorman, M., el-Hamdi, M. and Robbins, K. A. (1994b). Four types of chaotic dynamics in cellular flames. *Combust. Sci. and Tech., 98*, 79-93.

Groff, E. G. (1982). The cellular nature of confined spherical propane-air flames. *Combustion and Flame, 48*, 51-62.

Hamnett, A. (1997). Mechanism and electrocatalysis in the direct methanol fuel cell. *Catalysis Today, 38*, 445-457.

Hayes, R. and Kolaczkowski, S. (1998). *Introduction to Catalytic Combustion*: CRC Press.

Held, T. and Dryer, F. (1998). A comprehensive mechanism for methanol oxidation. *International Journal of Chemical Kinetics, 30*(11), 805-830.

Holladay, J., Jones, E., Phelps, M. and Hu, J. (2002). Microfuel processor for use in a miniature power supply. *Journal of Power Sources, 108*, 21-27.

Hu, Z., Boiadjiev, V. and Thundat, T. (2005). Nano-catalytic spontaneous ignition and selfsupporting room-temperature combustion. *Energy and Fuels, 19*, 855-858.

Hu, Z. and Thundat, V. (2006). Nanoscale energy conversion by using nano-catalytic particles. Proc. of 2006 ASME Power Conf. PWR2006**:** 545-550.

Istrov, A. G. and Librovich, V. B. (1966). *Prikl. Mat. Mekh., 30*, 451-466.

John Zink, C. (1991). *Innovations of Catalytic Combustion.* Paper presented at the AFRC/JFRC Jointly Sponsored International Symposium on Environmental Control of Combustion Processes Honolulu, Hawaii.

Jomaas, G., Bechtold, J. K. and Law, C. K. (2007). Spiral waves in expanding hydrogen-air flames: experimental and theory. *Proc. Combust. Inst., 31*, 1039-1046.

Joulin, G. and Clavin, P. (1979). Linear stability analysis of nonadiabatic flames: Diffusional-Thermal Model. *Combustion and Flame, 35*, 139-153.

Ju, Y. (1995). Lower-Upper Scheme For Chemically Reacting Flow With Finite Rate Chemistry. *AIAA Journal, 33*(8), 1418-1425.

Kadowaki, S. (1997). Numerical study on lateral movements of cellular flames. *Phys. Rev. E., 56*, 2966-2971.

Kadowaki, S. (1999). The influence of hydrodynamic instability on the structure of cellular flames. *Phys. Fluids, 11*, 3426-3433.

Kadowaki, S. (2000). Numerical study on the formation of cellular premixed flames at high Lewis numbers. *Phys. Fluids, 12*, 2352-2358.

Kim, J., Williams, F. A. and Ronney, P. D. (1996). Diffusional-Thermal instability of diffusion flames. *Journal of Fluid Mechanics, 327*, 273-302.

Kwon, S., Tseng, L. K. and Faeth, G. M. (1992). Laminar burning velocity and transition to unstable flames in $H_2/O_2/N_2$ and $C_3H_8/O_2/N_2$ mixtures. *Combustion and Flame, 90*, 230-246.

Landau, L. D. (1944). On the theory of slow combustion (in Russian). *Zurn. Eksp. Teor. Fiz., 14*, 240.

Lauterbach, J., Haas, G., Rotermund, H. H. and Ertl, G. (1993). A PEEM-investigation of spatio-temporal pattern formation during the CO oxidation on polycrystalline platinum. *Surf. Sci., 294*, 116-130.

Law, C. K. (2006). *Combustion Physics*: Cambridge Univeristy Press.

Law, C. K., Jomass, G. and Bechtold, J. K. (2005). Cellular instabilities of expanding hydrogen/propane spherical flames at elevated pressure: Theory and experiment. *Proc. Combust. Inst., 30*, 159-167.

Lechleiter, J. S., Girard, S., Peralta, E. and Clapham, D. (1991). Spiral calcium wave propagation and annihilation in Xenopus laevis oocytes. *Science, 252*, 123-126.

Leger, J. (2001). Mechanistic aspects of methanol oxidation on platinum-based electrocatalysts. *Journal of Applied Electrochemistry, 31*, 767-771.

Lenhert, D. and Manzello, S. (2008). *Effects of benzene and naphthalene addition on soot inception in a well stirred reactor/plug flow reactor.* Paper presented at the 32nd International Symposium on Combustion, Montreal, Canada.

Lenhert, D. and Manzello, S. (2009). Effects of benzene and naphthalene addition on soot inception in a well stirred reactor/plug flow reactor. *Proc. Combust. Inst., 32*(1), 657-664

Li, J., Kazakov, A., Chaos, M. and Dryer, F. (2007a). A PRF+toluene surrogate fuel model for simulating gasoline kinetics. 5th US Combustion Meeting, Western States Section of the Combustion Institute. San Diego, CA**:** Paper No. E26.

Li, J., Zhao, Z., Kazakov, A., Chaos, M., Dryer, F. and Scire, J. (2007b). A comprehensive kinetic mechanism for CO, CH2O, CH3OH combustion. *International Journal of Chemical Kinetics, 39*(3), 109-136.

Ma, Y. and Pearlman, H. (2005). Two-dimensional modeling studies of pattern formation in premixed gas flames. 4th Joint Meeting of the U.S. Section of the Combustion Institute. Philadelphia, PA**:** Paper No. D11.

Ma, Y. and Pearlman, H. (2007). Rotating spiral waves and target patterns in burner-stabilized premixed gas flames. 5th US Combustion Meeting, Western States Section of the Combustion Institute. San Deigo, CA**:** Paper No. A35.

Margolis, S. B. (1980). Bifurcation phenoena in burner-stabilized premixed flames. *Combust. Sci. and Tech., 22*, 143-169.

Margolis, S. B. (1981). Effects of selective diffusion on the stability of burner stabilized premixed flames. *Proc. Combust. Inst., 18*, 679-693.

Markstein, G. H. (1951). Experimental and theoretical studies of flame front stability. *J. Aeronaut. Sci., 3*, 18.

Markstein, G. H. (1952). Nonisotropic propagation of combustion waves. *J. Chem. Phys., 20*, 1051-1053.

Markstein, G. H. (1964). *Nonsteady Flame Propagation*. New York: Pergamon Press.

Matalon, M. and Matkowsky, B. J. (1982). Flames as gasdynamic discontinuities. *J. Fluid Mech., 124*, 239-259.

Matkowsky, B. J. and Olagunju, D. O. (1981). Pulsations in a burner-stabilized premixed plane flame. *SIAM J. Appl. Math., 40*, 551-562.

Merzhanov, A. G., Filonenko, A. K. and Borovinskaya, I. P. (1973). New phenomena in combustion of condensed systems. *Proc. Acad. Sci. USSR, Phys. Chem. Sect., 208*, 122-125.

Michelson, D. M. and Sivashinsky, G. I. (1977). Nonlinear analysis of hydrodynamic instability in laminar flames. Part II. Numerical experiments. *Acta Astronaut., 4*, 1207-1221.

Migliorini, F., De Iuliis, S., Cignoli, F. and Zizak, G. (2008). How "flat" is the rich premixed flame produced by your McKenna burner? *Combustion and Flame, 153*, 384-393.

Mitani, T. and Williams, F. A. (1980). Studies of cellular flames in hydrogen-oxygen-nitrogen mixtures. *Combust. and Flame, 39*, 169.

Mukerjee, S. (1990). Particle size and structural effects in platinum electrocatalysis. *Journal of Applied Electrochemistry, 20*(4), 537-548.

Nayagam, M., Ikeda, T. and Ishiwata, T. (2001). Three-dimensional numerical simulation of helically propagating combustion waves. *Journal of Material Synthesis and Processing, 9*, 153-163.

Nayagam, V. and Williams, F. A. (2000). Rotating spiral edge flames in von Karman swirling flows. *Physical Review Letters, 84*(3), 479-482.

Nicolis, G. and Progogine, I. (1977). *Self-Organization in Nonequilibrium Systems: From Dissipative Structure to Order through Fluctuations*. New York: John Wiley and Sons.

Norton, T. and Dryer, F. (1992). An experimental and modeling study of ethanol oxidation kinetics in an atmospheric pressure flow reactor. *International Journal of Chemical Kinetics, 24*(4), 319-344.

Nukiyama, S. and Tanasawa, Y. (1938-1940). Mathematical Model for Concentric Nebulizer Systems. *Trans. Soc. Mech. Eng., 4-6*(Reports 1 – 6).

Panfilov, V., Bayliss, A. and Matkowsky, B. J. (2003). Spiral flames. *Applied Mathematics Letters, 16*, 131-135.

Pearlman, H. (1997). Excitability in high-Lewis number premixed gas combustion. *Combustion and Flames, 109*, 392-398.

Pearlman, H. and Ronney, P. (1994a). Near-limit behavior of high Lewis number premixed flames in tubes at normal and low gravity. *Physics of Fluids, 6*(12), 4009-4018.

Pearlman, H. and Ronney, P. (1994b). Self-organized spiral and circular waves in premixed gas flames. *J. Chem. Phys., 101*(3), 2632-2633.

Pelce, P. and Clavin, P. (1982). Influence of hydrodynamics and diffusion upon the stability limits of laminar premixed flames. *Journal of Fluid Mechanics, 124*, 219-237.

Peracchio, A. A. and Proscia, W. M. (1999). Nonlinear Heat-Release/Acoustic Model for Thermoacoustic Instability in Lean Premixed Combustors. *Journal of Engineering for Gas Turbines and Power, 121*(3), 415-421.

Pfefferle, W. and Pfefferle, L. (1986). Catalytically stabilized combustion. *Progress in Energy and Combustion Science, 12*(1), 25-41.

Poling, B. E., Prausnitz, J. M. and O'Connell, J. P. (2001). *Properties of Gases and Liquids (5th Edition)*: McGraw-Hill

Quinard, J., Searby, G. and Boyer, L. (1984). *Lecture Notes in Phys., 210*, 331-341.

Ricciuti, C., Fellon, B., Ma, Y., Miller, T. and Pearlman, H. (2007a). The effect of particle size, morphology, and mass loading on the reactivity of nanocatalytic particles. ASME Proceedings of the 2nd Energy Nanotechnology International Conference. Santa Clara, CA**:** Paper No. ENIC2007-45049.

Ricciuti, C., Fellon, B., Maguire, J., Pearlman, H. and Miller, T. (2007b). Room-temperature catalysis using sub-micron size platinum particles. 5th US Combustion Meeting, Western States Section of the Combustion Institute. San Diego, CA**:** Paper No. D20.

Robbins, K., Gorman, M., Bowers, J. and Brockman, R. (2004). Spiral dynamics of pulsating methane-oxygen flames on a circular burner. *Chaos, 14*(2), 467-476.

Schreel, K. R. A. M., Rook, R. and De Goey, L. P. H. (2002). The acoustic response of burner-stabilized premixed flat flames. *Proceedings of the Combustion Institute, 29*(1), 115-122.

Scott, S. K. (1994). *Oscillations, Waves and Chaos in Chemical Kinetics*: Oxford University Press.

Scott, S. K., Wang, J. and Showalter, K. (1997). Modelling studies of spiral waves and target patterns in premixed flames. *J. Chem. Soc., Faraday Trans., 93*(9), 1733-1739.

Sharpe, G. J. (2003). Linear stability of planar premixed flames: Reactive Navier–Stokes equations with finite activation energy and arbitrary Lewis number *Combust. Theory Modelling, 7*, 45-65.

Siegert, F. and Weijer, C. (1989). Digital image processing of optical density wave propagation in Dictyostelium discoideum and analysis of the effects of caffeine and ammonia. *J. Cell Sci., 93*, 325.

Sivashinsky, G. I. (1977a). Diffusion-thermal theory of cellular flames. *Combust. Sci. and Tech., 15*, 137-146.

Sivashinsky, G. I. (1977b). Non-Linear analysis of hydrodynamic instability in laminar flames. Part I : derivation of basic equations. *Acta Astronaut., 4*, 1177-1206.

Sivashinsky, G. I. (1983). Instabilities, pattern formation, and turbulence in flames. *Ann. Rev. Fluid Mech., 15*, 179-199.

Sivashinsky, G. I. and Matkowsky, B. J. (1981). On stability of nonabiabatic flames. *SIAM J. Appl. Math., 40*, 255-260.

Smithells, A. and Ingle, H. (1892). The structure and chemistry of flames. *J. Chem. Soc., 61*, 204.

Talukdar, A. and Bhattacharyya, K. (2006). *Catalysis in Petroleum and Petrochemical Industries*: Alpha Science International, Ltd.

Tse, S. D. Y., Zhu, D. L. and Law, C. K. (2004). Optically accessible high-pressure combustion apparatus. *Rev. Sci. Instrument 75*, 233-239.

Turns, S. R. (2000). *An Introduction to Combustion*: Mc Graw Hill.

Vantelon, J. P., Pagni, P. A. and Dunsky, C. M. (1986). *Cellular flame strcutures on a cooled porous plug burner.* Paper presented at the Progress in Astronautics and Aeronautics Bowen.

Warnatz, J., Maas, U. and Dibble, R. (2001). *Combustion: Physical and Chemical Fundamentals, Modeling and Simulation, Experiments, Pollutant Formation*. Berlin: Springer-Verlag.

Watanabe, M., Saegusa, S. and Stonebart, P. (1989). Composites nanotubes de carbone. *J. Electroanal. Chem., 271*, 213-220.

Wieckowski, A., Savinova, E. and Vayenas, C. (2003). *Catalysis and Electrocatalysis at Nanoparticle Surfaces*: Marcel Dekker, Inc.

Wilke, C. R. (1950). Diffusional properties of multicomponent gases. *Chemical Engineering Progress, 46*.

Yahikozawa, K., Fujii, Y., Matsuda, Y., Nishimura, K. and Takasu, Y. (1991). Electrocatalytic properties of ultrafine platinum particles for oxidation of methanol and formic acid in aqueous solutions. *Electrochimica Acta, 36*(5-6), 973-978.

Yuan, J. (2006). *A Numerical Study of Coupled Hydrodynamic and Diffusional-Thermal Instabilities in Flame Propagation.* Princeton University, Princeton.

Yuan, J., Ju, Y. G. and Law, C. K. (2006). Pulsating and hydrodynamic instabilities at large Lewis numbers. *Combustion and Flame, 144*(1-2), 386-397.

Zeldovich, Y. B. (1944). *Theory of Combustion and Detonation of Gases*: Acad. Sci. USSR (In Russia).

Zeldovich, Y. B. (1966). An effect that stabilizes the curves front of a laminar flame. *Zh. Prikle. Mekh. Fiz., 1*, 102-104.

Zum Mallen, M. and Schmidt, L. (1996). Oxidation of methanol over polycrystalline Rh and Pt: rates, OH desorption, and model *Journal of Catalysis, 161*, 230-246.

Appendix A: NOMENCLATURE

c_P	Specific heat at constant pressure	$J/mol \cdot K$
D	Mass diffusivity	m^2/s
$D_{rate-\lim iting\ component}$	Mass diffusivity of the rate-limiting component into the mixture	m^2/s
d	Characteristic length of the process	m
$d_{3,2}$	Sauter mean diameter	μm
E	Convective flux vectors in the x direction	
E_v	Viscous flux vectors in the x direction	
E_a	Activation energy	J/mol
F	Convective flux vectors in the y direction	
F_v	Viscous flux vectors in the y direction	
G_r	Grashof number	$\frac{\nabla\rho}{\rho} gd^3 / v^2$
g	Gravitational acceleration	m/s^2
H	Heat loss coefficient	$W/m \cdot K$
h	Nondimensional heat loss	$H \exp(N)/(k\rho c)$
k	Preexponential factor	
k_I, k_{II}	Chemical reaction rate	s^{-1}
Le	Lewis number of the limiting reactant	$\alpha_{mixture} / D_{rate-\lim iting\ component}$
Le_c	Critical Lewis number	1-2/β
l	Markstein Length	m
l_f	Flame thickness	$(\lambda / c_P)/(\rho_u s_{f,u})$
MW	Molecular weight	kg/mol
N	Nondimensional activation energy	E_a / RT_H
n	Wave number	$2\pi/\lambda_v$
P	Pressure	Pa
P_{crit}	Vapor/liquid critical pressure	Pa
p_0	Constant reactant concentration	
Q	Heat release of exothermic reaction	kJ/kg
Q_g	Volume flow rate of gas	cm^3/s
Q_l	Volume flow rate of liquid	cm^3/s
Q_v	Volume flow rate of vapor	cm^3/s
R	Gas constant	$J/(mol \cdot K)$
Re	Reynolds number	ρvD/μ
R_f	Local radius of curvature of the flame	m

$R(t)$	Flame radius at time t	m
Re (ω)	Real part of the perturbation	
S	Vector of the reaction source	
$s_{f,u}$, s_L, s_u^0, s_b^0	Laminar flame speed	m/s
s_n	Local flame speed normal to the flame surface	m/s
t	Time	s
T	Temperature	K
T_a, T_0	Ambient temperature	K
T_b	Temperature of burned mixtures	K
T_{crit}	Vapor/liquid critical temperature	K
T_{ri}	Reduced temperature of the i th component	T / T_{crit}
T_u	Temperature of unburned mixtures	K
T^*	Dimensionless temperature	$kT / (\varepsilon_A \varepsilon_B)^{1/2}$
t_{chem}	Chemical time scale	s
t_N	Heat transfer time scale	s
U	Vector of the conservation variables	
u	Freestream velocity	m/s
V_{exit}	McKenna burner exit flow speed	cm/s
V_f	Radial propagation flame speed	m/s
v	Velocity difference of gas-liquid	m/s
x	Distance in x axis	m
χ_n	species composition	
Y	Non-dimensional species concentration	
y_i	Mole fraction of components i	
Ze	Zel'dovich number	$E_a(T_b - T_u)/RT_b^2$
α	Non-dimensionalized concentration	
$\alpha_{mixture}$	Thermal diffusivity of the mixture	m^2/s
β	Zel'dovich number	$E(T_b - T_u)/RT_b^2$
ε_i	characteristic Lennard-Jones energy	K
κ	Ratio of thermal to chemical time	t_N / t_{chem}
σ	Thermal expansion ratio	ρ_u / ρ_b
σ_A, σ_B	Hard-sphere collision diameters of species A and B	10^{-10}m
ω	Oscillation frequency	Hz
λ	Thermal conductivity	W./(m·K)
λ_i	Thermal conductivity of pure i	W./(m·K)
λ_m	Thermal conductivity of the gas mixture	W./(m·K)

λ_{tr}	Monatomic value of the individual translational thermal conductivity	W./(m·K)
λ_w	Wavelength	m
ϕ	Equivalence ratio	
δ	Mixing ratio	$\frac{5X_{propane}}{\left(0.5X_{hydrogen}+5X_{propane}\right)}$
δ_{st}	Stoichiometric value of δ	
ρ	Total density	kg/m^3
ρ_b	Density of burned mixtures	kg/m^3
ρ_u	Density of unburned mixtures	kg/m^3
θ	Non-dimensional temperature	$E_a\left(T-T_a\right)\Big/RT_a^2$
γ	Surface tension	dyn/cm
η	Liquid viscosity in Poise	dyn·s/cm^2
μ	Initial concentration of the precursor reactant	$\square k_1 t_N \frac{Qp_0}{C_p \square RT_a^2}\frac{E_a}{}$
ν	Kinematic viscosity	m^2/s
Ω_D	Collision integral	
Γ_i	Reduced inverse thermal conductivity of species i	$210\left\{\frac{T_{crit,i}M_i^3}{P_{crit,i}^4}\right\}^{1/6}$
ℓ	Reduced Lewis number	$\beta\left(Le-1\right)$

Appendix B: List of Experimental Conditions and Results

B.1 Flame Patterns in n-Butane-O_2-He Premixtures on a Stainless-Steel McKenna Burner

n-Butane Flow Rate (SLM)	Oxygen Flow Rate (SLM)	Helium Flow Rate (SLM)	Φ	V_{exit} (cm/s)	Patterns	Image
0.285	1.68	6.33	1.10	4.9	Stable planar flame	
0.285	1.76	6.63	1.05	5.1	Stable planar flame	
0.285	1.85	6.97	1.00	5.4	Stable planar flame	
0.285	1.95	7.33	0.95	5.6	Stable planar flame	
0.275	1.68	6.32	1.06	4.9	Stable planar flame	
0.275	1.78	6.69	1.00	5.2	Stable planar flame	
0.275	1.79	6.73	1.00	5.2	Stable planar flame	
0.265	1.72	6.48	1.00	5.0	Stable planar flame	
0.206	1.19	4.50	1.12	3.5	Irregular	
0.170	1.06	3.99	1.04	3.1	Irregular	
0.165	1.06	3.99	1.01	3.1	Irregular	
0.163	1.06	3.99	1.00	3.1	Irregular	
0.158	1.06	3.99	0.97	3.1	Irregular	
0.188	1.27	4.77	0.96	3.7	Irregular	
0.221	1.59	5.99	0.91	4.6	**Two arms**	Figure 27
0.285	2.10	7.90	0.88	6.1	**Complex spiral**	Figure 28
0.254	1.89	7.11	0.87	5.5	Complex spiral	
0.285	2.34	8.78	0.79	6.7	Complex spiral	
0.285	2.34	8.81	0.79	6.7	**Complex spiral**	Figure 29
0.206	1.45	5.44	0.93	4.2	Spiral	
0.221	1.60	6.00	0.90	4.6	Spiral	
0.277	2.10	7.90	0.86	6.1	Spiral	
0.250	1.92	7.23	0.85	5.5	**Spiral**	Figure 30
0.285	**2.20**	**6.60**	0.84	5.4	Spiral	
0.270	2.14	8.06	0.82	6.2	**Spiral**	Figure 31
0.285	2.28	8.57	0.81	6.6	Spiral	
0.285	2.29	8.60	0.81	6.6	Spiral	
0.285	2.38	8.93	0.78	6.8	Spiral	
0.285	**2.45**	**7.00**	0.76	5.7	**Spiral**	Figure 35
0.330	2.88	10.82	0.75	8.3	Spiral	Figure 33
0.243	1.89	7.11	0.84	5.5	Target	
0.265	2.14	8.06	0.80	6.2	**Target**	Figure 32
0.250	2.04	7.69	0.79	5.9	Target	
0.285	2.47	9.31	0.75	7.1	Target	
0.285	2.46	9.25	0.75	7.1	Target	

B.2 Flame Patterns in n-Butane-O_2-He Premixtures on a Bronze McKenna Burner

n-Butane Flow Rate(SLM)	Oxygen Flow Rate (SLM)	Helium Flow Rate (SLM)	Φ	V_{exit} (cm/s)	Patterns
0.43	2.45	9.21	1.14	7.13	Stable planar flame
0.43	2.45	9.21	1.14	7.13	Stable planar flame
0.38	2.25	8.46	1.10	6.54	Stable planar flame
0.455	2.7	10.15	1.10	7.85	stable planar flame
0.37	2.25	8.46	1.07	6.53	Stable planar flame
0.34	2.07	7.78	1.07	6.01	Stable planar flame
0.275	1.68	6.32	1.06	4.88	Stable planar flame
0.285	1.76	6.63	1.05	5.11	Stable planar flame (Figure 40)
0.43	2.68	10.08	1.04	7.77	Stable planar flame
0.393	2.45	9.21	1.04	7.11	Stable planar flame
0.36	2.25	8.46	1.04	6.53	Stable planar flame
0.33	2.07	7.78	1.04	6.00	Stable planar flame
0.39	2.45	9.21	1.03	7.11	Stable planar flame
0.43	2.75	10.34	1.02	7.97	Stable planar flame
0.475	3.1	11.66	1.00	8.98	Stable planar flame
0.52	3.44	12.93	0.98	9.96	Stable planar flame
0.47	3.1	11.66	0.99	8.98	Stable planar flame
0.35	2.25	8.46	1.01	6.52	Complex target
0.38	2.45	9.21	1.01	7.10	Complex target
0.32	2.07	7.78	1.00	6.00	Complex target
0.275	1.78	6.69	1.00	5.16	Complex target
0.37	2.45	9.21	0.98	7.09	complex target
0.31	2.07	7.78	0.97	5.99	Complex target
0.41	2.75	10.34	0.97	7.96	complex target
0.365	2.45	9.21	0.97	7.09	complex target
0.46	3.1	11.66	0.96	8.97	Complex target
0.36	2.45	9.21	0.96	7.09	complex target
0.455	3.1	11.66	0.95	8.97	Complex target
0.275	1.88	7.07	0.95	5.44	Complex target
0.285	1.95	7.33	0.95	5.64	Complex target(Figure 43)
0.51	3.5	13.16	0.95	10.12	Complex target
0.51	3.5	13.16	0.95	10.12	Complex target
0.45	3.1	11.66	0.94	8.96	Complex target
0.275	1.9	7.14	0.94	5.60	Complex target(Figure 44)
0.44	3.1	11.66	0.92	8.96	Complex target
0.43	3.1	11.66	0.90	8.95	Complex target
0.42	2.75	10.34	0.99	7.96	Complex target
0.34	2.25	8.46	0.98	6.51	Complex target
0.357	2.45	9.21	0.95	7.09	Target
0.4	2.75	10.34	0.95	7.95	Target

0.394	2.75	10.34	0.93	7.95	Target
0.35	2.45	9.21	0.93	7.08	Target
0.39	2.75	10.34	0.92	7.95	Target
0.34	2.45	9.21	0.90	7.08	Target
0.38	2.75	10.34	0.90	7.94	Target
0.425	3.1	11.66	0.89	8.95	Target
0.33	2.25	8.46	0.95	6.51	Target
0.3	2.06	7.75	0.95	5.96	Target
0.295	2.06	7.75	0.93	5.95	Target
0.285	2.06	7.75	0.90	5.95	Target(Figure 45)
0.26	1.8	6.77	0.94	5.20	Extinction
0.27	1.88	7.07	0.93	5.43	Extinction
0.271	1.9	7.14	0.93	5.49	Extinction
0.275	1.94	7.29	0.92	5.61	Extinction
0.245	1.76	6.62	0.90	5.08	Extinction
0.285	2.07	7.78	0.89	5.98	Extinction
0.375	2.75	10.34	0.89	7.94	Extinction
0.42	3.1	11.66	0.88	8.95	Extinction
0.33	2.45	9.21	0.88	7.07	Extinction
0.31	2	7.52	1.01	5.80	Spiral (Figure 41)

B.3 Flame Patterns in n-Heptane-Air Premixtures using the Nebulizer & Spray Chamber Setup on a Bronze McKenna Burner

n-Heptane Flow Rate (SLM)	Air Flow Rate (SLM)	Φ	V_{exit} (cm/s)	Patterns
0.18	8	1.20	4.82	Stable planar flame
0.18	8	1.15	4.82	Stable planar flame
0.17	8.01	1.09	4.82	Stable planar flame
0.16	8.01	1.04	4.82	Stable planar flame
0.15	8.02	0.98	4.82	Instabilities occur
0.14	8.03	0.92	4.82	Target
0.13	8.04	0.87	4.82	Target
0.13	8.05	0.81	4.82	Target
0.12	8.06	0.76	4.82	Target disappears
0.18	8.5	1.13	5.12	Stable planar flame
0.18	8.51	1.08	5.12	Stable planar flame
0.17	8.52	1.02	5.12	Stable planar flame
0.16	8.53	0.97	5.12	Instabilities occur
0.15	8.54	0.92	5.12	Target
0.14	8.55	0.87	5.12	Target
0.13	8.55	0.82	5.12	Extinction

0.13	8.56	0.76	5.12	Extinction
0.20	9.48	1.10	5.71	Stable planar flame (Figure 56)
0.19	9.5	1.06	5.71	Stable planar flame
0.18	9.5	1.01	5.71	Instabilities occur
0.18	9.51	0.96	5.71	Complex instabilities (Figure 57)
0.17	9.52	0.92	5.71	Complex instabilities
0.16	9.53	0.87	5.71	Target
0.15	9.54	0.82	5.71	Target (Figure 58)
0.14	9.55	0.78	5.71	Target
0.13	9.56	0.73	5.71	Extinction
0.22	9.96	1.14	6.00	Stable planar flame
0.21	9.97	1.09	6.00	Stable planar flame
0.20	9.98	1.05	6.00	Stable planar flame
0.19	9.99	1.00	6.00	Instabilities occur
0.18	10	0.96	6.00	Complex target
0.18	10	0.92	6.00	Complex target
0.17	10.01	0.87	6.00	Target
0.16	10.02	0.83	6.00	Target
0.15	10.03	0.78	6.00	Target
0.14	10.04	0.74	6.00	Target
0.13	10.05	0.69	6.00	Extinction
0.23	10.94	1.12	6.59	Stable planar flame
0.23	10.95	1.08	6.59	Stable planar flame
0.22	10.96	1.04	6.59	Stable planar flame
0.21	10.97	0.99	6.59	Stable planar flame
0.20	10.98	0.95	6.59	Instabilities occur
0.19	10.99	0.91	6.59	Complex target
0.18	11	0.87	6.59	Target
0.18	11.01	0.83	6.59	Target
0.17	11.01	0.79	6.59	Target
0.16	11.02	0.75	6.59	Extinction
0.15	11.03	0.71	6.59	Extinction
0.25	11.93	1.10	7.18	Stable planar flame
0.24	11.94	1.06	7.18	Stable planar flame
0.23	11.95	1.02	7.18	Stable planar flame
0.23	11.96	0.99	7.18	Instabilities occur
0.22	11.97	0.95	7.18	Complex target
0.21	11.97	0.91	7.18	Complex target
0.20	11.98	0.87	7.18	Complex target
0.19	11.99	0.84	7.18	Target
0.18	12	0.80	7.18	Target
0.18	12.01	0.76	7.18	Target
0.17	12.02	0.73	7.18	Target
0.16	12.02	0.69	7.18	Extinction

0.25	12.98	1.01	7.80	Stable planar flame
0.24	12.99	0.97	7.80	Instabilities occur
0.23	13	0.94	7.80	Complex instabilities
0.23	13.01	0.91	7.80	Complex instabilities
0.22	13.02	0.87	7.80	Complex target
0.21	13.03	0.84	7.80	Complex target
0.20	13.03	0.80	7.80	Target
0.19	13.04	0.77	7.80	Target
0.18	13.05	0.74	7.80	Target
0.18	13.06	0.70	7.80	Extinction
0.17	13.07	0.67	7.80	Extinction
0.28	13.95	1.03	8.39	Stable planar flame
0.27	13.96	1.00	8.39	Instabilities occur
0.26	13.97	0.97	8.39	Instabilities occur
0.25	13.98	0.94	8.39	Complex instabilities
0.24	13.99	0.90	8.39	Complex target
0.23	14	0.87	8.39	Complex target
0.23	14.01	0.84	8.39	Complex target
0.22	14.02	0.81	8.39	Complex target
0.21	14.03	0.78	8.39	Complex target
0.20	14.03	0.75	8.39	Target
0.19	14.04	0.71	8.39	Extinction
0.30	14.88	1.06	8.95	Stable planar flame
0.29	14.89	1.03	8.95	Stable planar flame
0.28	14.89	1.00	8.95	Stable planar flame
0.28	14.9	0.97	8.95	Instabilities occur
0.27	14.91	0.94	8.95	Complex instabilities
0.26	14.92	0.91	8.95	Complex instabilities
0.25	14.93	0.88	8.95	Complex instabilities
0.24	14.94	0.85	8.95	Complex instabilities
0.23	14.95	0.82	8.95	Complex target
0.23	14.95	0.79	8.95	Complex target
0.22	14.96	0.76	8.95	Complex target
0.21	14.97	0.73	8.95	Complex target
0.20	14.98	0.70	8.95	Complex target
0.19	14.99	0.67	8.95	Extinction
0.18	15	0.64	8.95	Extinction
0.32	15.92	1.04	9.57	Stable planar flame
0.31	15.93	1.01	9.57	Stable planar flame
0.30	15.93	0.99	9.57	Stable planar flame
0.29	15.94	0.96	9.57	Stable planar flame
0.28	15.95	0.93	9.57	Instabilities occur
0.28	15.95	0.90	9.57	Complex instabilities
0.27	15.96	0.87	9.57	Complex instabilities
0.26	15.97	0.85	9.57	Complex instabilities
0.25	15.98	0.82	9.57	Complex instabilities

0.24	15.99	0.79	9.57	Complex instabilities
0.23	16	0.76	9.57	Target
0.23	16	0.74	9.57	Target
0.22	16.01	0.71	9.57	Target

B.4 Flame Patterns in n-Heptane-O_2-He Premixtures using the Nebulizer & Spray Chamber Setup on a Bronze McKenna Burner

n-Heptane Flow Rate (SLM)	O_2 Flow Rate (SLM)	He Flow Rate (SLM)	Ratio of He: O2	Φ	Vexit (cm/s)	Pattern
0.18	1.71	6.88	4.02	1.18	5.17	Irregular
0.18	1.75	6.88	3.93	1.15	5.20	Extinction
0.18	1.83	6.40	3.50	1.10	4.96	Complex target
0.19	1.9	7.15	3.76	1.11	5.45	Extinction
0.23	1.32	6.23	4.72	1.88	4.58	Stable planar flame
0.23	1.66	6.23	3.75	1.49	4.78	Two split rotating arms
0.23	2.38	8.14	3.42	1.08	6.34	Complex target(Figure 60)
0.25	2.38	9.00	3.78	1.16	6.86	Stable planar flame
0.25	2.45	9.00	3.67	1.12	6.90	Complex target(Figure 61)
0.25	2.59	9.00	3.47	1.06	6.98	Target
0.26	2.89	9.08	3.14	0.98	7.21	Extinction
0.27	2.82	10.53	3.73	1.04	8.03	Target (Figure 62)
0.27	2.84	10.53	3.71	1.03	8.04	Extinction
0.28	2.50	10.53	4.21	1.25	7.85	Stable planar flame
0.28	2.60	10.53	4.05	1.20	7.91	Stable planar flame
0.28	2.70	10.53	3.90	1.15	7.97	Stable planar flame
0.28	2.80	10.53	3.76	1.11	8.03	Instabilities occur
0.28	2.85	10.53	3.69	1.09	8.06	Target
0.28	2.90	10.53	3.63	1.07	8.08	Target
0.28	3.00	10.53	3.51	1.04	8.14	Target
0.28	3.10	10.53	3.40	1.01	8.20	Target

0.28	3.15	10.53	3.34	0.99	8.23	Target
0.28	3.20	10.53	3.29	0.97	8.26	Target
0.30	3.00	10.53	3.51	1.10	8.15	Stable planar flame
0.30	3.20	10.53	3.29	1.03	8.27	Complex target
0.30	3.25	10.53	3.24	1.02	8.30	Target
0.30	3.30	10.53	3.19	1.00	8.33	Target
0.30	3.40	11.00	3.24	0.97	8.67	Target
0.30	2.00	6.23	3.12	1.65	5.03	Stable planar flame
0.30	2.30	6.23	2.71	1.43	5.21	Complex target
0.30	2.34	6.23	2.66	1.41	5.23	Target
0.30	2.35	6.23	2.65	1.40	5.24	Extinction

B.5 Flame Patterns in n-Octane-Air Premixtures using the Nebulizer & Spray Chamber Setup on a Bronze McKenna Burner

n-Octane Flow Rate (SLM)	Air Flow Rate (SLM)	Φ	Vexit (cm/s)	Patterns
0.17	8	1.23	4.81	Stable planar flame
0.16	8	1.17	4.81	Stable planar flame
0.15	8.01	1.12	4.81	Stable planar flame
0.14	8.02	1.06	4.81	Stable planar flame
0.14	8.03	1.00	4.81	Instabilities occur
0.13	8.03	0.95	4.81	Target
0.12	8.04	0.89	4.81	LFL
0.18	10	1.07	6.00	Stable planar flame
0.17	10.01	1.03	6.00	Instabilities occur
0.17	10.02	0.98	6.00	Target
0.16	10.02	0.94	6.00	Target
0.15	10.03	0.89	6.00	Target
0.14	10.04	0.85	6.00	Target
0.14	10.05	0.80	6.00	LFL
0.23	11.98	1.12	7.20	Stable planar flame
0.22	11.99	1.08	7.20	Stable planar flame
0.21	12	1.04	7.20	Stable planar flame
0.20	12.01	1.00	7.20	Instabilities occur
0.20	12.02	0.97	7.20	Complex instabilities
0.19	12.03	0.93	7.20	Complex instabilities
0.18	12.04	0.89	7.20	Target

0.17	12.04	0.85	7.20	Target
0.17	12.05	0.82	7.20	Target
0.16	12.06	0.78	7.20	LFL
0.24	12.99	1.10	7.80	Stable planar flame
0.23	12.99	1.07	7.80	Stable planar flame
0.23	13	1.03	7.80	Stable planar flame
0.22	13.01	1.00	7.80	Stable planar flame
0.21	13.02	0.96	7.80	Instabilities occur
0.20	13.03	0.93	7.80	Complex instabilities
0.20	13.04	0.89	7.80	Complex instabilities
0.19	13.04	0.86	7.80	Target
0.18	13.05	0.82	7.80	Target
0.17	13.06	0.79	7.80	Target
0.17	13.07	0.75	7.80	LFL
0.26	13.98	1.12	8.40	Stable planar flame
0.26	13.99	1.09	8.40	Stable planar flame
0.25	14	1.05	8.40	Stable planar flame
0.24	14	1.02	8.40	Stable planar flame
0.23	14.01	0.99	8.40	Stable planar flame
0.23	14.02	0.96	8.40	Instabilities occur
0.22	14.03	0.92	8.40	Complex instabilities
0.21	14.04	0.89	8.40	Complex instabilities
0.20	14.05	0.86	8.40	Complex instabilities
0.20	14.06	0.83	8.40	Target
0.19	14.06	0.79	8.40	Target
0.18	14.07	0.76	8.40	LFL
0.29	15	1.13	9.01	Stable planar flame
0.28	15.01	1.10	9.01	Stable planar flame
0.27	15.02	1.07	9.01	Stable planar flame
0.26	15.02	1.04	9.01	Stable planar flame
0.26	15.03	1.01	9.01	Stable planar flame
0.25	15.04	0.98	9.01	Instabilities occur
0.24	15.05	0.95	9.01	Complex instabilities
0.23	15.05	0.92	9.01	Complex instabilities
0.23	15.06	0.89	9.01	Target (Figure 64)
0.22	15.07	0.86	9.01	Target

B.6 Flame Patterns in n-Octane-O_2-He Premixtures using the Nebulizer & Spray Chamber Setup on a Bronze McKenna Burner

n-Octane Flow Rate (SLM)	O_2 Flow Rate (SLM)	He Flow Rate (SLM)	Φ	Vexit (cm/s)	Patterns
0.20	2.1	8	1.16	6.07	Stable planar flame
0.20	2.2	8	1.11	6.13	Instability occurs
0.21	2.4	8	1.10	6.26	Bi-state instabilities
0.21	2.4	8.4	1.10	6.49	Bi-state instabilities
0.21	2.42	8	1.09	6.27	Target
0.21	2.43	7.9	1.08	6.21	Bi-state instabilities
0.21	2.44	7.9	1.08	6.22	Complex target
0.21	2.5	9.4	1.05	7.14	Extinction
0.23	2.26	9.4	1.25	7.01	Stable planar flame
0.23	2.4	9.4	1.17	7.09	Instability occurs
0.23	2.45	9.4	1.15	7.12	Bi-state instabilities
0.23	2.47	9.4	1.14	7.13	Bi-state instabilities (Figure 66)
0.23	2.5	9.4	1.13	7.15	Bi-state instabilities
0.23	2.8	9.4	1.01	7.33	Target (Figure 67)
0.24	2.43	11.34	1.24	8.26	Stable planar flame
0.24	2.54	11.34	1.18	8.32	Instability occurs
0.24	3	11.34	1.00	8.60	Target

Appendix C: Enhanced Catalytic Combustion using Nano-Size Platinum Particles

Appendix C describes the supplemental work done by the author in the premixed combustion lab on nanocatalytic platinum particles enhancing the combustion rate of Methanol-air and Ethanol-air mixtures under room temperature. Section C.1 is the introduction of this research. Section C.2 describes the historical researches done in the past on the catalytic combustion using platinum. Section C.3 describes the experimental facility and methodology. Section C.4 describes the experimental results of Methanol-air and ethanol-air mixtures. Section C.5 provides closure for this appendix.

C.1 Introduction

Sub-micron and nano-size catalytic particles are significantly more reactive than their bulk counterparts and can be used to enhance the performance of catalytic combustors. Their high specific surface areas (typically 1-200 m^2/g) and unique morphologies clearly contribute to their enhanced reactivity. Differences in adsorbed species and/or their distributions may also play an important role, yet are not clear. The purpose of this study is to quantify the effects of particle size, catalyst loading, and flow residence time on the reactivity of methanol-air premixtures over dispersed Platinum (Pt) nanoparticles. As such, experiments were conducted in an atmospheric flow tube reactor seeded with 2-5nm, 200nm, and 500nm Pt particles distributed on a SiC fiber substrate. Temperature measurements and exhaust gas species analyses were obtained for different size particles, catalyst loadings and flow conditions. Materials characterization of the particles was also conducted and SEM images were compared before and after sustained reaction to assess

changes in their morphology and distribution owed to sintering and/or coalescence of the catalytic particles. Methanol-air premixtures were extremely reactive for a broad range of parameters (light-off at room-temperature), consistent with observations at Oak Ridge National Laboratory. Interestingly, the highest steady-state temperatures were measured with 200nm Pt particles with a small mass loading and 2-5nm particles with a high mass loading for a fixed flow residence time. The results suggest that the reactivity of methanol on Pt increases, and then decreases, with increasing surface area for small catalyst loadings whereas a monotonic increase in reactivity was observed with larger catalyst loadings. Preliminary observations obtained with ethanol-air premixtures are also reported.

C.2 A Historical Review of Catalytic Combustion

Catalysts are used to extend combustion operation ranges, reduce undesirable emissions, promote reforming and paralysis reactions, and generate heat (Hayes and Kolaczkowski, 1998; Pfefferle and Pfefferle, 1986; Talukdar and Bhattacharyya, 2006; Warnatz et al., 2001). Catalysts are also finding new applications in micro-scale combustors to promote flame stabilization and enable lower-temperature operation for improved thermal management (Ahn, 2005) in addition to microscale methanol reformers for use with miniature fuel cells (Holladay et al., 2002). In practice, however, the catalyst must be initially heated to its lightoff-temperature -- the temperature for 50% conversion efficiency, which typically ranges from 150^{o}C for alcohols (i.e., methanol, ethanol, isopropanol, and butanol) to 250^{o}C (or higher) depending on the feedstock and the catalyst material (John Zink, 1991). Preheating was accomplished by heating with

exhaust gases, electrically or otherwise.

Many catalyst applications would benefit if the catalyst light-off temperature could be reduced. Advantages include: mitigation of undesirable emissions produced during the preheat period (e.g., cold-start emissions in automotive applications), lower operating temperatures, extended catalyst lifecycles, and possibly the use of less expensive catalyst materials in particulate form. As demonstrated in this work and a recent experimental study conducted at Oak Ridge National Laboratory, small alcohols are highly reactive catalytic on Platinum particles and light-off at room-temperature (Hu et al., 2005; Hu and Thundat, 2006; Ricciuti et al., 2007a; Ricciuti et al., 2007b). The high surface area of the particles and associated number of active sites is believed to be the primary cause for the enhanced reactivity, yet the specifics are not well understood.

Knowing that catalytic particles can be highly reactive encourages additional research into the effects of the size, distribution, loading, and morphology of catalytically-active particles, which is especially relevant today as nanoparticle manufacturing techniques are being increasingly refined and commercialized. The specific objectives of this study are therefore to experimentally evaluate the effects of particle size, catalyst loading, and flow residence time on the reactivity of methanol-air premixtures using dispersed sub-micron and nano-size catalytic particles. Materials characterization is also conducted to assess possible changes of the particles owed to sintering, melting and/or redistribution. Methanol is selected as the primary fuel since it lights-off at room temperature and has many practical applications for chemical synthesis and fuel cells. While limited results are reported herein, preliminary experiments have also been conducted with ethanol-air

premixtures on Pt particles and light-off at room-temperature has also been recorded, albeit over a relatively narrow range of parameters compared with the methanol-air cases.

Computational models that can predict size dependent properties for methanol-air on Pt are not available. To the best of our knowledge, mechanistic rate information for methanol oxidation on Pt has yet to be tuned and validated at atmospheric conditions while studies to date have considered methanol oxidation at low pressures (2 Torr) and temperatures between 400 K to 1600 K (Zum Mallen and Schmidt, 1996). In these studies, lean, stoichiometric and rich cases were considered, yet no reactivity was observed for temperatures less than 400 K. Moreover, the published rate parameters unfortunately cannot be expected to capture the enhanced catalytic activity associated with nano-size and sub-micron size particles since they were tuned for low-pressure and species adsorption rates are known to be pressure dependent.

For completeness, it should be noted that a significant amount of work has also focused on electrocatalysis of aqueous methanol on Platinum, Palladium, Rhodium, and bimetallics for application to direct methanol fuel cells (Carrette et al., 2001; Hamnett, 1997; Wieckowski et al., 2003). In these systems, catalytic activity has been noted to change with the specific surface area of the catalyst (Gloaguen et al., 1997), albeit published results are contradictory (Atwood et al., 1980; Watanabe et al., 1989). On one hand, Atwood and co-workers suggest that the reactivity of methanol on Pt is a function of the specific surface area of the catalyst and report increased reactivity with increasing surface area to a limit beyond which the reactivity decreased. In other studies, the catalytic activity did not depend on the size of the particles nor the distance between them (Watanabe et al., 1989). In general, increasing specific surface area has been noted to

decrease catalytic activity for high specific surface areas (Yahikozawa et al., 1991), which has been attributed to adsorption of oxygenated species on the surface (Gloaguen et al., 1997). The distribution of absorbed species may also be different for bulk-layered versus dispersed particles (Leger, 2001; Mukerjee, 1990). Lastly, note that gold nanoparticles also have demonstrated activity at ambient temperature, are effective for oxidizing CO, and have size-dependent reaction rates (Cortie and Van der Lingen, 2002); in bulk form, gold is otherwise regarded as inert.

In a broader context, the use of catalytic nanoparticles for enhanced combustion in the transportation and energy sectors is expected to become increasingly important, especially as issues associated with energy and the environment become international priorities (Bui et al., 1997; Cho and Law, 1986; Deutschmann et al., 2000). New applications including high surface area catalytic coatings for advanced engine designs and after-treatment emissions control to name a few can benefit.

C.3 Experimental Facility and Methodology

A schematic of the experimental apparatus is shown in Figure 105. It consists of a cylindrical quartz flow reactor (0.38 cm i.d., 0.63 cm o.d., 15.2 cm long) seeded with 2-5 nm, 200 nm or 500 nm Pt particles that were electrostatically supported on a fused-silica fiber insert (2 cm long centered at 7.6 cm downstream of the reactor inlet; 100 mg). The 500 nm and 200 nm Pt particles were supplied by Technics, Inc. and the 2-5 nm particles were manufactured by Strem Chemicals. Fine-wire thermocouples (Type K, 0.0254 cm diameter, and closed sheath) were inserted through one of three side-mounted ports and used to measure the temperature of the reactants, the temperature at the center of the

fused-silica wool, and the temperature of the combustion products. The thermocouples were located at 3.8 cm, 7.6 cm, and 11.4 cm, respectively, from the entrance of the reactor.

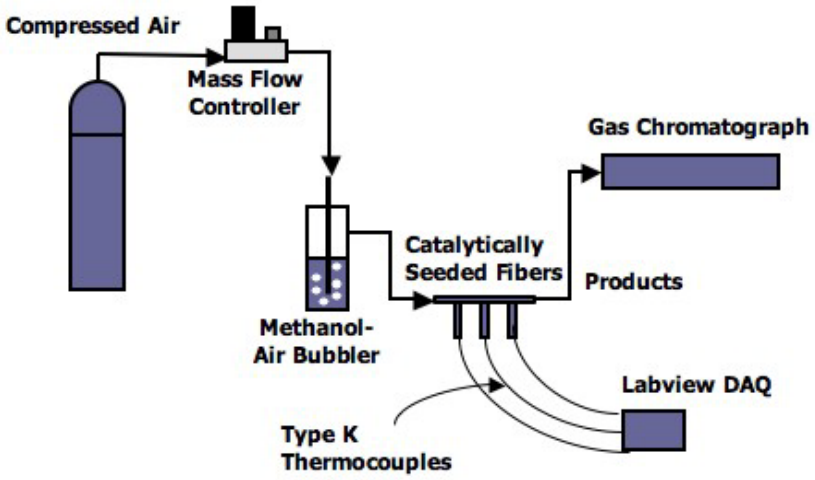

(a)

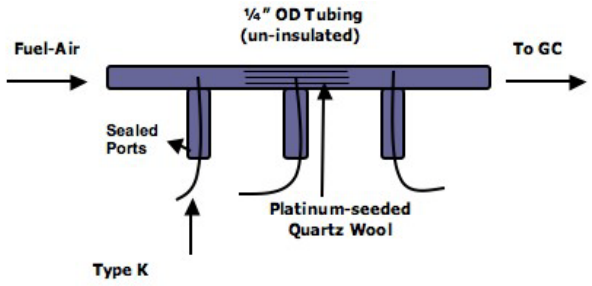

(b)

Figure 105: Experimental schematic of the reactor and mass flow system. (a) overall experimental setup; (b) flow reactor.

To characterize the dispersed catalytic particles, the Brunauer-Emmett-Teller (BET) method was used to determine the specific surface areas (S) of the 200nm and 500nm particles and determined to be 9.11m^2/g and 1.50m^2/g, respectively. The 2-5nm particles were characterized by the manufacturer using Transmission Electron Microscopy (TEM) and their specific surface area is estimated to range from 56.1m^2/g to 140m^2/g. This estimate assumes spherical particles and a homogeneous particle distribution where S (m^2/g) = 6/(ρd) x 10^3 (Gloaguen et al., 1997). Here, d is the particle diameter (in nm) and ρ is the density of Pt (21.4 g/cm^3).

For each size particle, catalyst mass loadings of 15mg and 30mg were examined in addition to 50mg and 60mg loadings for the 200nm and 500nm particles. In all cases, the catalyst inserts were prepared by dispersing the Pt particles on the fused-silica fibers in an analogous way to the sample preparation procedure used in previous studies (Hu et al., 2005; Hu and Thundat, 2006; Ricciuti et al., 2007a; Ricciuti et al., 2007b). Inspection of the 200nm and 500nm samples was then performed using a Scanning Electron Microscope (FEI/Philips XL30 ESEM), the results of which suggested a relatively uniform dispersion of the particles. A more heterogeneous size distribution owed to particle agglomeration was observed at higher magnifications as shown in Figure 106 where agglomerate sizes ranged from 1 to 2.5μm for the 500nm particles and 400nm to 2.0μm for the 200nm particles. Smaller primary particles were also visible, most notably with the 200nm particles, which suggests a higher surface area and increased number of available sites for molecular decomposition and heterogeneous reaction. Repeat sample preparations and SEM characterization produced catalyst distributions with similar features.

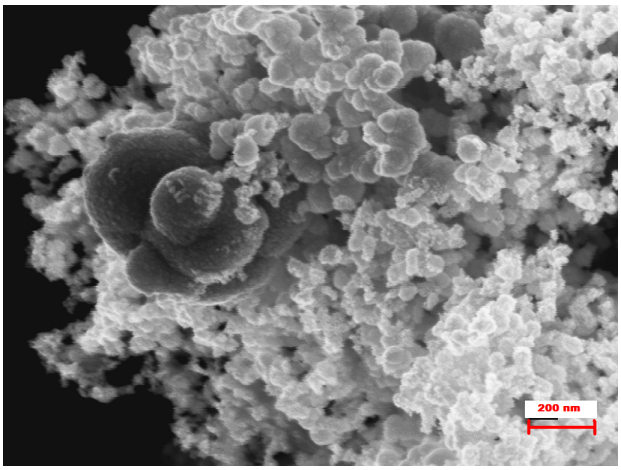

(a)

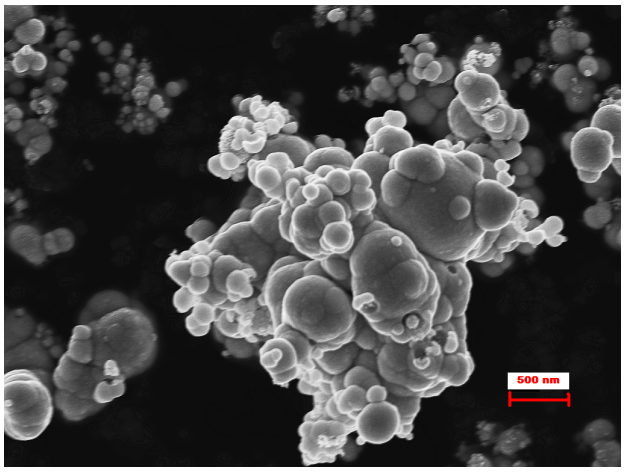

(b)

Figure 106: SEM images of Pt nanoparticles: (a) 500nm particles (indicator bar: 500nm); (b) 200nm particles (indicator bar: 200nm).

The platinum particles were examined for purity and crystallite sizing using powder x-ray diffractometry (Siemens D500 X-Ray Powder Diffractometer). Spectral scans were obtained over a 2θ range of 15–85° at a scan rate of 3° 2θ/min using increments of 0.05° 2θ and Cu K_α radiation (λ = 1.540Å). Peak positions and analyses, and relative intensities of the powder patterns were identified using the Jade MDI+ software and by comparison with reference spectra (International Center for Diffraction Data). The XRD

spectra matched the reference data file for Pt based on both peak location and relative magnitude. The average crystallite size of the platinum particles was determined using the Scherrer equation:

$$d_p = \frac{0.94\lambda}{\beta_{1/2}\cos(\theta)} \qquad (20)$$

where d_p is the average crystallite size, λ is the wavelength of the source emission (1.542 Å for this study), $\beta_{1/2}$ is the full width at half-maximum of the peak used for the analysis, and θ is the XRD scattering angle of the peak.

All sizes of Pt powder yielded similar XRD spectra (see Figure 107). The crystallite size was determined through averaging the (111), (200), and (220) peak crystallite size results for all powders. The 2-5 nm platinum yielded a crystallite size of $d_p = 10.4 \pm 0.4$ nm. The 200 nm platinum yielded a crystallite size of $d_p = 11.5 \pm 0.7$ nm. The 500 nm platinum yielded a $d_p = 11.7 \pm 0.6$ nm crystallite size.

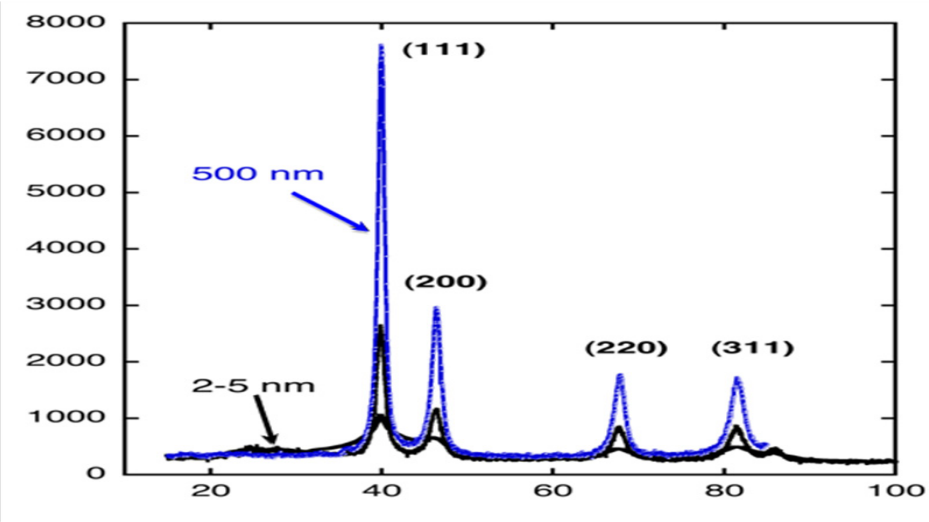

Figure 107: Representative x-ray diffraction spectra of the 2-5 nm and 500 nm platinum powder.

The vaporized fuel was delivered using a methanol bubbler connected to a metered dry air supply. The air flowed through the bubbler and into the flow reactor. All tests were conducted with methanol at room temperature (23^{o}C) and atmospheric pressure. Different flow rates were considered for each case with mean inlet cold flow speeds ranging from 2.5 to 25.0 cm/s. Assuming the premixture was completely saturated, the equivalence ratio (ϕ) for the methanol-air premixture was slightly rich (ϕ=1.25). To confirm inlet concentrations and avoid uncertainties introduced by fluctuations in room temperature (and thus fuel vapor pressure) and to ensure that the flow residence time was adequate, the reactants were analyzed using an Agilent 3000 Micro GC equipped with three different columns (Plot U, OV-1, MolSieve 5A) and a thermal conductivity detector. All samples were transferred through 1/16" activity-tested stainless-steel tubing and filtered upstream of the GC inlet with two-inline 7μm sintered stainless-steel filters. The equivalence ratio of the initial reactants as a function of mean inlet flow speed for methanol-air is shown in Figure 108 where each data point is the average of ten samples taken during steady operation. Clearly, the methanol concentration slightly decreases as the flow speed increases, which indicates that the residence time is increasingly too short for the air to fully saturate with methanol at the higher flow rates. A gas sample was also taken from the compressed air cylinder and the oxygen concentration for all tests was determined to be 19.7% by volume - balance nitrogen.

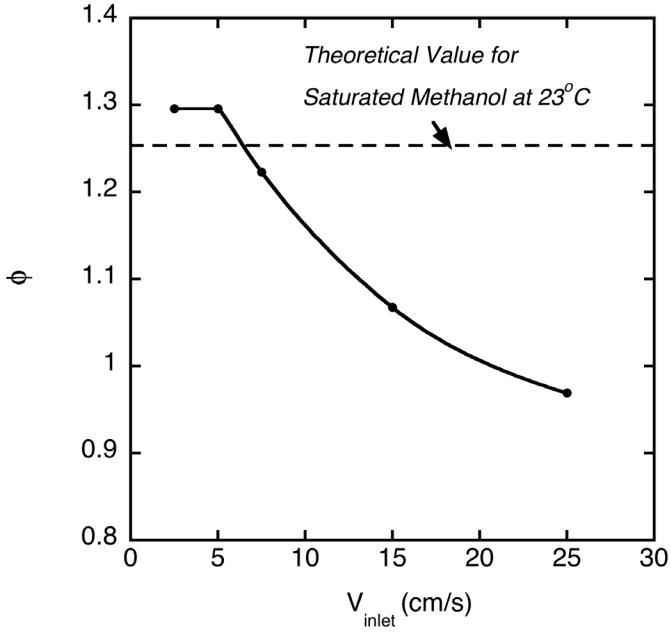

Figure 108: The equivalence ratio of the methanol-air premixture as a function of the inlet flow speed as determined via GC measurements.

Gas chromatography measurements were also taken of the products at multiple times during the course of the reaction after the temperature in the reactor reached a steady-state as determined by the thermocouple data. To quench the reaction in the exhaust gas samples, a heat exchanger was installed along the sampling line to cool the sample, while maintaining condensable species in the vapor phase.

C.4 Experimental Results

C.4.1 Effect of Particle Size

The temperature histories taken at the center of the reactor are plotted in Figure 109 for premixed methanol-air flowing in reactors seeded with the three different size particles and two different catalyst loadings (case a: 15mg Pt = 13% wt.; case b: 30mg Pt

= 23% wt.). The reactant inlet flow speed was fixed in both cases at 25 cm/s. Room-temperature was sufficient to light-off all conditions tested and a steady-state temperature was achieved following the initial transient, which resided for several minutes.

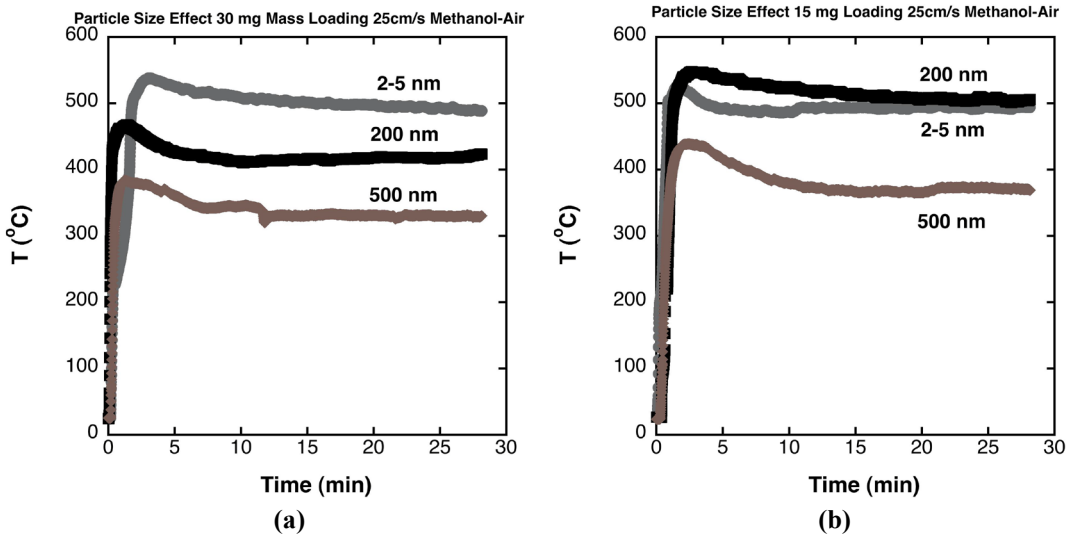

Figure 109: Temperature histories at the center of the reactor using near-stoichiometric methanol-air (Φ = 0.97) at 25 cm/s in reactors seeded with 2-5nm, 200nm and 500nm Pt particles; mass loading are: (a) 15mg and (b) 30mg.

The 500nm particles were less reactive than either the 2-5nm or 200nm particles for the 15mg catalyst loading (Figure 109a), while the steady-state temperature associated with the 2-5nm particles was slightly lower than that measured with the 200nm particles. This suggests a non-monotonic dependence on particle size. In contrast, the steady-state temperature using a 30mg catalyst loading monotonically increased with decreasing particle size, which suggests an increase in reactivity with the increasing specific surface area associated with the smaller particles (Figure 109b).

C.4.2 Effect of Mass Loading

The temperature histories associated with catalyst loadings from 15mg to 60mg are shown in Figure 110 for reactors seeded with: (a) 2-5nm, (b) 200nm, and (c) 500nm Pt particles. As shown, the steady-state temperatures for the 2-5nm particles with a 15mg and a 30mg catalyst loading asymptote to approximately the same value (500^{o}C), whereas the steady-state temperatures decrease with increased catalyst loading for both the 200nm and 500nm particles. The observed decrease in steady-state temperature suggests that the heat loss rate associated with the 200nm and 500nm test cases is greater than the heat generation rate owed to the exothermicity of the surface reactions, which was expected to increase with an increase in catalyst loading due to the increase in the number of active sites. To assess the importance of heat loss, additional nearly-adiabatic experiments were conducted in thermally-insulated reactors. In all cases, the measured steady-state temperatures were larger in the insulated reactors than in the uninsulated reactors, yet the trends remained consistent.

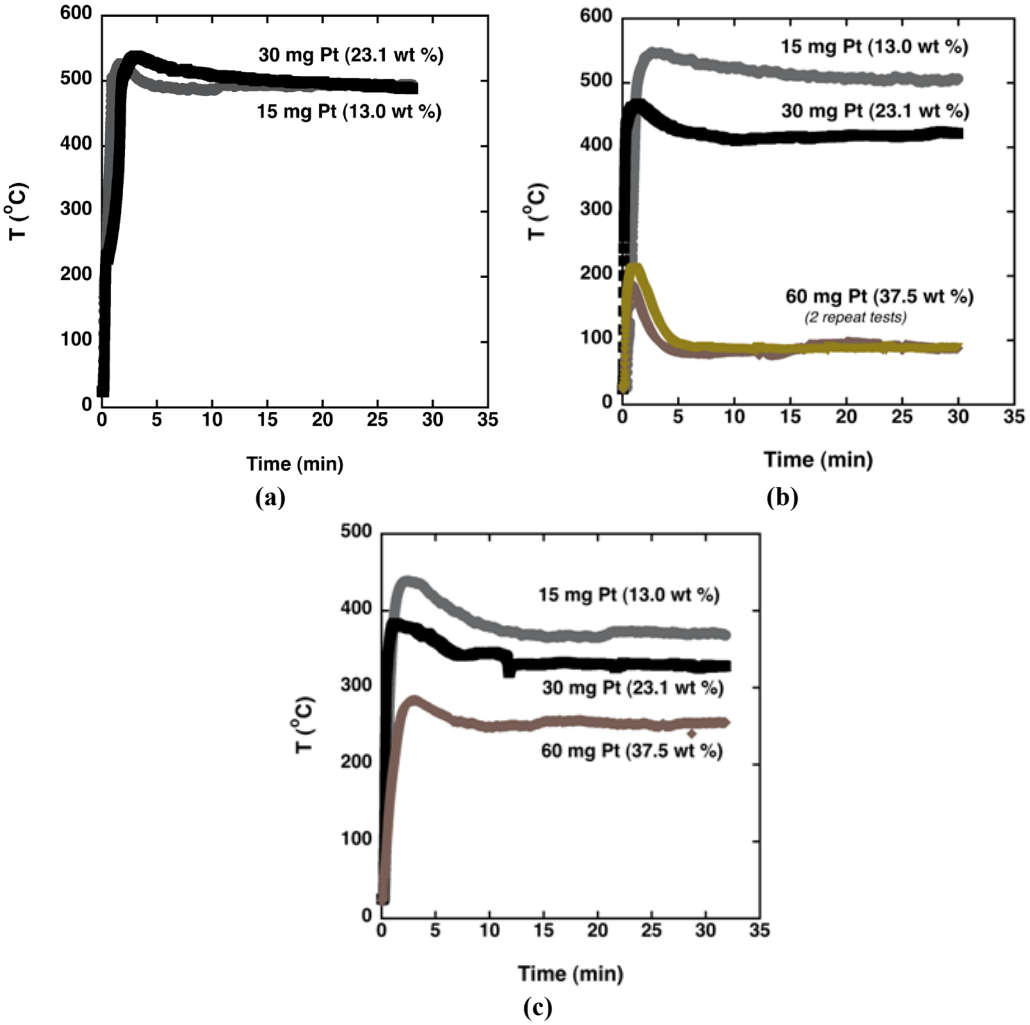

Figure 110: Temperature histories for different particle sizes: (a) 2-5nm, (b) 200nm, (c) 500nm and catalyst loadings in the range of 15mg to 60mg (methanol-air: Φ = 0.97 at 25 cm/s).

C.4.3 Effect of Flow Residence Time

Temperature histories obtained for different reactor inlet flow speeds in the range of 2.5–25.0cm/s are shown in Figure 111 for the 200nm and 500nm size particles, respectively, with a 15mg Pt loading. For the 200nm particle tests, the measured steady-state temperatures increased with an increase in inlet flow speed consistent with an

increase in available chemical energy. Two-stage ignition was also observed with both particle sizes, characterized by a transition from a low to a high temperature ignition regime (Figure 111a at 7.5cm/s, Figure 111b at 12.5cm/s) consistent with the first observations reported by Hu and co-workers (Hu et al., 2005; Hu and Thundat, 2006). A similar two-stage ignition process has been reported in H_2-assisted catalytic ignition of lean methane-air premixtures over bulk platinum where O_2 coverage on the platinum initially inhibits methane oxidation at low temperatures until the catalyst temperature was sufficient for the transition to ignition (Deutschmann et al., 2000).

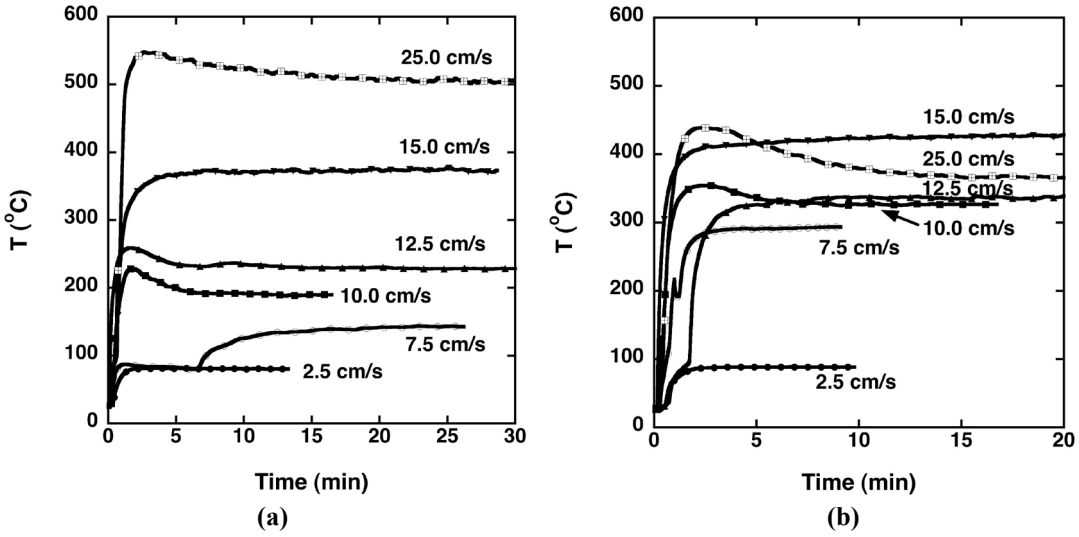

Figure 111: Temperature histories for different inlet flow speeds for: (a) 200nm and (b) 500nm Pt particles with a 15mg mass loading (methanol-air: Φ = 0.97 at 25 cm/s).

C.4.4 Effect of Heat Loss

Previous results were obtained under the non-insulation conditions. To study the effects of heat loss on the reactivity of nano-particles on Methanol-air premixtures,

reactors were also insulated and several cases were tested. The effect of heat loss on different mass loadings for 200 nm Pt particles is shown in Figure 112. For the insulated cases, the higher mass loading produced higher steady temperature, which is contrary to the previous observations for non-insulated cases, seen in Figure 110. This can be explained that more mass loading has more active reaction sites that can produce more heat. While the heat loss for more mass loading is larger when they are placed in a non-insulated reactor.

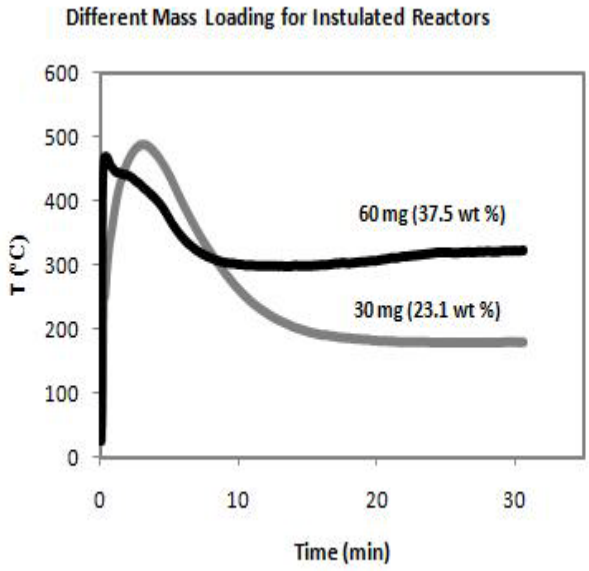

Figure 112: Temperature histories for different mass loading for insulated reactors using 200 nm Pt particles at 25 cm/s.

Also comparisons between insulated and non-insulated cases using 200 nm 30 mg at 25 cm/s and 2-5 nm also 30 mg mass loading at 25 cm/s were conducted and results are

shown in Figure 113(a) and (b). Higher steady temperatures were observed in insulated reactors since heat loss plays an important role in determining the steady temperatures.

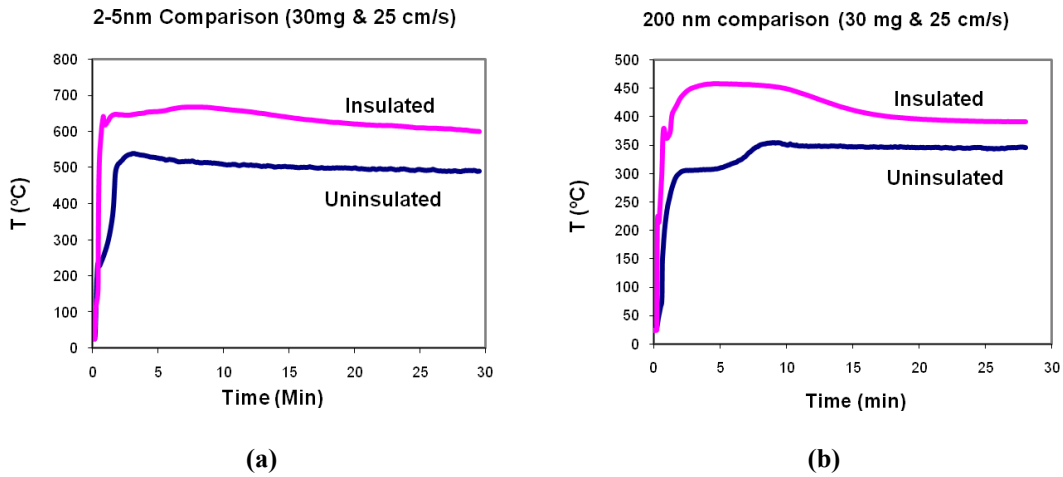

Figure 113: Temperature histories for comparison between uninsulated and insulated cases using 30 mg mass loading and 25 cm/s flow rate for (a) 2-5 nm and (b) 200 nm Pt particles.

C.4.5 Particle Characterization

SEM micrographs of the Pt particles were taken after 300 min of continuous operation for the 500nm and 200nm particles with a catalyst loading of 15mg (Figure 114a and b, respectively). Images were not taken for the 2-5nm particles since they were smaller than the minimum resolution of the SEM.

The micrographs indicate different extents of restructuring and coalescence of the particles noting that the 500nm particles remained relatively unagglomerated, yet exhibited evidence of surface pitting (Figure 114a), while the 200nm particles sintered and restructured (Figure 114b). For the 500nm and 200nm particle cases shown, the

corresponding steady-state temperatures were 326 (±29) ^{o}C and 284 (±13) ^{o}C, respectively, with indicated error bars determined from the standard deviation of the results of multiple repeat tests. To evaluate the effect of the restructured catalyst on the reproducibility of the measured steady-state temperature, multiple repeat tests were conducted and the center temperature was reproducible to within ± 20%.

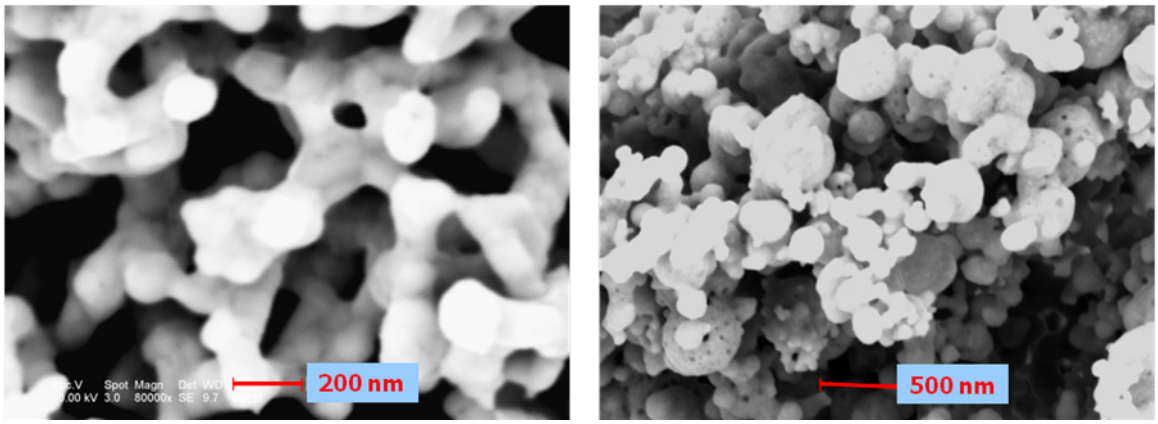

(a) (b)

Figure 114: SEM Images of Pt catalyst after a 300 min experiment using methanol-air (Φ = 1.17) at 10cm/s with a 15mg loading: (a) 200nm particles; (b) 500nm particles.

C.4.6 Gas Chromatography Results

The stable product species concentrations were analyzed for all particle sizes with a 30mg catalyst loading. The steady-state temperatures and corresponding concentrations of methanol, oxygen, and carbon dioxide are plotted in Figure 115. Nearly complete oxidation occurred in all cases noting that less than 2% methanol was detected in the product mixture and the CO_2 concentration was within one percent of the theoretical concentration for complete oxidation for a stoichiometric premixture (11.6% by vol.). A

small percentage of hydrogen was detected during the initial transient (t < 3 min.) for all cases but not detected thereafter.

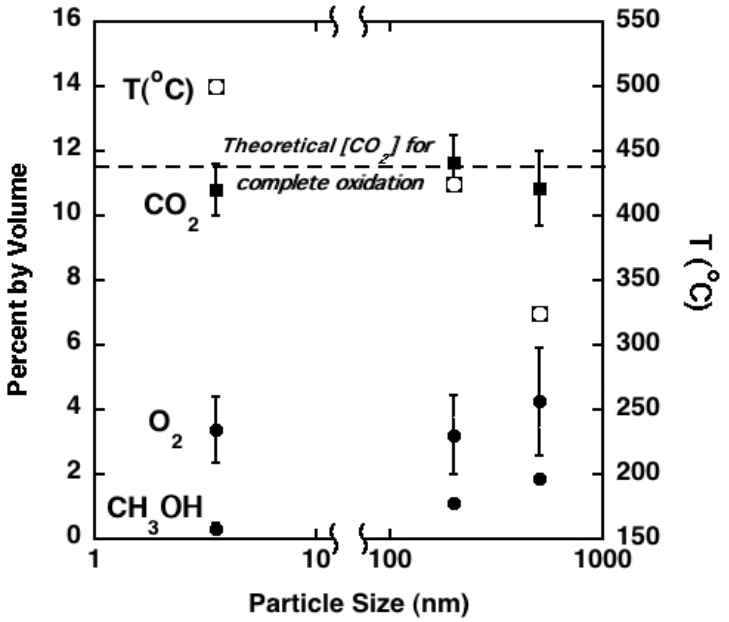

Figure 115: GC analyses of combustion products for methanol-air (Φ =0.97) over 2-5nm, 200nm, and 500nm Pt particles using a 30mg loading and an inlet flow speed of 25 cm/s.

C.4.7 Ethanol-Air Results

Ethanol-air mixtures (ϕ = 0.99) were also tested in reactors seeded with: 2-5nm particles with a 15mg and a 30mg Pt loading and 200nm and 500nm particles with a 30mg, 50mg and 60mg loadings at a fixed flow speed (25 cm/s). Without preheating the Pt particles, only the 2-5nm particles with a 30mg loading and the 200nm particles with a 50mg and 60mg loading produced a self-sustained reaction.

The temperature histories taken from TC#2 associated with the 2-5 nm particles for an ethanol-air flow speed of 25 cm/s is shown in Figure 116a and b for two different mass loadings (15 mg and 30 mg, respectively). Interestingly, for the 2-5nm Pt particles with a 15mg loading, the temperature was observed to initially increase 10^{o}C for approximately 2 minutes then decrease exponentially as the reaction self-arrested. With a higher mass loading (30mg), a steady temperature of 500^{o}C was maintained.

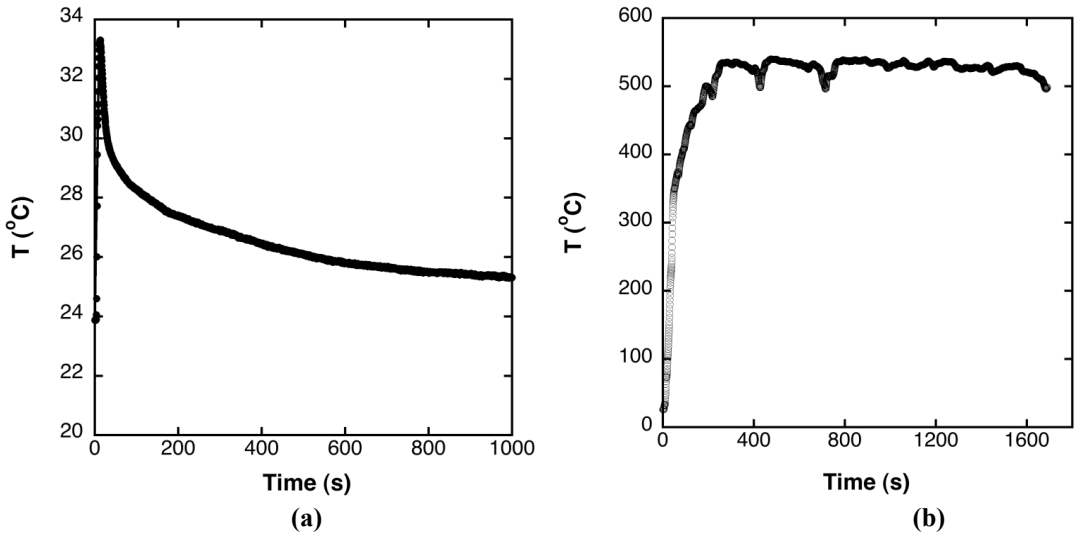

Figure 116: Temperature histories associated with a near-stoichiometric ethanol-air premixture initially at room-temperature at 25 cm/s in reactors seeded with 2-5 nm Pt particles with a mass loading of (a) 15 mg and (b) 30 mg.

Additional data were obtained at controlled initial temperatures to determine the light-off temperature versus particle size for a fixed mass loading (30mg). Figure 117 shows the temperature histories at the center of the reactors using all three sizes of particles at 25 cm/s and 30mg mass loading. The light-off temperature for 500 nm platinum particles was 90 ^{o}C and for the 200 nm was 40 ^{o}C, but for 2-5 nm particles was

room temperature which was 25 ^{o}C. This result tells us that the light-off temperature increases monotonically with increasing particle size.

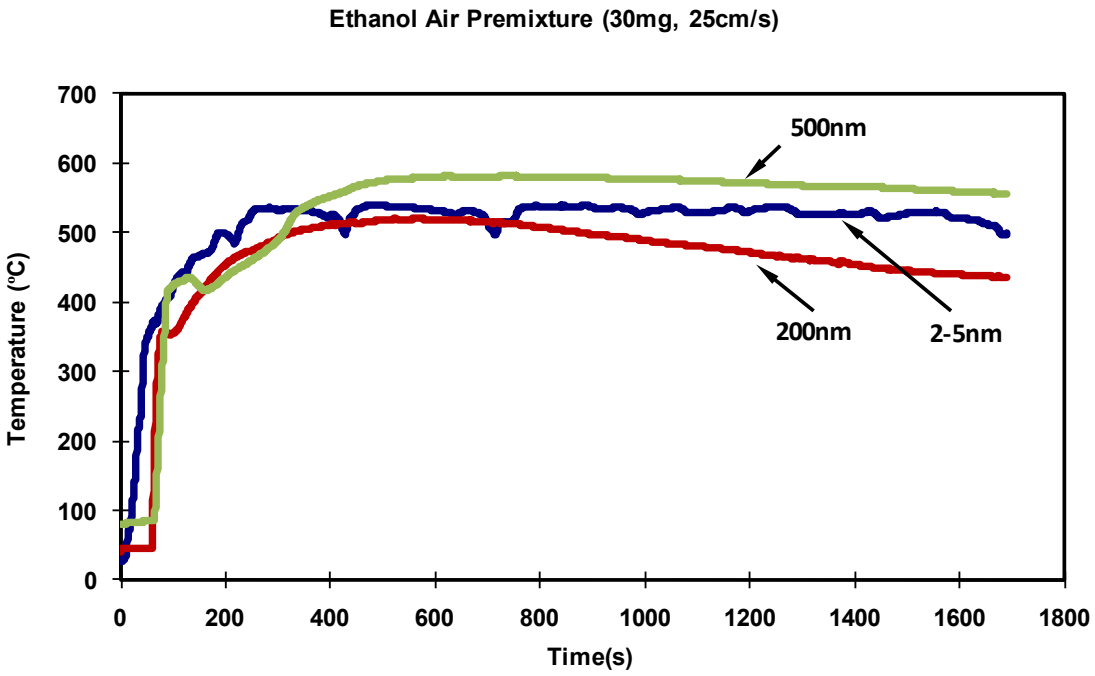

Figure 117: Temperature histories at the center of the reactor using near-stoichiometric ethanol-air at 25 cm/s in reactors seeded with 2-5nm, 200nm and 500nm Pt particles; mass loading are 30mg.

The temperature histories taken from three representative tests using 200 nm particles with different mass loading are also shown in Figure 118. The data were taken from three different quartz reactors under otherwise identical conditions except the initial light-off temperature of the nanoparticles. Two tests were again reactive at room-temperature for the higher mass loading (50mg and 60mg) and the temperature maintained a steady value after the first few minutes. But for the smallest mass loading for 200 nm particle, the light-off temperature was 40^{o}C. With respect to reproducibility, the steady state

temperature compared favorably within 20% (450°C vs. 375°C) for the 50mg mass loadings.

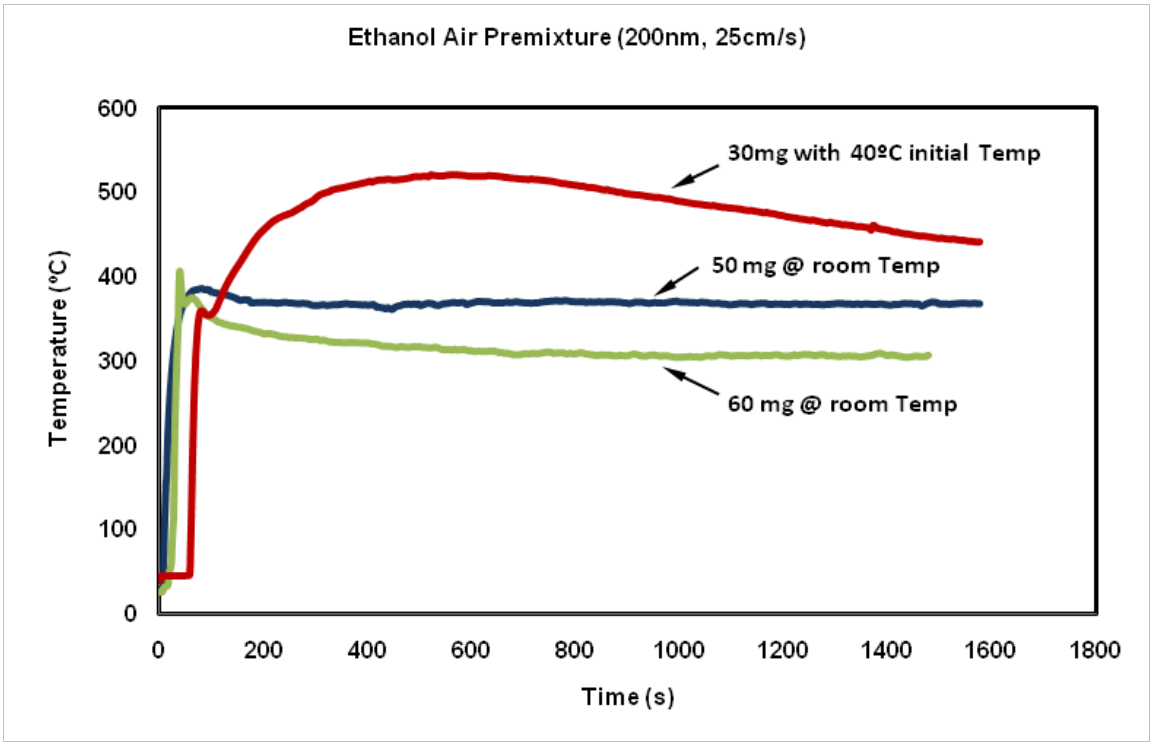

Figure 118: Temperature histories associated with a near-stoichiometric ethanol-air premixture for 200nm particles at 25 cm/s for different mass loading under different initial temperature.

The comparison between methanol-air and ethanol-air premixtures using 2-5 nm Pt particles at 30 mg mass loading and 25 cm/s flow rate is shown in Figure 119. The steady temperature for methanol-air mixtures was around 350 °C and the steady temperature for ethanol-air mixtures was around 500 °C. The results show that ethanol has higher energy density than methanol.

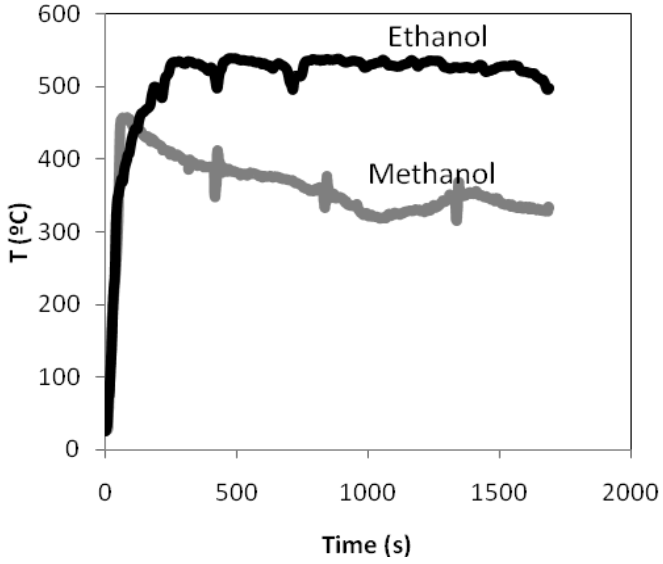

Figure 119: Temperature histories with the comparison between methanol and ethanol using 2-5 nm Pt particles at a mass loading of 30 mg and flow rate of 25 cm/s.

C.5 Discussion and Conclusion

Benchmark experiments conducted in an atmospheric flow tube reactor seeded with catalytic particles confirmed light-off at room-temperature for all methanol-air premixtures and some of ethanol-air premixtures. Methanol-air premixtures were extremely reactive over all experimental conditions with light-off occurring at room-temperature, which was also observed with ethanol-air for select conditions. For methanol-air premixtures, the highest steady-state temperature was measured with the 2-5nm Pt particles with a 30mg loading and the larger 200nm Pt particles using a smaller catalyst loading (15mg). As expected, the steady-state temperatures increased monotonically with decreasing particle size with the 30mg loading for both methanol-air and ethanol-air premixtures, while evidence of a non-monotonic trend was observed with

the 15mg loading for methanol-air premixture. Differences in adsorbed species and/or changes in the distribution of the adsorbed species may account for the non-monotonic behavior observed with the 15mg loading and should encourage spectroscopic studies. No difference was observed with the 2-5 nm particles for different mass loadings, while the temperature decreased for the 200 nm and 500 nm case with higher loadings. The competition between the changes in reactivity due to an increase in available active sites and the enhanced heat loss associated with the larger particles is likely responsible for the observed behavior. The importance of heat loss demonstrated in tests conducted in insulated reactors where the trend was reversed (higher temperature with higher catalyst loadings). For ethanol-air premixture, the light-off temperature for different particle size increases with the increasing particle size and decreases with increasing mass loading.

To model the experimental data in the future, the surface chemistry for nano-size Pt needs to be refined and coupled to detailed gas-phase kinetic mechanisms such as those reported and validated by Norton and Dryer (Norton and Dryer, 1992), Held and Dryer (Held and Dryer, 1998), Egolfogolous et al. (Egolfopoulos et al., 1992) and more recent work by Li and co-workers (Li et al., 2007a; Li et al., 2007b). While the major reaction pathways for methanol on Pt are known (Zum Mallen and Schmidt, 1996), these models need to be extended and validated for a broader range of operating conditions. It is clear that methanol is adsorbed on the surface, dissociates into CH_2OH and CH_3O, which can react and produce formaldehyde and/or formyl radicals that then produce CO, yet the role of the nanoparticle structure needs to be incorporated into future models since it can affect the distribution of the adsorbed species and the observed reactivity (Leger, 2001).

C.6 Closure

Additional work was performed in the area of the enhanced catalytic combustion using nano-size platinum particles. The purpose of this study was to quantify the effects of particle size, catalyst loading, and flow residence time on the reactivity of small alcohols on Platinum (Pt) nanoparticles. Experiments were conducted in an atmospheric flow tube reactor seeded with nanoparticles distributed on a SiC fiber substrate. Temperature measurements and exhaust gas species analysis were obtained for different reactor parameters. Materials characterization of the particles was also conducted to compare the particles before and after sustained reaction to assess the effects of sintering and potential restructuring of the catalyst. The results indicate that the nanoparticles are more reactive than their bulk counterparts in large part due to their high surface-to-volume ratio.

VITA

Yi Ma was born on December 15, 1979 in Hengdong County, Hunan Province, P. R. China. She attended Hengdong Elementary School until 5th grade, following which she continued her education at Hengdong No.1 Middle School and High School. She graduated from Hengdong No.1 High School in 1996.

Yi attended Zhejiang University in Hangzhou, Zhejiang Province, China as an undergraduate and majored in Mechanical and Energy Engineering. She graduated from Zhejiang University with B.S. degree with Distinguished Student Honor in 2000 and was admitted to Graduate School at Zhejiang University with entrance examination waived in the same year. Her master studies at Zhejiang University mainly focused on the clean coal combustion technology. Her research focused on desulfuration using sulfur-removal additives during the combustion and the formation of calcium sulphoaluminate from desulfuration process of coal combustion at high temperature, where she coauthored three technical papers. She graduated from Zhejiang University with her M.S. degree in March, 2003 and decided to pursue a Ph.D. degree at Drexel University in Philadelphia, PA in US. During her PHD program, she studied the high Le number flame instabilities of premixed combustion and enhanced combustion using sub-micron and nano-sized platinum particles with small alcohols and air premixtures, where she has coauthored five technical papers and made several technical presentations.

Yi is a member of the Combustion Institute and American Society of Mechanical Engineers.